Experimental Investigation of Single Bubbles and Bubble Interactions in Nucleate Boiling

Experimentelle Untersuchung zu Einzelblasen und Blaseninteraktionen beim Behältersieden
Zur Erlangung des akademischen Grades Doktor-Ingenieur (Dr.-Ing.)
genehmigte Dissertation von Dipl.-Ing. Axel Sielaff aus Langenhagen
Mai 2014 — Darmstadt — D 17

TECHNISCHE
UNIVERSITÄT
DARMSTADT

Fachbereich Maschinenbau
Institut für Technische Thermodynamik

Experimental Investigation of Single Bubbles and Bubble Interactions in Nucleate Boiling
Experimentelle Untersuchung zu Einzelblasen und Blaseninteraktionen beim Behältersieden

Genehmigte Dissertation von Dipl.-Ing. Axel Sielaff aus Langenhagen

1. Gutachten: Prof. Dr.-Ing. Peter Stephan
2. Gutachten: Prof. Dr.-Ing. habil. Andrea Luke

Tag der Einreichung: 09.12.2013
Tag der Prüfung: 12.02.2014

Darmstadt — D 17

This thesis is available online at:
URN: urn:nbn:de:tuda-tuprints-37039
URL: http://tuprints.ulb.tu-darmstadt.de/3703

Vorwort

Die vorliegende Arbeit entstand während meiner Zeit am Institut für Technische Thermodynamik der Technischen Universität Darmstadt unter der Leitung von Herrn Professor Stephan. Herrn Stephan möchte ich herzlich für die Möglichkeit zur Promotion und das mir entgegengebrachte Vertrauen danken. Durch dieses Vertrauen zur selbstständigen Arbeit, bei gleichzeitig stets offener Tür, schuf er ein sehr angenehmes und produktives Arbeitsklima. Darüber hinaus danke ich ihm für viele Anregungen und ertragreiche Diskussionen zu meiner Arbeit und über diese hinaus. Weiter danke ich ihm für die hervorragende Leitung des Institutes. Erst durch diese stehen neben den fachlichen auch die materiellen Voraussetzungen für erfolgreiche wissenschaftliche Arbeit zur Verfügung. Im diesem Rahmen danke ich ebenfalls der Deutschen Forschungsgemeinschaft für die Finanzierung dieser Arbeit.

Ein besonderer Dank gebührt ebenfalls Frau Professor Luke. Neben der Übernahme des Koreferats legte Frau Luke durch Ihre Förderung und Hilfestellung während meines Studiums einen Grundstein für die spätere Arbeit während meiner Promotion. Mein Studienaufenthalt in London und die vielen Erfahrungen, die ich während meiner Tätigkeit als hilfswissenschaftlicher Mitarbeiter an Ihrem Institut sammeln konnte, sind hierbei nur Beispiele Ihrer Unterstützung.

Meinen Kollegen möchte ich für die stets gute, freundschaftliche und produktive Zusammenarbeit danken. Die unzähligen Diskussionen inner- und außerhalb des Institutes haben einen nicht zu unterschätzenden Anteil am Gelingen dieser Arbeit. Diesbezüglich möchte ich mich vor allem für die stets konstruktive Kritik bedanken. Diese zeigte mir nicht nur das Interesse an meiner Arbeit, sondern half darüber hinaus Irrwege zu vermeiden. Dieser Dank gilt insbesondere meinen langjährigen Bürokollegen Stefan Batzdorf und Felix Crößmann. Für die darüber hinaus gehende Korrektur und Hilfestellung bei der schriftlichen Ausarbeitung möchte ich Jochen Dietl, Martin Freystein und Axel Dietrich danken.

Allen Studenten, die mich im Rahmen von studentischen Arbeiten oder hilfswissenschaftlichen Tätigkeiten unterstützt haben, danke ich für Ihren wertvollen Beitrag zu meiner Promotion. Hervorzuheben sind hierbei Philip Hänichen, Andreas Froitzheim, Tim Hartmann, Johannes Schuck und Niklas Stäter. Den Mitarbeitern der Werkstatt Dirk Feldmann, Matthias Felter, Dirk Oppermann, Reiner Engel und Werkstattleiter Roland Berntheisel danke ich für die hervorragende Zusammenarbeit. Neben höchster Qualität in der Fertigung der Anlagen, standen mir die Mitarbeiter der Werkstatt stets als kompetente Ansprechpartner für die Konstruktion und Auslegung der Versuchsanlagen zur Seite. Weiter möchte ich dem Techniker des Institutes, Robert Schrod, für gute und konstruktive Zusammenarbeit danken. Seine Erfahrung und Hilfestellung sind vor allem beim Aufbau komplexer messtechnischen Anlagen unerlässlich.

Von Herzen danke ich meiner Familie und insbesondere meinen Eltern für die jahrelange Unterstützung. Ohne ihre Fürsorge hätte ich meine schulische Ausbildung und das sich anschließende Studium sicherlich nicht mit der Möglichkeit zur Promotion abschließen können.

Abschließend möchte ich meiner zukünftigen Frau Julia danken. Ob sie sich geduldig Details meiner Arbeit anhörte, mich beriet oder motivierte, ob sie mir aktiv bei der Arbeit geholfen hat oder mir, durch die Übernahme anderer Tätigkeiten, Zeit für meine Arbeit einräumte, sie hat mit allem maßgeblich und über die zu erwartenden Maße hinaus am Gelingen dieser Arbeit beigetragen.

Hiermit versichere ich, die vorliegende Dissertation ohne Hilfe Dritter nur mit den angegebenen Quellen und Hilfsmitteln angefertigt zu haben. Alle Stellen, die aus Quellen entnommen wurden, sind als solche kenntlich gemacht. Diese Arbeit hat in gleicher oder ähnlicher Form noch keiner Prüfungsbehörde vorgelegen.

Darmstadt, den 9. Dezember 2013

(A. Sielaff)

"I often say that when you can measure what you are speaking about, and express it in numbers, you know something about it ; ..."

Sir William Thomson (Lord Kelvin) [146]

Abstract (English, German)

Abstract

Boiling processes are widely used in technical applications. The chemical industry, power plant technology, and refrigeration engineering are just a few examples. Intensive research on pool boiling processes has been undertaken for decades. Nevertheless, the physical phenomena are still not sufficiently understood. This is mainly caused by the large number of influencing factors and the wide range of length and time scales boiling processes act on.

Especially through the research on small length scales a better understanding of the underlying physical phenomena should be achieved. The subject of the present thesis is the experimental investigation of boiling processes with single bubbles and bubble interactions. In a further step, the reliability of the results obtained for a few interacting bubbles is tested on a technical length scale.

Within the framework of this thesis an experimental setup is designed and fabricated. By use of optical measurement methods (black/white and infrared) the shape of the bubbles and the temperature close to the heater surface are measured simultaneously. Within the experimental setup and method emphasis is put on the validity of the obtained data (especially the infrared measurements). The test setup is based on a thin stainless steel foil used as a Joule heater. The working fluid is FC-72. Almost all experiments are performed at subatmospheric pressure.

In this thesis general results for boiling experiments with single bubbles, for example concerning the departure diameter and frequency,

Kurzzusammenfassung

In sehr vielen technischen Prozessen finden Siedeprozesse Anwendung. Die chemische Industrie, Energie- und Kraftwerkstechnik sowie die Kältetechnik seien dabei nur einige Beispiele. Die zu Grunde liegenden physikalischen Prozesse sind, trotz jahrzehntelanger Forschung, bisher nicht ausreichend verstanden. Als Begründung dafür sind hauptsächlich die große Anzahl an relevanten Einflussparametern und die unterschiedlichen Längenskalen, die den Siedeprozess beeinflussen, zu nennen.

Durch Untersuchungen auf kleinen Längenskalen sollen die grundlegenden physikalischen Phänomene besser verstanden werden. Das Thema der vorliegenden Arbeit ist die experimentelle Untersuchung an einzelnen Blasen sowie der Interaktion mehrerer Blasen. Darüber hinaus wird untersucht in wieweit sich die erzielten Ergebnisse der Interaktion einzelner Blasen auf technische Siedeprozesse übertragen lassen.

Im Rahmen dieser Arbeit wird ein Versuchsstand konstruiert und aufgebaut. Mittels optischer Messtechnik (schwarz/weiß und infrarot) ist die simultane Erfassung der Blasenform sowie des Temperaturfeldes in der Nähe der Heizeroberfläche möglich. Ein Schwerpunkt liegt dabei auf der Zuverlässigkeit der Anlage und der verwendeten Auswertungsverfahren. Diesbezüglich ist vor allem die Untersuchung der Einflussfaktoren und deren Auswirkung bei der Nutzung der Infrarotthermografie zu nennen. Den Kern des Versuchsstandes bildet eine dünne Edelstahlfolie, die elektrisch beheizt wird. Als Versuchsfluid wird FC-72 verwendet. Die durchgeführten Experimente werden fast ausschließlich bei Unterdruck durchgeführt.

are presented. It is observed that for single bubbles a thin liquid layer can remain underneath a bubble after nucleation. By comparing bubble growth with and without this layer a first statement of the validity of the contact line and microlayer model is achieved. Experiments with bubbles coalescing show a clear dependency of the coalescence frequency on the system pressure, partly following a probability distribution. In comparison of a case with and without bubble coalescence an increased heat transfer is found for the coalescence case. This effect is mainly caused by hydrodynamic phenomena and sometimes also by the formation of residual droplets inside large bubbles. It is shown that the effects observed for the coalescence of two bubbles is not transferable to global boiling processes. With the help of a Monte-Carlo simulation these phenomena can be explained by different coalescence behavior. The experimental results furthermore give a possible explanation for the deviations between experimental and analytic bubble departure diameters due to the dynamic effects during bubble nucleation.

In der vorliegenden Arbeit werden Ergebnisse grundlegender Untersuchungen zum Sieden an Einzelblasen, wie z.B. des Blasenabreißdurchmessers und der -frequenz vorgestellt. Darüber hinaus kann beobachtet werden, dass für das Sieden einzelner Blasen ein dünner Flüssigkeitsfilm nach der Nukleation unter der Blase zurückbleiben kann. Ein Vergleich von Blasen mit und ohne Flüssigkeitsfilm ermöglicht eine erste Aussage zur Gültigkeit der Modelle der Kontaktlinien- und Dünnfilmverdampfung. In den Untersuchungen zur Blasenkoaleszenz ist eine Abhängigkeit der Koaleszenzfrequenz bezüglich des Systemdrucks festzustellen. Für bestimmte Drücke folgt diese Abhängigkeit einer Wahrscheinlichkeitsverteilung. Die Analyse der Wärmestromdichteprofile für vorliegende Blasenkoaleszenz ergibt eine Erhöhung des Wärmestroms gegenüber der Situation ohne Blasenkoaleszenz. Dieses ist maßgleich in einer veränderten Hydrodynamik und einem möglichen Zurückbleiben eines Tropfens innerhalb der Blase begründet. Weiter wird die Übertragbarkeit der Ergebnisse, die anhand weniger interagierender Blasen erzielt wurden, auf technische Siedeprozesse untersucht. Die Phänomene, die bei der Untersuchung an einzelnen Blasen festgestellt worden sind, können nicht reproduziert werden. Unter Verwendung einer Monte-Carlo Simulation, lassen sich diese Unterschiede auf ein unterschiedliches Koaleszenzverhalten zurückführen. Mittels der experimentellen Ergebnisse wird eine mögliche Erklärung für die häufige Abweichung zwischen analytischen und experimentellen Blasenabreißdurchmessern vorgestellt. Die Erklärung beruht auf den dynamischen Effekten bei der Nukleation einzelner Blasen.

Contents

Nomenclature

Latin Letters

A	dispersion constant	J
a	acceleration	$\mathrm{m/s^2}$
a	attraction parameter	$\mathrm{Pa\,m/mol^2}$
a	$\sqrt{2} \cdot$ capillary length (Fritz Eq. 2.5)	m
b	axis intercept	
b	repulsion parameter	$\mathrm{m^3/mol}$
C	phase fraction	-
C_{pm}	conversion factor	pixel/mm
c_0	speed of light	$3 \times 10^8\,\mathrm{m/s}$
c_p	specific heat capacity	J/(kg K)
D	depth	m
d	diameter	m
E_b	black body radiation	$\mathrm{W/m^2}$
F	force	N
f	frequency	1/s
g	earth gravity	$9.81\,\mathrm{m/s^2}$
h	Planck's constant	$6.63 \times 10^{-34}\,\mathrm{J\,s}$
h	heat transfer coefficient	$\mathrm{W/(m^2\,K)}$
Δh_v	enthalpy of vaporization	J/kg
I	intensity	-
I	electrical current	A
$J_{b,\lambda}$	spectral black body emission	$\mathrm{W/m^3}$
K	curvature	1/m
k	thermal conductivity	W/(m K)
k_B	Boltzmann constant	$1.38 \times 10^{-23}\,\mathrm{J/K}$

l	length	m
M	mass	kg
N	picture number	-
n	number of cavities	-
P	power	W
p	pressure	Pa
Q	heat flow	W
q	heat flux	W/m^2
q	leakage rate	mbar l/s
q_0	area projected heat source	W/m^2
R	cavity radius	m
$\overline{R}$	universal gas constant	J/(kmol K)
r	radius	m
S	cavity distance	m
S_{sp}	spacing parameter	-
T	temperature	°C / K / °F
V	volume	m^3
$\overline{V}$	molecular volume	m^3/mol
v	specific volume	m^3/kg
v	velocity	m/s
X	position	pixel
X_p	distance	No. of pixel
x	Cartesian coordinate	m
y	Cartesian coordinate	m
z	Cartesian coordinate	m

Greek Letters

α_t	temperature coefficient	1/K
α	thermal diffusivity	m^2/s
β	thermal expansion coefficient	1/K
δ	thickness	m
ζ	cavity angle	deg

η	dynamic viscosity	Pa s
Θ	contact angle	deg
λ	wavelength	m
ν	kinematic viscosity	m^2/s
ρ	density	kg/m^3
σ	surface tension	N/m
σ_{SB}	Stefan-Boltzmann constant	$5.67 \times 10^{-8}\,W/(m^2\,K^4)$
τ	time	s
Ψ	thermal interaction intensity	1/m

Subscripts

0	value at reference condition
3ph	three-phase contact
a	approximated
ad	adhesion
ap	apparent
av	advancing
b	bubble
buo	buoyancy
c	convection
calc	calculation
crit	critical
cl	contact line
cyc	cycle
e	earth
e	equilibrium
eq	equivalent
ev	evaporation
fo	foot
f	fluid
f	foil
H	heater

int	interface
l	liquid
l	left
m	mean
ml	microlayer
max	maximum
min	minimum
q	quenching
r	right
ref	reference
SB	Stefan - Boltzmann
sat	saturation
str	structured
sup	superheat
tot	total
tr	threshold
V	vector
v	vapor
wait	waiting

Abbreviations

CAD	Computer-aided design
CHF	Critical heat flux
DEPIcT	Detection of phase by infrared thermometry
EPDM	Ethylene propylene diene monomer
FDM	Finite difference method
FEM	Finite element method
FEP	Fluorinated ethylene propylene
FIB	Focused ionic beam
FVM	Finite volume method
IHTP	Inverse heat transfer problem
IQR	Interquartile range

IR	Infrared
LED	Light-emitting diode
LS	Level set
LIF	Laser-induced fluorescence
NSD	Nucleation site density
MTC	Microthermocouple
MTCP	Microthermocouple probe
ONB	Onset of nucleate boiling
PE	Polyethylene
PIV	Particle image velocimetry
PTFE	Polytetrafluoroethylene
VIS	Visible
VOF	Volume of fluid

Characteristic Numbers

Bo	Bond number	$\frac{\rho a L^2}{\sigma}$
Ja	Jacob number	$\frac{\Delta T c_p}{\Delta h_v}$
Ma	Marangoni number	$\frac{\mathrm{d}\sigma}{\mathrm{d}T}\frac{L \Delta T \rho^2 c_p}{k}$
Nu	Nusselt number	$\frac{hL}{k}$
Pr	Prandtl number	$\frac{\nu c_p \rho}{k}$
Re	Reynolds number	$\frac{vL}{\nu}$
L_c	Capillary length	$\sqrt{\frac{\sigma}{g(\rho_\mathrm{l} - \rho_\mathrm{v})}}$

Chapter 1

Introduction and Motivation

About 250,000 years ago the first technical boiling application was invented by using a hearth for food production [108]. With the passing of time further applications based on boiling processes (e.g. steel hardening) have been used. In the first century Hero of Alexandria invented the steam engine. Its improvement by James Watt (patented in 1769) paved the way for the industrial revolution [116]. Nowadays, boiling and evaporation processes can be found in countless technical applications, e.g. in the energy, chemical, and space industries. In the domestic sector boiling remained almost unchanged for a quarter of a million years for cooking. It can also be found in refrigerators and heat pumps and is upcoming for the cooling of electronic devices. Looking at this number of successfully working processes raises the question if further research on boiling processes is still necessary. On closer inspection it is apparent that a detailed description of boiling processes is still not possible due to physical phenomena that are still not sufficiently understood. The huge number of existing correlations for the prediction of boiling processes is almost completely based on former experimental investigations. An extrapolation of these correlations is only applicable in a narrow range.

New and upcoming applications (e.g. cooling of high-power electronics, desalination) and political regulations (e.g. the ban of specific refrigerants for environmental protection [38]) require the design and construction of new boiling devices with unknown characteristics. Furthermore, the decreasing availability of primary energy resources requires an enhancement in the efficiency of existing processes and machinery.

In order to meet these demands comprehensive scientific investigations on nucleate boiling are performed based on three major pillars. First, experimental research on a technical length scale; second, direct numerical simulation of boiling processes on a length scale of one or a few single bubbles; and third, experimental investigations on the same length scale as the numerical investigations. Analytic research has declined over the past years, probably due to the high complexity of the boiling process, but assists in each of the three pillars. By performing experimental research on a small length scale physical phenomena can be recognized and better understood. Moreover, these experiments are of major importance for the validation of the numerical models. Validated numerical models enable investigations and analyses not possible with experimental research. For example, the influence of a single fluid property can only be investigated in numerical research, as in experimental research all fluid properties generally change concurrently. The transferability of the results and the predictions made can be validated experimentally on a technical scale. Further, the experiments performed on a technical scale can identify phenomena worth being investigated on a smaller length scale. Additionally, research on a technical scale provides the most reliable predictions of the boiling process for comparable industrial processes.

In the scope of this thesis experimental research is performed on a small length scale with a single bubble and bubbles coalescing. Further, it is investigated experimentally whether the phenomena observed for nucleate boiling of single bubbles and bubble coalescence can be found within boiling processes on a larger length scale. Therefore a main test setup was designed, commissioned, and adapted due to the changing technical requirements. Several series of measurements were performed. For the large amount of data collected algorithms were developed for automated data processing. For the remaining data set the evaluation was performed manually. Afterwards, the results are compared in order to give a descriptive overview. The structure of the thesis is as follows: In chapter 2 a short overview of the relevant fundamentals on boiling is presented. Moreover, existing models as well as experimental investigations and results necessary for this thesis are introduced. Subsequently open scientific questions are discussed and the goals and approaches of the current work are presented. In chapters 3 and 4 the experimental setup and method are described. An emphasis is put on the reliability of the test setup and the infrared measurement technique. In chapter 5 the results obtained are presented and discussed. A concluding evaluation of the results is given in 5.3. Finally, a summary and conclusion of the thesis is given in chapter 6.

Chapter 2

State of the Art

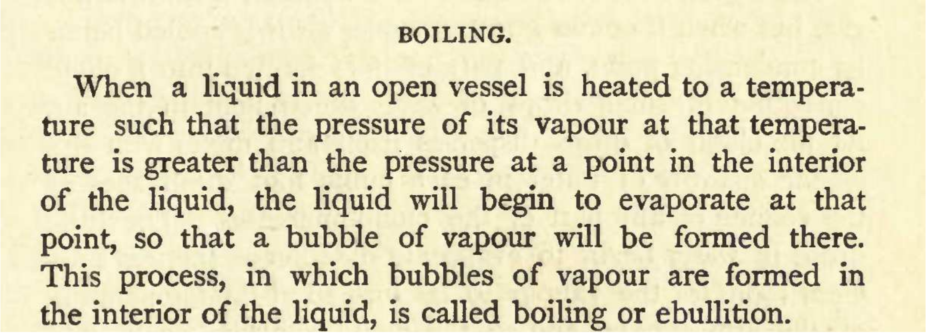

BOILING.

When a liquid in an open vessel is heated to a temperature such that the pressure of its vapour at that temperature is greater than the pressure at a point in the interior of the liquid, the liquid will begin to evaporate at that point, so that a bubble of vapour will be formed there. This process, in which bubbles of vapour are formed in the interior of the liquid, is called boiling or ebullition.

Theory of heat, orig. 1872 [97, p. 23]

With those words James C. Maxwell described the boiling process in 1871 in the introduction of Theory of heat. About 140 years ago already he described the existence of a superheated layer, the necessity of superheat to form the first bubble, the pressure dependency of the boiling processes, recondensation in subcooled boiling, degassing processes, and mixture effects[1].

In the following a short introduction to the boiling process is given. In section 2.2 an overview of the most common correlations and models concerning local phenomena in pool boiling is presented. Afterwards (section 2.3) more recent experimental and numerical investigations are shown focusing on local heat transfer phenomena. The following chapter is not intended to give a comprehensive overview but rather to describe the essential models, approaches, and results.

2.1 Introduction to pool boiling

In 1934 Nukiyama [107] published the probably most cited and best known results of a boiling experiment. In Fig. 2.1 the Nukiyama Curve is shown. It describes the relation between the transferred heat per area and time q and the temperature difference $\Delta T = (T_\mathrm{H} - T_\mathrm{sat})$, where T_sat is the saturation temperature and T_H the temperature of the heated surface. The ratio of both defines the heat transfer coefficient

$$h = \frac{q}{\Delta T}. \tag{2.1}$$

---

[1] The complete introduction of Theory of heat can be found in the appendix (A.1)

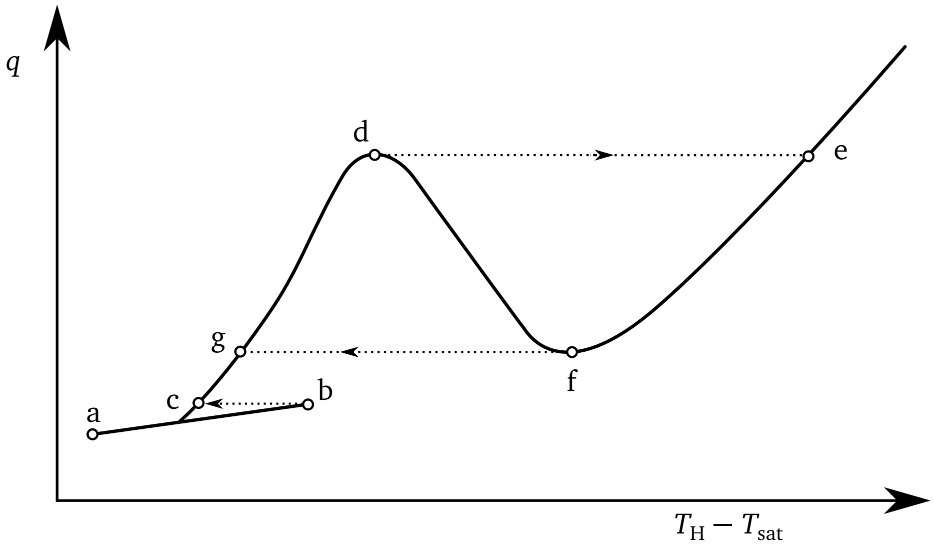

Figure 2.1: Nukiyama curve, adapted from Nukiyama [107]

The Nukiyama Curve (also known as *boiling curve*) can be divided into four regions (see Fig. 2.1). The region between (a) and (b) is the natural convection region at very low heat fluxes. In this region no boiling takes place[1]. Between the natural convection region and the critical heat flux (d) the nucleate boiling regime is located. The critical heat flux (CHF) describes the maximum heat flux transferable by nucleate boiling. At the transition between convective and nucleate boiling a hysteresis can occur as a superheated liquid layer is necessary to initiate the first bubble. At the onset of nucleate boiling (b) the superheat is decreased rapidly jumping to (c). For a decreasing heat flux this jump does not occur. In the nucleate boiling regime the transferred heat is increasing with rising temperature difference. An increase of heat flux higher than the CHF leads to a change of the boiling regime to film boiling. The heated wall is no longer in contact with the liquid phase due to a stable vapor layer on the heated surface. Due to the higher thermal resistance of the vapor the temperature difference jumps to (e). Reducing the heat flux the vapor layer is not removed immediately leading back to (d). Not until the applied heat is decreased to (f) (also called Leidenfrost point) does the vapor layer break up, jumping back to the nucleate boiling regime (g). Due to this hysteresis the region between (d) and (f) (transition boiling) can only be reached with a temperature controlled heater. A more detailed description can be found in any textbook about nucleate boiling (e.g. [17, 20, 139]).

A large number of experimental investigations have been performed to investigate the different influences of fluid and heater properties as well as system parameters (like pressure and heat flux) on the boiling process. Based on these experiments plenty of correlations can be found in the literature. As an example the equation by Stephan and Preusser [137] is given by

$$\frac{h d_{\mathrm{b}}}{k_{\mathrm{l}}} = 0.1 \left(\frac{q\, d_{\mathrm{b}}}{k_{\mathrm{l}}\, T_{\mathrm{H}}}\right)^{0.674} \left(\frac{\rho_{\mathrm{v}}}{\rho_{\mathrm{l}}}\right)^{0.156} \left(\frac{\Delta h_v\, d_{\mathrm{b}}^2}{\alpha_{\mathrm{l}}^2}\right)^{0.371} \left(\frac{\alpha_{\mathrm{l}}^2\, \rho_{\mathrm{l}}}{\sigma\, d_{\mathrm{b}}}\right)^{0.350} \left(\frac{\eta_{\mathrm{l}}\, c_{p,\mathrm{l}}}{k_{\mathrm{l}}}\right)^{-0.162}. \tag{2.2}$$

Several fluid properties as well as the heater temperature, the heat flux, and the bubble diameter are included within this correlation and combined to dimensionless factors. System properties like the heater's material or the surface roughness are neglected. Another widely used equation taken from the VDI Wärmeatlas [52] is

---

[1] This region is not included in the original Nukiyama curve [107]

$$\frac{h}{h_0} = \underbrace{\left(\frac{R_a}{R_{a,0}}\right)^{0.133} \left(\frac{k_\mathrm{s}\,\rho_\mathrm{s}\,c_{p,\mathrm{s}}}{k_{\mathrm{s},0}\,\rho_{\mathrm{s},0}\,c_{p,\mathrm{s},0}}\right)^{0.25}}_{\text{heater influence}} \quad \underbrace{F(p^*)}_{\substack{\text{pressure}\\ \text{influence}}} \quad \underbrace{\left(\frac{q}{q_0}\right)^{n(p^*)}}_{\substack{\text{heat}\\ \text{flux}\\ \text{influence}}}, \tag{2.3}$$

where a reference heat flux at reference conditions (index 0) is used for the calculation. The influences of the heater properties, the system pressure, and heat flux are considered individually and are combined by multiplication. $F(p^*)$ and $n(p^*)$ are functions of the reduced pressure p^*. Further information can be found in [52]. In [53] a revised version is presented to reduce the dependency on reference values which usually have to be determined experimentally. The already large number of influencing factors cannot capture all physical phenomena and the empirical origin limits the applicability to previously measured conditions. GORENFLO and KENNING summarize:

> *Despite the large number of treatises that have appeared on the subject in the literature [...] no coherent theory yet exists that would allow heat transfer coefficients during nucleate boiling to be predicted from first principles to the accuracy required in engineering.*

GORENFLO, KENNING in [53], 2010, page 761

2.2 Local phenomena and models

The boiling process is controlled by a large number of influencing factors, for example several fluid and heater properties as well as system parameters such as pressure and heat flux. Most of them are strongly coupled (like the vapor density and system pressure). An individual experimental analysis of the influencing variables is therefore not possible. The additional spatial and temporal averaging of measurements performed on a technical length scale makes the understanding of the physical phenomena even more difficult. For this reason local experimental and numerical research is conducted on individual and multiple interactive nucleation sites. Measurements concerning bubble departure diameter and frequency were conducted at an early stage. With the improvement of measurement techniques local temperature and heat flux measurements came up in the 1990s. The fast development of computing capacity as well as the improvement of numerical routines enables researchers to perform highly resolved numerical simulations these days.

2.2.1 Bubble departure diameter and frequency

Concerning the bubble departure diameter a clear definition is necessary as different conventions can be found. One aspect is the particular instant taken for the evaluation of the bubble departure diameter. On the one hand, the moment when the bubble starts to detach can be taken. This is usually the case when the bubble foot diameter d_fo reaches its maximum and starts to decrease. On the other hand, the moment the bubble has no more contact to the heated surface can be considered. Due to a more reliable evaluation (cf. chapter 4) the second definition is used for the results presented in this thesis. A further aspect is the difference between the apparent bubble diameter $d_\mathrm{b,ap}$ and the equivalent diameter for a spherical bubble of the same volume V_b (cf. Fig. 2.2). The difference between both definitions strongly depends on the contact angle Θ.

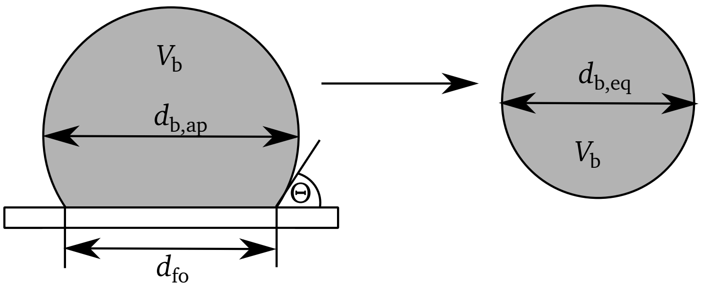

Figure 2.2: Definition of bubble departure diameter

Table 2.1: Dependency of the bubble departure diameter on the contact angle, from Fritz 1935, [42]

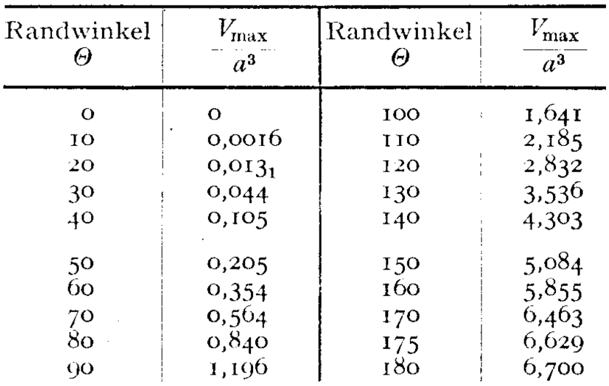

Randwinkel Θ	$\frac{V_{max}}{a^3}$	Randwinkel Θ	$\frac{V_{max}}{a^3}$
0	0	100	1,641
10	0,0016	110	2,185
20	0,013$_1$	120	2,832
30	0,044	130	3,536
40	0,105	140	4,303
50	0,205	150	5,084
60	0,354	160	5,855
70	0,564	170	6,463
80	0,840	175	6,629
90	1,196	180	6,700

Randwinkel = contact angle (translation by the author)

One of the best known correlations for the bubble departure diameter is the Fritz equation

$$d_b = 0.0208\,\Theta\sqrt{\frac{\sigma}{g\Delta\rho}}. \tag{2.4}$$

However, in the original publication by Fritz in 1935 [42] this correlation is not published. Fritz introduced equation 2.5 for the calculation of the maximal bubble volume V_{max},

$$\frac{V_{max}}{a^3} = \varphi(\Theta) \tag{2.5}$$

with

$$a = \sqrt{\frac{2\,\sigma}{g\Delta\rho}}.$$

The correlation between V_{max}/a^3 and Θ is given in table 2.1. By application of Eq. 2.4 the maximal bubble volume can be calculated for the apparent bubble diameter,

$$V_{b,ap} = \frac{4}{3}\pi\left(\frac{d_{ap}}{2}\right)^3 - \frac{1}{3}\pi h^2\left(3\left(\frac{d_{ap}}{2}\right) - h\right) \tag{2.6}$$

with

$$h = \frac{d_{ap}}{2}\left(1 - cos(\Theta)\right),$$

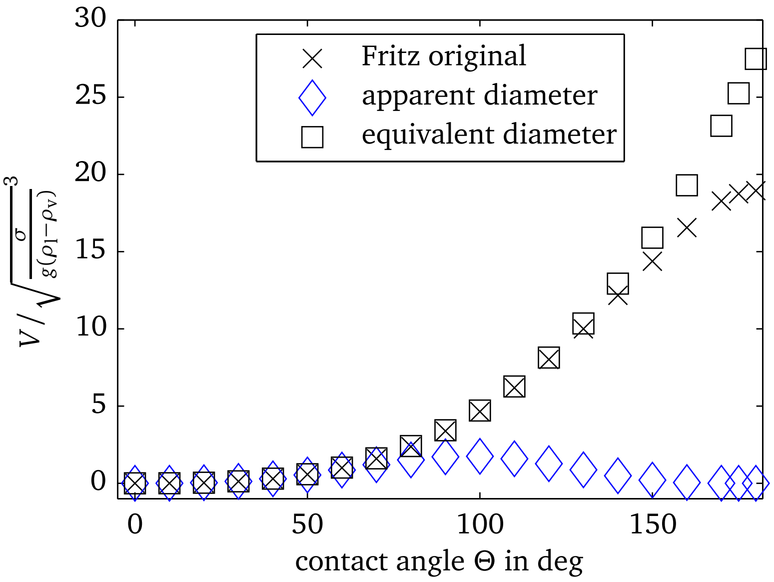

Figure 2.3: Comparison of the original Fritz [42] data with the equivalent and apparent bubble departure diameter

and the equivalent bubble diameter,

$$V_{\mathrm{b,eq}} = \frac{4}{3}\pi\left(\frac{d_{\mathrm{eq}}}{2}\right)^3 . \tag{2.7}$$

In Fig. 2.3 the equivalent and the apparent normalized volume is compared to the original data of Fritz. It can be seen that the Fritz equation (Eq. 2.4) is valid only for the equivalent diameter. An obvious deviation can be observed for higher contact angles ($\Theta > 120°$) comparing the original data of Fritz with the Fritz equation. Despite an extensive literature search no publication was found fitting the original data to the well-known Fritz equation.

Several publications can be found for the calculation of the bubble departure diameter considering further influencing factors, such as the heat flux and superheated thermal layer (Zuber [158]) or the enthalpy of evaporation (Cole [27]). A review on correlations concerning the bubble departure diameter is given by Carey [17, pp. 242–247].

The bubble frequency is consistently defined as number of bubble departures per time. The bubble frequency is in interdependence with the bubble departure diameter and heat flux. It depends on the waiting time[1] and the growth rate of the bubble. Several equations can be found in literature taking different influencing factors into account. An overview is given by Carey [17, pp. 242–247].

2.2.2 Nucleation

Within boiling processes nucleation describes the transition of a liquid into a vapor volume, where the vapor is completely surrounded by liquid or liquid and solid. Therefore it is differentiated from evaporation in which the phase change occurs at a free liquid-vapor interface. Nucleation can be divided in homogeneous nucleation, where the vapor volume emerges completely surrounded by liquid, and heterogeneous nucleation, where the vapor volume is also in contact with a solid [17, pp. 210–226]. As

---

[1] The time between the complete departure of one bubble and the nucleation of the next one.

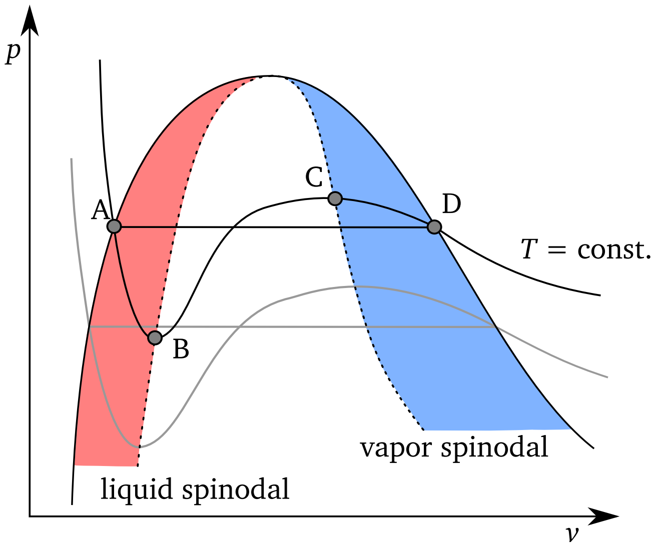

Figure 2.4: *p-v* diagram with spinodals

the vapor is completely surrounded by the liquid (or the wall and the liquid) the pressure in the vapor is higher than the pressure in the liquid. This is caused by the curvature K of the interface. The relation is described by the Young-Laplace equation

$$p_\mathrm{v} = p_\mathrm{l} + K\sigma. \tag{2.8}$$

Within the vapor the saturation temperature is increased compared to the saturation temperature of the liquid as a consequence of the increased pressure. As this temperature difference $T_\mathrm{sat,v} - T_\mathrm{sat,l}$ cannot be overcome by the nucleation itself, a nucleation can only occur in the existence of a thermodynamic metastable state[1]. Assuming that the Van-der-Waals equation

$$p = \frac{\overline{R}\,T}{\overline{V} - b} - \frac{a}{\overline{V}^2} \tag{2.9}$$

is also valid for these non-equilibrium conditions the limits of superheated liquid and supercooled vapor can be calculated for an isotherm by differentiating Eq. 2.9 with respect to the volume and postulate

$$0 = \frac{\partial p}{\partial v} = \frac{\partial \left(\frac{\overline{R}\,T}{\overline{V} - b} - \frac{a}{\overline{V}^2} \right)}{\partial v}, \tag{2.10}$$

where $\overline{R}$ is the universal gas constant, $\overline{V}$ the molar volume, T the temperature, a attraction, and b the repulsion parameter[2]. In Fig. 2.4 a schematic of the spinodals is shown. For a constant temperature the limits of the metastable conditions are marked by (B) and (C). (A) and (D) represent the equilibrium saturation conditions. The connections of the metastable limits for each temperature are the spinodals (compare second isotherm). The red area indicates the possible superheat of the fluid and the blue area the supercooling of the vapor. The area between the liquid and vapor spinodal cannot be reached. This can also be seen in the used Van-der-Waals equation (Eq. 2.9) as in this region the volume would increase with increasing pressure. A detailed description and derivation is given by Carey [17, pp. 151–203].

---

[1] Vapor supercooled below or liquid superheated above the equilibrium saturation temperature.

[2] a,b are material constants and can be calculated from the material properties at critical condition.

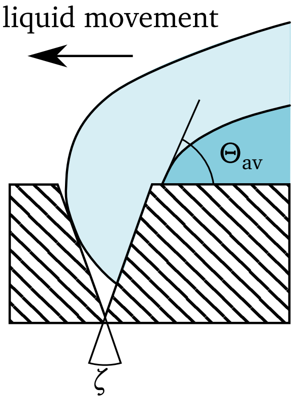

Figure 2.5: Vapor entrapment in a cavity

Nucleation on a technical heater in stationary boiling processes

In a stationary technical boiling process *nucleation* is normally used to describe the development of an apparent bubble, even though this bubble is usually formed out of a remaining vapor volume inside a cavity. The vapor entrapment of a rewetting cavity (e.g. after bubble departure) is shown in Fig. 2.5 for a moving liquid with an advancing contact angle θ_{av} and a cavity angle ζ. If

$$\Theta_{\mathrm{av}} > \zeta \tag{2.11}$$

vapor is entrapped in the cavity. For a cylindrical cavity vapor remains inside the cavity for

$$\Theta_{\mathrm{av}} > \arctan \frac{2\,R}{D}, \tag{2.12}$$

when D is the depth and R the radius of the cavity. Therefore, a slim deep cavity has a greater potential for vapor entrapment.

The overpressure necessary to form a bubble (cf. Eq. 2.8) requires a superheating of the liquid or a supercooling of the vapor to achieve mechanical equilibrium conditions. As a metastable condition cannot be reached after phase change a superheated liquid is necessary for nucleation. This superheat can be calculated by use of Eq. 2.8 and the Clausius-Clapeyron equation

$$\Delta h_v = T\left(v_{\mathrm{v}} - v_{\mathrm{l}}\right)\frac{\mathrm{d}p}{\mathrm{d}T}. \tag{2.13}$$

Approximating

$$\frac{\mathrm{d}p}{\mathrm{d}T} = \frac{p_{\mathrm{v}} - p_{\mathrm{l}}}{T_{\mathrm{sup}}} \tag{2.14}$$

leads to

$$r = \frac{T_{\mathrm{sat}}(p_{\mathrm{l}})\left(v_{\mathrm{v}} - v_{\mathrm{l}}\right)2\sigma}{\Delta h_v T_{\mathrm{sup}}}. \tag{2.15}$$

From Eq. 2.15 it is obvious that a bubble with a smaller radius (bigger curvature) needs a higher superheat to exist. For an idealized cavity (compare Fig. 2.6) and a contact angle $\Theta \leq 90°$ (which is

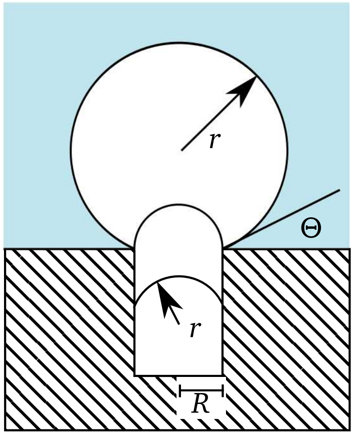

Figure 2.6: Minimum radius at bubble nucleation

normally the case in technical applications) the minimal radius of the bubble located at the edge of the cavity is $r = R$. Therefore the minimal temperature for bubble generation is

$$T_{\text{sup}} = \frac{T_{\text{sat}}(p_{\text{l}})\left(v_{\text{v}} - v_{\text{l}}\right) 2\sigma}{\Delta h_{v} R}. \tag{2.16}$$

Taking the thickness of the superheated layer into account, also a maximum radius for a cavity can be calculated depending on the superheat (Hsu [65]). Further information can be found in [17, pp. 210–226]. The analyses result in contradictory design of the surface structures to enhance nucleation. On the one hand, for active cavities having small superheat for nucleation, cavities with a large radius are necessary. On the other hand, cavities with a small radius enhance the vapor storage and therefore the probability for the formation of a bubble.

2.2.3 Heat transfer by a single bubble

The transferred heat is one of the major criteria in nucleate boiling. Considering local phenomena this corresponds to the heat transferred by a single bubble. The various publications can be classified into four major models of boiling heat transfer. A recent review is given by KIM [87] using the applied classification.

The **Convection analogy model** and the **Transient conduction model** do not account for the evaporation process itself. An example of the **Convection analogy model** is given by FORSTER AND ZUBER [40], who applied the analogy of heat transfer and fluid flow. They express the Nusselt number (Nu) by a function of the Reynolds (Re) and Prandtl (Pr) number, which are adapted to the boiling process,

$$Nu = f(Re, Pr). \tag{2.17}$$

Further publications on this model are given by ZUBER [158, 159].

The **Transient conduction model** (see for example MIKIC AND ROHSENHOW [99], HAN AND GRIFFITH [54, 55]) basically acts on the assumption that the superheated layer necessary for nucleate boiling (cf. section 2.2.2) is disturbed by a growing and rising bubble. After bubble departure this area of influence has to be reheated from bulk temperature (compare Fig 2.7). Both models were developed in the

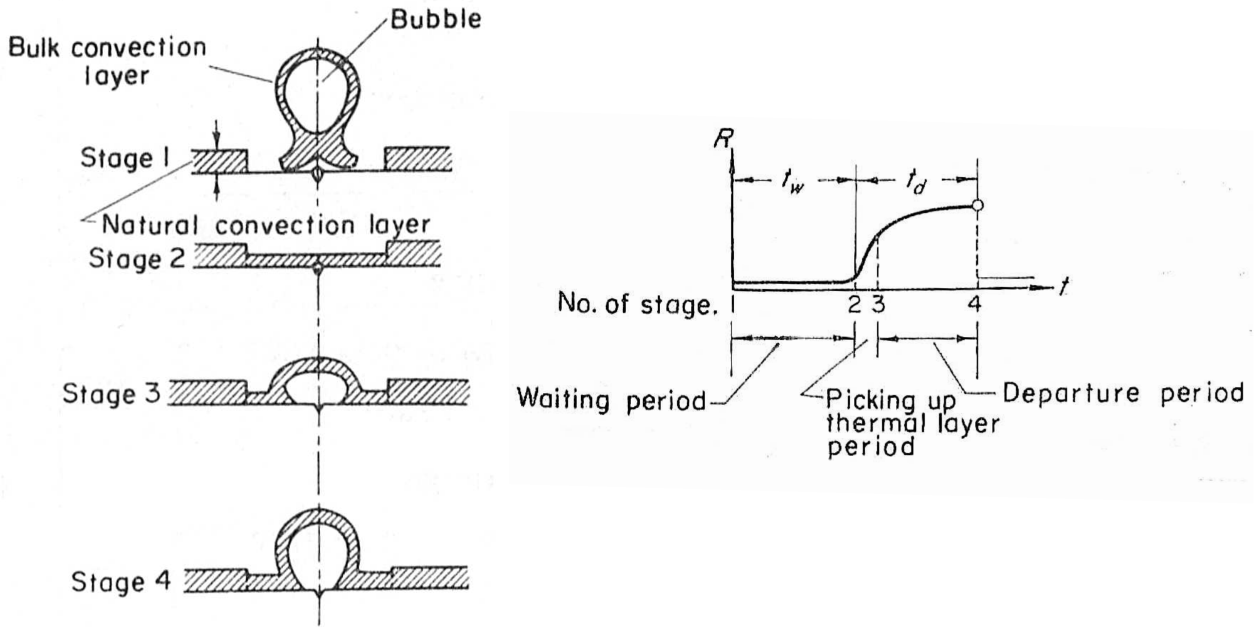

Figure 2.7: Transient conduction model - R: Radius of bubble, t_w: waiting period, t_d: departure period, from Han and Griffith [55]

1950s and '60s. Therefore no possibility of an experimental heat flux evaluation in the necessary resolution existed. Today both models find minor attention. Especially the **Transient conduction model**, leading to a higher heat flux after bubble departure, could not be confirmed by more recent experimental investigations (cf. section 2.3). The **Microlayer model** and the **Contact line model** predict the boiling process best according to recent experimental results. In the following both models are described in detail.

Contact line model

The Contact line model is shown in Fig. 2.8 (cf. Stephan and Hammer [141]). One of the main assumptions is a non-evaporating liquid layer underneath the bubble caused by an increase of the equilibrium interface temperature $T_{\mathrm{int,e}}$ due to intermolecular forces between liquid and solid

$$T_{\mathrm{int,e}} = T_{\mathrm{sat}}(p_{\mathrm{v}}) \left(1 + \frac{\sigma K + A\delta^{-3}}{\Delta h_v \rho_{\mathrm{l}}}\right). \tag{2.18}$$

The term σK represents the influence of the curvature K (compare 2.2.2). A/δ^{-3} represents the intermolecular forces for non-polar fluids also called "disjoining pressure," where A is the dispersion constant[1] and δ the thickness of the fluid layer. Assuming FC-72[2] (at $p = 1$ bar) as working fluid for a flat interface and a superheat of $T = 20\,°\mathrm{C}$ ($A \approx 1 \times 10^{-21}$ J) the remaining liquid film thickness is $\delta \approx 6.2 \times 10^{-10}$ m. The molecule diameter is in the same order of magnitude [41]. Therefore an experimental detection

---

[1] The dispersion constant is related to the Van-der-Waals forces.

[2] FC-72 is a widely used fluid for experimental research in pool boiling.

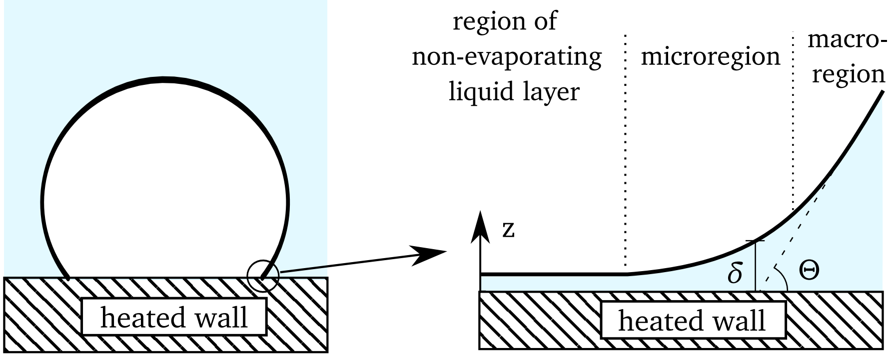

Figure 2.8: Schematic of the Contact line model

could not be achieved up to now. Further information about the disjoining pressure can be found in Israelachvili [72], Wayner, and Potash and Wayner [110, 153]. The influence of the disjoining pressure strongly decreases with increasing film thickness. For the given example a superheat of 5×10^{-3} °C would result in an adsorbed layer of 1×10^{-8} m thickness.

In the macroregion the thermal resistance from the wall to the liquid-vapor interface is increased due to the rapidly increasing film thickness. This results in a reduced superheat at the liquid-vapor interface. Therefore the evaporation rate is decreased. In the microregion both effects are of minor importance as the film thickness is thick enough for minor influence of the disjoining pressure and thin enough for a minor heat resistance. The increase in curvature has less influence on the necessary superheat than the former mentioned factors, leading to a strong evaporation in the microregion. Kim [87] proposes for the validation of the model the existence of an "*extremely high heat transfer [...] at the three phase contact line*."[1] Further, the heat transfer should be less in the bubble departure than in the bubble growth phase due to the larger advancing contact angle Θ and therefore greater film thickness. A clear increase in heat flux corresponding to the microregion is experimentally shown for example by Wagner [149] and Schweizer [119]. Contrary to the assumption of Kim, Schweizer measured an increase in heat transfer at bubble departure in the microregion. Kunkelmann [90] performs comparable numerical simulations with the same result. He explains the increase in heat transfer by a higher superheat underneath the vapor and a supporting change in liquid flow near to the microregion. One recent validation for this model is given by Ibrahem et al. [68–70] performing experiments on stationary and controlled moving liquid menisci. The summarized experimental and numerical results are published in Kunkelmann et al. [91].

At first glance the Contact line model is not consistent with most correlations for bubble departure diameter. Within most correlations a static force balance between the buoyant force F_{buo} and the adhesion force[2] F_{ad}

$$F_{\mathrm{buo}} = V_{\mathrm{b}}\, g\, (\rho_{\mathrm{l}} - \rho_{\mathrm{v}}) \;=\; \sigma\, l_{\mathrm{slv}}\, \sin\Theta = F_{\mathrm{ad}}, \tag{2.19}$$

which leads to

$$\frac{V_{\mathrm{b}}}{l_{\mathrm{slv}}\, \sin\Theta} = \frac{\sigma}{g\,(\rho_{\mathrm{l}} - \rho_{\mathrm{v}})}, \tag{2.20}$$

is included (compare for example [119]). σ is the surface tension, Θ the contact angle, and l_{slv} the length where solid, liquid, and vapor are in contact with each other. The force balance is shown simplified in

---

[1] Three-phase contact line is used as a synonym for the microregion.

[2] This is not the adhesion force leading to the non-evaporative fluid layer.

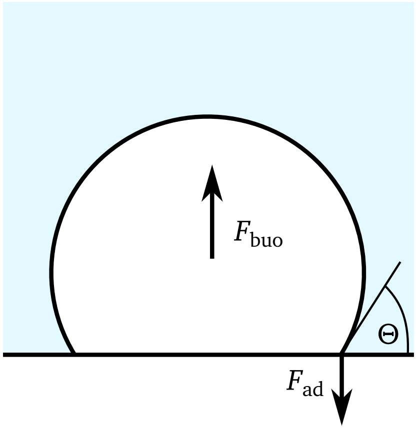

Figure 2.9: Static force balance with a single bubble

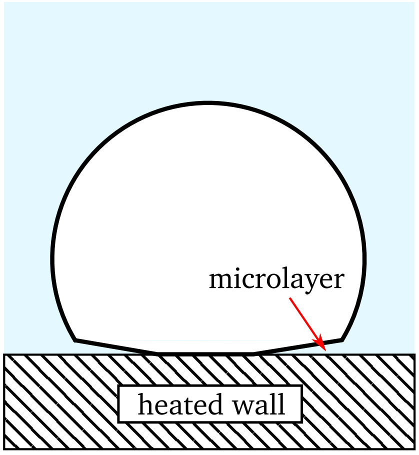

Figure 2.10: Schematic of the Microlayer model

Fig. 2.9. As within the Contact line model there is no contact between the vapor and the wall, there is no adhesion force. Based on this model MANN [96] performed a detailed analysis of the forces at the liquid-vapor interface, leading to a comparable force able to hold the bubble at the heater surface.

Microlayer model

The Microlayer model is based on the assumption of a liquid film remaining under a growing bubble (cf. Fig. 2.10). Within the growth phase of the bubble the liquid underneath is not completely evaporated or replaced by the vapor. The thickness of this liquid layer is orders of magnitudes thicker than the non-evaporative layer introduced in the Contact line model. Therefore adhesive forces can be neglected. This remaining liquid layer underneath the bubble has been proposed by SNYDER AND EDWARDS [130][1]. Already in 1961 MOORE AND MESLER [100] measured the temperature under a single bubble using a 0.127 mm (0.005 in) thick thermocouple. In Fig 2.11 a temperature measurement for water at atmospheric pressure is shown. A temperature drop of ≈ 11 to 17 °C (20 to 30 °F) could be observed. Due to this result MOORE AND MESLER support the Microlayer model. They further present the two extrema of this model: "*By calculating the thickness of a film of water that has the same latent heat as the heat removed during the temperature drop*" [100] the thickness of the film is estimated to 1.98–2.26 µm (78–89 µin). Similar measurements were performed by COOPER and LLOYD [29] in 1969.

---

[1] According to [87], as the original source was not available to the author.

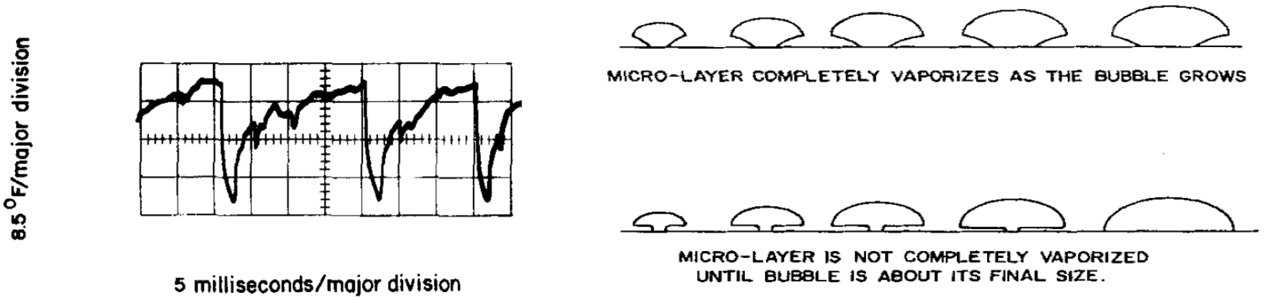

(a) Temperature drop under a single bubble - $q = 425,871 W/m^2$ $(135,000\, Btu\, /h\, ft^2)$

(b) Sketch of two ways the microlayer might vaporize

Figure 2.11: Microlayer model, from Moore and Mesler [100]

For bubble growth in accordance with this model a high heat transfer should exist due to the remaining film, especially in the bubble's growth phase. The high heat flux results from the small heat resistance of the thin liquid layer. To measure the thickness of a microlayer interference phenomena were used for the first time by Jawurek [73] in 1968. Jawurek used a mercury arc lamp with several optics to create a monochromatic collimated beam. The interference pattern and the bubble shape were captured by a rotating prism camera. In Fig. 2.12(a) the microlayer history is shown. The connected lines represent a constant thickness of the microlayer. In Fig. 2.12(b) the shape of the bubble is shown in combination with the dry patch (cf. (a)). The measurements are performed with methanol at $q = 62.3$ kW/m^2 and $p = 0.24$ bar system pressure. Further experimental investigations were performed by Koffman [88] and Koffman and Plesset [89]. In Fig. 2.13 the measured thickness of the microlayer for ethanol at atmospheric pressure ($q = 26.5$ kW/m^2) is shown. Kim and Buongiorno [85] measured the thickness of the microlayer for nucleate boiling of water using interference phenomena in infrared thermometry. According to their work the thickness of the microlayer increases with the radius of the bubble foot and reaches up to 6 µm. For smaller radii the microlayer evaporates completely. Recently, Jung and Kim [76] performed similar measurements on a 10 mm thick calcium fluoride glass coated with indium tin oxide (ITO). In contrast to Kim and Buongiorno a Helium-neon laser ($\lambda = 632.8$ nm) is used for the measurement of the microlayer thickness. By the use of high-speed IR and VIS[1] cameras the temperature profile and shape of the bubble is observed. For water at atmospheric pressure a microlayer thickness of up to 5.5 µm is observed. With increasing size of the bubble a dry spot forms in the center underneath the bubble. The experiments are performed at $q = 53$ kW/m^2. Golobič et al. [51] validated this model by boiling experiments on thin foils. Next to the evaporation processes and models discussed, heat is also transferred by several other ways within pool boiling. In Fig. 2.14 different possibilities of heat transfer paths are shown as presented by Stephan et al. [142].

2.3 Recent experimental and numerical investigations

For about 20 years the research in nucleate boiling has been complemented by numerical simulations. As boiling phenomena happen on various length scales (down to less than 1 µm), numerical simulations offer the advantage of a theoretically infinite resolution, only limited by computational power and time. Further advantages of numerical simulations are the possibility to change individual properties independently. In addition to that the obtained number of physical quantities is larger in numerical simulation.

---

[1] VIS describes cameras detecting mainly light with wavelength within the range which is visible for humans (400 nm to 700 nm).

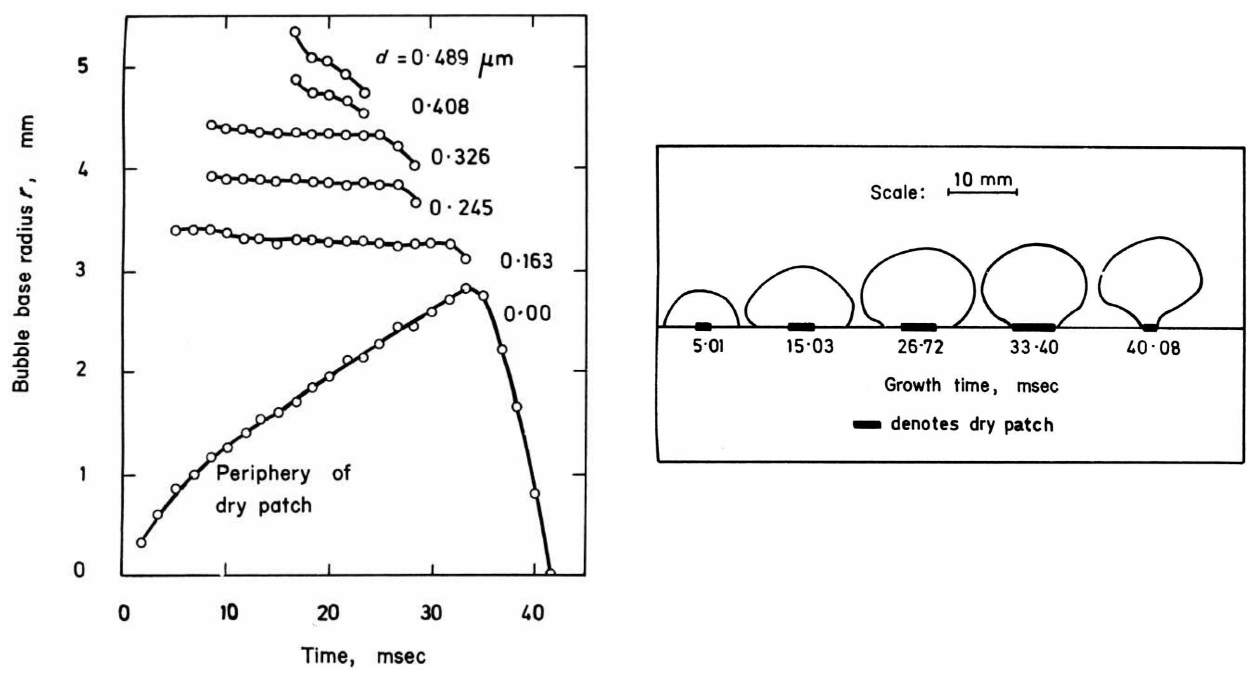

(a) Microlayer history **(b)** Bubble profiles including the dry patch

Figure 2.12: Microlayer measurements and bubble shape, from Jawurek [73]

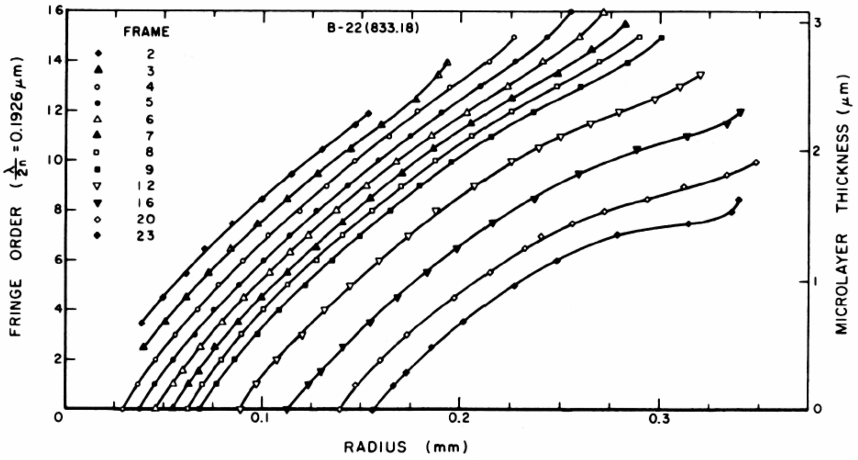

Figure 2.13: Microlayer profile under an ethanol bubble (subcooling: 5.7 °C - Framerate: 13990/s), from Koffman and Plesset [89]

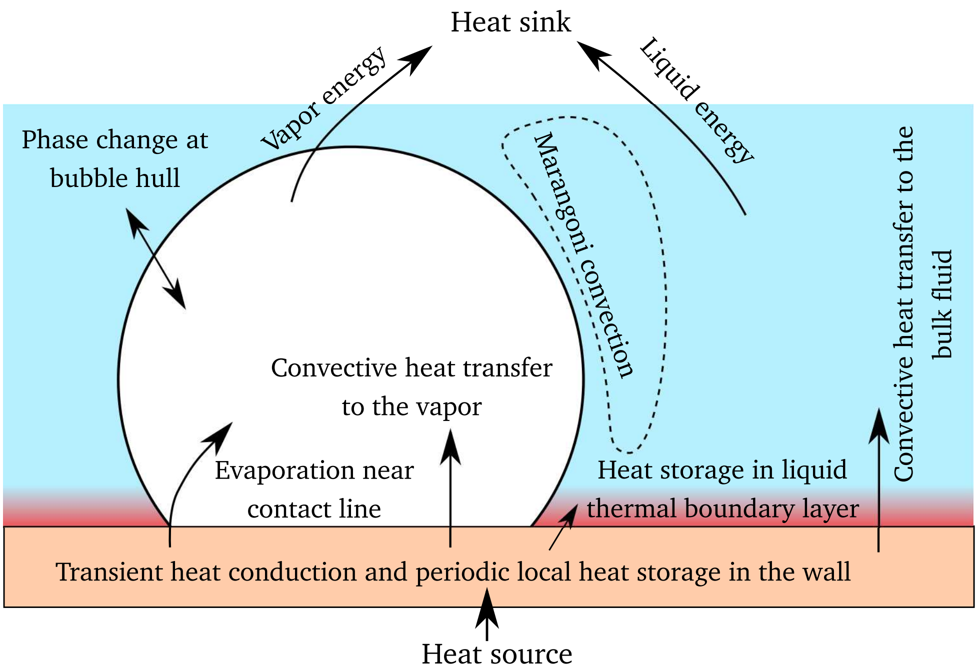

Figure 2.14: Heat paths during a single bubble nucleate boiling process, adapted from Stephan et al. [142]

Whereas in experimental research every measurand (e.g. temperature, pressure, velocity) requires an individual measurement device, which causes additional interactions with the measurement itself, in numerical simulations all desired measurands can be obtained simultaneously. Due to the implementation of additional models the physics of nucleate boiling could be covered more precisely over the last years. These models capture the interaction with the heated wall (e.g. [3, 154]), phase change (e.g. [56]), evaporation at the three-phase contact line (e.g. [135, 141]), and mixture effects (e.g. [84]). To ensure the applicability numerical results have to be validated based on experimental results or analytical solutions, if available. Therefore, a close collaboration between numerical simulation and experimental research is desirable, establishing the possibility of a deeper insight into the phenomena of nucleate boiling processes. In [142] a recent review of numerical simulations of pool boiling processes can be found.

Within the experimental research one focus is the highly temporally and spatially resolved measurement of the surface temperature. The different experimental approaches can be divided by the technique of measurement and the subsequent heat flux calculation. On the one hand conventional temperature measurement techniques based on the Seebeck effect (e.g. thermocouples) or the temperature-dependent electrical resistance (e.g. PT100) can be found. On the other hand optical methods (e.g. IR thermometry) are used.

As the focus of this thesis is experimental, the presented investigations are basically experimental, grouped by the used measurement technique, and complemented by individual numerical investigations. Further publications about numerical investigations can be found by the group of Welch [2, 154, 155], Tryggvason [37, 122, 147], Dhir [1, 3, 34, 101, 102, 120, 134–136], and Stephan [43, 82–84, 90–93, 124, 140, 141].

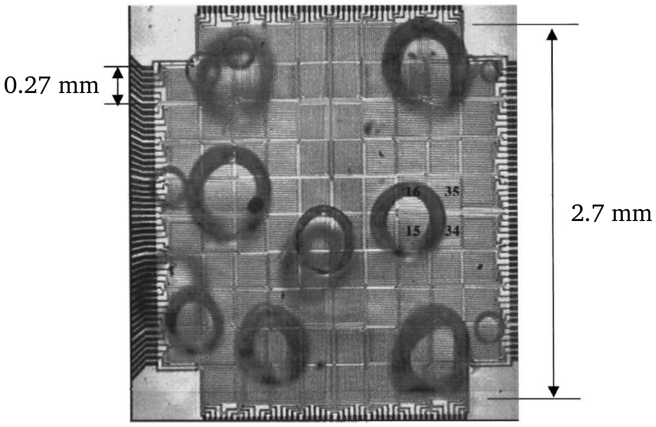

Figure 2.15: Photograph of the heater used by Kim and coworkers, from Bae et al. [7]

Conventional measurement approaches

Kim and coworkers [7, 30, 31, 61, 103, 112–115] used a "microheater array" developed in the late nineties. The heater consists of 96 individually controlled resistance heaters and is built by platinum deposition on a wafer. Heater sizes varying from 0.1 x 0.1 mm^2 to 0.7 x 0.7 mm^2 are used for a single heater element. A picture of a heater within a boiling process is shown in Fig. 2.15. The meandering deposition of each heater can be seen. The nominal resistance varies for the different heaters between $250\,\Omega$ and $8000\,\Omega$ for a single element. The dynamic of a heater element is given with 15kHz. As this is much faster than the dynamic of the boiling process (up to 1kHz) the heater can be operated in a constant temperature mode. Therefore also measurements in the transition regime between nucleate and film boiling are possible. Furthermore, the platinum coating enables temperature measurements averaged over one heater element. The temperature coefficient is about $2 \times 10^{-3}\,\Omega/°\text{C}$. Kim and coworkers also performed measurements in hyper, reduced, and zero gravity.

Rule and Kim [115] performed measurements at the critical heat flux (CHF) and found that the heaters at the edge of the heater array reach the CHF at higher wall superheat than the heaters in the middle of the array. To investigate the influence of the heater size experiments were performed with a different number of powered heater elements. It was found that the influence of the heater size can be neglected if the heater edge length is about twice the size of the capillary length[1] L_c with

$$L_c = \sqrt{\frac{\sigma}{g\,(\rho_\text{l} - \rho_\text{v})}}. \tag{2.21}$$

As the experiments were performed at atmospheric pressure the change in the capillary length is caused by a change in gravity [112]. A gravity scaling parameter is introduced [114] to calculate the heat flux q for an unknown gravity condition based on a known heat flux and gravity (e.g. at earth gravity - subscript e)

$$q = q_\text{e}\left(\frac{a}{a_\text{e}}\right)^m, \tag{2.22}$$

where a is the acceleration and m a function depending on the wall temperature at the onset of nucleate boiling (ONB) and the temperature at the CHF. Further experiments in variable gravity conditions [113] have shown a hysteresis in heat flux for smaller wall superheats (≈ 9 °C), depending on an increase

---

[1] Also known as Laplace length.

or decrease of gravity. The heat flux is less for the change from lower to higher gravity compared to the change from higher to lower gravity. As the low superheat was not sufficient for nucleation, this phenomenon is explained by the difference in time which is required to achieve steady state conditions by natural convection only. For a superheat of ≈ 44 °C no hysteresis occurs. Concerning the dependency of the acceleration on the heat flux two heat transfer regimes have been identified. For an acceleration ≤ 0.1 g the heat flux was significantly less compared to the heat flux for an acceleration > 0.1 g. The difference was mainly attributed to bubbles which do not depart from the heated surface. Schweizer [119] performed similar experiments separating the regimes at 0.07 g. As the transition between both regimes is not sharp the results fit well to each other. Measurements on the smallest heater (0.1 x 0.1 mm^2/single heater) [103] show a higher heat flux in the bubble departure phase[1] than in the growth period of the bubble. As it is assumed that this is caused by the rewetting process at bubble departure, transient conduction is postulated as the dominant heat transfer mechanism. This assumption was recently further deepened [30]. For bubbles with shorter growth times the single-phase heat transfer like transient conduction and micro-convection is claimed to be the dominant heat transfer mechanism. For bubbles with longer growth time the two-phase heat transfer like microlayer or contact line evaporation is claimed to be dominating.

The group of Auracher and Ziegler [5, 6, 15, 63] designed highly sophisticated heaters in technical dimensions. The heaters are powered electrically in a distance of 7 to 10 mm from the boiling surface. By applying a feedback temperature control, also measurements in the transition region between nucleate and film boiling and measurements with transient heating and cooling can be conducted. To measure the temperature close to the surface micro-thermocouples (MTCs) are implemented into the heater by electroplating. The top of the heater is sputtered with a 2.5 µm thick copper, a 0.1 µm thick titanium, and a 1 µm thick gold layer. The MTCs consist of a 38 µm thick constantan wire and are placed in a 6 x 6 grid with 200 µm distance each. Next to this grid further thermocouples are placed with a wire diameter of 50 µm. For all MTCs the sputtered copper layer acts as second conductor. A stability analysis for such boiling devices was performed by Blum et al. [10]. An inverse heat transfer problem (IHTP) has to be solved for calculating the heat flux at the boiling surface. For a detailed description of the IHTP the reader is referred to publications by the cooperating group of Marquardt and coworkers (e.g. [57–60]). To measure local phenomena in the fluid further micro-thermocouple probes (MTCP) are constructed using a 13 µm constantan wire coated with an approximately 1 µm thick gold layer. Optical probes consisting of an etched glass fiber are used for phase detection between liquid and vapor. The tip size of this probe is smaller than 1.5 µm [14]. A picture of a double optical probe with an additional distance calibration wire is shown in Fig. 2.16. By employing multiple probes also an interface determination can be achieved. For measurements with transient heating (+50 K/s) an increase of the CHF of ≈ 400% was observed. The heat transfer coefficient was strongly increased in the nucleate boiling regime. For transient cooling (-4 K/s or uncontrolled) a decrease of the CHF and a reduction of the heat transfer coefficient was observed. For the cooling case the CHF describes the local heat flux maximum between the transition and nucleate boiling regime. This decrease was less pronounced compared to the heating case. It was assumed that this behavior was caused by convective heat transfer. Based on measurement data with optical and micro-thermocouple probes [6, 63], a nucleation site density of about 1×10^8 to $1 \times 10^9\,\mathrm{m}^{-2}$ was estimated for measurements with FC-72 (at ≈ 1.3 bar) as working fluid. Further, the superheated layer, the vapor temperature, and the void fraction was measured close to the heated surface. For the nucleate boiling regime the vapor temperature was lower than the liquid temperature[2]. In film boiling the vapor was superheated up to 40 °C measured at a distance approximately 100 µm above the surface [15]. A good overview of the experimental approaches and results is given in [5]. A similar

---

[1] The bubble still has contact to the wall with an advancing contact line.

[2] This is in good agreement with the theoretical assumption (cf. 2.2.2).

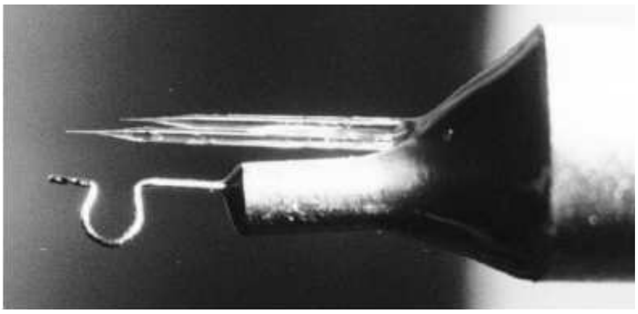

Figure 2.16: Double optical probe with distance calibration wire, from Buchholz and Auracher [14]

measurement technique was used by Iida and Kobayasi [71] in 1969. They used a single insulated lead wire for phase detection based on the differences in the electrical resistance of both phases. Water was used as working fluid.

Siedel et al. [125–127] focused their work on the shape of a single bubble. Therefore a single bubble was generated on a polished copper plate at an artificial cavity. The working fluid was n-pentane. It was found that the bubble detachment diameter is constant for different wall superheats. The bubble frequency rises approximately linearly with wall superheat. For higher superheats an oscillation of the bubble center of gravity was found. It was attributed to the influence of the previously departed bubble [125]. Based on the experimental data the forces on a single bubble and the momentum balance during bubble growth has been analyzed [127].

Optical measurement approaches

One of the first studies using optical temperature measurements in pool boiling was published by Raad and Myers [111] in 1971. They used an approximately 25 µm (0.001 in) thick stainless steel plate coated with cholestric liquid crystals. The temperature field was measured with a rate of 64 Hz. Thereafter, several measurements using thermochromic liquid crystals[1] (TLCs) were published by the group of Kenning (e.g. [77–81, 156]). Pool boiling experiments were conducted on a 0.13 mm thick stainless steel plate coated with a TLC layer (0.010 mm) on the backside. The working fluid was water at atmospheric pressure [77, 79]. Kenning and Yan [79] applied the following method to calculate the local heat flux from the heated surface to the fluid

$$q = q_0 + k_{\mathrm{H}}\,\delta\left(\frac{\partial^2 T}{\partial x^2} + \frac{\partial^2 T}{\partial y^2}\right) - \rho_{\mathrm{H}}\,c_{p,\mathrm{H}}\,\delta\,\frac{\partial T}{\partial \tau}, \tag{2.23}$$

where q_0 is the source term by Joule heating projected on the heated area, k_{H} the thermal conductivity, ρ_{H} the density, and $c_{p,\mathrm{H}}$ the specific heat capacity of the heater material. δ is the thickness of the plate and q the heat flux from the heater to the fluid. A detailed description of the method is given in section 4.2. Kenning and Yan [79] found a significant temperature drop underneath the bubble. For a growing bubble this effect was associated with microlayer evaporation. From the experimental data Kenning and Yan derived that models assuming a "*uniform temperature cannot represent the fundamental physics of boiling*." Using a similar experimental setup measurements have been conducted for bubbles sliding under an inclined superheated wall [156]. For these bubbles a strong interaction between the evaporative and convective heat transfer could be observed. Yan et al. [156] mentioned that the results

---

[1] TLCs have a temperature-depended color. The temperature range in which visible light is emitted is called colorplay.

could be influenced by the thickness of the used wall (0.075 mm). A summary of these experiments is given by Kenning et al. in [78]. The potential of liquid crystal thermometry is also discussed. Additional experiments for sliding bubbles can be found in [9, 80, 81].

The same measurement technique was used by the group of Stephan. For an improved temporal response behavior thin stainless steel foils ($\delta \leq 20\,\mu\text{m}$) were used. Sodtke et al. [133] performed boiling experiments under the absence of gravity to slow down the bubble dynamics. In contrast to former experiments the bubble was located underneath the heated foil. Therefore, the bubble was pressed against the heated foil for gravity-influenced measurements. A clear temperature drop at the position of the three-phase contact line could be observed. A comparison of experimental and numerical data was also given (see Fig. 2.17)[1]. The numerical calculation was based on the model described in section 2.2.3. For a more detailed description Sodtke refers to Kern and Stephan [84]. Sotdke used TLCs to measure the temperature profile of a sessile droplet [132]. For measurements with structured surfaces (no TLCs used) Sodtke found an increase of the heat transfer coefficient compared to flat surfaces. He associates this increase with the increase of contact line length [131].

Höhmann performed measurements on a stationary meniscus [64]. The meniscus was located between two walls. One wall was built of a thin steel foil acting as a Joule heater coated with TLCs. A similar temperature drop as observed by Sodtke was observed at the three-phase contact line. A good agreement was found by comparison of experimental and numerical results based on the model described in chapter 2.2.3[2].

Infrared (IR) thermography has widely replaced measurements using TLCs due to disadvantages like the narrow temperature range. The first heat transfer measurements using IR thermography were published in 1968 by Thomann and Frisk [145]. Already in 1985 Sgheiza and Myers [121] performed IR thermography measurements for pool boiling experiments. They used a 1 mm thick electrically heated stainless steel plate. Despite the relatively thick plate, temperature fluctuations could be observed on the backside of the heater. The nucleation side density was evaluated for water and organic fluids. Theofanous et al. [143, 144] coated a borosilicate glass with a 140 nm to 1000 nm thick titanium layer. The temperature near the heater surface was measured by an IR camera. Additionally, flash X-ray imaging was used for void fraction measurements close to the heated surface. Theofanous et al. observed an increasing nucleation site density with increasing heat flux and superheat. Temperature fluctuations attributed to bubble cycles could be observed.

Golobič et al. [49] used IR thermography for the observation of boiling processes on an electrically heated 6 µm thick platinum foil. The backside of the foil was coated with a black layer to enhance the emissivity. Water was used as working fluid at atmospheric pressure. Golobič observed fast-growing bubbles (about 3 ms growth time) adhering a multiple of the growth time at the heated surface (≈ 50 ms). A high heat flux during the growing period was followed by smaller or even negative[3] heat fluxes. In [51] similar experiments were performed on a titanium foil with a thickness of 25 µm. For nucleate boiling of a single bubble microlayer evaporation was found. However it is mentioned that "*this model [...] is not fully consistent with the observations*." Golobič and Gjerkeš [46] used 25 µm thick copper and titanium foils heated by laser radiation from underneath. On both foils experiments up to the CHF were performed. By splitting the laser beam different sizes of heated area were realized. The area of the inner (mainly) heated surface and the area of the outer (surrounding) heated surface could be set individu-

---

[1] ξ represents the coordinate parallel to the wall. The order of magnitude has to be corrected to 10^{-3}.

[2] For a detailed description of the used model Höhmann refers to [82, 138].

[3] The heat flux was less than the averaged heat source by Joule heating.

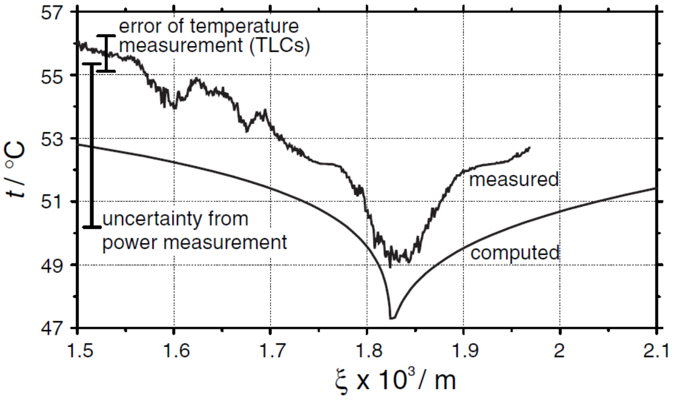

Figure 2.17: Comparison of computed and measured (low-g) wall temperature distribution close to the three-phase contact line, from SODTKE et al. [133]

ally. In [47, 48] GOLOBIČ and GJERKEŠ used the same measurement technique focusing on coalescence (cf. page 27).

BUONGIORNO and coworkers used a thin sapphire glass coated with ITO in their experimental research on nucleate boiling. As the thin ITO layer is opaque to IR radiation but transparent to visible light it is possible to observe the boiling process from underneath with IR and VIS high-speed cameras simultaneously [44, 45]. Thereby, the IR camera measured the temperature profile comparable to the measurements using a thin foil (e.g. used by GOLOBIČ). The VIS camera recorded the shape of the bubble from underneath. A dichroic beamsplitter is used to separate the individual wavelength ranges. As working fluid water was used at atmospheric pressure. The bubble departure diameter and frequency and the waiting and growth time were compared to common correlations. The results are used in a heat flux partitioning model[1]. In this model the total heat flux

$$q_{\mathrm{tot}} = q_{\mathrm{ev}} + q_{\mathrm{q}} + q_{\mathrm{c}} \tag{2.24}$$

is the sum of the latent heat flux transferred by evaporation q_{ev}, the necessary heat flux to reheat the thermal boundary layer after bubble departure q_{q} (quenching), and the heat flux transferred by convection independent of the bubble cycle q_{c}. It was found that the quenching heat flux has the major contribution to nucleate boiling heat transfer [45] for the presented conditions. Further, KIM AND BUONGIORNO used a silicon heater for phase detection on the heated wall in two-phase systems (e.g. pool boiling or droplet evaporation and condensation). The "*DEtection of Phase by Infrared Thermometry*" (DEPIcT) is based on the usage of an infrared transparent heater (e.g. an optical grade silicon wafer) in combination with a fluid sufficiently opaque for infrared radiation (e.g. water). Direct Joule heating can be applied by using silicon as heater material. Therefore, an additional coating (like ITO), which is generally infrared opaque, is not necessary. The liquid which is in direct contact with the heated wall has approximately the wall temperature. Therefore a high temperature (approximately the temperature of the heated surface) should be measured by IR thermometry. If the heated wall is in contact with vapor, the temperature of the next liquid layer (e.g. the top surface of a vapor bubble) is measured as the vapor is almost infrared transparent. This temperature is approximately saturation temperature (for pool boiling) and therefore lower than the temperature at the heated surface. A schematic of this method is shown in Fig. 2.18. The same design is used to measure the thickness of a thin liquid layer by interference phenomena (cf. section 2.2.3). With this measurement technique a similar microlayer was measured as found by JAWUREK

---

[1] It is referred to [94] and [12] for further descriptions. [12] was not available to the author.

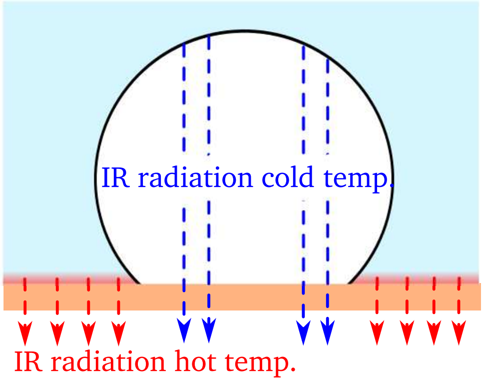

Figure 2.18: Schematic of DEPIcT method (Kim and Buongionro [85, 86])

(cf. Fig. 2.12) and Koffman and Plesset (cf. Fig. 2.13). Duan et al. [35] additionally measured the velocity field around the bubble by particle image velocimetry (PIV).

Wagner and Stephan [151] used a 20 µm thick electrically heated stainless steel foil for measurements at a single nucleation site. To force a nucleation of a single bubble at a defined position small artificial cavities were fabricated in the foil by laser surface treatment or focused ion beam (FIB) [149]. HFE-3284, FC-84, and mixtures of both are used as working fluids at subatmospheric pressure. Consistent with other experimental results (e.g. in VDI Heat atlas [53]) and with theoretical analysis (e.g. Kern and Stephan [84]) a reduced heat transfer coefficient was observed for the mixtures compared to both pure fluids. Wagner and Stephan describe a high heat flux at the three-phase contact line as predicted by the contact line model. For the mixture the contact line heat flux was found to be similar to the heat flux of the pure fluids in the growth period of the bubble. In the departure phase the contact line heat flux was found to be significantly lower for the mixture than for the pure fluids. This effect is attributed to an increased concentration of the less volatile component in the vicinity of the three-phase contact line. In [150] Wagner et al. used a 25 µm thick stainless steel foil within the same measurement setup. Additionally a MTCP developed and built by the group of Auracher (comp: page 18) was used to measure the temperature close to and inside a single vapor bubble with a measurement rate of 10 kHz. In Fig. 2.19 the temperature measured by the MTCP is shown with regard to different stages in the bubble cycle. The measurements were performed with HFE-7100 at 450 mbar (T_{sat} = 36.9 °C). The penetration of the bubble by the MTCP can be seen by the temperature drop (≈ 7 °C) within approximately 0.5 ms. The vapor temperature inside the bubble was constant. In the wake of the bubble the reheating of the thermal boundary layer can be seen. For the superheat of the vapor (≈ 3 °C) no explanation could be found. The superheat due to an increased pressure caused by the curvature of the bubble is less than 1 °C (comp: Eq. 2.16).

The influence of differences in the shape of artificial cavities on pool boiling with single bubbles has been investigated by Shoji and Takagi [123] and Hutter et al. [66]. Shoji and Takagi performed experiments with conical, cylindrical, and reentrant cavities within a 0.1 mm thick copper disk. The reentrant and cylindrical cavities showed a more stable behavior than the conical one. The stable behavior was represented by a lower superheat and temperature fluctuation as well as a more periodic boiling process. Hutter et al. used a silicon chip. The cavities have a depth of 40 µm to 100 µm. A clear influence of the different shapes of the cavities on the boiling parameters could not be observed.

Schweizer used the same heater design as Wagner and focused on the influence of gravity on single bubble nucleate boiling [119]. As working fluid FC-72 was used. For these experiments an edged cavity

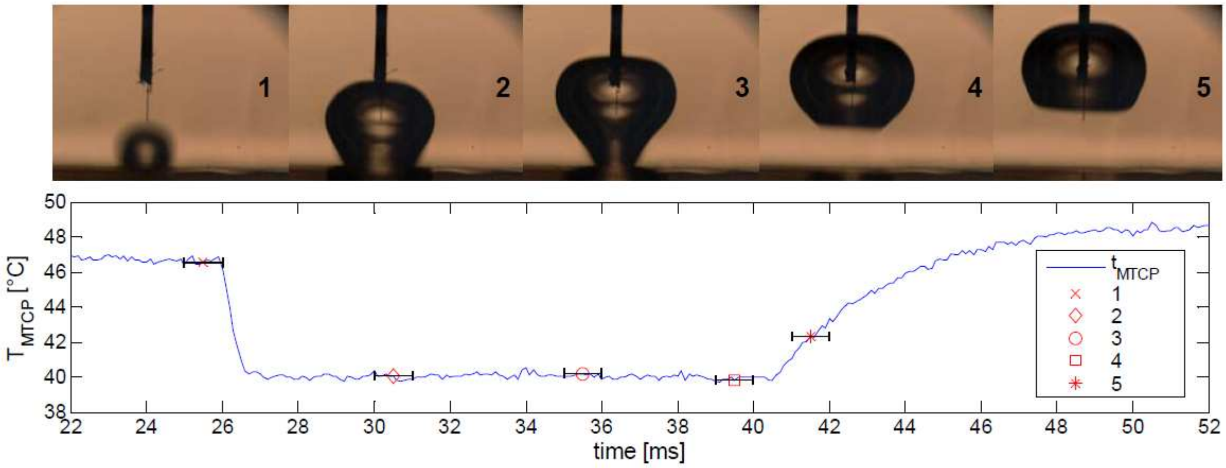

Figure 2.19: Bubble cycle with temperature profile measured by MTCP, from Wagner et al. [150]

with a rough surface topology was used. With a diameter of approximately 0.2 mm these cavities are about ten times larger than the ones used by Wagner. Through the structured topology inside the cavity numerous possible positions are created for initial bubble nucleation. As the bubble diameter is much larger for experiments in reduced gravity the influence of such a large cavity on the boiling process after nucleation could be neglected. Schweizer analyzed the fluid dynamics like the bubble departure diameter and frequency as well as the rate of ascent. Based on a force balance he suggested a new correlation for the bubble departure diameter[1]

$$d_{\mathrm{b,ap}} = \sqrt{\frac{\sigma}{g(\rho_{\mathrm{l}} - \rho_{\mathrm{v}})}}\sqrt{\frac{24\ \sin(\Theta)}{4-(1-\cos(\Theta))^2(2+\cos(\Theta))}}. \tag{2.25}$$

Schweizer found a dependency of the contact line velocity on the transferred heat at the three-phase contact line. In Fig. 2.20 the heat flow per unit contact line length is plotted versus the contact line velocity. The measurements are performed in the transition from $0.37g$ to $0.14g$ at a pressure of approximately 600 mbar. A positive velocity represents an advancing contact line. Kunkelmann found the same characteristic by numerical simulations and attributed it to a higher superheat of the foil for an advancing contact line and differences in the fluid flow close to the three-phase contact line. In Fig. 2.21 a clockwise fluid flow can be seen in the growth period of the bubble. In the departure phase the fluid flow is counterclockwise bringing colder liquid from the bulk closer to the heated surface.

Nam et al. [104] applied the same force balance as Schweizer. In both works the equations fit the experimental data well. In this context, it should be mentioned that both authors compared the apparent bubble departure diameter (from their calculation) with the equivalent one (from their measurement). Further, the viscous drag and liquid inertia forces are compared by numerical simulations. It is shown that shortly before bubble departure buoyancy and tension forces are dominant. In the initial stage of bubble growth the liquid inertia force can have a major influence on bubble growth.

The heater concept of Schweizer and Wagner was also employed by Ibrahem et al. [68–70] using a 10 μm thick stainless steel foil. Ibrahem et al. performed experiments with a stationary and moving meniscus using HFE-7100 as working fluid at approximately 500 mbar (cf. Fig. 2.22). It was

---

[1] Corrected by the author.

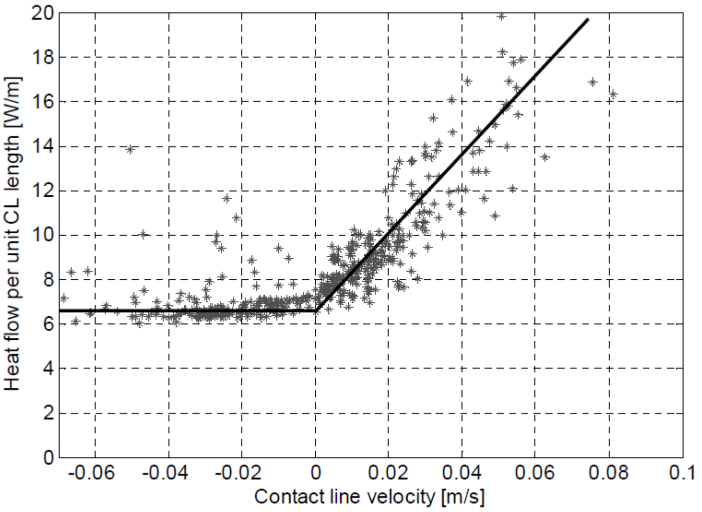

Figure 2.20: Heat flow per unit contact line length versus contact line velocity, from Schweizer [119]

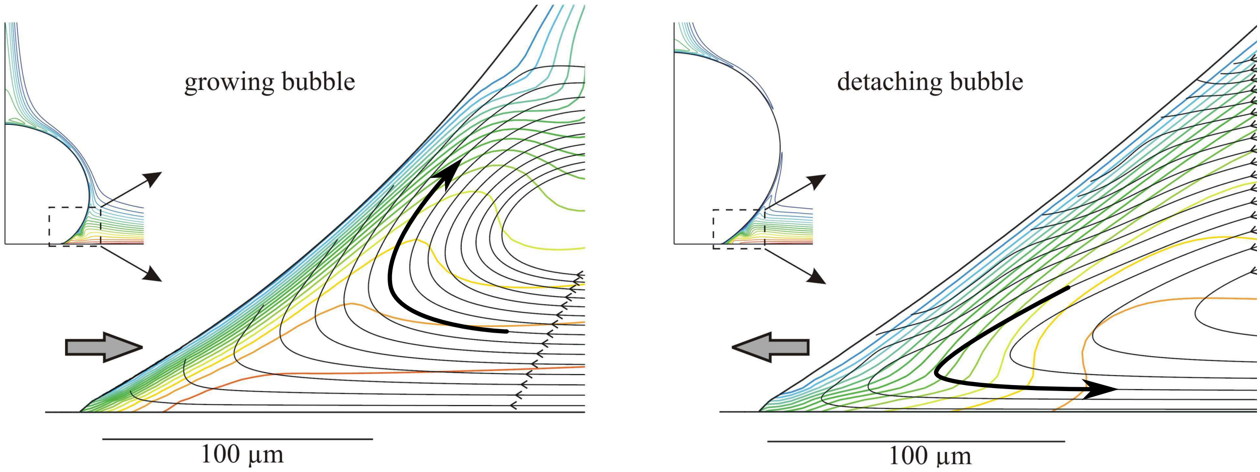

Figure 2.21: Isotherms and streamlines of relative velocity for bubble growth and detachment, adapted from Kunkelmann [90]

found that the heat flux at the three-phase contact line increases with increasing heat input. Comparing the heat flux at the three-phase contact line during advancing and receding movement it was observed that the heat flux of the advancing case was about twice as high as the heat flux of the receding case. For an advancing meniscus the heat flux at the three-phase contact line increased with increasing velocity. For the receding meniscus this effect was not observed by Ibrahem et al. Furthermore, from the published measurement data of Ibrahem et al. it can be seen that for specific higher receding velocities a higher heat flux is reached (10.3 mm/s and 18.5 mm/s in the right-hand graphic of Fig. 2.22).

The possible influences on the boiling process using such thin heated walls (e.g. by the lower capacity of energy storage) are mentioned by several authors (e.g. Kenning and Yan [79], Golobič et al. [51]). To overcome this problem a new heater design was developed (Fischer et al. [39]). Comparable to the heater design of Theofanous et al. [144] an IR-transparent glass is coated with an electrical conductive layer. In addition to a pure conductive layer (≈ 400 nm thick) a further chromium-based layer is used to enhance the emissivity for IR thermometry. Further information about the coating can be found in Slomski [129].

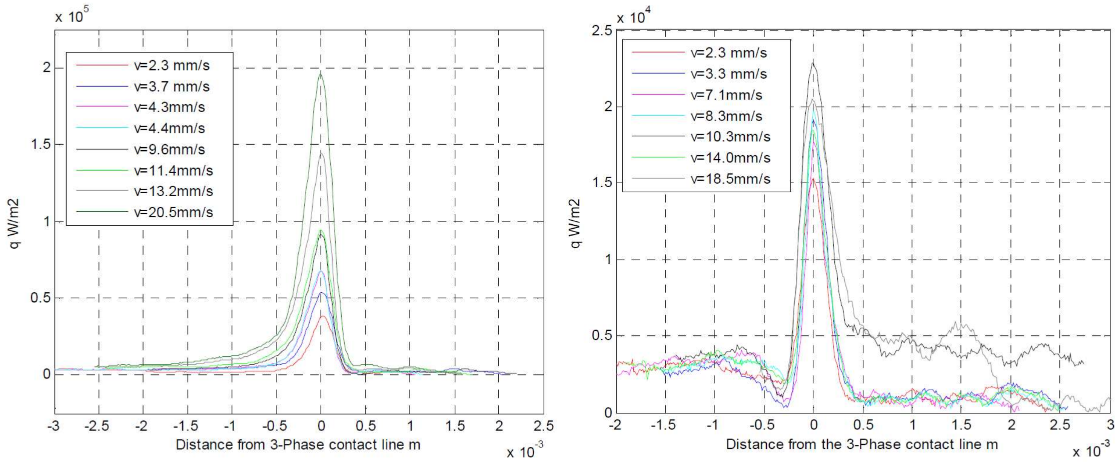

Figure 2.22: Heat flux at the three-phase contact line for a moving meniscus (left: advancing; right: receding), from Ibrahem et al. [69]

Further experiments on a single evaporating meniscus were performed by the group of Garimella. Dhavaleswarupu et al. [33] used two horizontal plates to form a meniscus. The temperature in the vicinity of the three-phase contact line was measured by an IR camera. The top plate, made of acrylic, has an outer diameter of 58.42 mm and is coated with polytetrafluoroethylene (PTFE). For the bottom plate a 500 μm thick fused quartz wafer is used coated with a titanium layer from underneath for heating purposes. Heptane was used as working fluid having a transmission of over 80 % over a wide range within the infrared regime. It was found that the apparent contact angle increases with increasing heat flux. Small changes (≈ 20 %) in the channel height hardly affected the shape of the meniscus. A temperature drop was found at the three-phase contact line. Using a heat balance it was shown that about 70 % of the overall heat is transferred in the vicinity of the three-phase contact line. For the evaluation a 50 μm width "*region of interest*" is used. Migliaccio et al. [98] performed similar experiments with a heater with a V-groove type structure. In this configuration the shape of the meniscus is influenced by the fluid feeding rate. The ratio of the overall heat transferred in the vicinity of the three-phase contact line was ≈ 45 %. Wang et al. [152] carried out numerical calculations for the same setup. Within the simulation the heat transferred in the vicinity of the three-phase contact line was ≈ 43 %. A vortex forced by thermocapillary convection was observed in the numerical simulations. This thermocapillary convection was investigated experimentally by Dhavaleswarupu et al. [32] and Chamarthy et al. [21] with a horizontal capillary tube filled with methanol. For the application of μPIV[1] fluorescent polymer microspheres were added. To minimize distortion due to different refraction indices the capillary tube is made of fluorinated ethylene propylene (FEP) and placed in water confined by two parallel glass plates. Two counterrotating vortices were found in the horizontal plane. In the vertical plane a single vortex could be observed. Further, it was found that the flow is mainly driven by thermocapillarity for tube diameters under a critical value. For larger diameters the flow characteristic becomes three dimensional by the influence of buoyancy.

The group of Tadrist performed experiments to analyze thermocapillary convection for single bubbles. Arlabosse et al. [4] injected an air bubble in a silicon oil bath from the top of the test cell. The test cell, containing the silicon oil, was heated from above and cooled from below to induce a temperature gradient. The temperature field was measured by holographic interferometry. The velocity field was determined by PIV. The influence of the Marangoni number Ma, the Bond number Bo, and the Prandtl number Pr was investigated. It was found that the Reynolds number Re of the fluid around the bub-

---

[1] μPIV describes particle image velocimetry in the micrometer length scale.

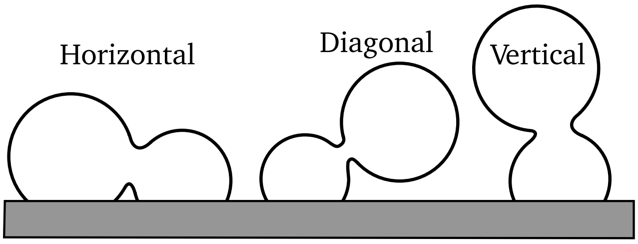

Figure 2.23: Different types of coalescence

ble increased with increasing Marangoni and decreasing Prandtl and Bond numbers. Further, the heat transferred with an air bubble compared to the heat transferred by pure conduction (in the absence of an air bubble) increased with increasing Marangoni number[1]. BARTHES et al. [8] performed similar experiments with FC-72 as working fluid at atmospheric pressure. In contrast to ARLABOSSE et al., BARTHES et al. generated the bubble by nucleation underneath a heated surface. Experiments were performed in degassed and non-degassed liquid. For the non-degassed case convection instabilities were observed. They were related to thermocapillary convection.

2.3.1 Bubble interaction and coalescence

The first investigations on bubble interactions were published by CHEKANOV [24][2] in 1977 and EDDINGTON, KENNING, AND KORNEICHEV [36] in 1978. EDDINGTON et al. investigated the stability of different nucleation sites and proposed a thermal interference between them. CHEKANOV investigated the nucleation of a bubble influenced by another existing bubble next to it. A dimensionless spacing parameter

$$S_{sp} = \frac{S}{d_\mathrm{b}} \tag{2.26}$$

is introduced, where S is the distance between two active cavities and d_b the bubble departure diameter. Based on the theory of pulse processes, CHEKANOV made the assumption that for spacing parameters $S_{sp} < 3$, the interaction prevents the second cavity from nucleation. For $S_{sp} > 3$ the interaction enhances the probability of a nucleation at a second cavity. Similar experiments have been performed by CALKA AND JUDD [16]. Their findings are comparable to the results obtained by CHEKANOV. For a spacing parameter of $0.5 < S_{sp} < 1$ the probability for nucleation at a second cavity is increased. For $S_{sp} > 3$ no interaction was found.

ZHANG AND SHOJI [157] performed experiments on a 0.2 mm thick silicon heater with artificial cavities and divided the interactions further into hydrodynamic interaction, thermal interaction, and coalescence. The cavities were heated by laser radiation from below. The working fluid was water. The same spacing parameter is used for a classification of the different interactions. The results are shown in table 2.2. Further, a promotive influence on the bubble departure frequency was observed for $S_{sp} \leq 1.5$ and $2 < S_{sp} \leq 3$. Bubble coalescence itself can be divided into horizontal, diagonal, and vertical coalescence. In the following, only the horizontal coalescence is considered. For this work a horizontal coalescence is defined by both bubbles being in contact with the heated wall at the moment of the coalescence (cf. Fig. 2.23).

---

[1] For a definition of the dimensionless numbers it is referred to [4].

[2] Taken from [16] as the original source was not available to the author.

Table 2.2: Types of interactions for different spacing parameters, from ZHANG AND SHOJI [157]

Spacing parameter	Type of interactions
$S_{sp} > 3$	no interaction
$2 < S_{sp} \leq 3$	hydrodynamic
$1.5 < S_{sp} \leq 2$	hydrodynamic, thermal
$S_{sp} \leq 1.5$	hydrodynamic, thermal, coalescence

CHATPUN et al. [22, 23] used a silicon heater with artificial cavities. They observed that the arrangement of the cavities influences the bubble characteristics. For a linear arrangement a better heat transfer coefficient was observed than for a triangular arrangement. SATO et al. [117] used a silicon wafer with artificial cavities heated by laser radiation. The working fluid was water. Contrary to other publications the spacing parameter is defined using the capillary length L_c (see Eq. 2.21) instead of the bubble departure diameter d_b. For spacing parameters of $S_{sp} = S/L_c < 0.8$ coalescence is the dominant form of interaction. A thermal interaction intensity[1] Ψ is defined, basically depending on the temperature fluctuation at a cavity attributed to the bubble cycle at a second cavity. For spacing parameters smaller than 1.2 the thermal interaction intensity was strongly increased.

GOLOBIČ AND GJERKEŠ [47, 48] performed experiments on 25 µm thick copper and titanium foils. By splitting a laser beam, different positions could be heated from underneath by radiation. It was found that the activity of nucleation sites is reduced by decreasing the distance between them, allowing a nucleation site to be inactivated.

CHEN AND CHUNG [25, 26] used a microheater array with 96 individually controllable heater elements (270 x 270 μm^2 each). The heater design is comparable to the one described on page 17. The working fluid was FC-72 at atmospheric pressure. The fluid temperature was ≈ 25 °C[2]. By using this heater concept single bubbles could be nucleated at defined positions. In [25] the heat transfer for coalescing bubbles is compared to the heat transfer by single bubbles. An increase of approximately 70 % was found for the coalescence case. While single bubbles had peaks in heat flux at nucleation and departure a further peak could be observed at the coalescence of two bubbles. Further, the merged bubble caused a higher heat flux up to the departure. In Fig. 2.24 the heat transfer of a single heater element is shown for both cases. CHEN AND CHUNG attribute an increased heat transfer to an increased movement of the contact line. In addition, an increase in the bubble departure frequency was found due to coalescence. In [26] the coalescence of multiple bubbles was investigated. The increase in heat transfer was related to a rewetting of the heater with colder liquid and turbulent mixing effects. A similar heater was used by JINGLIANG et al. [75] with subcooled FC-72 as working fluid. A enhancement in heat transfer was found due to bubble coalescence.

---

[1] The thermal interaction intensity is introduced in [23].

[2] As the saturation temperature of FC-72 is $T_{sat} \approx 56\,°C$ at 1 atm the fluid was subcooled.

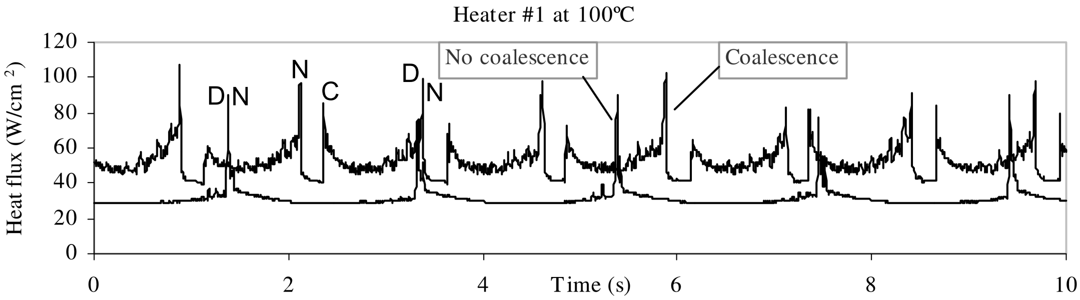

Figure 2.24: Heat transfer from a single heater for coalescence and non-coalescence cases, from Chen and Chung [25] (N: Nucleation, C: Coalescence, D: Departure - added by the author)

Jiang et al. [74] performed experiments on a massive copper and stainless steel heater with artificial cavities of 50 μm diameter and 100 μm depth. The distances of the cavities are in the range of 1 mm to 6 mm[1]. Jiang et al. used the same classification for the spacing parameter as introduced in Eq. 2.26. The working fluid was water at atmospheric pressure. It was found that the probability of a bubble coalescence increases with decreasing spacing parameter. On the copper surface coalescence occurred at higher spacing parameters. The measurement data were fitted to a hyperbolic tangent function (see Fig. 2.25). For smaller cavity spacings ($S_{sp} < 0.8$) the bubble departure diameter was increased. For larger cavity spacings the bubble departure diameter was smaller than for a single cavity. It was found that the bubble frequency decreases with increasing spacing parameter for all $S_{sp} \leq 1.05$. For $S_{sp} > 1.05$ the opposite behavior was observed.

Hutter et al. [67] used a silicon wafer with artificial cavities as heating surface. Temperature microsensors are placed around the 16 cavities located in distances from 0.84 mm to 3 mm. The cavities are cylindrical with a diameter of 40 μm and a depth of 80 μm. The working fluid was FC-72. For the smallest cavity distance of 0.84 mm an increase in the coalescence frequency could be observed with increasing superheat. The general trends concerning bubble departure diameter and frequency are comparable to the trends determined by Jiang et al. [74]. Furthermore, Hutter et al. analyzed the influence of the superheat on the bubble departure diameter and frequency. It was found that with increasing superheat the bubble departure diameter and frequency is increased. Hutter et al. and Jiang et al. [66, 74] also observed an increased bubble departure diameter with increasing superheat for single bubbles. Contrary to this, Siedel et al. [125] observed a constant departure diameter and a decreased growth time of the bubbles with increased superheat at single nucleation sites using n-pentane as working fluid. They used a copper plate as heater. For bubble coalescence no significant increase in vapor production could be observed. Images recorded with 27 kHz have shown a capillary wave propagation on the interface after coalescence.

Golobič et al. [50, 51] performed further measurements on 25 μm thick titanium foils without artificial cavities focusing on the influence of coalescence on heat transfer. The measurement setup was comparable to the one described on page 20. The working fluid was water. The observed coalescences were not induced (e.g. by artificial cavities) but occurred randomly. Golobič et al. found that for two bubbles with different growth rates the heat flux in the apparent contact area of the slower growing bubble was reduced. The faster growing bubble was not affected. It is suggested that the faster growing bubble pushes superheated liquid under the slower growing bubble leading to a reduction in heat transfer. Contrary to

---

[1] Corrected by the author, since 1 μm to 6 μm as mentioned in [74] seems not to be reasonable.

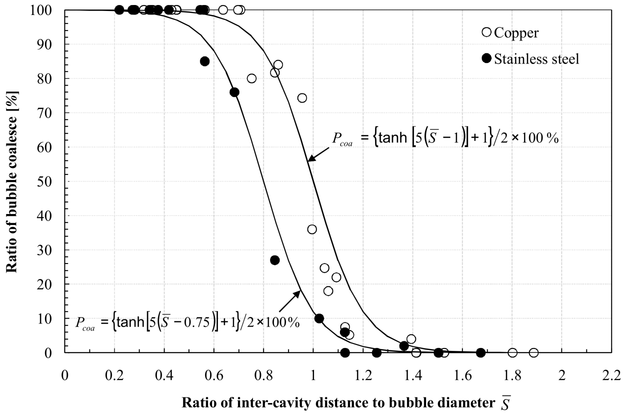

Figure 2.25: Influence of cavity spacing on bubble coalescence, from Jiang et al. [74]

Chen and Chung [25] a general increase in heat flux could not be observed due to bubble coalescence. Further, it was observed that bubble coalescence led to strong oscillations of the shape of the bubble.

Bonjour et al. [11] investigated coalescence phenomena on a vertical wall. The heated surface contains three artificial cavities and is covered by glue to avoid parasitic nucleations. The cavities are arranged in a triangular shape with a center to center distance of 0.26 mm to 1.82 mm each. The working fluids were pentane and R-113 at 1 bar. An increased heat transfer could be observed due to coalescence. Coalescence occurred for smaller spacing parameters ($S_{sp} < 0.5$) and higher Jacob numbers ($Ja > 20$). In this work the Jacob number[1] is defined as

$$Ja = \frac{\rho_\mathrm{l}\, c_{p,\mathrm{l}}\, T_\mathrm{sup}}{\rho_\mathrm{v}\, \Delta h_v}. \tag{2.27}$$

Nimkar et al. [106] also performed measurements on a vertical wall. The silicon heaters were etched with multiple pyramidal micro-reentrant cavities in a square array. The working fluid was water at atmospheric pressure. The spacing between each cavity was varied from 0.5 mm to 1 mm. The best heat transfer coefficient was found for a spacing of 0.75 mm. The surface with a spacing of 0.5 mm showed a worse heat transfer coefficient than the plain surface used as a reference. This was related to an interaction between different cavities and a hindered mixing of the thermal boundary layer.

The group of Dhir [101, 134] investigated bubble coalescence experimentally as well as numerically. The experiments are performed on a silicon heater with artificial cavities at a distance of 1.25 mm to each other. The comparison of bubble growth rate and shape shows a good agreement between experiments and numerical results. An increase of heat transfer due to coalescence could be found. Further vapor bridges could be observed with liquid underneath during coalescence.

Carey [18] applied the film capillarity theory together with molecular dynamic simulations to investigate the stability of thin liquid films. Below a critical thickness the film ruptures, which is the equivalent of a bubble merger in boiling processes. By adding for example salt like sodium chloride to the water, the critical thickness can be reduced, inhibiting the coalescence process. Experiments with air bubbles formed at opposing injection tubes in water validate the theoretical results. In pool boiling this effect should also occur even if it is reduced by the higher dynamics of the process [19].

---

[1] The Jacob number is typically defined as $Ja = \frac{c_{p,\mathrm{l}}\, T_\mathrm{sup}}{\Delta h_v}$ representing the relationship between the sensible and latent heat.

2.4 Résumé of the state of the art and scope of the presented work

Considering the presented models and results, especially the controversy between the microlayer and the contact line model is striking. Both are validated by a large number of experimental investigations. Conspicuous are the different experimental conditions (especially the working fluids) validating each model. Furthermore, most of the experimental research presented has a limited range of variation in system parameters. Concerning bubble coalescence the number of investigations performed is small compared to single bubble experiments and measurements on a technical length scale. Influencing factors, like the pressure, have hardly been investigated. Furthermore, the experiments presented in chapter 2 show controversial results. Another shortcoming can be identified in the connection of the three major pillars mentioned in the introduction. In contrast to the experimental and numerical investigations acting on the same (small) length scale a clear deficit can be found in the connection between the small experimental and the technical length scale. To the knowledge of the author an experimental investigation of a transferability of results between different length scales has not been done up to now. Due to the huge number of influencing factors on boiling processes high demands are put on this investigation concerning a general comparability of different measurement results.

Out of this, the main goals of the present thesis are deduced:

- By means of experimental research on **single bubbles** it will be investigated whether bonding possibilities between the microlayer and the contact line model exist.
- Investigation of **bubble coalescence** processes will be performed by variation of system parameters.
- The transferability of the gained results on a small length scale to boiling processes on a larger length scale will be studied by experiments on a **technical length scale**.
- The experimental results should provide a **database** for comparison with and validation of numerical simulations.

To achieve these aims an experimental test setup will be constructed and fabricated. In this context, especially the high demand of setting and control of the physical properties has to be mentioned. The investigation of boiling processes of single bubbles and bubble coalescence as well as technical boiling processes should be possible. To do so, the measurement of a spatial and temporal high resolved wall temperature, heat flux, and bubble shape is necessary. Through the use of optical measurement techniques an examination of the reliability has to be performed, especially concerning the IR measurement technique, as its results are the basis of the heat flux calculations.

CHAPTER 3

Experimental Setup and Procedure

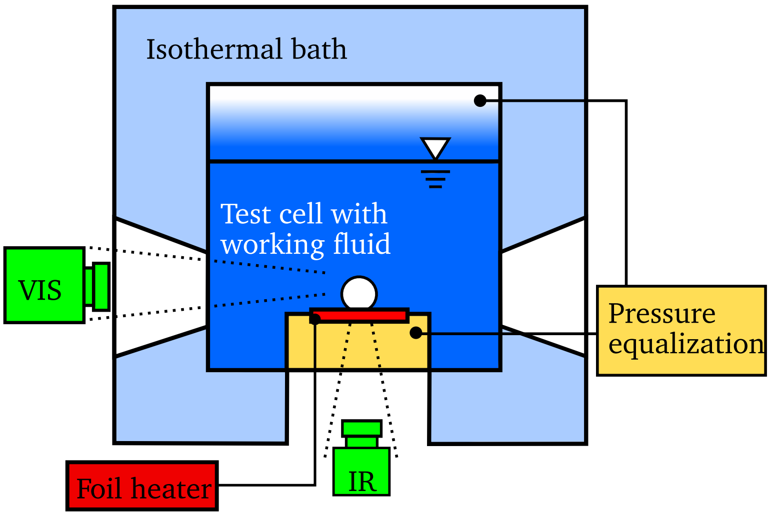

Figure 3.1: Schematic of the test facility

An experimental setup has been designed and fabricated to conduct the experiments mentioned in section 2.4. The basic requirements of the test setup were

- the nucleation of a single bubble and multiple bubbles at defined positions,
- a variable system pressure,
- a pure substance atmosphere,
- an optical accessibility to observe the shape of the bubble(s), and
- the measurement of the temperature profile close to the solid fluid interface with the possibility of a heat flux calculation with a high spatial and temporal resolution.

For measurements with laser-induced fluorescence (LIF) and Raman Spectroscopy further optical accesses and a high chemical resistance against alcohols and ketone (especially acetone and isopropanol) should be provided. These measurements are not discussed within this report because they are part of another PhD thesis at the author's institute. Therefore, the design measures concerning these requirements are not described in detail. Measurement results using LIF with acetone as working fluid conducted in the described test facility are presented by VOGT [148]. The experimental setup consists of six major components schematically shown in Fig 3.1:

- the test cell with the working fluid and five optical accesses,
- the isothermal bath to set the experimental conditions,
- the optical measurement systems (VIS and IR),
- the heater based on an electrical heated thin stainless steel foil,
- the pressure equalization to ensure a minimal pressure difference over the thin heating foil,
- the measurement and control systems (not shown in Fig. 3.1).

Regarding all requirements the constructed test facility allows measurements in steady-state saturated pure substance conditions in a range of 250 mbar to 1000 mbar and 10 °C to 65 °C for refrigerants, alcohols, ketone, and water. In the following the single components are described in detail. A list of the purchased parts is given in the appendix (A.3).

3.1 Test cell

The test cell is made of stainless steel and has five optical accesses. The filling volume is ≈ 150 ml. In Fig. 3.2 the body of the test cell is shown on the baseplate of the isothermal bath without connections and sight glasses. For the use of laser measurement techniques the optical accesses in the front and back have a shorter optical path (42 mm) than the accesses on the right and left side (58.5 mm). This design has been chosen to ensure a short optical path for the measurements and a reduction of the power density at the glasses where the laser beam passes in and out of the test cell. At the top the pressure transducer, the temperature sensors, the pressure equalization[1], and two bellow-type valves are implemented. As sealant ethylene propylene diene monomer (EPDM) is used. The resistance against fluorocarbons, ketone, and alcohol was tested by inserting the sealant into the liquid and vapor phase for about two weeks. The criterion for exclusion was a discoloration of the liquid or a change in the sealant's structure (e.g. brittleness). Especially for ketone the compound of the EPDM was important concerning the chemical resistance. The isothermal bath is made of acrylic glass. A picture of the test setup is shown in Fig. 3.3.

3.2 Heater

The heater is the main component of the test facility (see Fig. 3.4). The heat flux is provided by Joule heating within a 20 μm thick and approximately 24 mm wide stainless steel foil ⑩. In table A.3 (appendix) the physical properties of the foil are given. The foil is fixed onto the foil carrier ② by adhesive tape ⑪. The adhesive tape is double-sided and electrically insulating. The foil carrier and the adhesive tape have a ⌀12 mm center hole as optical access for IR thermometry of the backside of the stainless steel foil (cf. Fig. 3.4e). In this area the stainless steel foil is coated with a thin black layer to provide a high emissivity for IR thermometry. The foil is electrically connected by the electrodes ③. As the foil has an electrical resistance of < 100 mΩ a small contact resistance between the electrodes is of major importance for the experiments. A large contact resistance leads to intensive parasitic boiling between the electrodes and the foil. To minimize the contact resistance an optimized local alignment

---

[1] For version 1 (cf. 3.4)

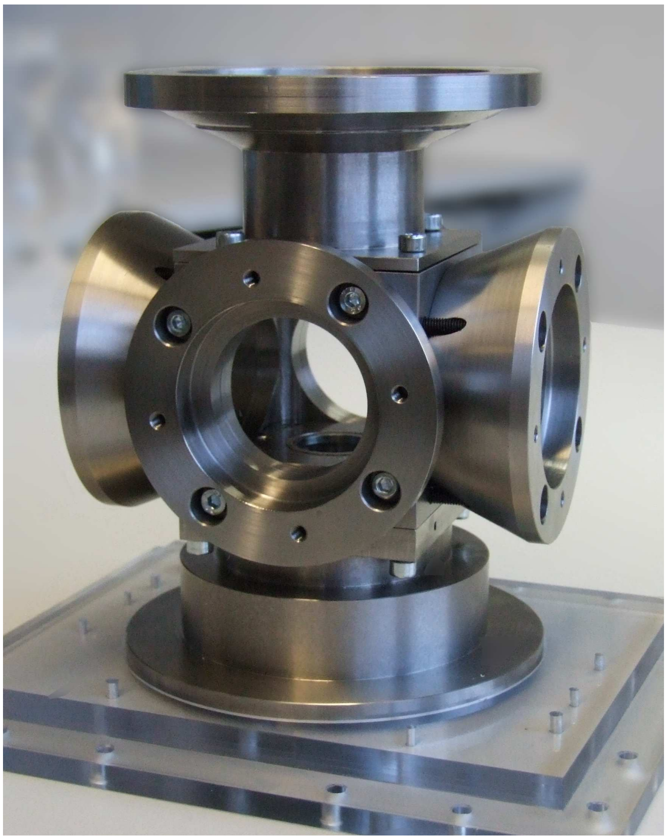

Figure 3.2: Basic body of the test cell

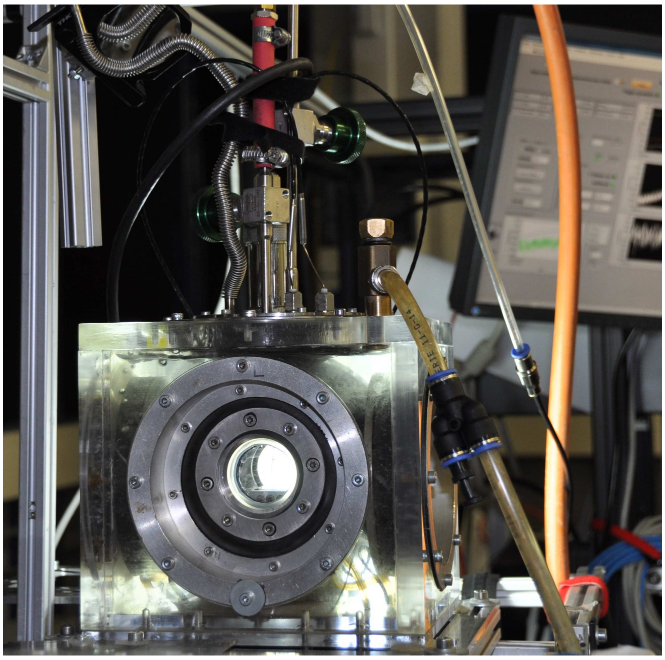

Figure 3.3: Photograph of the test setup - camera removed

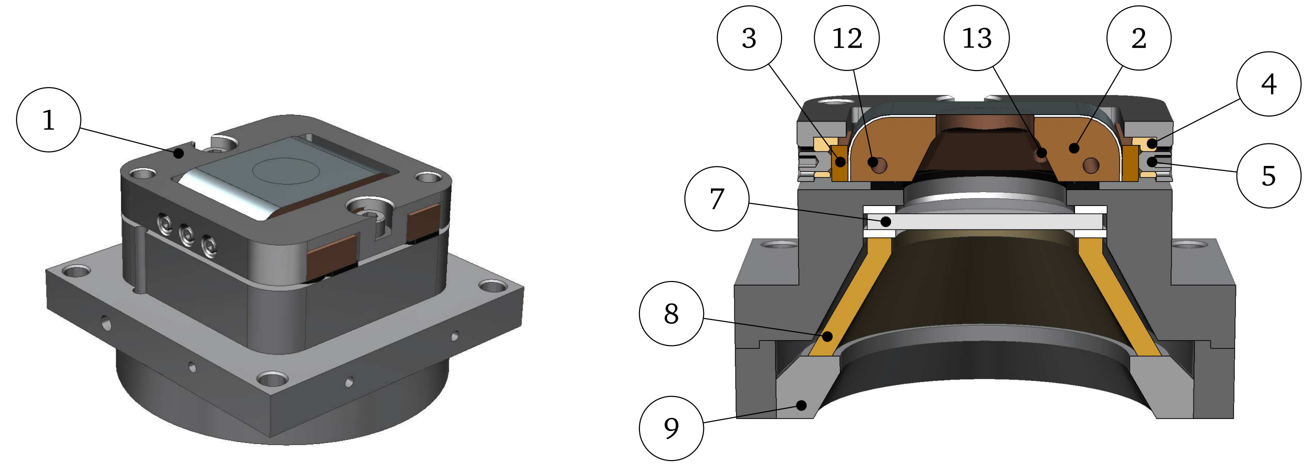

(a) Heater with baseplate of the test cell

(b) Sectional view of the heater with baseplate

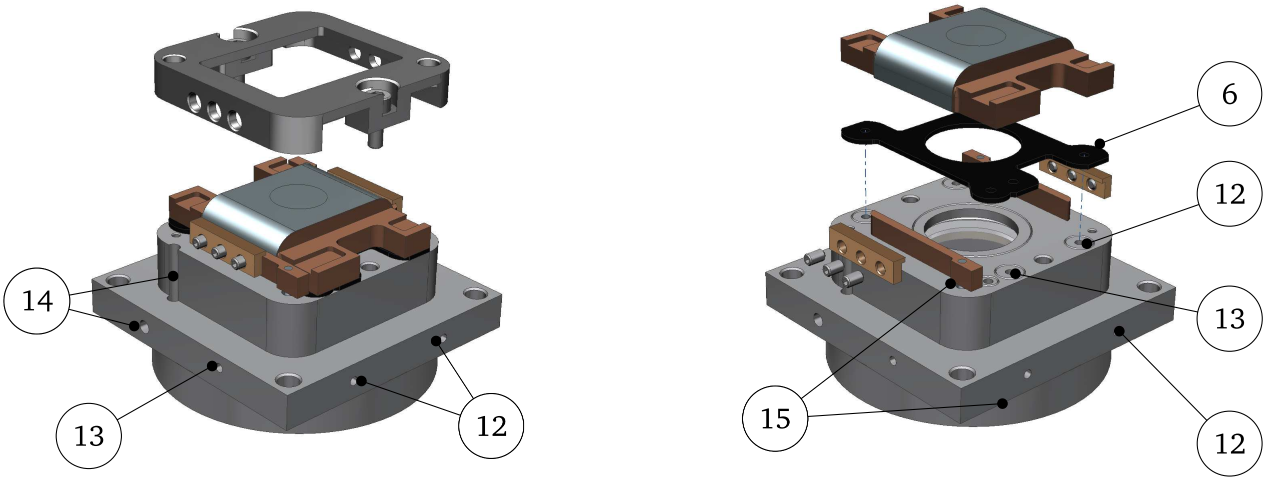

(c) Electrical connections

(d) Sealing and fluid feed-throughs of pressure equalization and electrode cooling

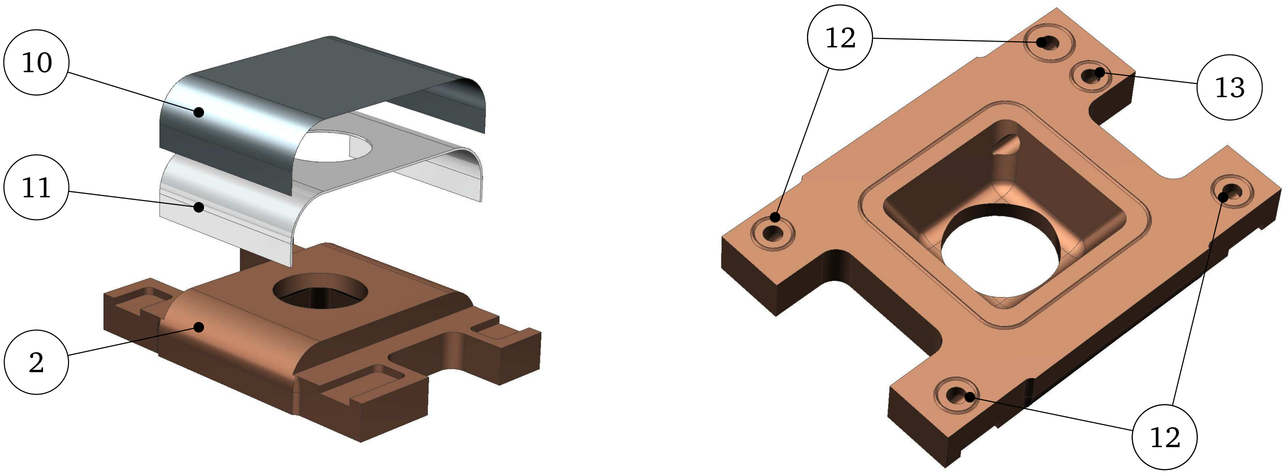

(e) Foil carrier with stainless steel foil and adhesive foil

(f) Bottom of the foil carrier with sealing enhancement and fluid feed-throughs

Figure 3.4: Heater of the test facility

Table 3.1: Components of the heater

①	Cover profile	⑥	Sealing	⑪	Adhesive tape
②	Foil carrier	⑦	IR-transparent glass	⑫	Electrode cooling feed-through
③	Electrode	⑧	Distance tube	⑬	Pressure equilisation feed-through
④	Electrode clamp	⑨	Ring nut	⑭	Working fluid feed-through
⑤	Grub screw	⑩	Stainless steel foil	⑮	Electronic connection

between each electrode and the foil is necessary. Therefore, the electrodes are connected by flexible cables. The cables are PTFE insulated and pass through the base plate of the test cell ⑮. The sealing of the fluid feed-through is achieved by a combination of a chemically highly resistant grouting and epoxide adhesive. By tightening the grub screws ⑤ the electrodes are pressed against the foil. For electrical insulation the electrode clamps ④ are made of polyether ether ketone (PEEK) (cf. Fig. 3.4c). To rule out boiling between the electrodes and the foil a further cooling channel is implemented within the foil carrier close to the electrodes ⑫. Via a fluid feed-through in the base plate liquid can be pumped through the foil carrier to cool at the position of the connection between the electrode and the stainless steel foil. A closed volume under the heated foil is provided by use of infrared transparent glass ⑦. This enables the setting of the pressure under the foil for pressure equalization and provides an optical access to the backside of the foil. The air used for the pressure equalization is passed through the base plate and the foil carrier ⑬. The pressure control under the foil is described in section 3.4. The IR-transparent glass is mounted by a distance tube ⑧ and a ring nut ⑨ to ensure a free optical path for IR thermometry (cf. Fig. 3.4b). The foil carrier is fixed on the base plate with the cover profile ①. As the electrode cooling and the pressure equalization passes through sealing ⑥ the foil carrier and the base plate is profiled to enhance the tightness. The sealing ⑥ is made of EPDM. The fluid feed-through ⑭ enables the exchange of the working fluid. For the use of solvents as working fluid the adhesive tape ⑪ is replaced by a polyethylene (PE) foil. The bonding results from the thermoplastic behavior of PE by heating up the foils pressed on the foil carrier.

3.3 Artificial cavities

To ensure nucleation at a defined position artificial cavities are implemented into the heating foil. Therefore methods like

- chemical etching,
- electrolytic abrasion,
- laser sintering,
- laser surface treatment,
- focused ion beam (FIB), and
- mechanical scratching and puncture

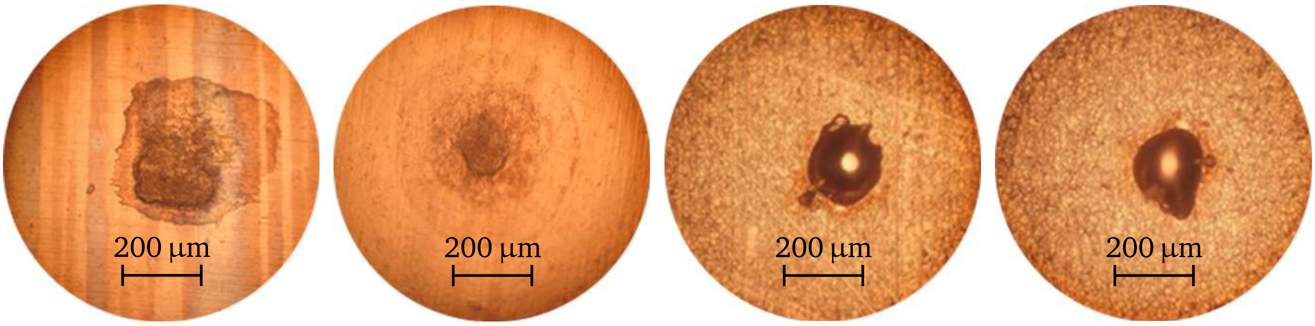

(a) Etched cavity **(b)** Etched cavity **(c)** Sintered cavity **(d)** Sintered cavity

Figure 3.5: Chemical etched and sintered artificial cavities

can be used. To ensure boiling at an artificial cavity the necessary superheat for nucleation has to have a minimum at this position compared to the rest of the heating foil (cf. section 2.2.2). Measurements with bubble coalescence pose a particular challenge for the preparation of the artificial cavities. The thermal interaction of both cavities can result in an activation of natural cavities before the second artificial cavity can be activated. In addition, the size of the cavity is strongly limited by the distance between both cavities. This accentuates the particular importance of reproducible artificial cavities. Schweizer [119] and Wagner [149] observed that rough cavities could be activated more easily than smooth ones. This effect has been attributed to a higher number of possible nucleations in the cavity. Therefore the requirements especially for coalescence measurements are

- a rough surface of the cavity,
- a diameter $d \leq 150\,\mu\text{m}$, and
- reasonable production costs.

Therefore electrolytic abrasion, FIB as well as mechanical scratching and puncture could not be used due to low reproducibility (electrolytic abrasion, scratching), the size of the cavity (electrolytic abrasion), or the high production costs (FIB). A further description of these methods is given by Schweizer [119] and Wagner [149].

Investigations of the reproducibility and the possible activation of cavities created by chemical etching, laser sintering, and laser surface treatment have been performed. For chemical etching an adhesive foil was punctured with a heated wire (diameter $\approx 100\,\mu\text{m}$) and was fixed on the stainless steel foil. A solution consisting of iron(III)chloride ($FeCl_3$), hydrochloric acid (HCl), nitric acid (HNO_3), and water (H_2O) is placed on the stainless steel foil masked by the adhesive tape. Different compositions of the solution, dwell times (15 min to 120 min), and temperatures (20 °C to 65 °C) are tested. In Fig. 3.5a and 3.5b, pictures of an etched cavity are shown. An enlargement of the cavity caused by creeping effects under the mask can be seen. The method has a deficient reproducibility as both cavities are produced under the same conditions. Within boiling tests the possibility of activation was moderate. In contrast to all other methods material is added to the foil by laser sintering[1]. Therefore a thin layer of stainless steel powder is placed on the foil. Afterwards the powder is welded by laser radiation. The geometry is given by CAD data. In Figs. 3.5c and 3.5d two cavities produced by laser sintering with the same CAD model are shown. A good reproducibility and small dimensions are possible using this method. Due to the very smooth surface there is little possibility of activation.

---

[1] The laser sintering was performed by the Institute of Production Management, Technology and Machine Tools (PTW) (Technische Universität Darmstadt). Used machine: Eosint M 270.

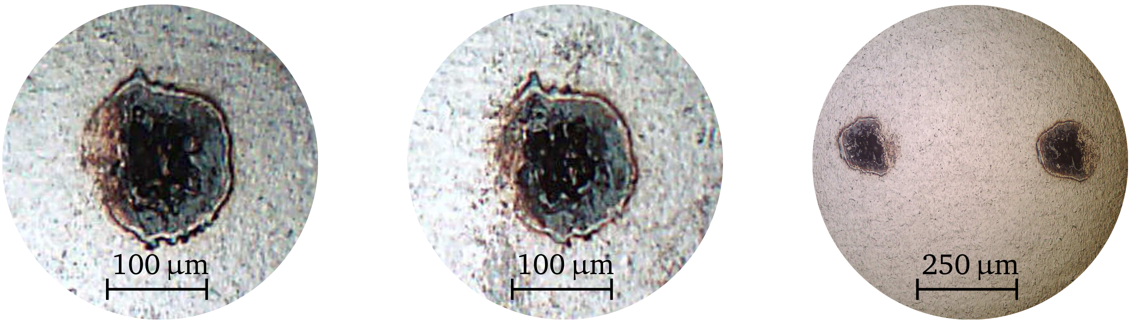

(a) Single cavity **(b)** Single cavity **(c)** Cavities with 500 µm distance

Figure 3.6: Artificial cavities created with laser surface treatment

Using laser surface treatment[1] next to the spatial arrangement of the laser pulses itself, several process parameters can be adapted influencing the geometry of the artificial cavities. The most important are

- the distance from the stainless steel foil to the focal point of the laser,
- the laser power,
- the number of laser pulses, and
- the waiting time between each pulse.

The influence of the single parameters are shown in the appendix (A.5). In Fig. 3.6 artificial cavities produced by laser surface treatment are shown. A good reproducibility can be seen. The picture indicates a structured geometry. The diameter of the cavities is approximately 150 µm. In Fig. 3.6c two cavities for coalescence measurements with a distance of 500 µm are shown. The possibility of activation has been tested successfully in the test facility. Therefore, these cavities are used for the experiments presented in this thesis. The laser parameters used for the shown cavities are listed in table A.4.

3.4 Pressure equalization

The pressure equalization ensures a minimum pressure difference across the thin stainless steel foil. Within the scope of this thesis two different kinds of pressure equalization systems have been used. In the following the differences of both systems are described leading to the adaption of the pressure equalization system. The measurement results are not influenced by the used pressure equalization system. In contrast to that the operability of the measurement facility is affected significantly.

The first pressure equalization system is based on the design of Wagner [149] and shown in Fig. 3.7. The vapor phase of the test cell is connected to a flexible PE bellow ①. The bellow is placed inside a box ②, which is connected to a pressure controller ④. The pressure controller can either reduce (by use of a vacuum pump) or increase (by an inflow of ambient air) the pressure inside the box ②. Thereby the flexible bellow ① transfers the pressure into the system. The working range is between 0 mbar and 1000 mbar. Between the box and the controller a stainless steel tank ③ is placed to avoid liquid reaching the vacuum pump. The box ② is heated to reduce the amount of condensed liquid in the bellow. It is placed above the test cell to ensure the drainage of any condensed liquid into the test cell. This is necessary for the use of mixtures as working fluid to avoid an enrichment of the less volatile component in the test cell.

---

[1] The laser surface treatment has been performed at the Institute for Production Engineering and Forming Machines (PTU) (Technische Universität Darmstadt). Used machine: Micrmac 3D- microstructure ns532

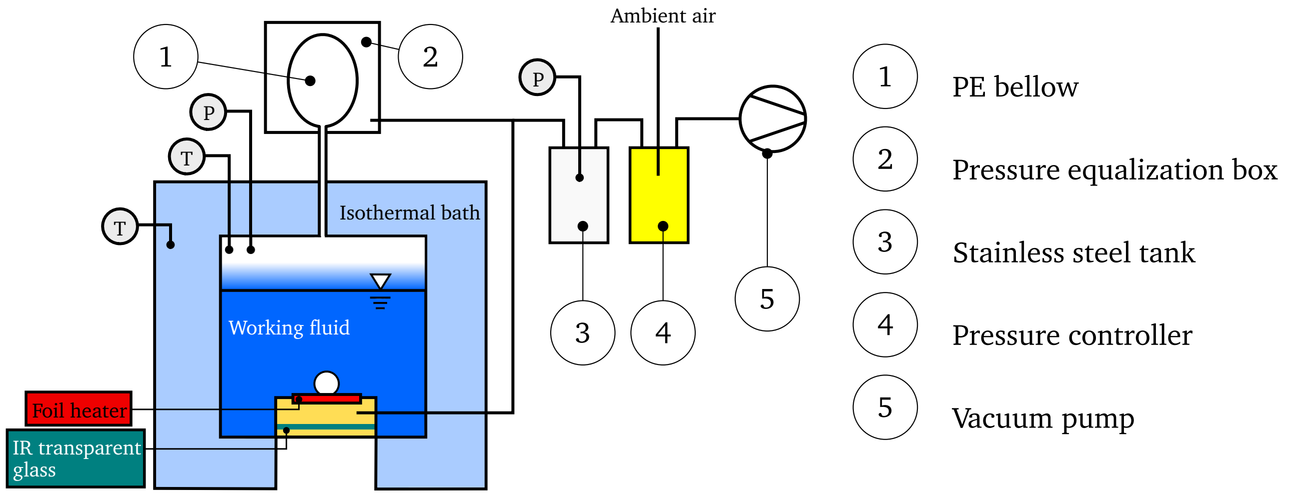

Figure 3.7: Pressure equalization (version 1)

The system behavior using this pressure equalization is shown in Fig. 3.8. The measured pressures in the test cell (red) and the box[1] (black) are shown as well as the measured temperatures in the test cell[2] (green) and the isothermal bath (blue) (cf. Fig. 3.7). In the top part the system behavior is shown for a non-degassed case with decreasing system pressure. In the bottom part the system behavior is shown for a degassed case with increasing pressure, as the degassing is performed at a pressure of approximately 300 mbar. For a comparison the temperatures are converted into a pressure value by use of the saturation curve of FC-72[3]. For the non-degassed case it can be seen that the pressure values in the box and the test cell correspond with each other, whereas the temperature in the test cell (especially for lower pressures) is related to the temperature of the isothermal bath (right detail). The small difference between the pressure in the test cell and the box (especially for lower pressures) is related to the measurement position of the pressure transducer and a minor leakage of the box which was deliberately implemented for a more stable system control. The influence of the non-condensible gas can be seen in the left detail as the measured pressure is higher than the converted temperature. For a degassed case (bottom) it can be seen that the system pressure and the temperature follow the temperature of the isothermal bath (right detail) independently of the controlled pressure in the box. The lower value of the pressure in the test cell can be related to slightly superheated fluid (< 500 mK) as the degassing is performed by boiling and the temperature sensor in the liquid is close to the heated surface. The existence of a pure substance system can be seen in the left detail.

The usage of ambient air for the pressure equalization can cause condensation between the foil and the IR-transparent glass. Especially for warm and humid weather conditions the condensation temperature of the air humidity was lower than the temperature of the electrode's cooling. A picture of condensed water after the degassing process at 300 mbar is shown in Fig. 3.9.

To avoid the mentioned drawbacks an enhanced pressure equalization was designed, commissioned, and used (see Fig. 3.10). As for a pure component system a pressure setting using the flexible bellow is not possible it has been removed. Instead the measured pressure in the test cell is used as input for the pressure controller. To prevent condensation compressed air ($p \approx 6$ bar to 8 bar) at room temperature is filtered (carbon filter) and reduced in pressure (≈ 1.1 bar) ⑥. The stainless steel tank is used to

---

[1] The measurement point is in the stainless steel tank.

[2] The temperature is averaged by the vapor and liquid temperature.

[3] A saturation curve is given in A.2.

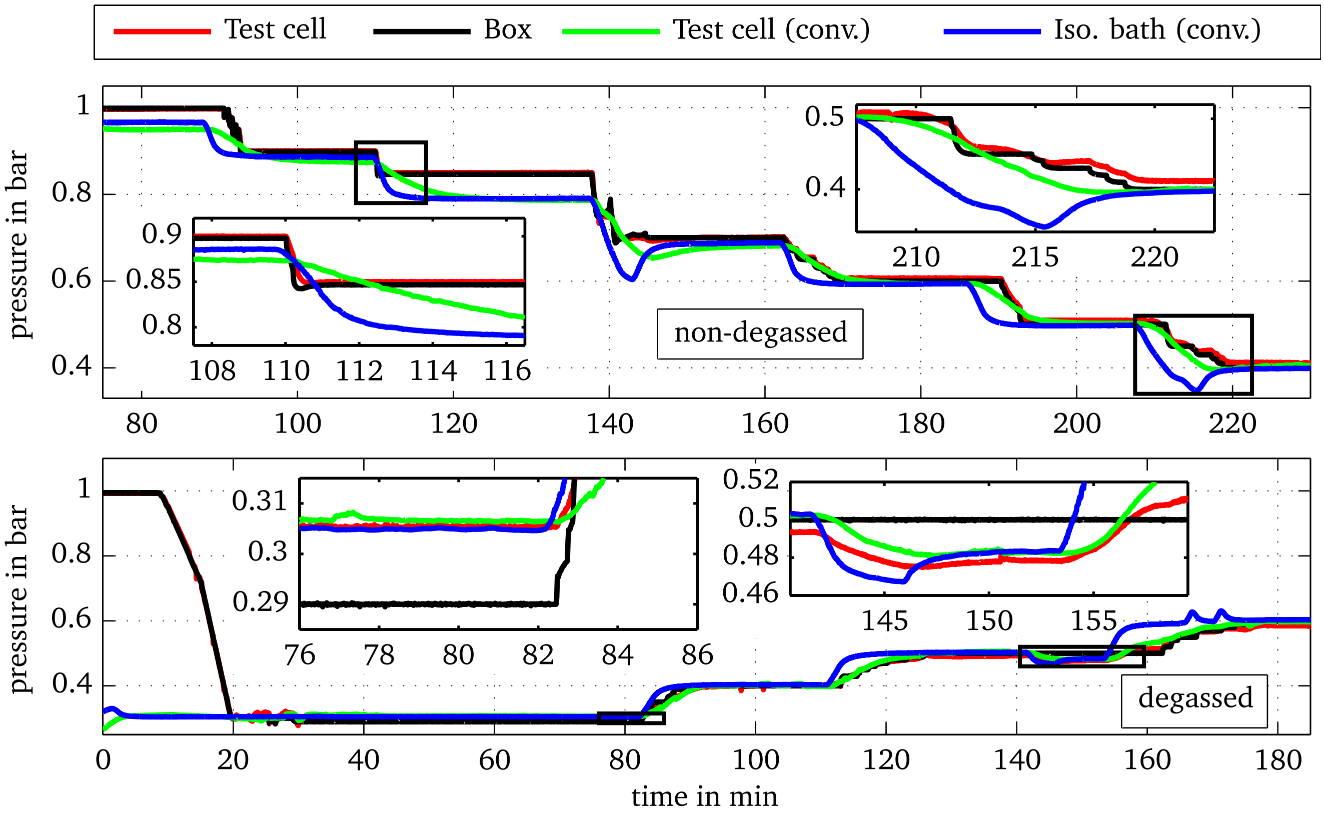

Figure 3.8: System behavior with non-degased (top) and degased (bottom) fluid (version 1)

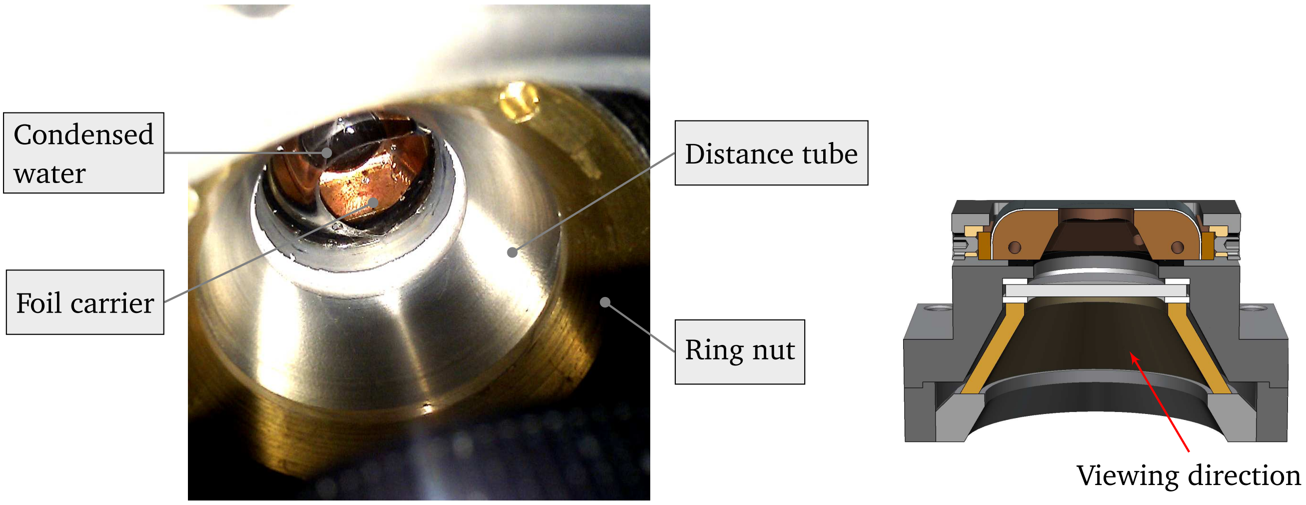

Figure 3.9: Condensed water between the heated foil and the IR-transparent glass (cf. Fig. 3.4b)

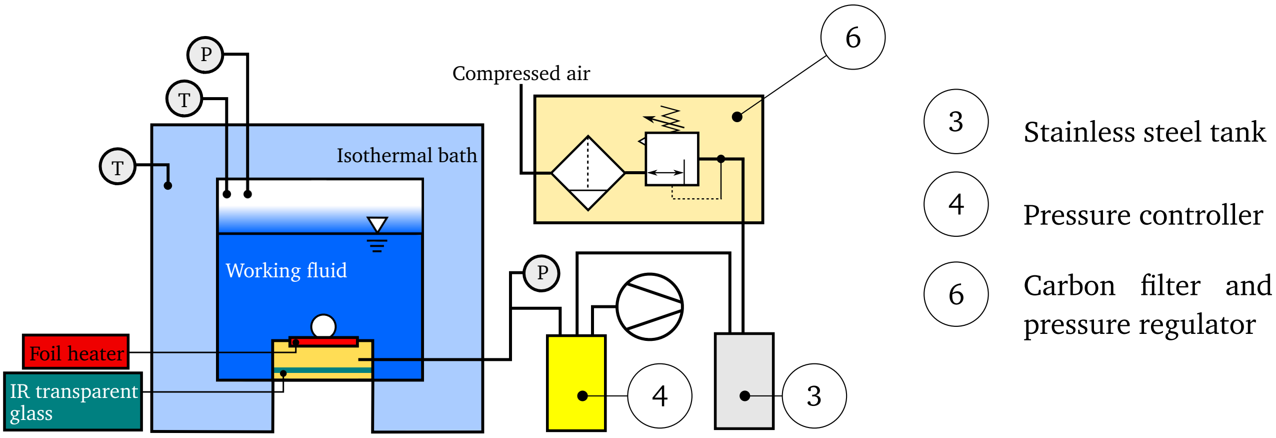

Figure 3.10: Pressure equalization (enhanced version)

compensate possible pressure fluctuation. The usage of this system places a higher demand on the operative reliability as a possible pressure difference has to be directly compensated by the thin foil.

3.5 Measurement and control system

The temperature in the system is measured by thermocouples and platinum resistance thermometers (PT100). All temperatures relevant for the evaluation are measured by use of PT100 because of the better accuracy compared to thermocouples. These are in particular the temperature of the vapor and the liquid in the test cell and the temperature of the isothermal bath. The temperature sensors were calibrated with a calibration bath using a reference sensor. The accuracy of the used sensors (over the complete section of measurements) is ±150 mK. The pressure transducer had been calibrated by the supplier. The accuracy is ±0.01 % of the measurement range, corresponding to ±0.1 mbar. The accuracy of the analog input module is in the same order of magnitude. Therefore the accuracy of the pressure measurement is less than 1 mbar. A massive heater replacement without a foil is used for a leakage test. The test is performed for a pressure level less than 100 mbar with a leakage rate of $q < 3 \times 10^{-4}$ mbar l/s. The leakage of the foil's sealing is evaluated by comparing saturation temperature and pressure over time. A standard leakage test could not be performed for the foil as it would be destroyed by the pressure difference. Tests were regularly performed between different series of measurements. All measurements were conducted at a leakage rate of $q \approx 1 \times 10^{-3}$ mbar l/s. The approximation is based on the combination of the leakage tests of the cell and the foil. As the measurement time is within the range of a few minutes and a further degassing can be performed between single measurements this leakage range is sufficient for measurements with a pure substance. As measurement system a National Instruments cRio and for data acquisition and system control a LabView program is used. By use of an operational amplifier a current driver is added to the analog output to provide a sufficient output power for external control. For the observation of the temperature of the heater a high-speed IR camera with a wavelength range of 3 µm to 5 µm is used. For observation of the bubble shape a high-speed black and white camera is used. A triggerable high-power LED system is implemented together with a holographic diffuser for illumination. By pressing an external trigger the light source is switched on and a further trigger (controlled by the illumination system) starts the IR and the VIS cameras as well as the data recording simultaneously. After a measurement sequence (≤ 5 s) the light source is automatically switched off. A continuous operation of the illumination leads to a temperature increase of $\Delta T \geq 500$ mK due to radiation heat transfer measured with the PT100 in the fluid. For the short measurement time no change in temperature could be observed. The optical measurement techniques are further explained in the following chapter 4. The heating foil is powered by a current controlled DC power supply. The

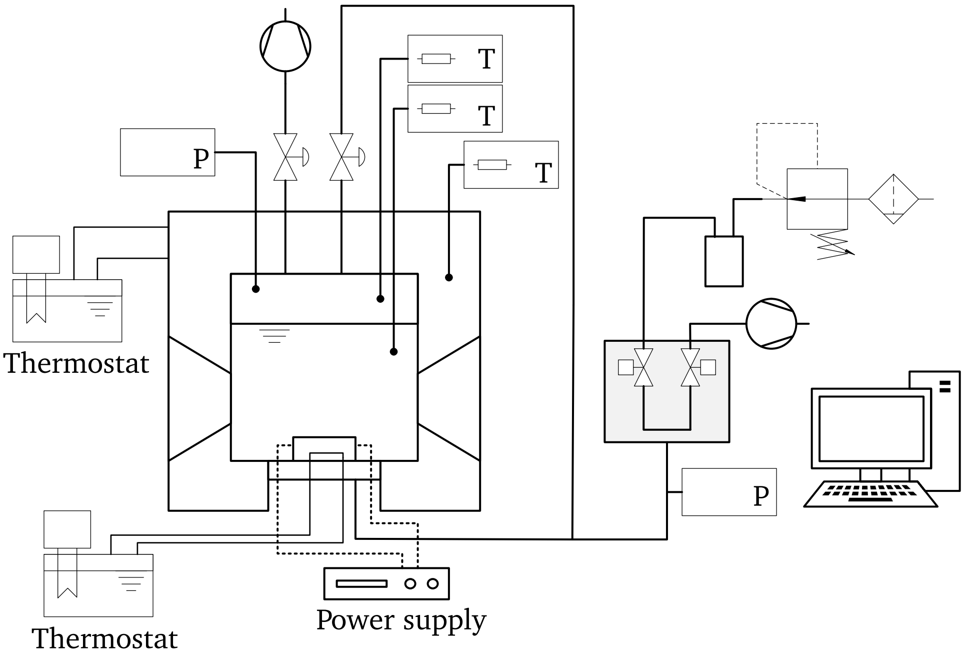

Figure 3.11: Process diagram of the test facility

temperature of the isothermal bath and the electrode cooling is controlled by two external refrigerated heating circulator baths. In Fig. 3.11 a process diagram of the test facility is shown.

3.6 Experimental procedure

After the heater has been fixed to the baseplate (cf. Fig. 3.4a) a laser is focused on the artificial cavity to set the field of view for the IR thermometry. Afterwards the test cell and the isothermal bath are reassembled. The test cell is evacuated and filled with the working fluid. The isothermal bath is filled with water. The working fluid is degassed by boiling. The existence of a pure substance system is checked by comparing the saturation pressure and temperature (cf. Fig. 3.8). For the measurements the electrode cooling is switched on to avoid boiling between the electrodes and the foil. In general the temperature of the cooling system was set 5 °C below the saturation temperature. Nucleation is initiated by high heat fluxes. For single bubble boiling or coalescence measurement the heat flux is afterwards reduced up to intended boiling behavior. Measurements for different pressures and heat fluxes are perfomred with increasing pressure and degresing heat flux.

Chapter 4

Optical Measurements and Data Evaluation

4.1 Measurement of the shape of the bubble

The usage of high-speed photography usually entails a large number of images. The experimental investigation in this work contains about 10^6 single black and white images. Therefore an automatic evaluation is essential. The evaluation is performed within Matlab detecting the equivalent bubble diameter at the detachment of the bubble, the bubble frequency, the growth, waiting, and cycle times as well as the apparent contact angle and the interface velocity at the apparent three-phase contact line. In Figure 4.1 the basic principle of the evaluation is shown. In the histogram (b) of the original 8-bit image[1] (a) two major peaks can be observed. The peak at the lower intensity represents the dark bubbles and the peak at the higher intensity the background. By means of a cumulative distribution (c) an individual threshold is defined for every picture to create a binary image (d) separating the bubbles from the background. To define the position of the threshold, the minimum and maximum gradient is detected within the cumulative distribution. The minimum gradient is detected by applying a linear fit to the interval $[I, I+50]$ in a range of $(0 < I < 150)$, where I is the intensity of the picture. This intensity I_{min} is shown by the red square in Fig 4.1c. The maximum gradient is detected similarly in a range of $50 < I < 200$ represented by the green triangle I_{max}. The threshold (vertical black line) is calculated by

$$I_{\text{tr}} = \frac{b_{\text{max}} - b_{\text{min}}}{m_{\text{min}} - m_{\text{max}}} - \frac{I_{\text{max}} - I_{\text{min}}}{2}, \tag{4.1}$$

where b is the axis intercept and m the gradient of the linear fits (red and green lines). With regard to Fig. 4.1c it has to be noted that I_{min} and I_{max} represent the first value of the respective interval. The equivalent bubble diameter is calculated by

$$d_{\text{eq}} = \frac{1}{C_{pm}} \sqrt[3]{1.5 \sum_{\text{n}} \Delta X_P^2 \cdot 1\ \text{pixel}} \tag{4.2}$$

for the picture where the bubble departure is detected. ΔX_P is the number of pixels detected as vapor in row n of the bubble. C_{pm} is the conversion factor between pixel and mm. The detected bubble shape is shown in Fig. 4.1 (e). The apparent contact angle (f) is calculated by a linear fit of the interface position (taken from the binary image) using the lower seven pixel rows. It should be mentioned that this contact angle gives more an impression of the bubble shape near the heater than a contact angle as introduced in chapter 2.

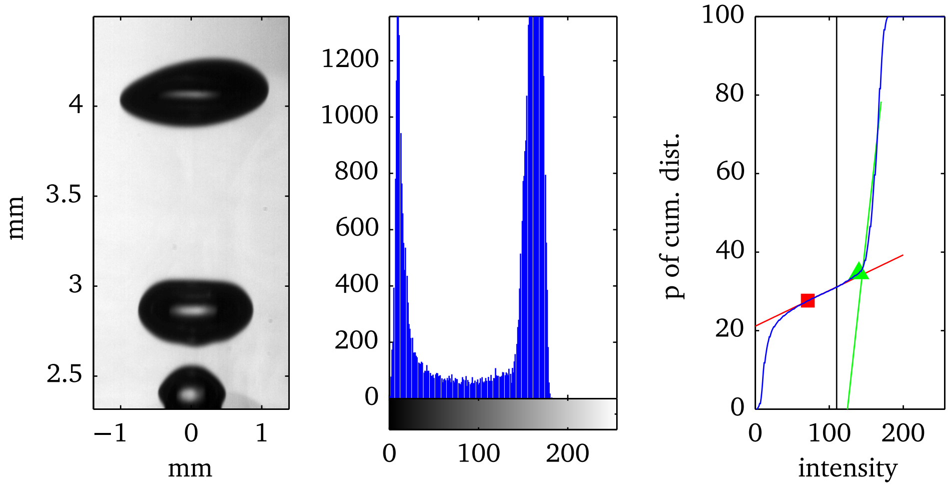

(a) Original image **(b)** Histogram **(c)** Cumulative distribution

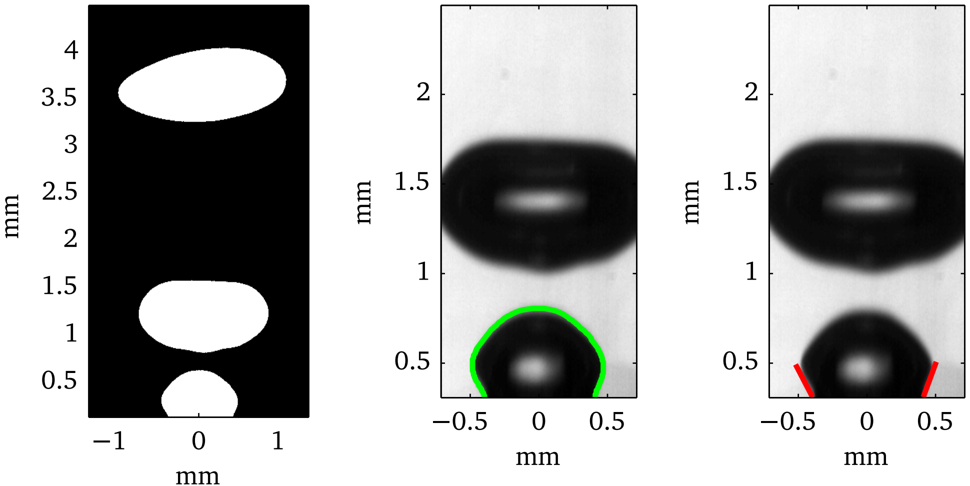

(d) Binary image **(e)** Bubble shape **(f)** Apparent contact angle

Figure 4.1: Data analysis of bw images

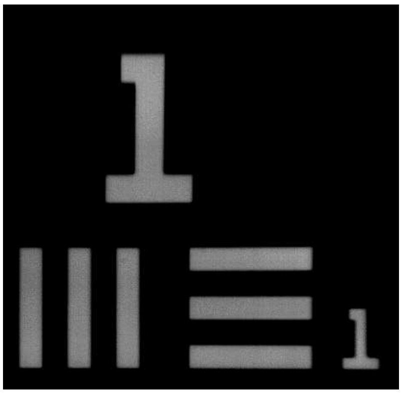

Figure 4.2: USAF1951 resolution test chart

Table 4.1: Accuracy of the optical measurements

	Value	**Error**	d_{eq}	Δd_{eq}
C_{pm}	137.5 Pixel/mm	±5 %	1.46 mm	43 %
ΔX_P		8 Pixel	0.5 mm	36.6 %

The resolution of the camera and with this the conversion factor C_{pm} is measured using a known length scale. In Fig. 4.2 a detail of a used USAF 1951 resolution test chart is shown. For the determination of the bubble's size two kinds of uncertainties have to be considered. The first one is related to the length of the intensity drop from the bright background to the dark bubble. For the shown measurements this uncertainty is approximately 8 pixels. A less obvious but more substantial uncertainty results from the optical setting itself as the reference measurement cannot be performed in situ in most cases. This uncertainty is exemplified by means of Figs. 4.3 and 4.4. In Fig. 4.3 a simplified optical setup containing an object, a lens with iris, and an image plane is shown. The dimensions are related to the optical setup used for the measurements. In Fig. 4.4 the original object (top) and the calculated images for different optical conditions are shown. The images are calculated by a one-dimensional ray-tracing algorithm neglecting spherical and chromatic aberration. If the object is placed at the object distance for a sharp image the diameter of the iris has no effect on the sharpness or resolution (left side). If the object is placed out of the object distance the image is blurred as expected. For a small iris diameter (large f-number) another conversion factor would be calculated by an apparently sharp image. The apparently sharp image is caused by a higher depth of sharpness. In the shown example this uncertainty is about 17 %. The observation of a boiling process usually requires a higher depth of sharpness. If the reference measurement is not performed in situ (including the working fluid at defined conditions) this effect has to be considered. The effect can be eliminated by the use of a coherent light source. Contrary to the positive effect on the resolution a coherent illumination results in a stronger appearance of schlieren influencing the evaluation of the pictures negatively. A similar effect can be observed by a changed refraction index (e.g. by use of a different working fluid or measurements over a large temperature range). Correcting this apparent change in the object distance by focusing the lens rather than adapting the object distance, a change in resolution can be observed. Despite carefully setting up the optical system the inaccuracy of the used converting factor has to be considered conservatively with ± 5 %. Therefore the resulting error for the bubble diameter can be calculated [62] by

$$\Delta d_{\text{eq}} = \left| \frac{\partial d_{\text{eq}}}{\partial C_{pm}} \Delta C_{pm} \right| + \left| \frac{\partial d_{\text{eq}}}{\partial \Delta X_P} \Delta(\Delta X_P) \right| . \tag{4.3}$$

The calculated error for two bubbles of different sizes is shown in table 4.1.

The automatic detection of a bubble departure requires a separate condition for a bubble cycle with and without waiting time. For the case without waiting time neither bubble is separated from each other in the binary image. Therefore the apparent position of the contact line over time is used for the detection of a bubble departure. The detailed definition combining both requirements for the detection of a bubble departure is given in the appendix (chapter A.6). In Fig. 4.5 the detected bubble departures and nucleations are shown for a medium pressure of 650 mbar together with the position of the apparent contact line. The axes are exchanged for a better comparability with the shown pictures. On the right side an example of a bubble departure without waiting time is shown. The bubble departure is detected at 0.0139 s. The green contour represents the detected shape of the bubble at departure.

---

[1] An intensity of 0 represents black and 255 represents white.

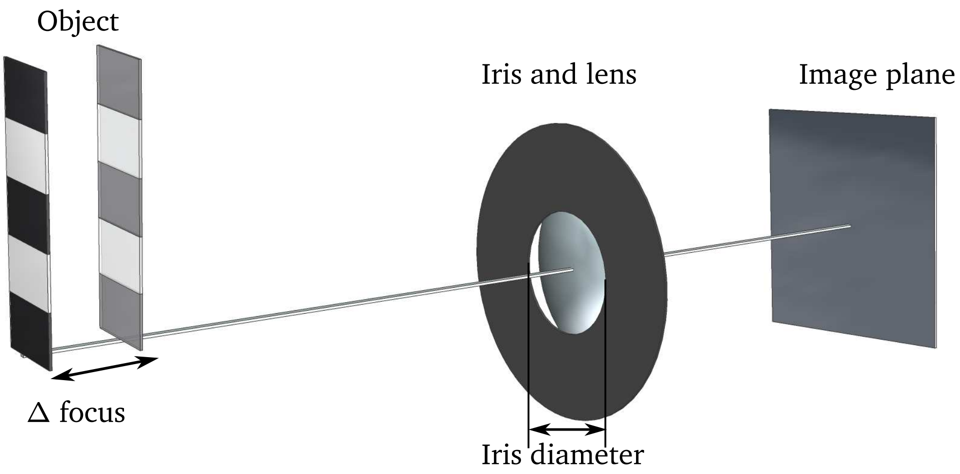

Figure 4.3: Schematic of a simplified optical setup

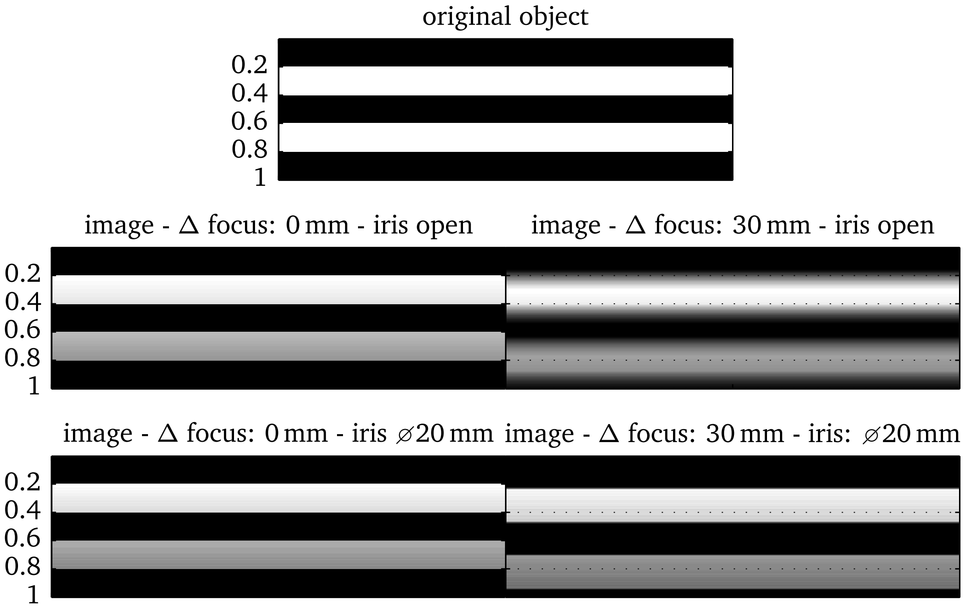

Figure 4.4: Influence of depth of sharpness on the resolution

4.2 Temperature measurement and heat flux calculation by infrared thermometry

The IR measurement technique offers a convenient way to measure the temperature of the heater and calculate the heat flux at the heater surface. Contrary to the simple applicability the evaluation of the IR data is very sensitive to calibration and evaluation. To show the sensibility and effects, different assumptions and methods concerning

- the kind of calibration,
- assumptions for thin foils, and
- the calculation of the heat flux profile

are compared in the following.

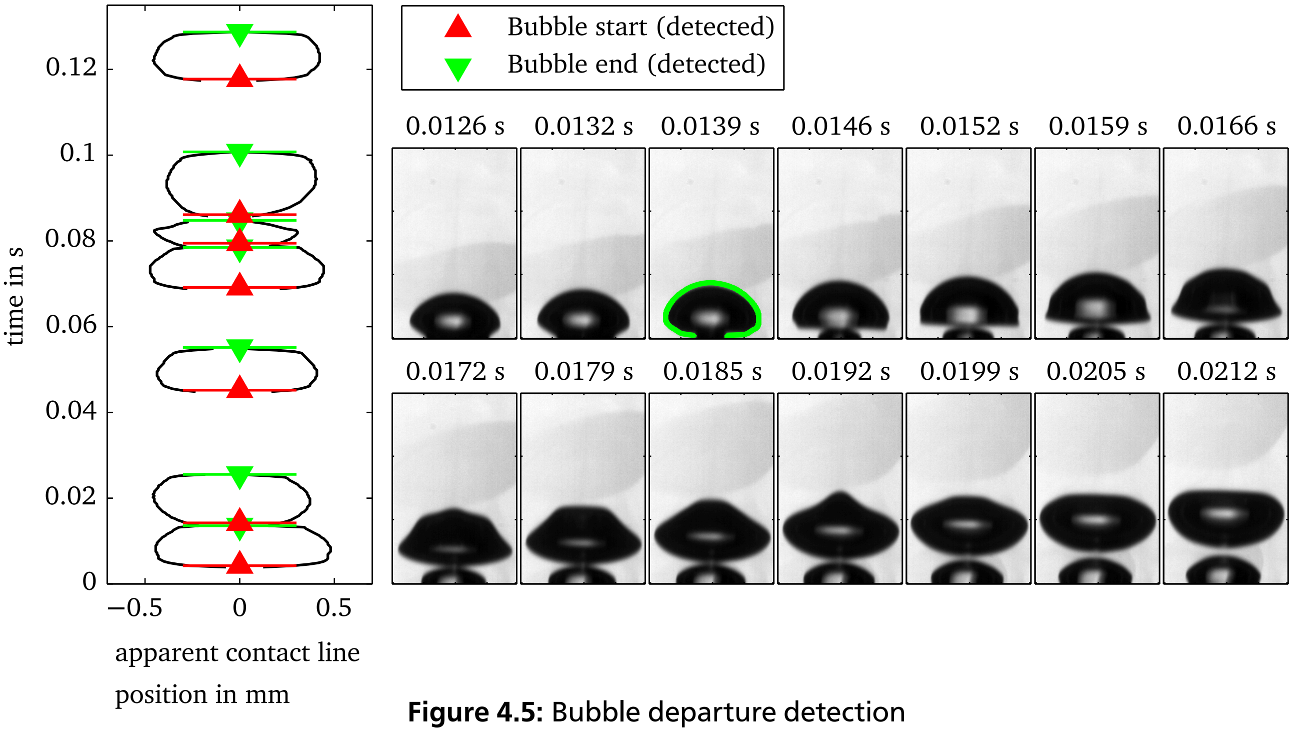

Figure 4.5: Bubble departure detection

4.2.1 Calibration of infrared data

Every camera measures an intensity signal. Using an IR camera the temperature of the object can be determined from this intensity. To do so, a calibration is necessary. For the described experiments the calibration is performed by applying a stable and homogeneous temperature to the foil. For this the cell was filled with distilled water and tempered by the isothermal bath (cf. Fig. 3.1). To fit the temperature T over the intensity I a physical based function should be applied. Hence, ***Planck's law***

$$J_{b,\lambda}(\lambda, T) = \frac{K_1}{\lambda^5 \left(e^{\left(\frac{K_2}{\lambda T}\right)} - 1 \right)}, \tag{4.4}$$

where

$$K_1 = 2\,\pi\,h\,c_0^2 = 3.71x10^{-16}\text{W m}^2 \quad \text{and} \quad K_2 = h\,c_0/k_B = 1.44\times10^{-2}\text{m K}, \tag{4.5}$$

and ***Stefan-Boltzmann law***

$$E_b(T) = \sigma_{SB} T^4 \tag{4.6}$$

can be considered. $J_{b,\lambda}$ is the intensity of light with the wavelength λ at the temperature T. The physical constants are the speed of light c_0, the Boltzmann constant k_B, and the Planck's constant h. Integrating Eq. 4.4 over wavelength leads to Eq. 4.6, where E_b is the emission of a black body and σ_{SB} $= 5.67\times10^{-8}$ W/(m^2 K^4) the Stefan-Boltzmann constant. The corresponding curve fitting functions are

$$T = \frac{C_1}{\ln\left(\frac{1}{I + C_2}\right)} + C_3 \tag{4.7}$$

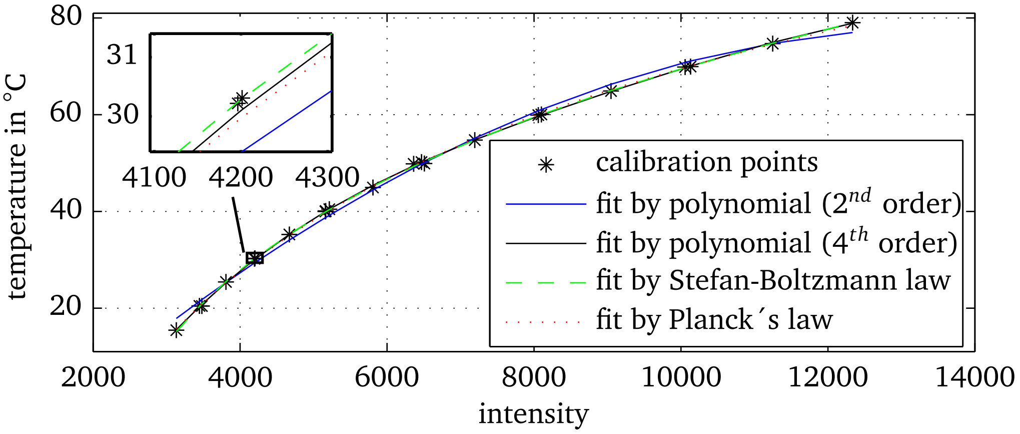

Figure 4.6: Comparison of different curve fittings

Table 4.2: Least square of different calibration fits

	$S_{\mathrm{i}}/S_{\mathrm{SB}}$
Stefan Boltzmann	1
Planck's Law	2.15
Polynomial 4^{th} order	1.08
Polynomial 2^{nd} order	29.21

for the ***Planck's Law*** and

$$T = C_1 \left((I + C_2)^{(1/4)} + C_3 \right) \tag{4.8}$$

for the ***Stefan-Boltzmann Law***.

In Fig. 4.6 four different fits for $T = T(I)$ are compared. For this comparison the intensity values from a single pixel element of the IR camera are used. Additionally to the physically based functions polynomial functions of second and fourth order are applied. Some temperatures are calibrated repeatedly to ensure the stability of the calibration procedure. The least squares S [13] of the different fits are given in table 4.2 compared to the Stefan Boltzmann fit for the calibration interval of [15, 80] °C. As the calibration based on the Stefan Boltzmann law fits the data best it is used in the following.

As the measured intensity of an IR camera is not directly related to the temperature of the object but also a function of different characteristics of the pixel of the camera sensor, differences in the emissivity of the object, and vignetting[1] the calibration curves can differ from pixel to pixel. A comparison of a pixel-wise and a global calibration is shown in Fig. 4.7 using a calibration sequence at 60.05 °C[2]. For the global

---

[1] 'Vignetting is the radial attenuation effect of the image's brightness intensity from the center of the optical axis to the edges.' [109].

[2] 60.05 °C corresponds to the averaged temperature measured by the PT100 used for the calibration and therefore the set point for calculation of the calibration curve. The absolute accuracy of the PT100 has to be considered for the absolute accuracy of the temperature measurement.

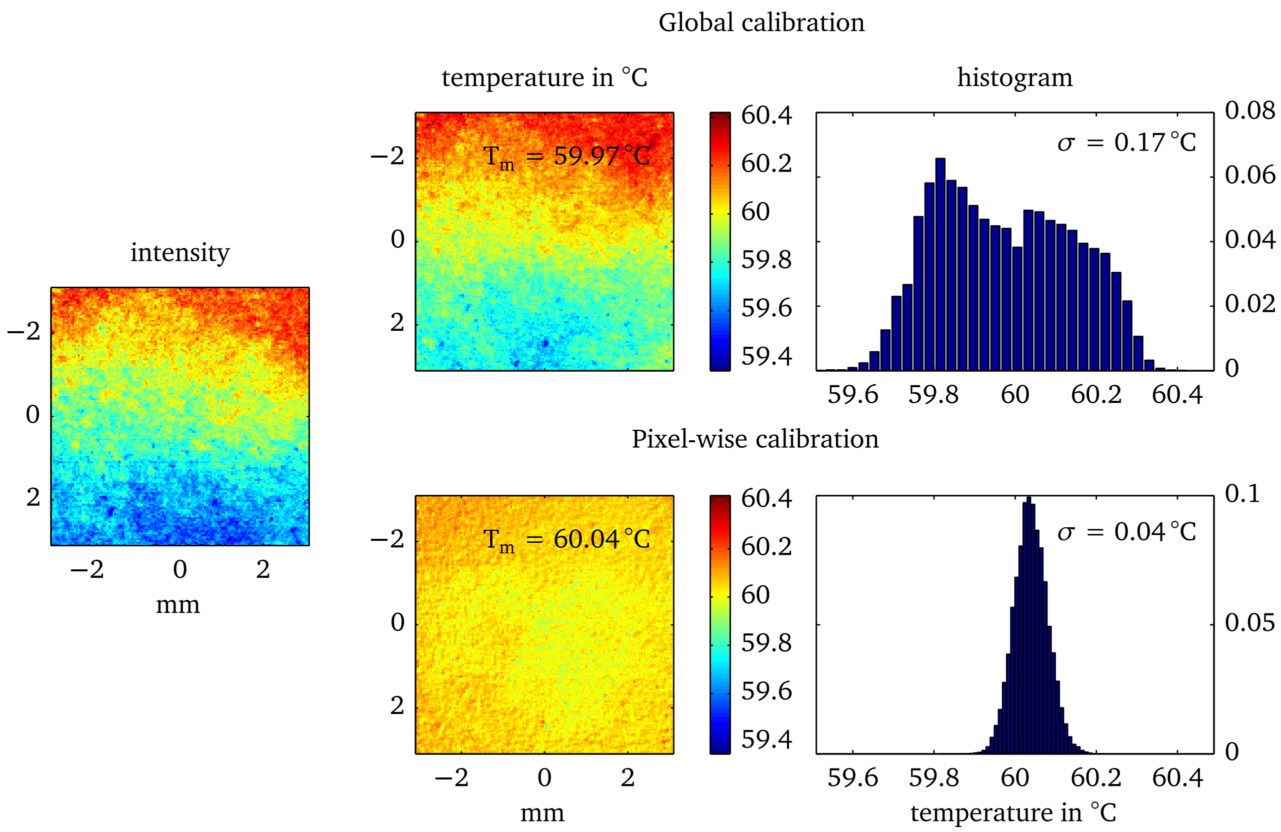

Figure 4.7: Comparison of global and pixel-wise calibration

calibration the calibration coefficients of the pixel at $x = y = 0$ mm are used. The standard deviation of the global calibration is about four times higher than for the pixel-wise calibration. Furthermore, the mean temperature deviates from the calibration temperature using the global calibration. The necessity of a pixel-wise calibration is obvious and therefore used in the following.

4.2.2 Calculation of the heat flux profile

For the calculation of the heat flux at the top surface of the heater two methods can be applied, either a 3D inverse heat conduction problem (IHCP) (cf. Heng et al. [57, 59, 60]) or a pixel-wise energy balance introduced by Kenning and Yan [79] in 1996 for measurements with Thermochromic Liquid Crystals (see Eq. 2.23). Applied on a single pixel the energy balance shown in Fig. 4.8 results. The application of Fourier's law leads to

$$q = q_0 + k_{\mathrm{H}}\,\delta \left(\frac{\partial^2 T}{\partial x^2} + \frac{\partial^2 T}{\partial y^2} \right) - \rho_{\mathrm{H}}\, c_{p,\mathrm{H}}\, \delta\, \frac{\partial T}{\partial \tau}, \tag{4.9}$$

where q_0 is the source term projected on the area A (e.g. by Joule heating), k_{H} the heat conduction, ρ_{H} the density, and $c_{p,\mathrm{H}}$ the specific heat capacity of the heater's material. δ describes the thickness of the foil and q the heat flux from the foil to the fluid. The bottom side is assumed to be adiabatic. The method introduced by *Kenning* follows a more basic approach and can be applied more easily. Nevertheless, it is based on the assumption of a negligible perpendicular temperature difference from the measurement (bottom) to the boiling (top) surface.

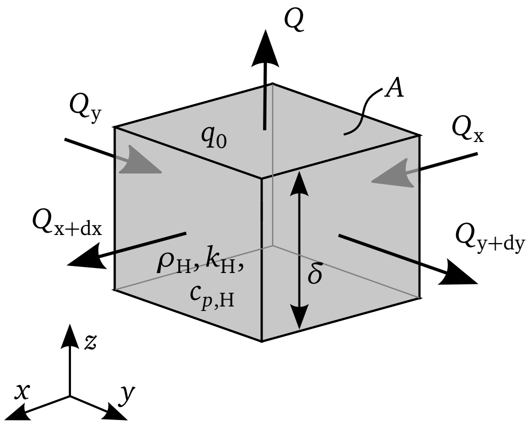

Figure 4.8: Energy balance of a single pixel

Simulation of a temperature profile for a thin foil

To validate the applicability of the energy balance by Kenning the temperature profile at the back side is simulated for a given temperature profile at the top side. For the simulation a 20 µm thick stainless steel foil is used as in the experiments. The applied temperature profile is based on measurement data by Schweizer [119], who carried out similar experiments. The simulation is conducted by using the finite element method within COMSOL. The simulation is performed as 2D rotationally symmetrical. According to an exemplary bubble cycle a Gaussian distributed temperature drop with a maximum radius of r_max is assumed. The position of the temperature drop, representing the position of the three-phase contact line, is set by a trigonometrical function. All initial and boundary conditions are listed in table 4.3. The timestep within the simulation is $\tau = 1 \times 10^{-5}$ s. The mesh consist of 2400 equally distributed elements in r-direction and 50 elements in z-direction. In z-direction an element ratio of 50 is used due to the higher gradients at the top surface. An illustration of a section of the mesh distribution is shown in Fig. 4.9. In Fig. 4.10 the temperature profile at $\tau = 5$ ms is shown. The differences in the temperature profiles of the top and the back side, caused by heat conduction in the radial direction, can be seen.

The spatial and temporal resolution of the numerical simulation is much higher than the resolution of the experimental measurement setup (IR camera). Hence, the temperature profiles from the top to the bottom side measured by an IR camera would differ less than in the numerical simulation. In Fig. 4.11 the temperature profile of the numerical results and the adapted ones, concerning the maximum resolution of the IR camera, are compared. The temperature profiles are shown for the top and the bottom surface for $\tau_1 = 2.5$ ms, $\tau_2 = 10$ ms, and $\tau_3 = 15$ ms. A difference in the temperature drop from the top to the back side of about 60 % can be seen within the numerical results (left column). Adapting the temperature profile to the maximum temporal and spatial resolution of the high-speed IR camera (1000 fps - 10 µm/pixel) a clear dependency of the temperature profile on the velocity of the temperature drop can be seen. By comparison of the temperature profile at the top and back side of the foil adapted to the IR camera the difference is less than 10 % for a moving temperature drop (τ_1, τ_3). For a stagnant temperature drop the difference is in the order of 50 %. As the residence time of the temperature drop increases with increasing radius the temperature profile is more affected with increasing radius. Further, the direction of the moving temperature drop can be seen by the shifted minimum of the temperature profile at the back side of the foil. Both effects are more obvious in the adapted case.

As a 3D inverse method leads to similar deviations [59] its application is not necessary especially with respect to the more complex evaluation. It has to be mentioned that this is only valid for the given

Table 4.3: Initial and boundary conditions for the numerical simulation of the temperature profile

Boundary conditions:

$q\left(r = r_0\right) = 0 \rightarrow \text{adiabatic}$

$q\left(r = 0\right) = 0 \rightarrow \text{adiabatic}$

$q\left(z = 0\right) = 0 \rightarrow \text{adiabatic}$

$T\left(z = z_0, r, \tau\right) = T_\mathrm{m} - \mathrm{e}^{-0.5\left(\left(r - r_\mathrm{max}\sin\left(\frac{\pi\tau}{\tau_\mathrm{cyc}}\right)\right)\sigma^{-1}\right)^2 \Delta T}$

Initial conditions:

$r_0 = 600\,\mu\mathrm{m}$

$z_0 = 20\,\mu\mathrm{m}$

$\tau_\mathrm{cyc} = 20\,\mathrm{ms}$

$r_\mathrm{max} = 500\,\mu\mathrm{m}$

$\sigma = 7\,\mu\mathrm{m}$

$\Delta T = 1\,^\circ\mathrm{C}$

$T_\mathrm{m} = 60\,^\circ\mathrm{C}$

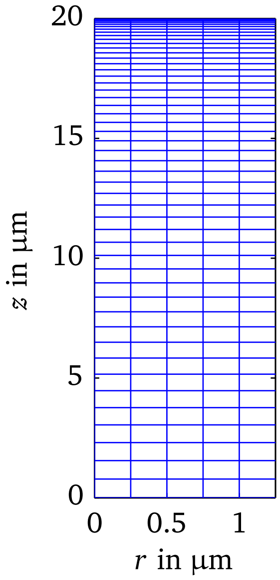

Figure 4.9: Grid section of numerical simulation

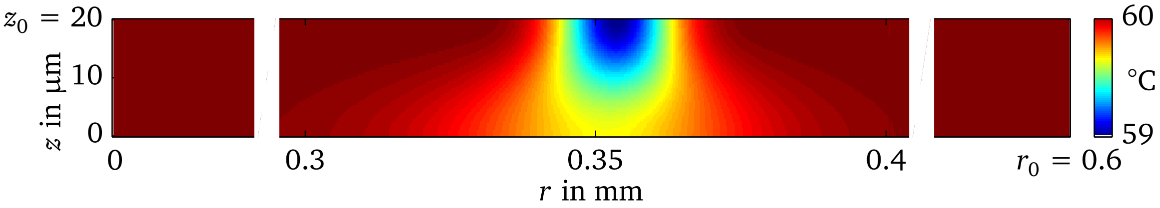

Figure 4.10: Temperature profile from numerical simulation at $\tau = 5\,\mathrm{ms}$

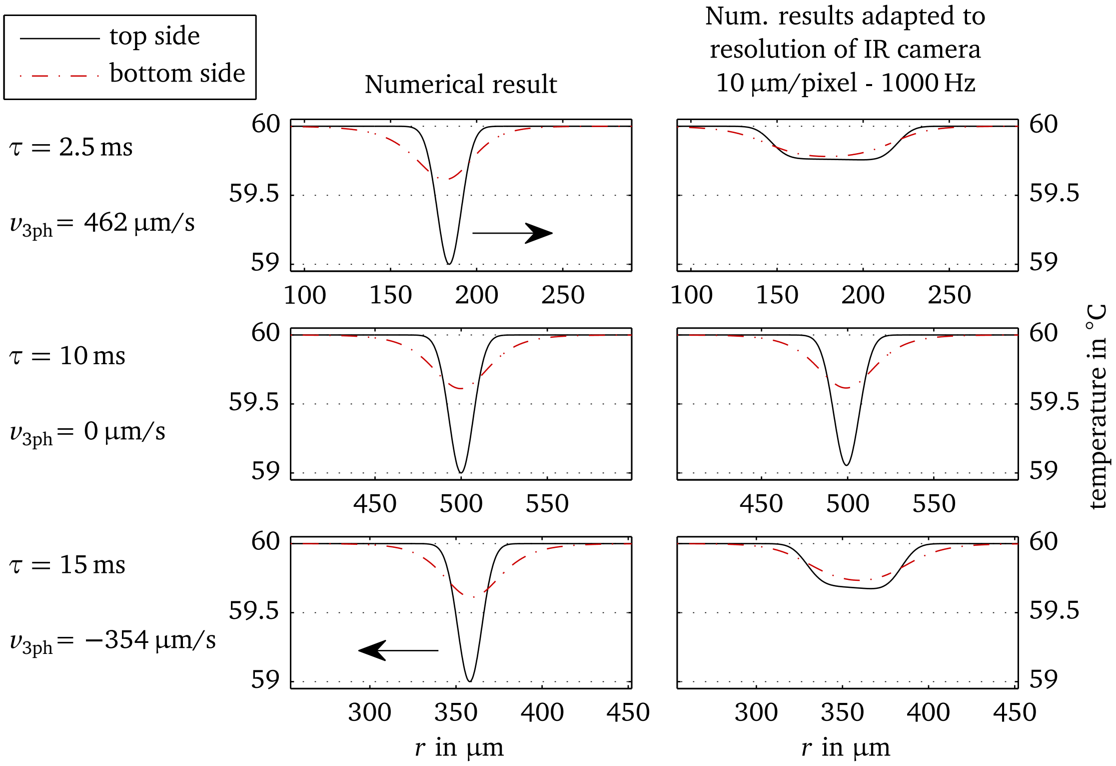

Figure 4.11: Calculated temperature profile at the top and back side of the foil

case. As the assumption of a negligible perpendicular temperature difference (compare the adapted case) from the top side to the bottom side can be made the method by Kenning is used in the following for the calculation of the heat flux profiles.

Applicability of the energy balance

As the measurement data is discrete, the 1^{st} and 2^{nd} derivatives in Eq. 4.9 have to be approximated. To demonstrate the sensibility of this approximation on the heat flux calculation two methods are compared. Due to the negligible perpendicular temperature difference, the heat flux is evaluated for the same temperature profile used in the numerical simulation (cf. table 4.3). In order to account for the measurement noise of the IR camera a white Gaussian noise of 24 db is added to the temperature profile. This signal-noise ratio is taken from measurement data of a calibration at 60.05 °C (cf. Fig. 4.12). In Fig. 4.13 the different methods are compared for $\tau = 12$ ms. The heat flux is evaluated with a spatial resolution of 10 µm/pixel and a temporal resolution of 1000 Hz. Possible deviations between the used methods caused by the averaging of the temperature profile would be enhanced during the further calculation. Therefore, the heat flux profiles are first calculated with a resolution of 1 µm/pixel and 10 000 Hz and averaged afterwards.

In the upper row a finite difference method is used. The 2^{nd} derivative in x-direction is approximated by

$$\frac{\partial^2 T}{\partial x^2} \approx \frac{T_{x+1,y,\tau} - T_{x,y,\tau}}{\Delta x^2} + \frac{T_{x-1,y,\tau} - T_{x,y,\tau}}{\Delta x^2}. \tag{4.10}$$

The approximation in y-direction is equivalent. The 1^{st} derivative is approximated by

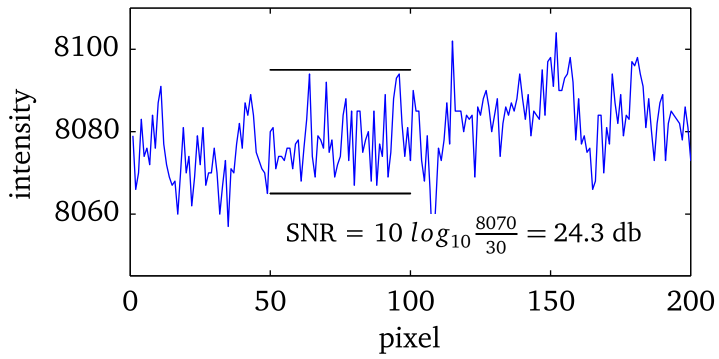

Figure 4.12: Signal-noise ratio of infrared measurement

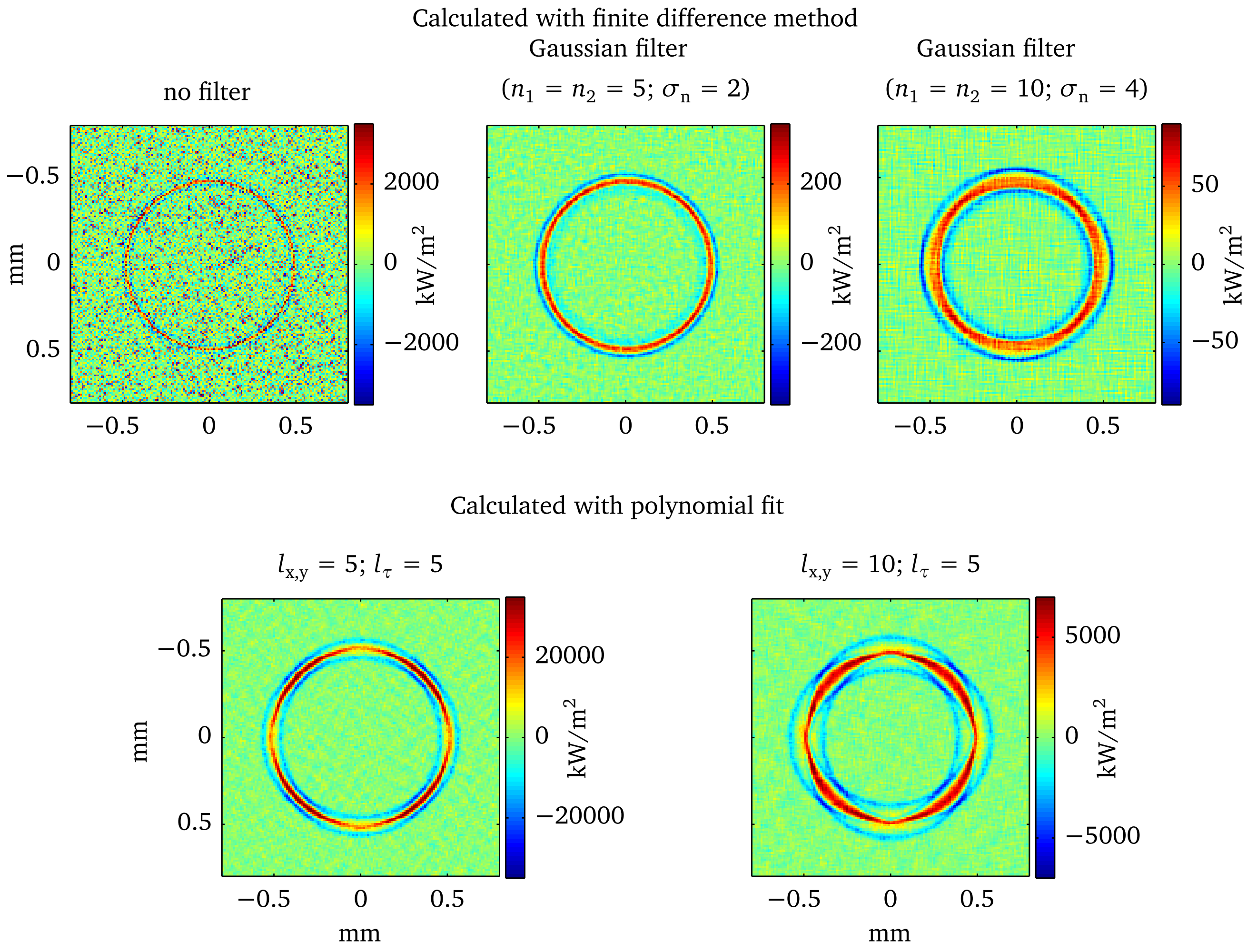

Figure 4.13: Influence of the approximation of the second derivative on the heat flux profile for $\tau = 10\,ms$

$$\frac{\partial T}{\partial \tau} \approx \frac{T_{\mathrm{x,y},\tau} - T_{\mathrm{x,y},\tau-1}}{\Delta\tau}. \tag{4.11}$$

As in this method only six different pixels are used for the calculation of the surface heat flux, it is very prone to the given noise (Fig. 4.13 top left). This sensitivity can be suppressed by filtering the temperature signal. A Gaussian filter is applied due to the expected temperature profile and the results of SCHWEIZER [119]. For the discrete filter the length in x and y-direction as well as the standard deviation is given in number of pixels n_1 and n_2 as well as the standard deviation σ_{n}. Therefore the filtered temperature is

$$T_{\mathrm{x,y},\tau} = \sum_{\mathrm{i}}\sum_{\mathrm{j}} \frac{T_{\mathrm{x+i,y+j},\tau}\, h_g(i,j)}{\sum\limits_{\mathrm{i}}\sum\limits_{\mathrm{j}} h_g} \tag{4.12}$$

with

$$h_g = e^{\frac{-\left(i^2+j^2\right)}{2\sigma_{\mathrm{n}}^2}}$$

for

$$i = \left[-\frac{n_1-1}{2}\ \frac{n_1-1}{2}\right]$$

and

$$j = \left[-\frac{n_2-1}{2}\ \frac{n_2-1}{2}\right].$$

In temporal direction a weighted filter is used

$$T_{(\mathrm{x,y},\tau)} = 0.25\, T_{(\mathrm{x,y},\tau-1)} + 0.5\, T_{(\mathrm{x,y},\tau)} + 0.25\, T_{(\mathrm{x,y},\tau+1)}. \tag{4.13}$$

For $n_1 = n_2 = 5$ and $\sigma_n = 2$ the filter is shown in Fig. 4.15. Applying this filter to the temperature field a clear noise reduction can be seen in the heat flux profile. At the same time the peak heat flux is smeared and reduced in magnitude (Fig. 4.13 top middle). With an increased size of the filter ($n_1 = n_2 = 10$, $\sigma_{\mathrm{n}} = 4$) this effect is increased as well (Fig. 4.13 top right). An influence of the growth direction on the heat flux profile can be seen. For a vertical or horizontal growth direction the peak heat flux is less than for a diagonal one. This is caused by the radial computation of the temperature drop and the Cartesian filter and evaluation of the heat flux. This effect is explained further in A.7.

In the lower row of Fig 4.13 a polynomial fit of 2^{nd} order is used for the approximation of the 1^{st} and 2^{nd} derivatives. The vector

$$T_{\mathrm{V}} = \left[T_{\mathrm{x-(1/2),y},\tau}\, T_{\mathrm{x+(1/2),y},\tau}\right] \tag{4.14}$$

is approximated by

$$T_{\mathrm{V,a}} \approx C_2x^2 + C_1x + C_0. \tag{4.15}$$

Hence the 2^{nd} derivative is

$$\frac{\partial^2 T}{\partial^2 x} \approx 2C_2. \tag{4.16}$$

The calculation is equivalent for y and τ. In Fig. 4.13 (bottom left) the heat flux is shown for $l_{\mathrm{x,y},\tau} = 5$. As for this method a larger number of pixels is used it is not as prone to noise as the finite difference method. By applying a larger filter ($l_{\mathrm{x,y}} = 10$, $l_{\tau} = 5$) the result is also smeared. This method has an increased dependency of the heat flux profile on the growth direction.

By adapting the filter properties for the finite difference method and the interval length for the polynomial method, a reasonable compromise between noise reduction and smearing can be reached with both methods for a given measurement. Concerning the influences of the calculation methods on the heat flux profiles no obvious advantage can be seen. Beyond this the finite difference method is energy conservative, which is an advantage for the calculation of the heat transfer coefficient (cf. section 4.2.3). Further, the calculation time is one order of magnitude smaller. Therefore, this method is used in the further course of this study.

Comparability of different measurements

It is shown that the used filter has a major influence on the calculated heat flux profile. In the following the comparability of different measurements is analyzed using the example of different spatial resolutions[1]. To do so, the heat flux profile is evaluated for the temperature profile given by the numerical simulation (cf. table 4.3). The temporal resolution is 1000 Hz and the chosen time 15 ms. Enhancing (reducing) the spatial resolution the object is depicted on a larger (reduced) number of pixels on the camera chip. Hence, the filter has to be adapted to cover the same **physical length** of the object. This filter is called *adapted filter* in the following. In contrast, the noise of the camera chip is not related to the used resolution. Therefore the used filter has to have the same **pixel length** concerning an equivalent noise reduction. This filter is called *original filter* in the following. For the comparison different spatial resolutions of the temperature field are used with both mentioned filters (see Fig. 4.14). The filter properties are given additionally in converted (pixel) and real (μm) dimensions. In the top row the heat flux profile is shown for a spatial resolution of 10 μm/pixel. The used filter has a length of 200 μm (20 pixels) with a standard deviation of 40 μm (4 pixels). On the left side the results are shown for a temperature field without noise. On the right side a measurement noise of 24 db is added to the temperature profile. Reducing the spatial resolution to 20 μm/pixel and 40 μm/pixel (middle and bottom row) the heat flux profile is shown for an identical pixel-wise filter (original filter) and for an identical real dimension filter (adapted filter). All filter parameters are shown in table 4.4.

By applying an original (pixel-wise) filter the heat flux profile is smeared and reduced in magnitude comparable to Fig. 4.13. By adapting the used filter to the real dimensions a similar result is obtained, which is pixelated due to the given spatial resolution (cf. Fig. 4.14 without noise). As the noise of the temperature field is not related to the real dimensions but to the different pixels an equivalent noise reduction is achieved by using the same pixel-wise filter. By adapting the filter to the same real dimensions the influence of noise can be clearly seen (cf. Fig. 4.14 with noise). Therefore, a quantitative comparison of measurements performed under different conditions is hardly possible.

---

[1] For example due to the usage of different object lenses.

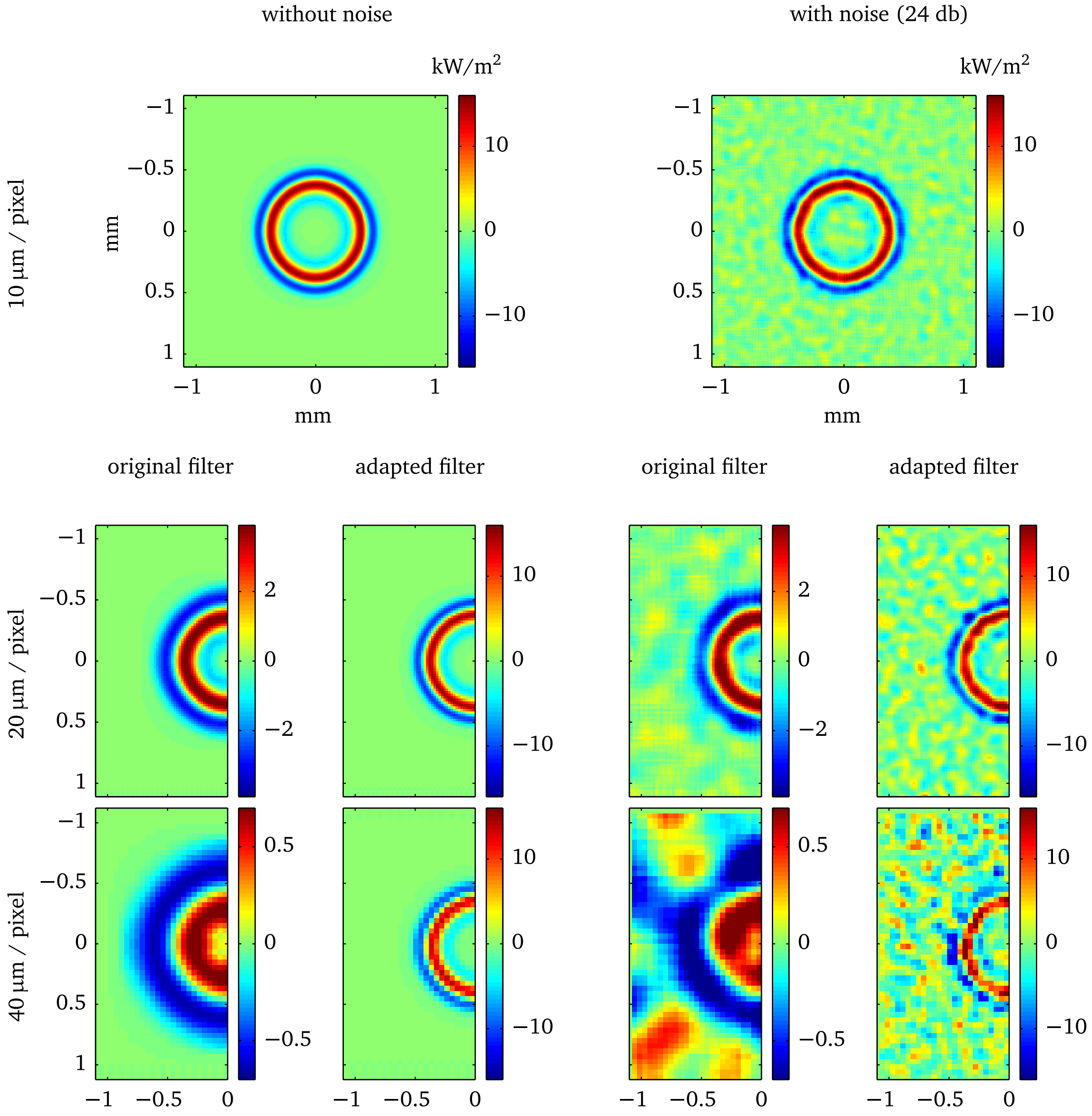

Figure 4.14: Influence of the applied filter for different spatial resolutions

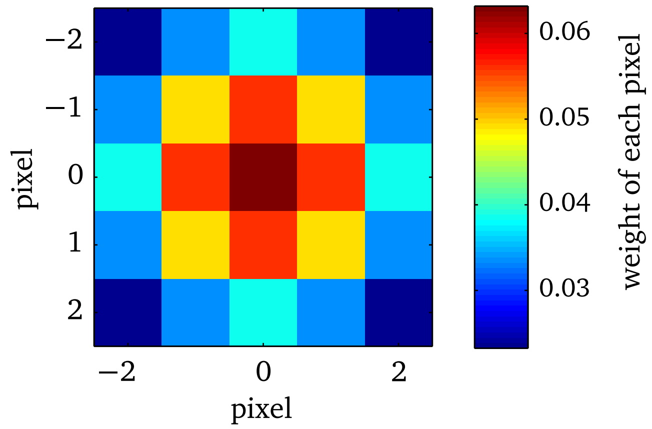

Figure 4.15: Gaussian filter

Table 4.4: Filter settings for the comparison of different spatial resolutions

Spatial resolution	= 10 µm/pixel	
Filter length	200 µm	
	20 pixels	
Standard deviation	40 µm	
	4 pixels	
Spatial resolution	= 20 µm/pixel	
	original filter	*adapted filter*
Filter length	400 µm	200 µm
	20 pixels	10 pixels
Standard deviation	80 µm	40 µm
	4 pixels	2 pixels
Spatial resolution	= 40 µm/pixel	
	original filter	*adapted filter*
Filter length	800 µm	200 µm
	20 pixels	5 pixels
Standard deviation	160 µm	40 µm
	4 pixels	1 pixel

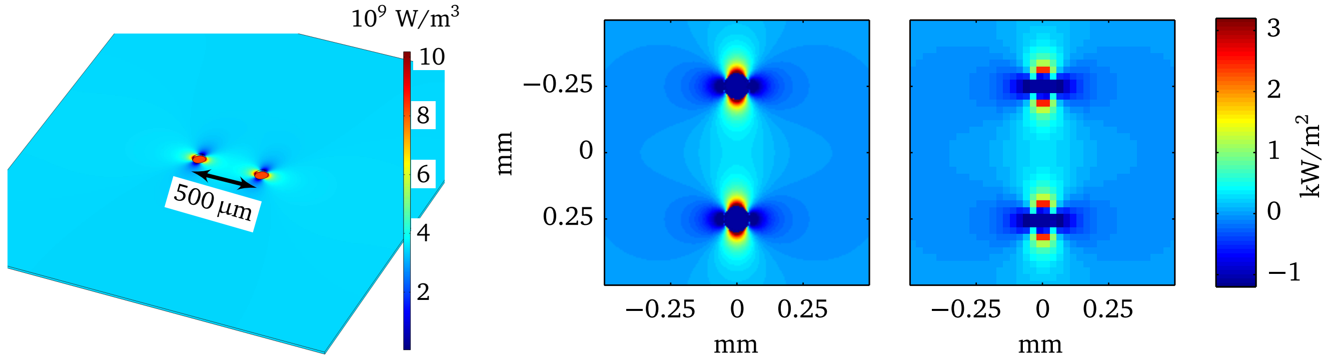

(a) Volumetric heat source

(b) Projected heat source

Figure 4.16: Simulated heat source distribution for two artificial cavities - S = 500 µm

Calculation of the heat source term

The calculation of the heat source term is an additional aspect which has to be taken into account for the heat flux evaluation. WAGNER [149] has shown that a calculation of the heat input by

$$P = U \cdot I, \tag{4.17}$$

where U is the voltage and I the current of the used power supply, results in rather low accuracy, due to the unknown contact resistances in the electrical circuit. Here especially the contact resistance between the foil and the electrode has to be mentioned. In order to avoid this, the source term q_0

$$q_0 = \frac{\rho_{20}\left(1 + \alpha_t\left(T - 20\,°\mathrm{C}\right)\right)}{W_\mathrm{f}\delta_\mathrm{f}} I^2 \tag{4.18}$$

is calculated with the electrical current I and the temperature-dependent resistance of the foil. This resistance is calculated from the material properties, where ρ_{20} is the electrical resistance (at 20 °C), α_t the temperature coefficient, W_f the width, and δ_f the thickness of the foil. As defined in Eq. 4.9 q_0 is the heat source projected on the heated surface and therefore given in W/m^2. The error estimation is performed analogue to Eq. 4.3. For the whole measurement range the error is between 10 % and 15 %. The values used for the calculation are listed in the appendix (table A.3). Further, the shares of the single influencing factors are shown in the appendix (Fig. A.2). The material properties and the width of the foil are the largest share. The temperature, the current, and the thickness of the foil can be neglected in comparison with the other influencing factors.

Influence of nucleation sites on heat flux distribution

A further aspect influencing the accuracy of the presented measurement and evaluation technique are the artificial cavities. By removing or adding material to the foil a uniform heating can be disturbed. In Fig. 4.16 the calculated volumetric heat source with two artificial cavities is shown. The heat generation is simulated for a $3 \times 3 \times 0.02$ mm^3 stainless steel foil within COMSOL. Each cavity is 15 µm in depth and has a diameter of 100 µm. The spacings between both cavities is 500 µm according to the measurements presented in section 5.2.1. Perpendicular to the axis through the cavities a current of 10 A is applied. At the bottom side of the foil a convective cooling with a heat transfer coefficient of 1.5 kW/(m^2 K) is applied with an external temperature of 60 °C, to achieve a steady-state system. All other surfaces are adiabatic. The simulation is performed with constant material properties and thermal expansion is neglected. In Fig. 4.16a it can be seen that the highest volumetric heat source is located underneath the cavities, where the remaining foil has a thickness of 5 µm. Within the heat flux evaluation (cf. Eq. 4.9) the heat source term is applied on the projected surface area in W/m^2. In Fig. 4.16b the calculated heat source is shown subtracted by its mean value. As the removal of the material at the position of the cavities is neglected the heat flux is reduced at this position by the application of this method. Next to cavities (perpendicular to the electric current) the heat flux is underestimated. On the right side of Fig.4.16b the numerical result adapted to a resolution of 25 µm/pixel is shown. As a result of this the maximum deviation is reduced to approximately $2\,kW/m^2$. As the position and the structure of the cavities are not known to a sufficient accuracy, this effect cannot by compensated by the calculation.

4.2.3 Conclusive evaluation of the IR measurement technique

In this chapter the influences of the assumptions and used evaluation methods on the temperature measurement and heat flux calculation was shown. An error estimation for the heat flux source term and possible influences caused by the structure of the surface were presented. It was shown that a quantitative comparison of measurements performed or evaluated under different conditions is hardly possible. Due to the significant influence of the used filter and evaluation method an error estimation (as presented in Eq. 4.3) is not reasonable for the heat flux calculation. Further, an important distinction has to be made between an averaged heat flux and the calculated heat flux of a single pixel. The accuracy of the averaged heat flux mainly depends on the accuracy of the heat source calculation and the energy conservation of the used calculation method, whereas the heat flux for a single pixel mainly depends on the used filter. Independently of the used method for the heat flux calculation a carefully performed calibration is absolutely essential. Using the same temperature sensor for the measurement of the calibration temperature and the fluid temperature of the working fluid during the experiments is desirable for a calculation of the heat transfer coefficient, even if the saturation temperature is calculated from the pressure data.

Next to the mentioned influences concerning the evaluation of the data a temperature measurement as close as possible to the boiling surface enhances the robustness of the data due to a less smeared temperature signal. In contrast to the enhancement in the evaluation the usage of very thin heaters has an insufficient comparability to technical heaters due to the reduced capability of energy storage. An alternative is the sputtered IR-transparent heater developed at the institute of the author [39] (cf. page 24).

Nevertheless, since introduced by Theofanous et al. in 2002 ([143, 144]) the IR measurement technique is, to the knowledge of the author, still the most precise and efficient way to measure the temperature field with such a high temporal and spatial resolution. Despite the mentioned drawbacks, the detection and evaluation of the phenomena shown in chapter 5 would not be possible using a non-optical measurement technique. Due to the reasons mentioned above in the further thesis a measurement error is not given for the presented heat flux data. For a qualitative comparison the same measurement setup and evaluation method is used.

CHAPTER 5

Results

In this chapter the results of the present thesis are shown and discussed. They are separated into the results obtained from single bubble experiments and bubble interactions. The bubble interactions are further separated into bubble coalescence of two individual bubbles, experiments performed on structured foils with multiple artificial cavities and experiments performed on a single embedded wire. All experiments conducted at the test setup explained in chapter 3 are performed with FC-72 as working fluid in a pressure range of 0.3 bar to 1 bar. The experiments on the single embedded wire are obtained with a different type of experimental setup, shown in section 5.2.3. These experiments are also performed with FC-72 as working fluid in a pressure range of 0.4 bar to 1.9 bar. For the data presentation the boxplot is often used as graphic rendition. An explanation of a boxplot is given in the appendix (A.8). All results presented in this chapter are subject to the measurement uncertainties discussed in section 3.5 and chapter 4 and summarized in section A.9.

5.1 Single bubble experiments

For the single bubble experiments a stainless steel foil with a single artificial cavity is used. A picture of such a cavity is shown in Fig. 3.6b. To perform experiments with a single cavity over a pressure range the heat flux has to be adapted. The required heat flux decreases with increasing pressure. For the lower pressures ($p \approx 400\,\mathrm{mbar}$) the heat flux is approximately $10\,\mathrm{kW/m^2}$ and approximately $6\,\mathrm{kW/m^2}$ for higher ones ($p \approx 950\,\mathrm{mbar}$). Where possible the heat flux is varied by approximately $1\,\mathrm{kW/m^2}$ for a single pressure value. In the shown results this is indicated by *high heat flux* or *low heat flux*, respectively. If for a single pressure value a measurement with just a single heat flux could be performed it is allocated to the *low heat flux*. By applying a heat flux value beyond this range multiple bubbles occur or boiling terminates. The experiments are performed with increasing pressure and decreasing heat flux. The temperature profile (IR) is recorded with 1502 fps and a resolution of 27.5 µm/pixel. The framerate of the IR camera cannot be set directly, but is coupled to the chosen spatial resolution. For the b/w camera both parameters can be set individually. In order to enhance the comparability the pictures of the bubble's shape (b/w) are recorded with twice the framerate of the IR camera (3004 fps) and a resolution of 7.3 µm/pixel.

The results obtained at a single cavity are separated into three parts. The first part (5.1.1) focuses on general influences of system pressure and heat flux on boiling characteristics of single bubbles, e.g. bubble departure diameter. Afterwards two different mechanisms of bubble growth are described. The influence of pressure and heat flux concerning the mechanisms are presented. In the subsequent discus-

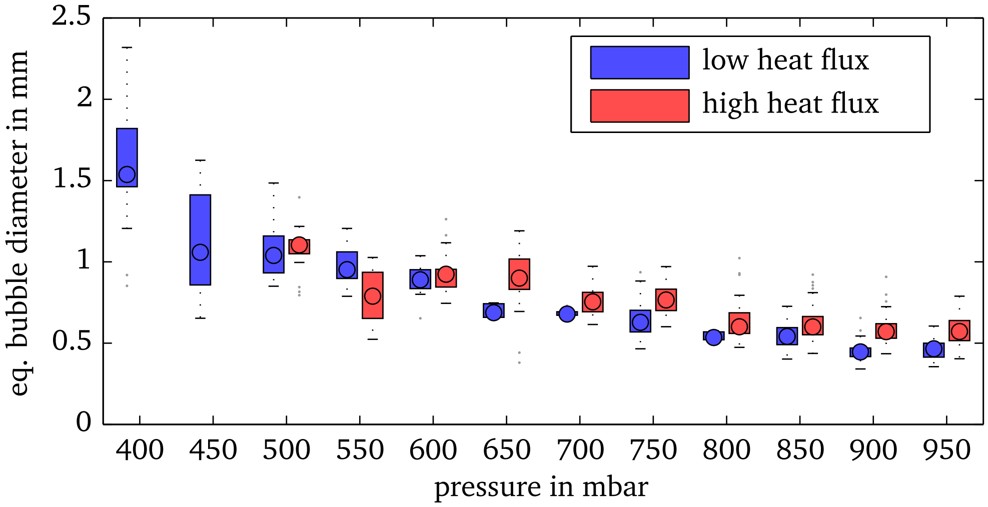

Figure 5.1: Influence of heat flux and pressure on the equivalent bubble departure diameter

sion of these results a first step for a combination of the microlayer (cf. section 2.2.3) and contact line model (cf. section 2.2.3) is presented.

5.1.1 Bubble departure diameter, frequency, and cycle periods

In Fig. 5.1 the equivalent bubble departure diameter is shown over pressure. The definition of the equivalent diameter is given in section 2.2.1. The bubble departure diameter decreases with increasing pressure. Especially at higher pressures the bubbles generated at a higher heat flux are bigger than the bubbles generated at a lower heat flux. Further, it can be seen that the deviation of the bubble departure diameter is larger at lower pressures. The results qualitatively confirm the results and analysis presented in literature. Without a separation into different heat fluxes the bubble departure diameter is compared to the correlations of FRITZ (Eq. 2.4), SCHWEIZER (Eq. 2.25), and COLE AND SHULMAN [28] (cf. Fig. 5.2). The correlation of COLE AND SHULMAN is given in Eq. 5.1

$$d_{\mathrm{eq}} = \frac{1000}{p} \sqrt{\frac{\sigma}{g\left(\rho_{\mathrm{l}} - \rho_{\mathrm{v}}\right)}} \quad (p \text{ in mmHG}). \tag{5.1}$$

The correlations by FRITZ and SCHWEIZER are based on a static force balance and are not suitable to represent the increasing bubble departure diameter for decreasing pressure. The correlation of SCHWEIZER furthermore overestimates the bubble departure diameter in general. As the correlation of SCHWEIZER gives the apparent bubble departure diameter the curve in Fig 5.2 is adapted to the equivalent bubble departure diameter. The correlation of COLE AND SHULMAN, especially developed for a sub-atmospheric pressure range, represents the experimental results qualitatively well even though it overestimates the measurement results, too. As the equation of COLE AND SHULMAN is, comparable to SCHWEIZER and FRITZ, also based on the capillary length the different slope is caused by the multiplication with $1/p$, which is of empirical origin.

In Fig. 5.3 the influence of the pressure on the bubble frequency is shown. As mentioned in section 4.1 the evaluation is performed automatically due to the large amount of measurement data. Afterwards deficiently evaluated bubbles are excluded manually. Hence, the bubble frequency f_{b} is defined by

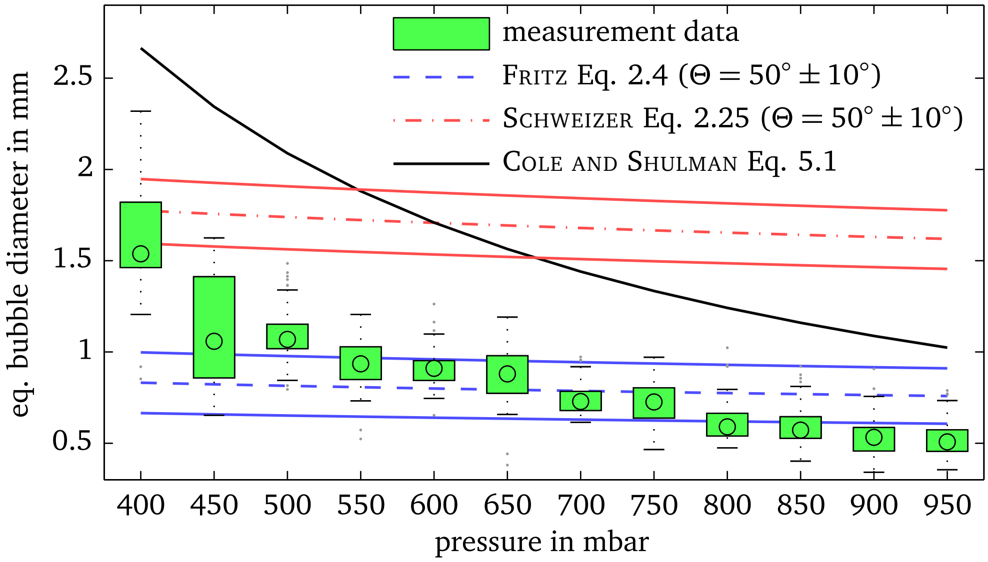

Figure 5.2: Comparison of the equivalent bubble diameter with analytic and empirical equations

$$f_\mathrm{b} = \frac{1}{\tau_\mathrm{wait} + \tau_\mathrm{cyc}}, \tag{5.2}$$

where τ_wait is the waiting and τ_cyc the cycle time of a bubble. The waiting time is defined as the time between the departure of a bubble and the nucleation of a subsequent one. The cycle time is defined as the time between nucleation and departure of one bubble. The median values of the bubble frequency are slightly increased for higher heat fluxes even though the interquartile ranges (IQR) for a single pressure overlap. Further, a slight increase of the averaged bubble frequency for higher pressures can be seen[1]. Conspicuous are the values at 600, 650, 700, and 800 mbar for the lower heat fluxes. In comparison with the b/w images, the lower frequencies for these measurements can be attributed to a heat flux quite close to the termination of the boiling process. The small number of bubbles (small IQR) is an additional indication of this boiling condition.

In Fig. 5.4 the waiting time is shown for the different heat fluxes over pressure. As a waiting time of 0 s is also an expected value as a threshold, setting a lower limit, the boxplot is not an appropriate method of presentation. Therefore, the values are plotted as individual asterisks. It can be seen that for higher pressures the maximum waiting time is reduced. In general bubbles have a shorter waiting time at the higher heat flux than bubbles nucleated at the lower heat flux. Further, for 650 mbar, 700 mbar, and 800 mbar every bubble nucleates after a waiting time. This also points to a boiling characteristic close to the termination of nucleate boiling. Especially for the lower heat fluxes at lower pressures it seems that the waiting time is not uniformly distributed. Either the bubbles nucleate without a waiting time or they have to overcome a specific value.

The cycle time of a bubble is plotted in Fig. 5.5 over pressure. No significant dependency on heat flux or pressure can be seen. This indicates that the dependency in the bubble frequency is primarily caused by the waiting time. Summarizing, an increase in heat flux does not directly lead to an increase of bubble departure diameter or frequency but rather to an interaction of both of them. The results shown in Figs. 5.2, 5.4, and 5.5 are further used in section 5.2.1.

---

[1] As in a boxplot the median values are shown this can be seen by the larger IQR and whiskers.

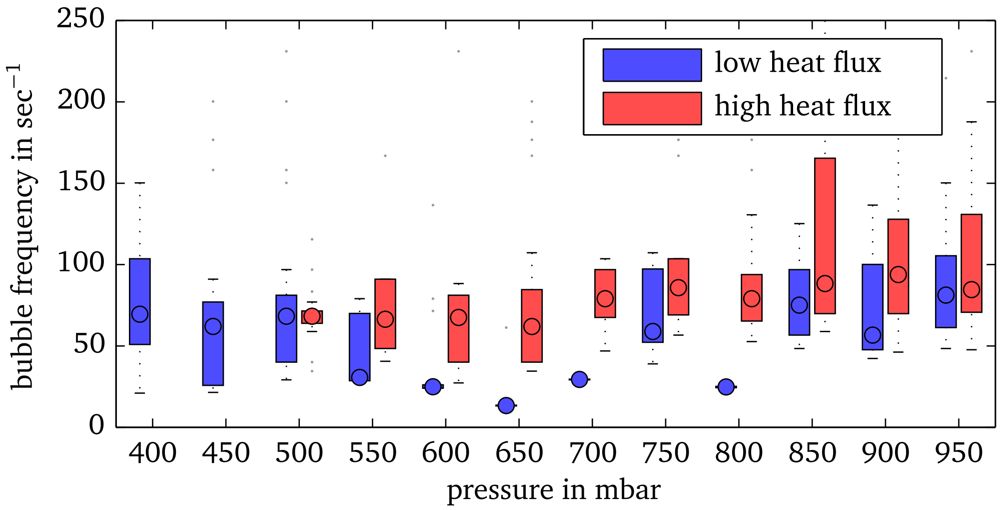

Figure 5.3: Influence of heat flux and pressure on the bubble frequency

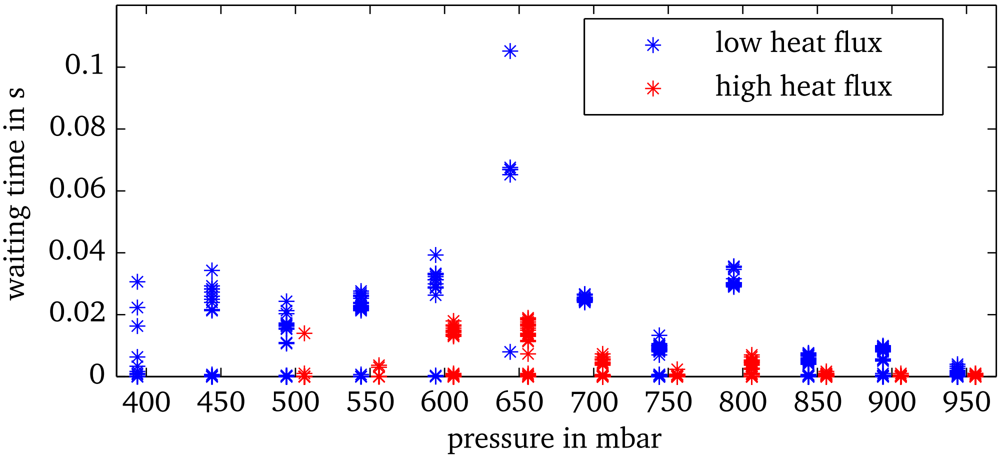

Figure 5.4: Influence of heat flux and pressure on the waiting time

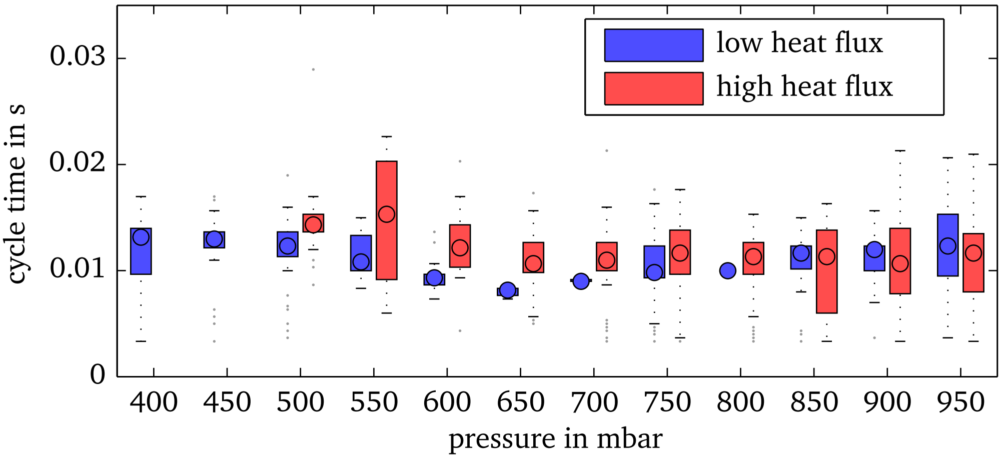

Figure 5.5: Influence of heat flux and pressure on the cycle time

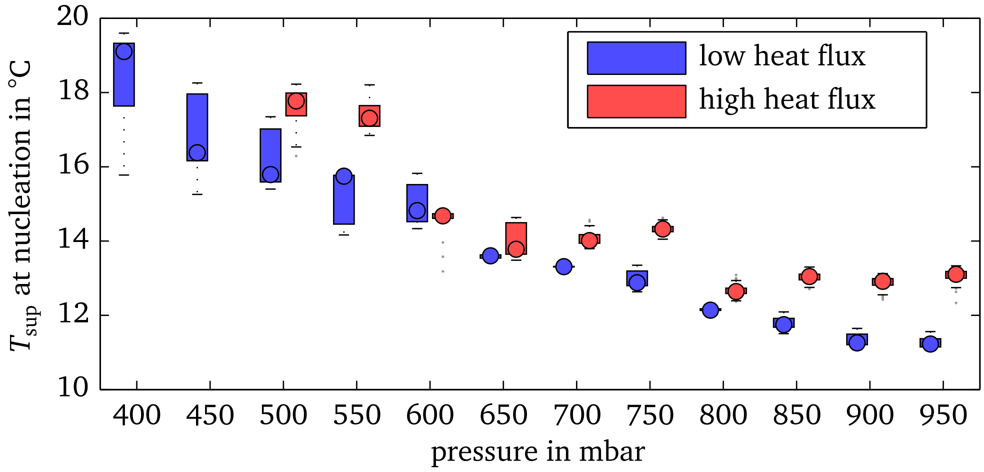

Figure 5.6: Influence of heat flux and pressure on the superheat at nucleation

In Fig. 5.6 the superheat T_{sup}

$$T_{sup} = T_f - T_{sat} \tag{5.3}$$

necessary for a nucleation of a bubble is shown over pressure. To determine the foil temperature T_f the measurement data of the IR thermometry is used. The temperature is averaged over ≈ 300 × 300 µm^2 (11 × 11 pixels) around the nucleation site. For the evaluation the temperature data of the picture before nucleation is used. The saturation temperature T_{sat} is calculated from the pressure in the test cell[1]. In general the superheat decreases with increasing pressure. This characteristic agrees with the analytic considerations shown in section 2.2.2. In Fig. 5.7 the necessary superheat for a nucleation of FC-72 is plotted over pressure for Eq. 2.16 and the analysis by Hsu [65]. As in both equations the necessary superheat depends on the size of the cavity the ordinate is plotted as superheat times cavity radius. As the analysis by Hsu is not implicitly solvable it is plotted as parameter variation from 1 µm to 36 µm cavity radius in 5 µm steps. The same trend as in the experimental data can be observed for both methods. Further, in Fig. 5.6 it can be seen that for an individual pressure the superheat is higher for the higher heat fluxes. The momentary increase of the superheat with increasing pressure (cf. 650–750 mbar and 800–950 mbar for the higher heat fluxes) is caused by adapting the heat fluxes to the boiling process of a single bubble. As the heat flux is calculated after the measurement the electrical current is used as actuating variable in the experiment. The current was adapted in 1 A steps. For the higher heat flux the measurements from 800 mbar to 950 mbar are performed with 8 A. The measurements from 600 mbar to 750 mbar are performed with 9 A. Due to the increase in saturation temperature the heat flux also increases, from 800 mbar to 950 mbar for an identical electrical current. This is caused by increasing electrical resistance with increasing temperature (cf. Eq. 4.18). For the lower heat fluxes this phenomena cannot be observed. Similar to the higher heat flux the measurements from 600 mbar to 750 mbar and 800 mbar to 950 mbar are performed with 9 A and 8 A, respectively. Despite an equivalent increase of the heat flux with the saturation temperature the superheat at nucleation decreases constantly. A further effect influencing the results is the different area affected by a bubble, as the bubble size depends on the system pressure. As the area for the temperature evaluation is equal over the whole pressure range and the area affected by a bubble decreases with increasing pressure, a larger area not involved in the boiling process is included in the temperature measurement. Further, taking into account spatial and temporal smearing of the temperature data the apparent dependence of the nucleation temperature on the heat flux has to be relativized.

---

[1] Saturation data is given in the appendix A.1.

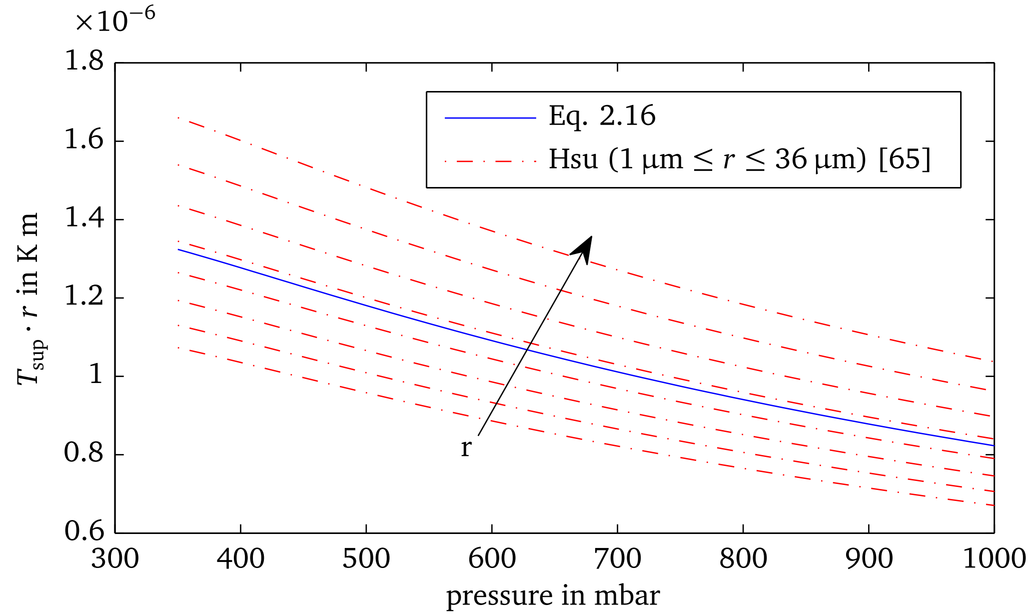

Figure 5.7: Calculation of the necessary superheat for the nucleation of a bubble

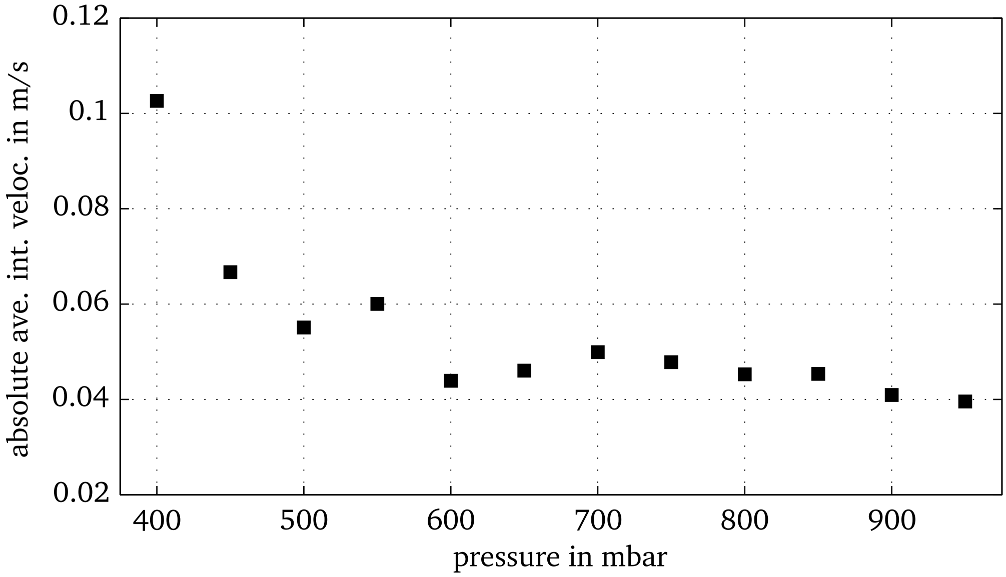

Figure 5.8: Absolute velocity of the apparent contact line

5.1.2 Differences in bubble growth

By comparing Fig. 5.1 and Fig. 5.5 it can be seen that for lower pressures the bubbles reach a larger departure diameter after about the same time. Consequently, the interface velocity is higher. In Fig. 5.8 the arithmetic average of the absolute interface velocity is plotted over pressure[1]. For the evaluation of the interface velocity the velocity of the apparent contact line is used (compare section 4.1). As the cycle time has no significant dependency on pressure the mean interface velocity increases with decreasing pressure and therefore has a similar profile as the bubble departure diameter. Regarding the velocity at the apparent contact line (in the following: contact line velocity) differences for individual bubbles can be observed. In Fig. 5.9 the contact line velocity is plotted over time for a measurement condition of 450 mbar and 9.8 kW/m^2. Comparable to Fig. 4.5 the ordinate and abscissa are interchanged. A receding contact line (during bubble growth) is specified by a negative contact line velocity and an advancing contact line (during bubble departure) by a positive velocity. In Fig. 5.9 bubble nucleation is indicated by a red triangle and bubble detachment by a green one. It can be seen that the contact line velocity has a negative maximum shortly after bubble nucleation. For a contact line velocity of 0 m/s the dry patch under the bubble is maximal in diameter. In the receding phase the interface velocity increases until detachment. This increase of the interface velocity in the receding phase has also been reported by Schweizer [119] and Kunkelmann [90]. Further, it can be seen that the contact line velocity at nucleation depends on the time passed after the detachment of the previous bubble. For an existing waiting time between two bubbles the initial contact line velocity of the subsequent bubble is much higher compared to a bubble which nucleates directly after the detachment of a previous one. In the shown example the initial velocity is about two to seven times higher for a bubble nucleated after a previous waiting time compared to a bubble without a previous waiting time.

In Fig. 5.10 the contact line velocity at nucleation is plotted over the waiting time for the whole measurement range. The waiting time is accumulated into intervals of 10 ms. The shown values represent the mean value of each interval. All bubbles nucleated without a previous waiting time are excluded and presented individually (0 s). It can be seen that there is a clear increase in the initial contact line velocity for bubbles nucleated after a previous waiting time. It seems to be reasonable that this phenomenon is related to the superheat at nucleation. In Fig. 5.11 the initial interface velocity is plotted over superheat[2]. On the left side measurements at low heat fluxes are shown, on the right side measurements at high heat fluxes. For lower pressures two different regimes of nucleation can be seen. At 450 mbar with the low heat flux bubbles nucleating at a superheat of approximately 16 °C have an initial interface velocity < 0.3 m/s. Between a superheat of 16.5 °C to 18 °C hardly any bubbles nucleate. Bubbles nucleating at approximately 18 °C have an initial interface velocity > 0.3 m/s. For clarification a red line is included. This results indicate that a temporary inactivity (even for just a few milliseconds) leads to a hysteresis process concerning the nucleation of the next bubble. This is comparable to the phenomena presented concerning the waiting time (cf. Fig. 5.4). For the higher heat flux the effects can be observed in a weaker form with a shift of approximately 150 mbar to higher pressures. With increasing pressure ($p \geq 850$ mbar) this effect is reduced and vanishes completely. A similar behavior can be found for the bubble departure diameter. In Fig. 5.12 the departure diameter is plotted over the waiting time at the example of the lower heat flux. Comparable to the lower pressures in Fig. 5.11 no nucleation occurs for waiting times between 0 s and a specific threshold. Comparable to the interface velocity this effect van-

---

[1] As the whole bubble cycle is used for the evaluation the boxplot is not an appropriate method of presentation due to the usage of the median value.

[2] A similar presentation (like in Fig. 5.10) of the initial interface velocity over superheat would not give a meaningful result. This is caused by the interdependence of superheat and pressure (cf. Fig. 5.6). The same applies for the bubble departure diameter.

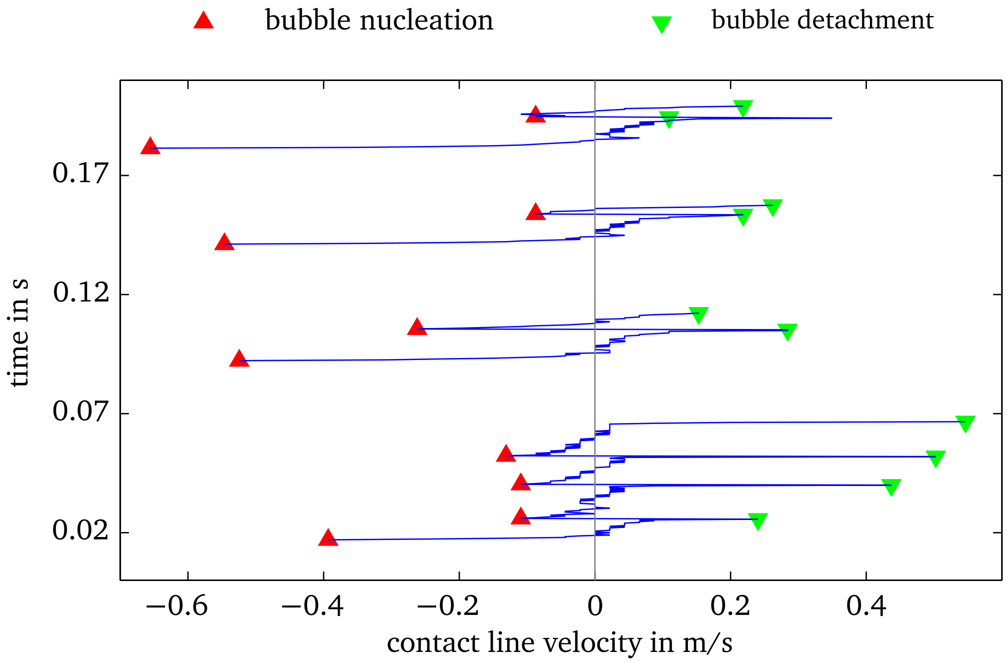

Figure 5.9: Contact line velocity of different bubbles

ishes with increasing pressure. Further, bubbles nucleating after a longer waiting time generally show larger departure diameters. For those bubbles also a larger apparent contact angle could be observed.

Concerning the heat flux, similar effects between single bubbles can be observed. In Fig. 5.13 the averaged surface temperature and the averaged heat flux are plotted for a single measurement sequence over time. For the heat flux calculation an area of $\approx 1.6 \times 1.6\,\mathrm{mm}^2$ (60×60 pixels) is used. To emphasize the fluctuations the heat flux and temperature are normalized with the mean values. As the amplitudes strongly depend on pressure different scales are used. In general the heat flux is oscillating. These oscillations can be attributed to the individual bubble cycles. An obvious difference can be seen in the heat flux profile for pressures ≤ 700 mbar and ≥ 750 mbar at the lower heat flux. For lower pressures peaks in heat flux can be observed. The peaks have roughly a constant frequency. For these peaks the heat flux is up to $15\,\mathrm{kW/m^2}$ higher than the averaged one. Comparing these data with the data from the b/w camera it is found that each peak corresponds to a nucleation of a bubble after a previous waiting time. The heat flux for bubbles that nucleated without a prior waiting time is significantly lower. These bubbles are represented by the lower peaks in the heat flux profile. In the temperature profile similar oscillations can be observed. A peak in heat flux is always followed by a drop in temperature. For heat fluxes lower than the average one the temperature is increasing. For lower pressures the amplitudes of the temperature oscillations reach up to 0.5 K. The amplitudes of the oscillations in heat flux and temperature decrease with increasing pressure. At 700 mbar the peaks in heat flux are approximately $2\,\mathrm{kW/m^2}$ higher than the averaged heat flux. For the temperature oscillations an amplitude of approximately 0.1 K can be observed. In contrast to this oscillating heat transfer (hereinafter called *oscillation heat transfer mode*) a less fluctuating heat transfer can be observed for higher pressures. For this mode (hereinafter called *constant heat transfer mode*) the amplitudes of the observed oscillations are five to ten times smaller than the amplitudes in the oscillation heat transfer mode. The mode of heat transfer can change during the boiling process. This can be seen in the case of 500 mbar and 550 mbar for the higher heat flux. Further, it can be seen that the averaged temperature of the heated surface is lower for the oscillating heat transfer. In the shown example the temperature difference between both heat

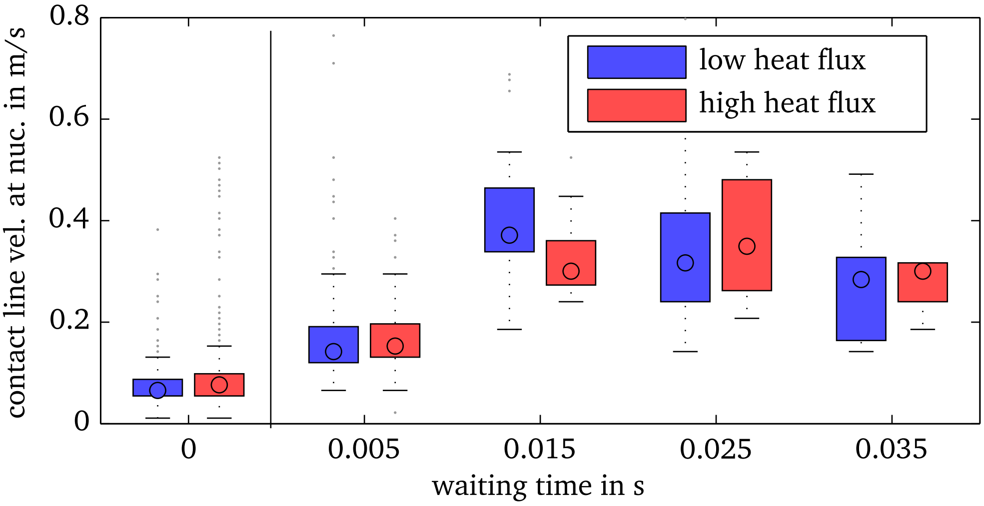

Figure 5.10: Influence of the waiting time on the contact line velocity at nucleation

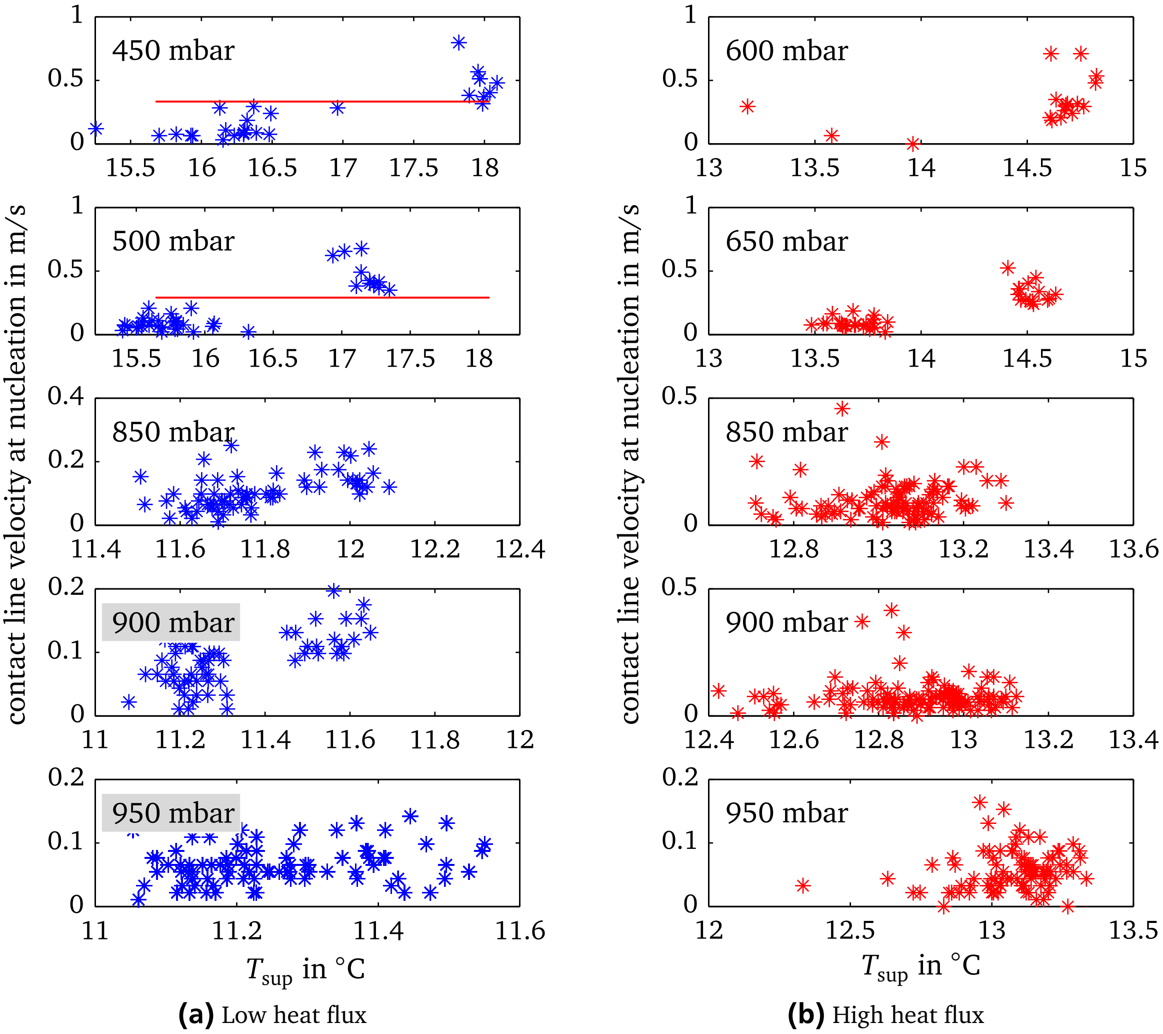

(a) Low heat flux

(b) High heat flux

Figure 5.11: Influence of the superheat on the velocity of the apparent contact line at nucleation

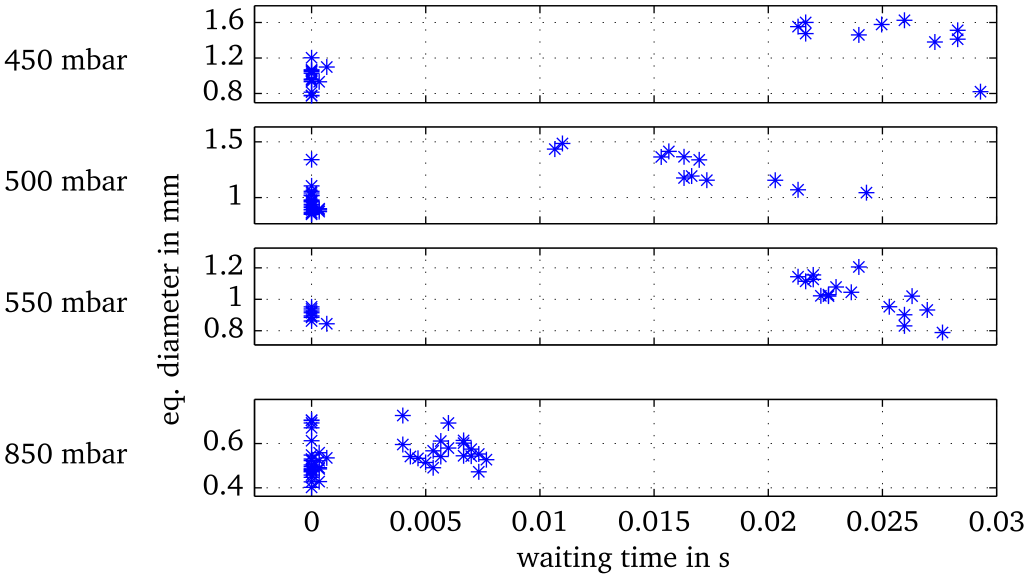

Figure 5.12: Influence of waiting time on bubble diameter

transfer modes is approximately 2 K. It has to be noted that a better heat transfer coefficient cannot be concluded from the lower temperature values for the oscillation heat transfer mode. As mentioned before, during this mode bubbles nucleate after a prior waiting time. As shown in Fig. 5.12 the bubble diameter is also increased for these kinds of bubbles. Therefore a larger area is affected by evaporation and convective heat transfer. Because of the fixed area for the data evaluation this can lead to a lower averaged temperature. Generally it has to be mentioned that the absolute values are strongly affected by the chosen area for averaging the heat flux and temperature. The dependency of the bubble diameter on pressure also affects the results. For higher pressures only the constant heat transfer mode can be observed. For the higher heat flux the transition from the oscillation to the constant heat transfer mode occurs at lower pressures.

The described differences in the boiling process can also be observed in the heat flux profiles. In Fig. 5.14 heat flux profiles and the according shapes of a bubble nucleated with and without some waiting time are shown for a system pressure of 400 mbar. The heat flux is illustrated with false-color pictures, where red regions represent higher and blue regions lower heat fluxes. For purposes of representation the scale is limited from 17.5 kW/m^2 to 40 kW/m^2 even though single values are higher or lower. The time interval between each picture is 0.665 ms (1503 frames per second). The first bubble shown nucleated after a prior waiting time. After nucleation of the first bubble a large circular area of high heat flux can be observed. 2.6 ms after nucleation a circular area of lower heat flux is spreading out from the center of the area of the high heat flux (annotation A). This leads to a small ring of high heat flux which can be attributed to contact line evaporation. In the receding phase the heat flux increases until bubble departure. The subsequent bubbles nucleate without a prior waiting time. For this case the area influenced by evaporation (represented by the high heat flux) is much smaller. Further, no completely filled area of high heat flux develops. Instead, the ring-shaped form typical of contact line evaporation can be observed. In the receding phase of the bubble (bottom row), which corresponds to an advancing contact line, an increase in heat flux can be seen. The effect of an increased heat flux at bubble departure has been discussed in detail by Schweizer [119] and Kunkelmann [90]. A short explanation is also given in section 2.2.3. In Fig. 5.15 the heat flux profile for the nucleation of the first bubble is shown from nucleation using a broader heat flux scale from 20 kW/m^2 to 100 kW/m^2. It can be seen that the inner

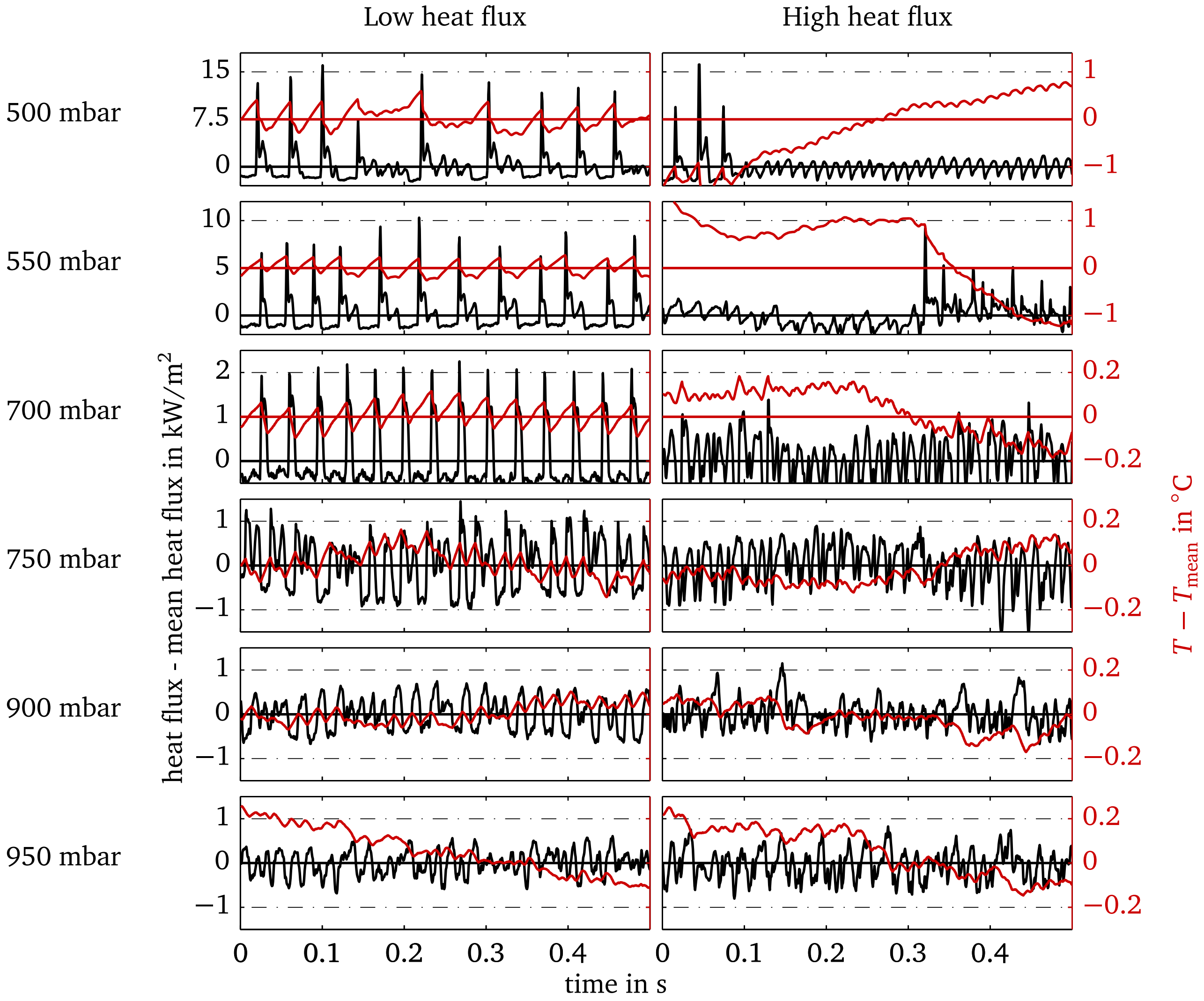

Figure 5.13: Different heat transfer modes during nucleate boiling

circle starts to develop earlier and the local heat flux reaches up to 100 kW/m^2. These differences in bubble nucleation can also be observed for higher pressures. Comparable to the differences discussed before (like interface velocity and departure diameter) the effect is reduced with increasing pressure. In Fig. 5.16 the heat flux profiles for a bubble nucleation after a prior waiting time are shown for pressures between 450 mbar and 650 mbar. It can be seen that the area where evaporation occurs is reduced with increasing pressure. In addition, the time to the transition to contact line evaporation increases with increasing pressure. For higher pressures ($>$ 650 mbar) a meaningful presentation is not possible due to the restrictions in the resolution of the IR camera. The complete bubble cycles for these pressures are shown in the appendix (Fig. A.9 to Fig. A.13). Although no direct measurements of a liquid film underneath a bubble can be performed with the used experimental setup, it can be concluded that the presented heat flux profiles result from microlayer evaporation. The extremely high heat fluxes over such a large area cannot be explained by means of the contact line evaporation model.

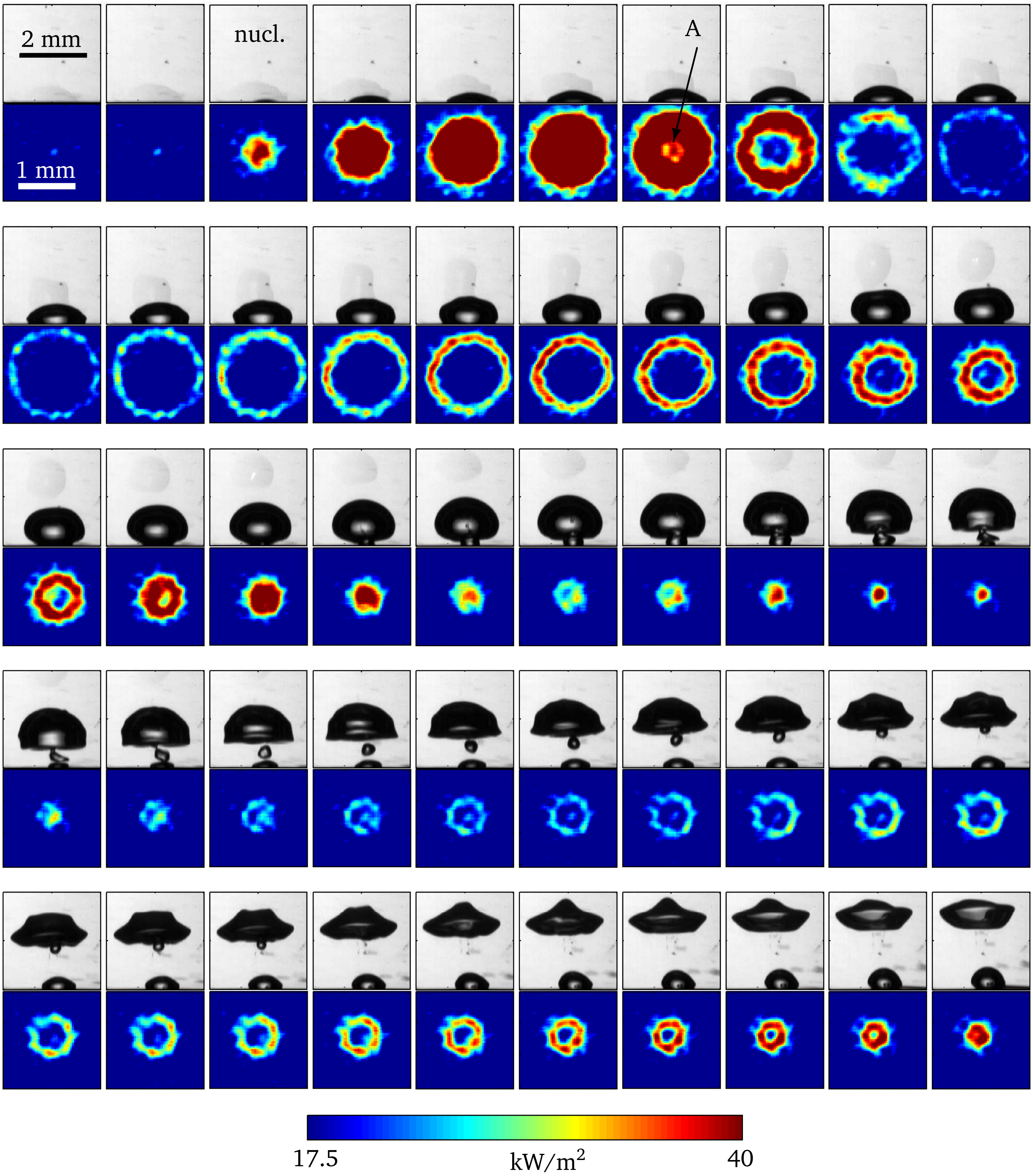

Figure 5.14: Heat flux profiles and bubble shapes at p = 400 mbar (time increment = 0.665 ms/picture)

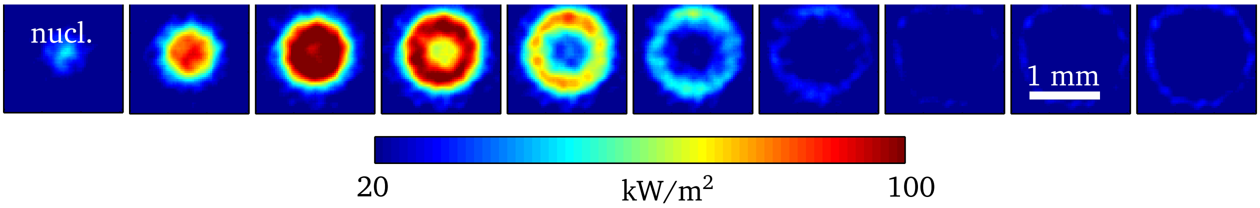

Figure 5.15: Heat flux profiles and bubble shapes at p = 400 mbar (time increment = 0.665 ms/picture - detail)

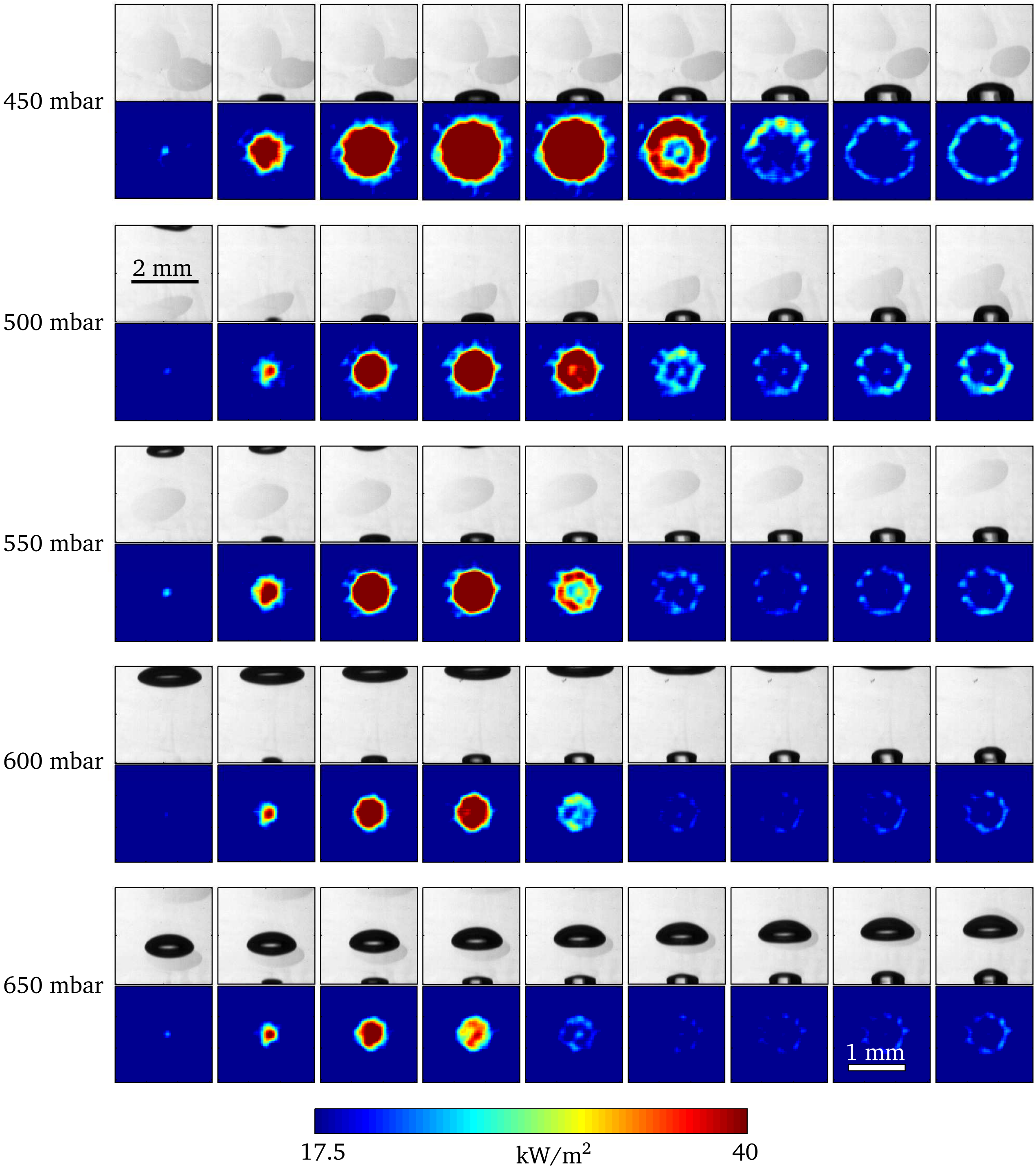

Figure 5.16: Microlayer evaporation at different pressures (time increment = 0.665 ms/picture)

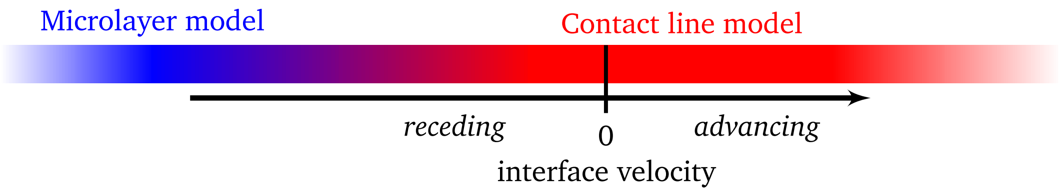

Figure 5.17: Transition from the microlayer to the contact line evaporation model

5.1.3 Conclusion of the single bubble experiments

Based on the results presented in this chapter and the presented experimental investigations described in chapter 2 conclusions concerning the boiling process can be drawn. It is experimentally verified that the necessary superheat for the nucleation of a bubble decreases with increasing pressure. The increase of the nucleation site density with increasing pressure, often observed in technical boiling processes and experiments, is directly related to this effect. Cavities on a technical heater require different superheats for nucleation. The decrease of the required superheat with increasing pressure increases the number of cavities where a nucleation is possible at a specific superheat. Furthermore, different phenomena are observed for the nucleation of a single bubble especially at lower pressures. The phenomena are characterized by differences in the superheat at nucleation, the size and dynamic of the bubble as well as the waiting time. A clear distinction between cause and effect cannot be drawn from the experimental data. Based on theoretical basics it is expected that the temperature at the cavity is the determining factor.

The results shown in section 5.1.2 (especially the heat flux profiles) enable a first step towards a combination of the so far rather competitively discussed contact line model (section 2.2.3) and microlayer model (section 2.2.3). It seems that for a fast-growing bubble the liquid cannot be displaced or evaporated completely and a thin liquid layer remains between the bubble and the heated surface. This results in microlayer evaporation. For advancing and slowly receding contact lines such a film is not built up and the evaporation process at the wall is well described by the contact line model (cf. Fig. 5.17). Considering the different investigations presented in literature the microlayer model is principally validated by experiments performed with water as working fluid. Experiments validating the contact line model are mostly conducted with refrigerants (mostly FC-72). For nucleate boiling the velocity of the contact line is not a material property or process variable. In order to get a better understanding of the transition between the contact line and microlayer evaporation further investigations are necessary. A useful contribution could be given by numerical simulations as the single properties and process variables can be set individually. To the knowledge of the author so far no numerical investigation has combined both models of evaporation.

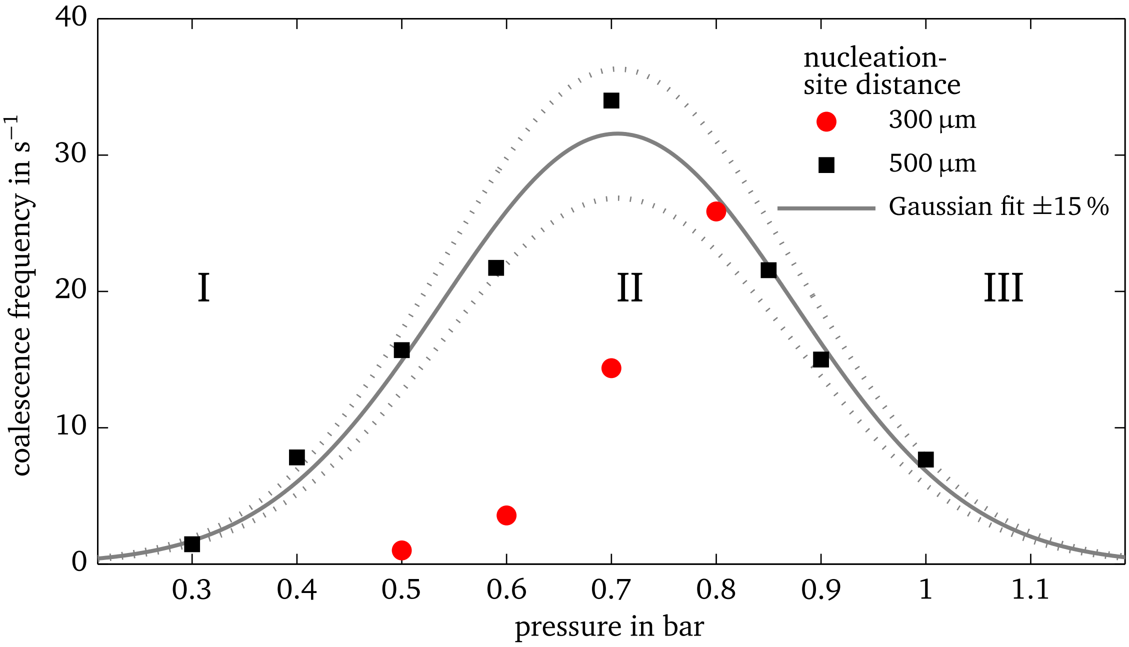

Figure 5.18: Horizontal coalescence frequency for S = 500 µm and S = 300 µm

5.2 Bubble interaction

The results on bubble interactions are separated into bubble coalescence as interaction of two individual bubbles, the interaction of multiple bubbles from multiple artificial cavities, and the interaction of bubbles nucleated on a single embedded wire. The results obtained for the boiling process at multiple artificial cavities corresponds well to boiling processes in technical application.

5.2.1 Bubble coalescence

The experiments of bubble coalescence are performed on two different heating foils containing two individual cavities each. The distance between the cavities is 500 µm and 300 µm, respectively. The same measurement technique is used as for the experiments with a single cavity. The temporal resolution of the optical measurement is approximately 1000 fps (IR and b/w). The spatial resolution is 27.5 µm/pixel (IR) and 4.4 µm/pixel (b/w).

Coalescence frequency

The measurements for bubble coalescence are performed at a heat flux where both cavities are active. In Fig. 5.18 the frequency of horizontal coalescence is plotted over pressure for a cavity distance S = 500 µm and of S = 300 µm. For S = 500 µm a maximum in the coalescence frequency can be seen at a pressure of approximately 700 mbar. For lower and higher pressures the coalescence frequency f_c is approaching zero. For S = 300 µm the curve seems to be shifted by approximately 200 mbar in the direction of higher pressures [128]. Measurements at higher pressures could not be conducted due to the restrictions of the measurement facility. The profile of the coalescence frequency (for S = 500 µm) is similar to a probability distribution. Therefore they are fitted to a Gaussian distribution

$$f_c = a\frac{1}{b\sqrt{2\,\pi}}e^{-0.5\left(\frac{p-c}{b}\right)} \tag{5.4}$$

with $a = 13.30,\ b = 0.71,\ c = 0.17$.

In Fig. 5.19 the bubble dynamics are shown for $S = 500\,\mu\text{m}$. By comparing Fig. 5.18 and Fig. 5.19 three different phenomena can be identified. They are indicated in Fig. 5.18 as Region I, II, and III. In Region I ($p \leq 500\,\text{mbar}$) the bubble diameter is too large for the given cavity spacing. Therefore, two individual bubbles cannot nucleate next to each other. A representative bubble cycle is show in Fig. 5.19a. In Region II ($p \approx 700\,\text{mbar} \pm 200\,\text{mbar}$) the bubble diameter and the cavity spacing are in a range where two bubbles can nucleate next to each other and coalesce (cf. Fig. 5.19b). For a further increase in pressure (Region III) the bubble diameter gets too small for coalescence. The bubbles nucleate next to each other and depart without coalescence. A representative cycle is shown in Fig. 5.19c for $p = 900\,\text{mbar}$.

Concerning the conditions which are necessary for the coalescence of two bubbles these phenomena can be further analyzed by using the results of section 5.1. The two necessary conditions for the coalescence of two bubbles are

- nucleation of a bubble during the presence of a bubble at the neighboring cavity (or simultaneous nucleation) (Condition A) and
- a distance between both bubbles which is small enough for them to get in contact with each other (Condition B).

For both conditions the main influences are the cavity spacing S, the maximum bubble diameter d_b, and the interface velocity of a growing bubble v_I. For the experiments with a single cavity it was observed that the bubble diameter and the interface velocity decrease with increasing pressure (cf. Figs. 5.1, 5.8). In Table 5.1 and Fig. 5.20 the relations between the coalescence frequency and their influencing properties are shown for both conditions. For condition A the coalescence frequency is proportional to S/v_I as the nucleation at the second cavity has to occur before the contact line of the bubble nucleated at the first cavity reaches the second one. For condition B the coalescence frequency is proportional to d_b/S as the bubbles have to have the opportunity to reach each other before departure. As the bubble diameter and the interface velocity are decreasing with increasing pressure the coalescence frequency is increasing with pressure for condition A and decreasing for condition B. In Fig. 5.20 (solid line) exemplary profiles are shown for both conditions and a given cavity spacing. The intersection of the lines for both conditions indicates the pressure for a maximal coalescence frequency. By changing the spacing between both cavities ($S/2$) the gradient of the curves is increasing for condition A and decreasing for condition B (dashed line). Therefore the pressure for a maximum in coalescence frequency changes to higher pressures. This can also be observed in the experimental results (cf. Fig. 5.18).
For $S = 300\,\mu\text{m}$ the influence of the heat flux on the coalescence frequency is investigated. In Fig. 5.21 the coalescence frequency is plotted over pressure for three different heat fluxes. It can be seen that the coalescence frequency increases with increasing heat flux. In this case this is mainly caused by a general increase in bubble frequency.

Monte-Carlo simulation of bubble coalescence phenomena

The results of Fig. 5.20 lead to the assumption that the profile of the coalescence frequency over the cavity spacing is also a probability distribution for a constant pressure. To get a more precise overview

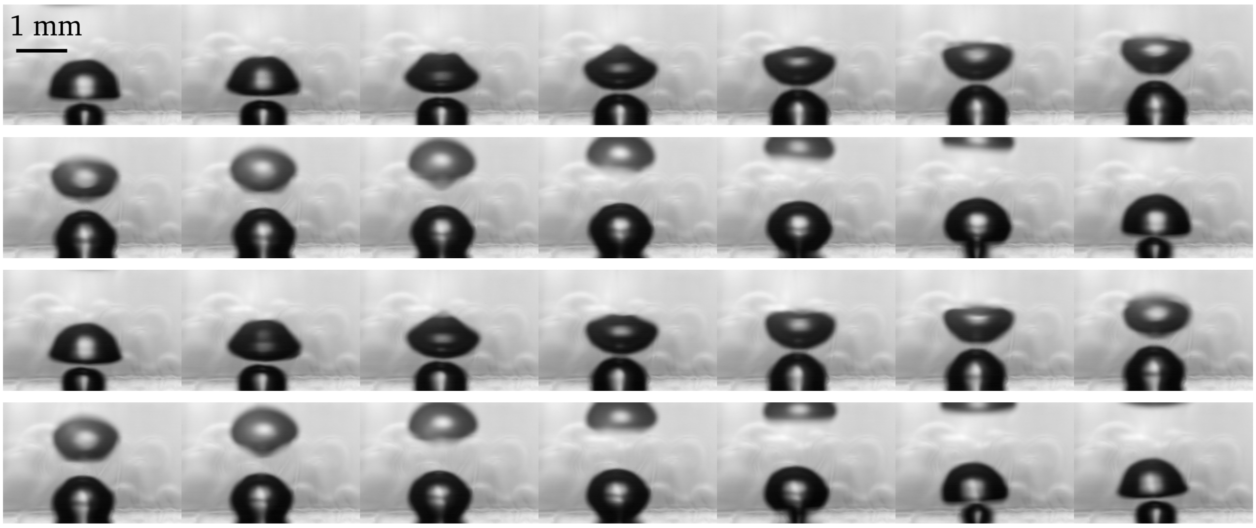

(a) 500 mbar - no coalescence due to bubble growth similar to growth at a single cavity

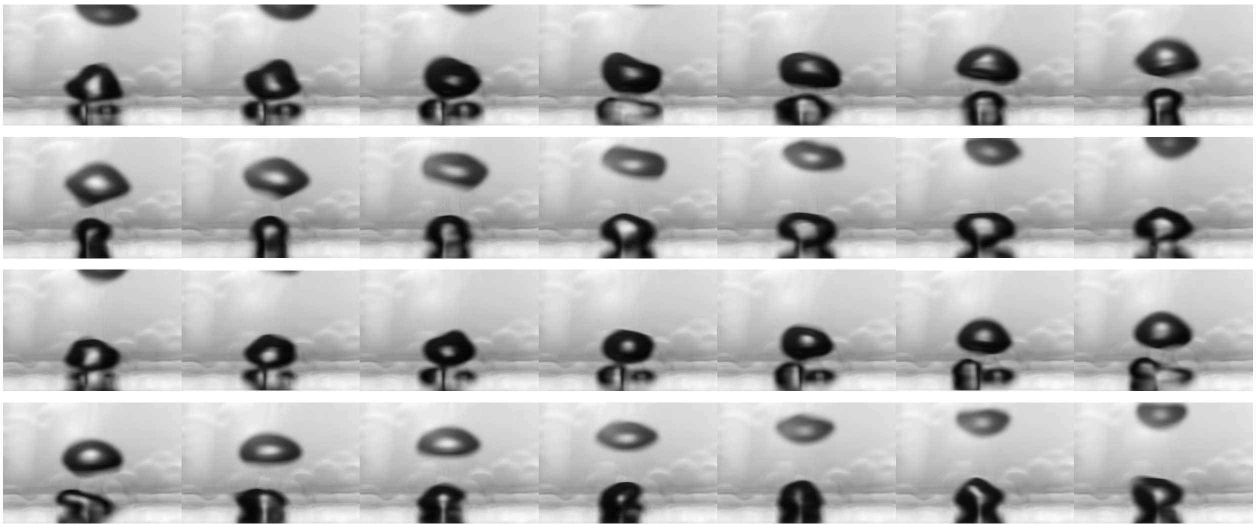

(b) 700 mbar - horizontal coalescence

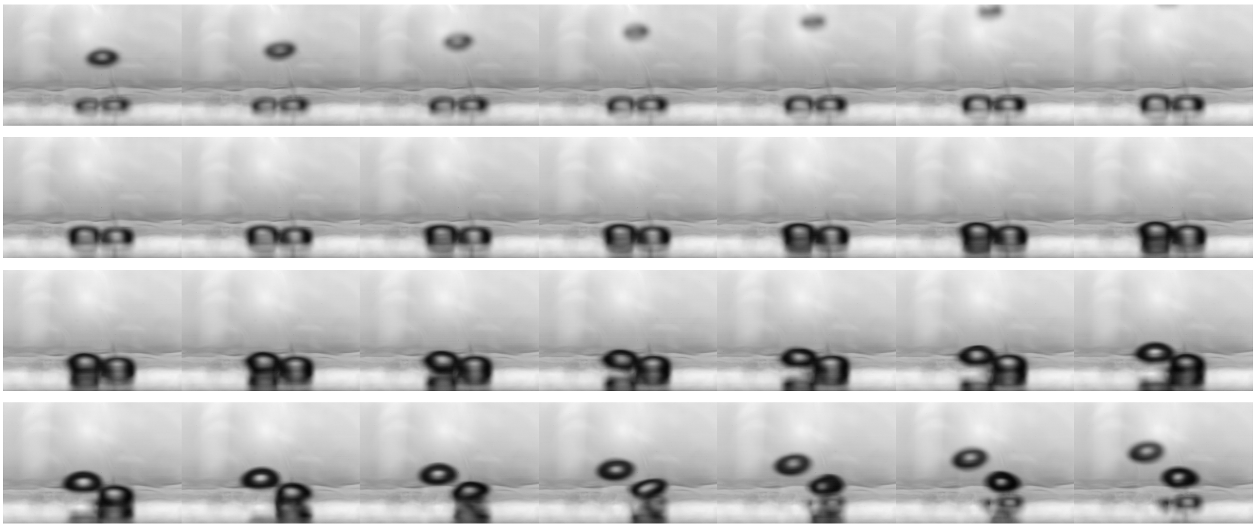

(c) 900 mbar - bubbles grow next to each other without coalescence

Figure 5.19: Bubble dynamics at different pressures - S = 500 μm, time increment = 1 ms/picture

Table 5.1: Influences on bubble coalescence

Condition	A	B
f_{coal}	S/v_{I}	d/S
$p\uparrow$	$v_{\mathrm{I}}\downarrow$	$d\downarrow$
	$f_{\mathrm{coal}}\uparrow$	$f_{\mathrm{coal}}\downarrow$

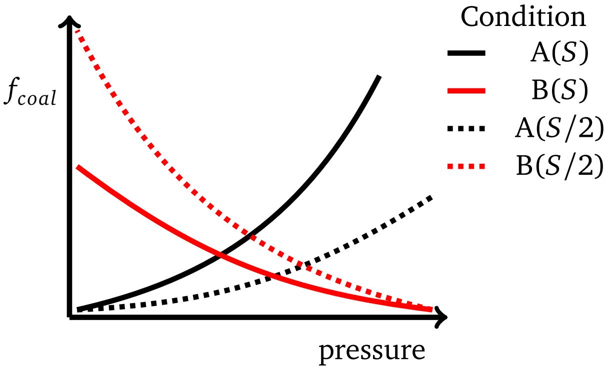

Figure 5.20: Dependency of coalescence frequency on pressure and cavity distance

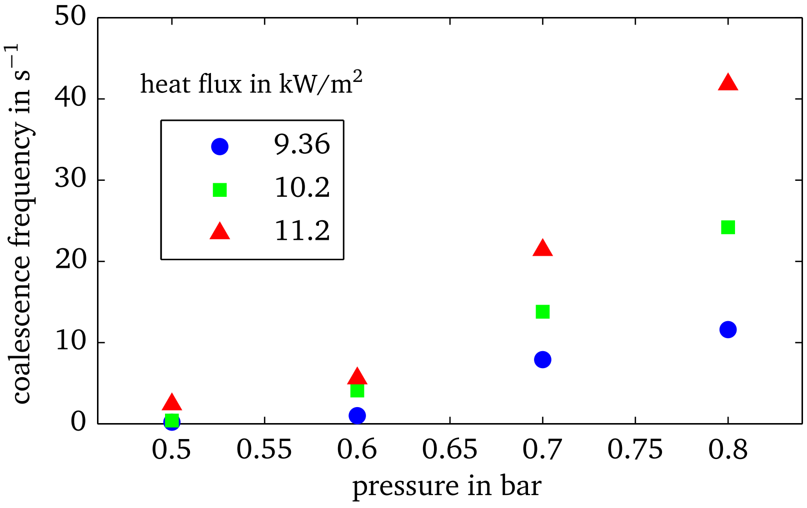

Figure 5.21: Influence of heat flux on coalescence frequency for S = 300 µm

of these phenomena a Monte-Carlo simulation is performed of the coalescence process of two bubbles at artificial cavities. For this simulation the results from the single cavity experiments (waiting time (Fig. 5.4), cycle time (Fig. 5.5), and bubble diameter (Fig. 5.1)) are used. For the three mentioned parameters the mean value and standard deviation are taken from the experiment and curve fitted over pressure. These functions are used afterwards in the Monte-Carlo simulation within a function for the *waiting time*, *cycle time*, and *bubble radius*. The flow chart of the performed simulation is shown in Fig. 5.22. At first for both cavities a waiting time is calculated. For the time period calculated by the waiting time function the cavity is inactive. Afterwards it is checked whether nucleation is possible. A nucleation is not possible if the interface of a bubble nucleated at the other cavity is closer than a specific value s. This requirement represents condition A (cf. Fig. 5.20). For the determination of the bubble's size the apparent diameter of the bubble is used. If nucleation is possible the bubble radius and cycle time is calculated. The time-dependent radius is stored in an individual vector for each cavity. After bubble departure a waiting time is calculated. If nucleation is not possible a waiting time is calculated directly. This procedure is performed for both cavities up to a given time limit. After this calculation the interface positions of the bubbles from both cavities are compared and the number of coalescences is counted (not shown in Fig. 5.22). The following simplifying assumptions are made:

- Coalescence has no effect on the bubble's dynamic or shape.
- A constant contact angle of $\Theta = 50°$ and a spherical shape is assumed for the bubble.
- As the mean value and standard deviation from the single bubble experiments just give a departure diameter and a cycle time representing the whole bubble cycle, the position of the bubble's interface is fitted by a quadratic function over time.
- The threshold to prevent nucleation is $s = 150\,\mu\text{m}$ (which is approximately the diameter of the cavity in the experiment).
- As for the calculation the mean value and standard deviation are used, non-physical values can result. Therefore the bubble diameter is restricted to $d \geq 0.3$ mm, the cycle time to $\tau_{\text{cyc}} \geq 1.66$ ms, and the waiting time to $\tau_{\text{wait}} \geq 0.33$ ms, which represents one time step in the calculation.
- The calculation time is set to 15 min of boiling. The time step is 1/3000 s.

The calculation is performed for a pressure range of 400 mbar to 1000 mbar and a cavity spacing of 0.15 mm to 1.5 mm. The result of the calculation is shown in Fig. 5.23. Below a cavity distance of 150 µm no coalescence occurs due to the assumptions described above. For a constant pressure a probability distribution can be found. The cavity spacing that the maximum coalescence frequency occurs at increases with decreasing pressure. In the investigated pressure range the maximum coalescence frequency is at 1000 mbar and a cavity spacing of approximately 350 µm.

In Fig. 5.24 the experimental data is compared to the results of the Monte-Carlo simulation. The solid lines represent the simulated coalescence frequency for $S = 500\,\mu\text{m}$ (black) and $S = 300\,\mu\text{m}$ (red). The dashed lines represent a deviation in cavity spacing of $1 \pm 10\,\%$ of the basic value. A good qualitative agreement can be seen. For a cavity spacing of $S = 540\,\mu\text{m}$ (solid green line) the calculated coalescence frequency fits qualitatively well to the experimental data of $S = 500\,\mu\text{m}$. Considering the simplicity of this shows this constitutes a good agreement between model and experiment.

Heat transfer during bubble coalescence

For measurements where one or two individual bubbles nucleated and lift off without coalescence similar phenomena as for the nucleation at a single cavity could be observed. Therefore, this case will not

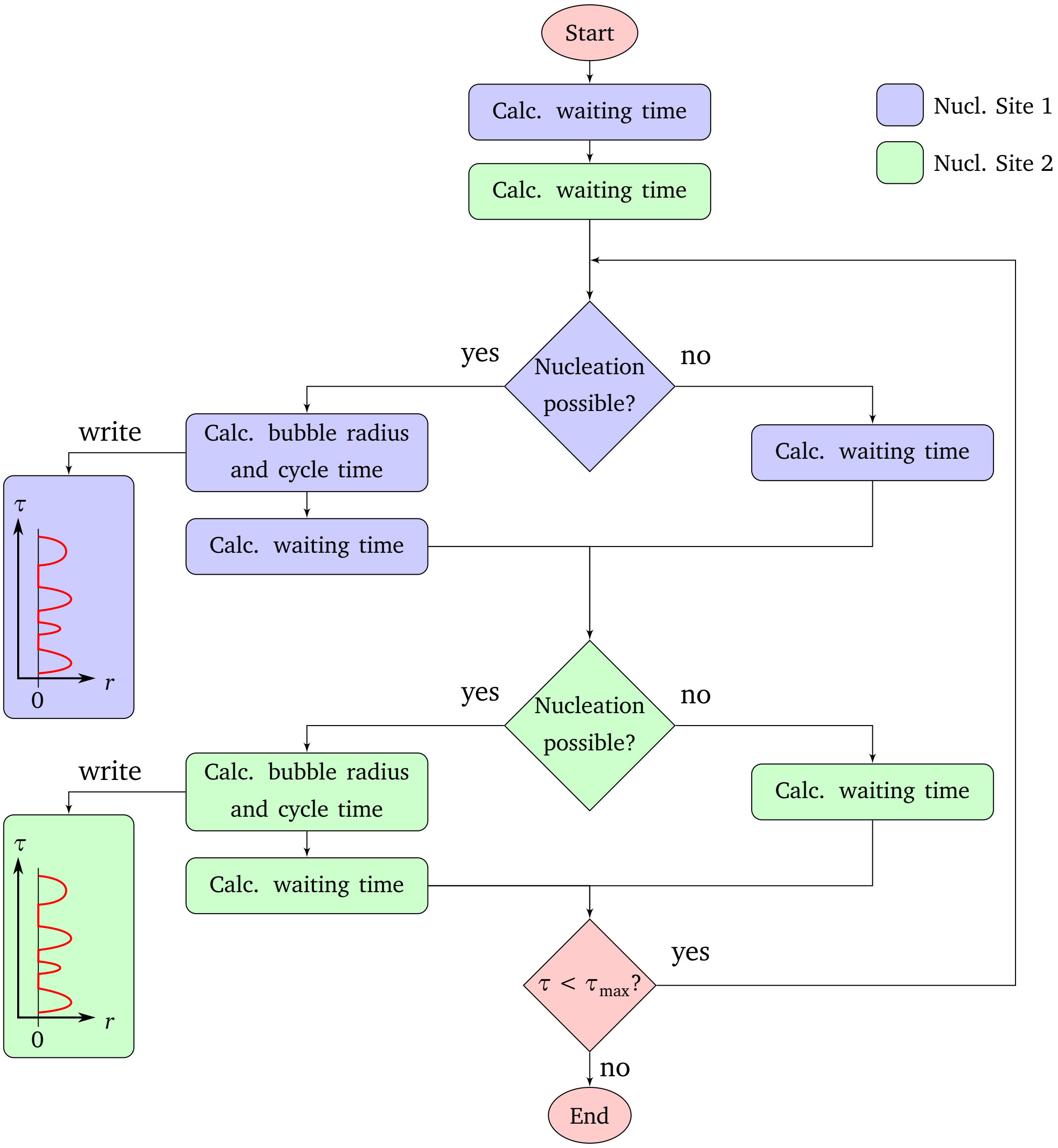

Figure 5.22: Flow chart of the Monte-Carlo simulation for bubble coalescence

be discussed in the thesis. A phenomenon observed for bubble coalescence at lower pressures is the formation of a residual droplet inside the coalesced bubbles. This effect is only observed for $p \leq 600\,\text{mbar}$. In Fig. 5.25 bubble coalescence with a residual droplet is shown for a cavity spacing of $S = 300\,\mu\text{m}$ ($p = 500\,\text{mbar}$, $q = 10.9\,\text{kW/m}^2$). After nucleation an area of high heat flux can be observed. The influence of the other bubble can be seen by the deformation (compared to a circle) of the area of high heat flux. Afterwards contact line evaporation can be observed. At 7 ms (first picture in the bottom row) the bubble coalescence is completed and a circular region of higher heat flux can be seen inside the bubble. This points to a liquid layer (droplet) evaporating inside of the bubble. The high heat flux at the left side of the contact line is assigned to the nucleation of a smaller bubble. In Fig. 5.26 coalescence with and without a remaining droplet is compared for a cavity spacing of $S = 500\,\mu\text{m}$ ($p = 500\,\text{mbar}$, $q = 10.3\,\text{kW/m}^2$). Comparable to the coalescence at $S = 300\,\mu\text{m}$ in both cases a relatively high heat flux can be observed right after nucleation of the bubbles. Afterwards contact line evaporation can be identified for the case with a remaining droplet (picture 7,8). After coalescence a higher heat flux in the middle of the coalesced bubble indicates a remaining droplet comparable to the observation shown

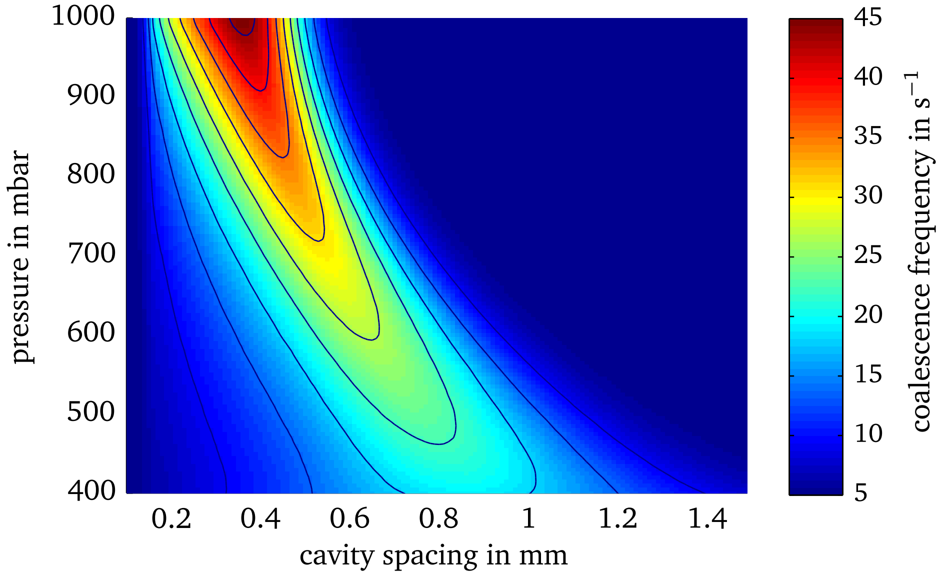

Figure 5.23: Simulated coalescence frequency over pressure and cavity spacing

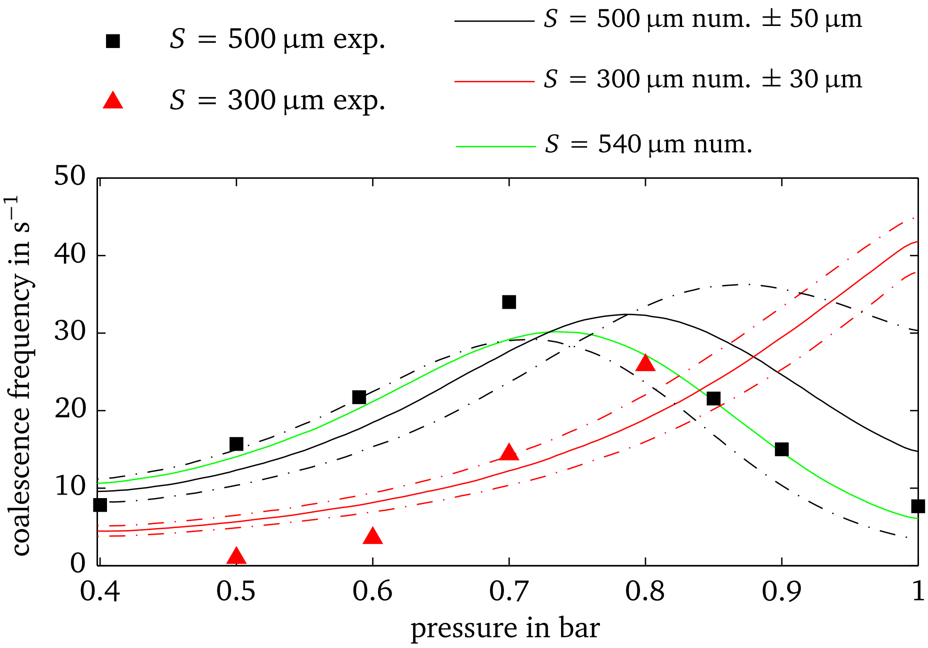

Figure 5.24: Comparison of simulated and experimental coalescence frequencies

in Fig. 5.25. This phenomena occurs preferentially for larger bubbles with a higher interface velocity. As mentioned for the single bubble experiments the interface velocity is increased in the presence of microlayer evaporation. Therefore it can be assumed that microlayer evaporation assists the occurrence of a remaining droplet. As the bubble coalescence is a highly statistical phenomenon a comparison of the heat flux between a coalescence with and without a remaining droplet is difficult to draw. This also applies for the heat flux of two bubbles with or without coalescence. Because of the differences in time and length scale there is a lack of a sufficient reference scale. For the shown case the heat transferred for the case of coalescence with a remaining droplet is approximately 8 % higher than the heat flux for the case of coalescence without remaining droplet. For the evaluation the heat flux and temperature are averaged over the area and measurement time is shown in Fig. 5.26. For two individual pictures the increase in heat flux is approximately 17 %. For the coalescence of two bubbles a higher heat flux is observed compared to the heat flux of two bubbles without coalescence. This is mainly attributed to the increase in contact line velocity. As shown by SCHWEIZER [119] and KUNKELMANN [90] this leads to an increase in heat transfer. As a rough estimation an increase in a range of about 10 % seems to be realistic. Further information about this can be drawn out of numerical investigations as performed by DIETL in SIELAFF ET AL. [128]. In order to obtain a heat transfer coefficient and evaluate a possible enhancement in heat transfer, the wall superheat needs to be calculated. Averaged over the full cycle the superheat is 19.8 °C for coalescence without remaining droplet and 17.8 °C for the coalescence with remaining droplet. This corresponds to an enhancement in the heat transfer coefficient of approximately 20 % over the full cycle and approximately 30 % for an individual picture.

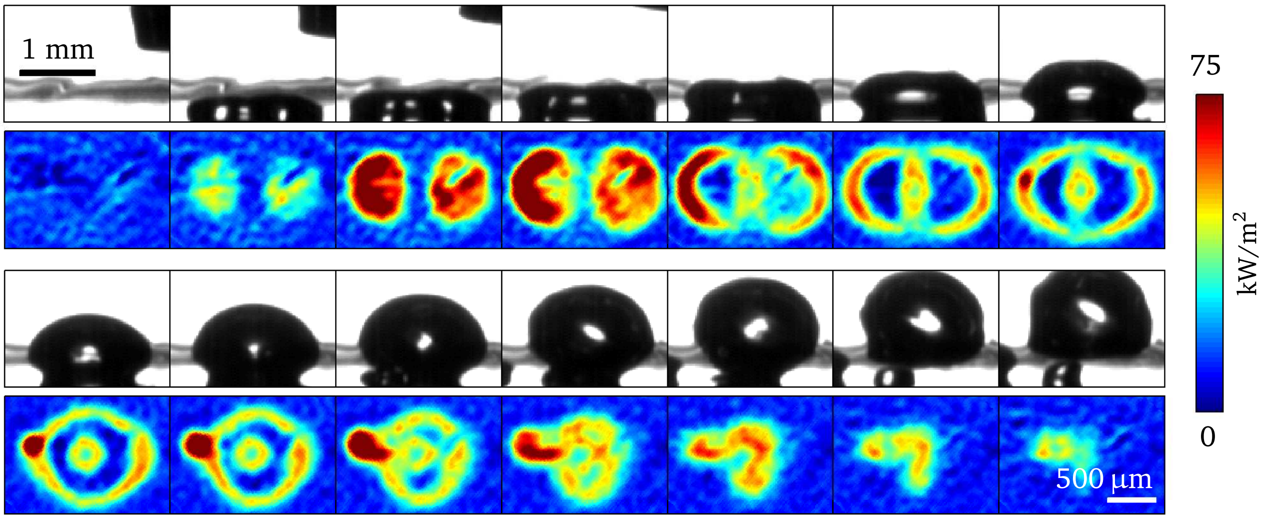

Figure 5.25: Heat flux profile and bubble shape for a bubble coalescence - S = 300 µm, p = 500 mbar, q = 10.9 kW/m^2, time increment = 1 ms/picture

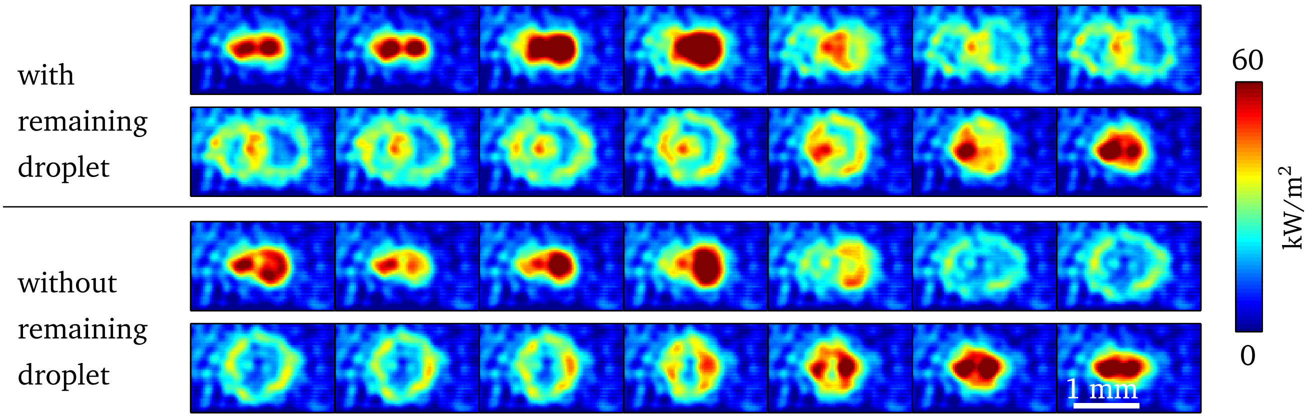

Figure 5.26: Comparison of heat flux profiles for a coalescence with and without a remaining droplet - S = 500 µm, p = 500 mbar, q = 10.3 kW/m^2, time increment = 1 ms/picture

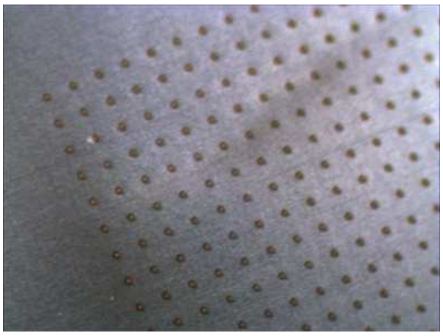

Figure 5.27: Structured foil with 500 µm cavity distance

5.2.2 Interaction of multiple bubbles

In the following it is discussed whether the results obtained from the experiments of the bubble coalescence can be transferred to processes of multiple interacting bubbles, which represents a technical boiling process. Therefore, experiments on an unstructured (reference) foil as well as structured foils with artificial cavity distances of 600 µm and 500 µm are performed. For the structured foils the same surface treatment is used as for the single and coalescence cavities. The artificial cavities are arranged in a square of approximately 12 x 12 mm. A picture of the 500 µm structured foil is shown in Fig. 5.27. The measurements are performed with a temporal resolution of approximately 500 fps for the IR camera. The spatial resolution is 40.8 µm/pixel. Data obtained with the b/w camera cannot be used for a detailed evaluation because of the large number of bubbles at the heated surface. The measurements are performed with increasing pressure and decreasing heat flux.

Influences on the heat transfer coefficient

In Figs. 5.28 – 5.30 the heat transfer coefficient is plotted over heat flux for different system pressures[1]. It can be seen that the heat transfer coefficient increases with increasing heat flux and pressure. Furthermore, the unstructured reference foil has a lower heat transfer coefficient than the structured foils. The results are in good qualitative agreement with the state of the art and other experimental results (cf. e.g. [52]). To identify a possible effect of coalescence phenomena on heat transfer in Fig. 5.31 and Fig. 5.32 the heat transfer coefficient of the structured foils is compared to the heat transfer coefficient of the reference foil. The enhancement in percent ($(h_{\mathrm{str.}} - h_{\mathrm{ref.}})/h_{\mathrm{ref.}} \cdot 100$) is plotted over heat flux for different system pressures. In general it can be seen that the enhancement increases with increasing pressure. For the 500 µm structured foil it can be seen that the enhancement in heat transfer is increasing with increasing heat flux for lower pressures, but decreasing with increasing heat flux for higher pressures. At approximately 650 mbar the enhancement of the heat transfer is nearly constant over the investigated heat flux range. In contrast to the 500 µm structured foil the heat transfer enhancement for the 600 µm is generally increasing with increasing heat flux and pressure. To compare both structured foils with each other in Fig. 5.33 the quotient of the heat transfer enhancement (500 µm to 600 µm foil) is plotted. It can be seen that the 500 µm structured foil has a higher heat transfer enhancement than the 600 µm structured foil. With increasing heat flux and pressure the enhancement of the 500 µm structured foil decreases.

From the results presented in Figs. 5.28 – 5.33 no significant effect of bubble coalescence on the heat transfer coefficient can be deduced. As shown in section 5.2.1 a significant increase of bubble coales-

---

[1] A presentation like presented in [52] is not useful due to the low pressure range of $0.015 < p^* = p/p_{\mathrm{crit}} < 0.054$.

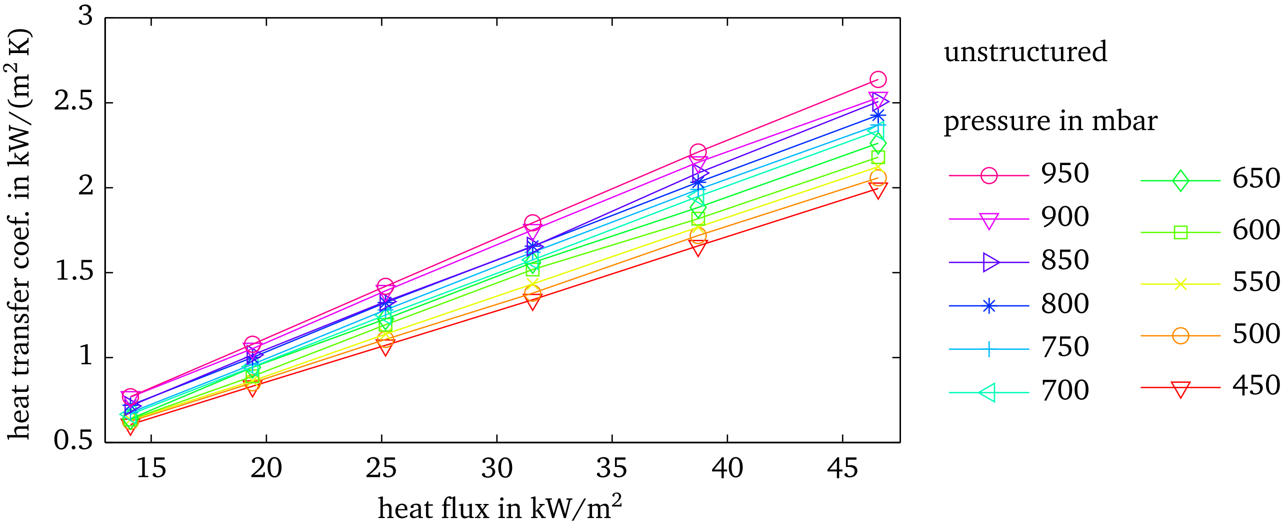

Figure 5.28: Dependency of the heat transfer coef. on pressure and heat flux for an unstruct. foil

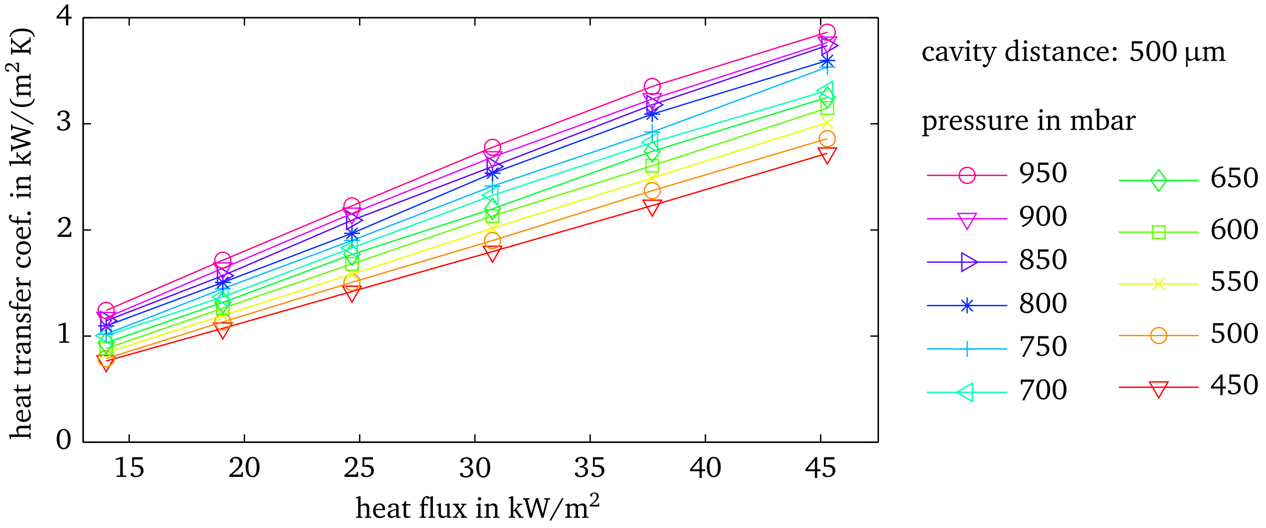

Figure 5.29: Dependency of the heat transfer coef. on pressure and heat flux for a struct. foil - S = 500 μm

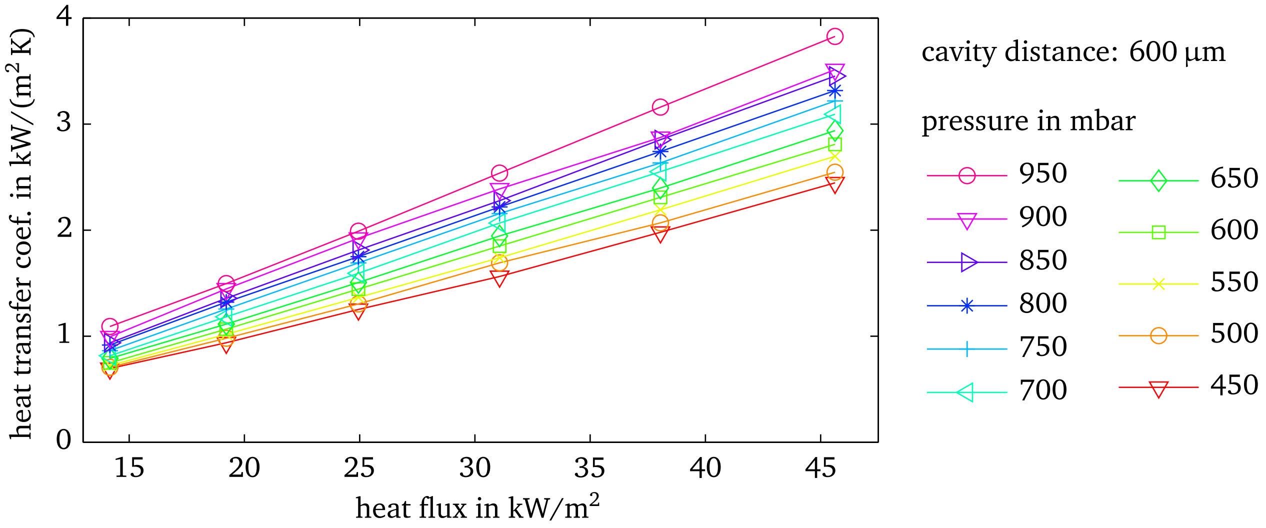

Figure 5.30: Dependency of the heat transfer coef. on pressure and heat flux for a struct. foil - S = 600 μm

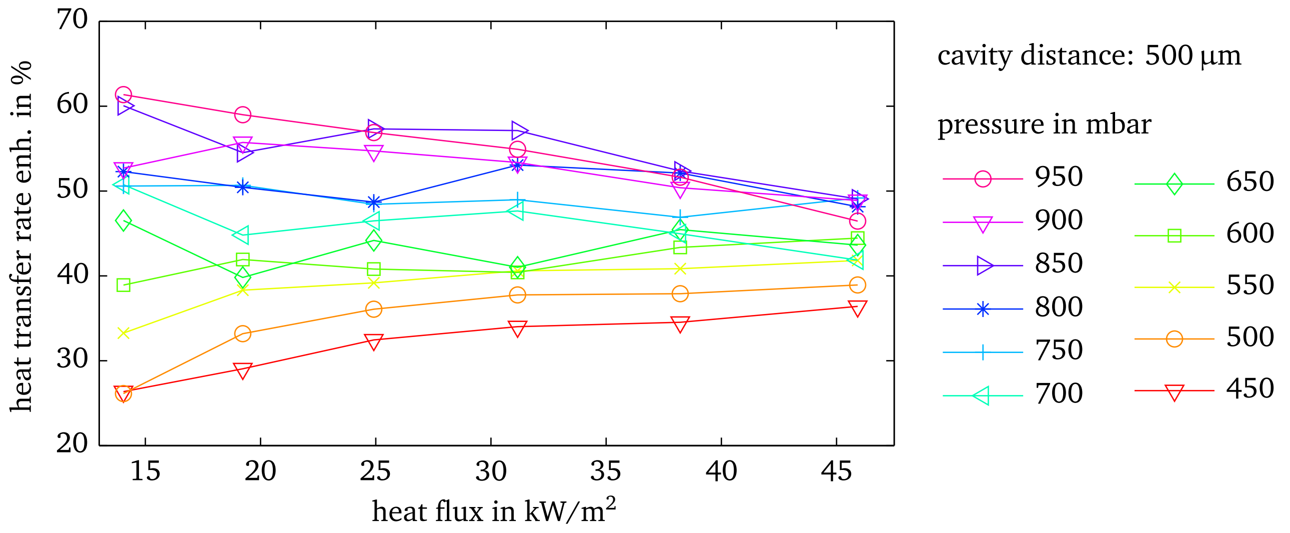

Figure 5.31: Heat transfer enhancement of a structured foil - S = 500 µm compared to an unstructured

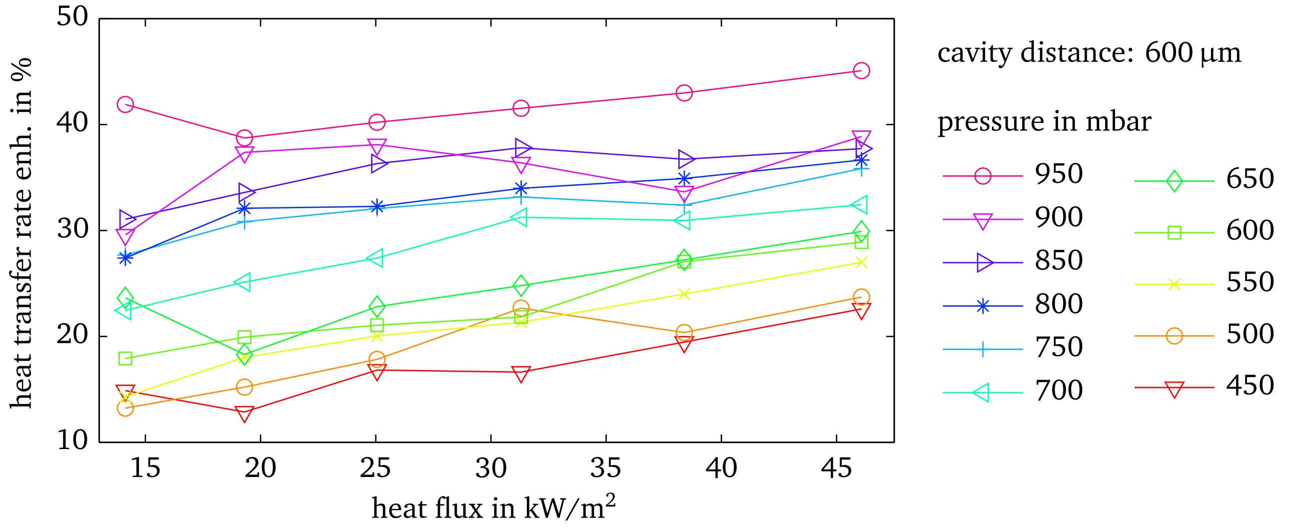

Figure 5.32: Heat transfer enhancement of a structured foil - S = 600 µm compared to an unstructured

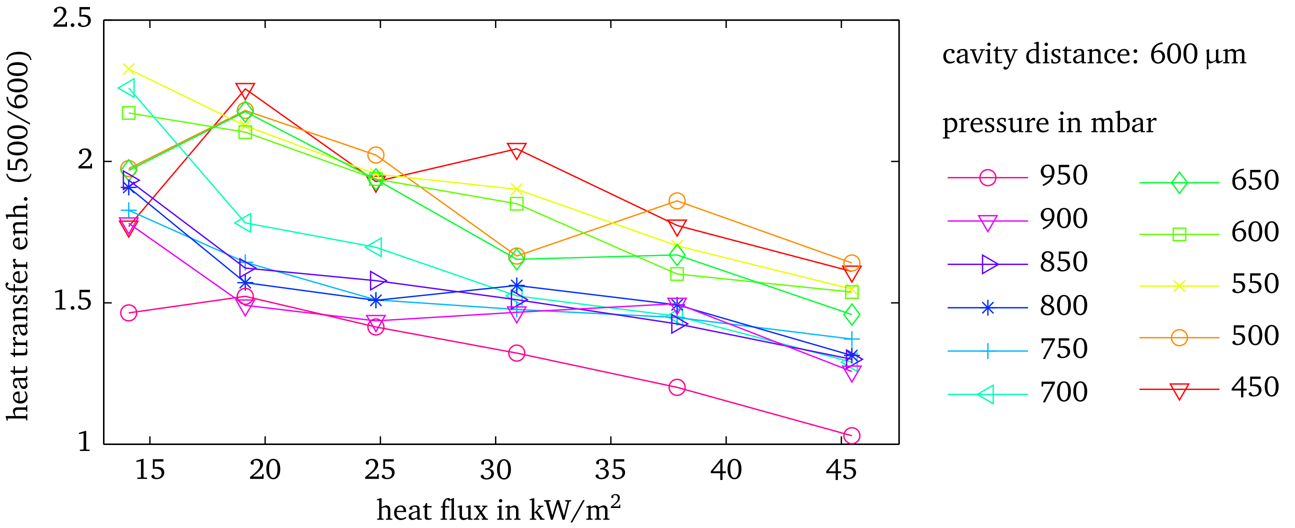

Figure 5.33: Heat transfer enhancement of a structured foil - S = 500 µm compared to S = 600 µm

cence is observed for a specific pressure. In addition the coalescence process enhances the heat transfer as well as the heat transfer coefficient. For a significant effect of bubble coalescence on the heat transfer coefficient an increase of the heat transfer coefficient would have had to be observed for a specific pressure. Therefore, it can be concluded that either no significant number of bubble coalescences occur or the effect of bubble coalescence on the heat transfer is negligible.

Nevertheless, the different phenomena observed for the two structured foils (cf. Figs. 5.31, 5.32) is further discussed. In Fig. 5.34 and Fig. 5.35 the heat transfer profiles are plotted for the structured foils at different heat fluxes and pressures. Inside of the black circle, representing the area of evaluation, the heat flux is averaged over time for each pixel. To compare the different profiles the used scale is adapted to each picture individually. The lower limit (dark blue) of the scale is 1.05 times the minimum heat flux of the averaged individual sequence. The upper limit (dark red) is 0.95 times the maximum heat flux. A presentation using a fixed scale cannot be applied due to the differences in the heat source term. On the left side the approximate heat flux is shown for the heat flux profile in the according row. The used false-color scale is shown on the right side. Outside of the black circle the mean heat flux of each sequence can be seen. For lower pressures it can be seen that the heat is transferred by a few individual spots. The other parts of the foil show a heat flux less than the averaged one. As the averaged heat flux is closer to the minimum of the heat flux range a significant amount of the energy produced by Joule heating is transferred within the spots of high heat flux. For higher pressures two major differences can be observed in comparison of both foils. First, the averaged heat flux for the 500 µm structured foil is still in a lower sector of the heat flux range (blue color out of the evaluation area). For the 600 µm structured foil the averaged heat flux is for higher pressures in an intermediate range (yellow color). This means that for the 500 µm foil still certain positions exist where a higher amount of the overall heat flux is transferred in. In contrast to this the heat flux profile at the 600 µm foil is more uniform. Second, for the 500 µm foil the structure of the topside of the foil can be identified by the positions where high heat flux values occur. For the heat flux profile of the 600 µm foil also indications on the structure of the top surface can be found. However, on closer analysis there is no significant accordance to the structure of the top side of the foil. In Fig. 5.36 the averaged heat flux distribution of the 500 µm structured foil is shown for $p = 950\,\mathrm{mbar}$ and $q_0 \approx 46\,\mathrm{kW/m^2}$. On the right side of the figure the heat flux is plotted for the shown rectangle. An oscillation in the heat flux profile can be seen with the peaks of the heat flux having the same distance as the cavities on the top of the foil. The amplitude of this oscillation is up to $10\,\mathrm{kW/m^2}$. These results lead to the assumption that the decrease in the heat transfer enhancement for higher pressures and heat fluxes (cf. Fig. 5.31) is caused by fixing the bubbles to the artificial cavities. A more uniform heat transfer over the whole heating foil results in a lower temperature (averaged over the whole foil) and therefore in a better heat transfer coefficient. The generally increased heat transfer coefficient of the 500 µm structured foil is mainly caused by the increased cavity density (44%). It has to be mentioned that this effect is superimposed by all other effects discussed before, which lead to a general increase of the heat transfer coefficient with increasing heat flux and pressure. These results are obtained on a very thin heating foil. For thicker heaters other heat distributions can occur due to heat conduction perpendicular to the surface, which can lead to different effects.

For a deeper understanding of the influence of bubble coalescence on the heat transfer processes on a technical length scale the Monte-Carlo simulation presented in section 5.2.1 is adapted to boiling on a structured foil. For the simulation the 500 µm structure is used with 20 x 20 cavities. As the calculation time is proportional to

$$t_{\mathrm{calc}} \propto \frac{n^2(n^2+1)}{2}, \tag{5.5}$$

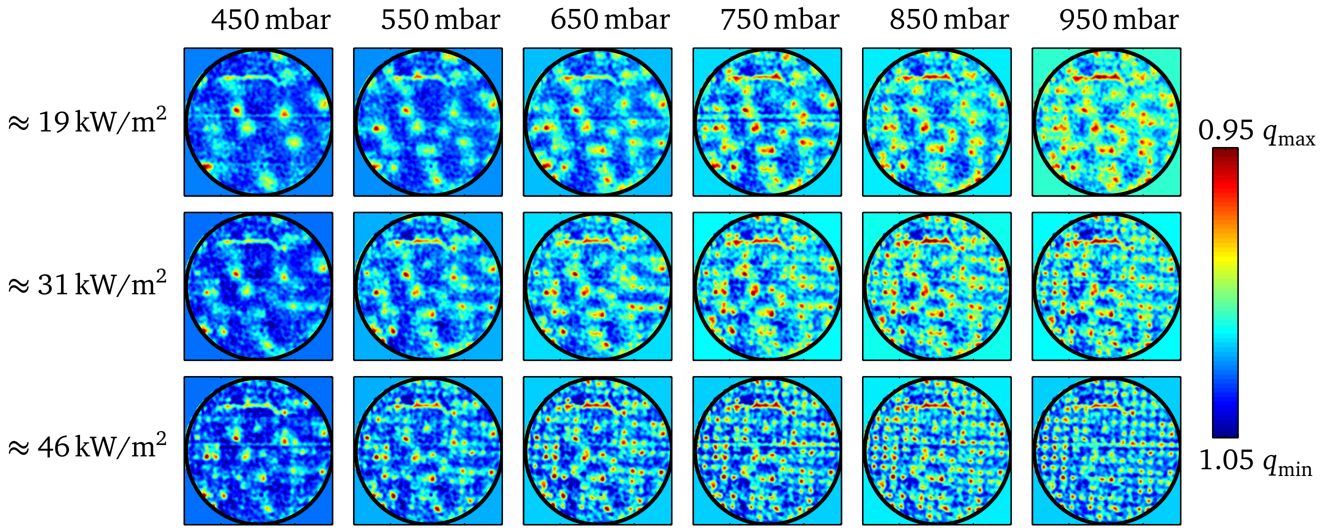

Figure 5.34: Time-averaged heat transfer distribution of a structured foil - S = 500 µm

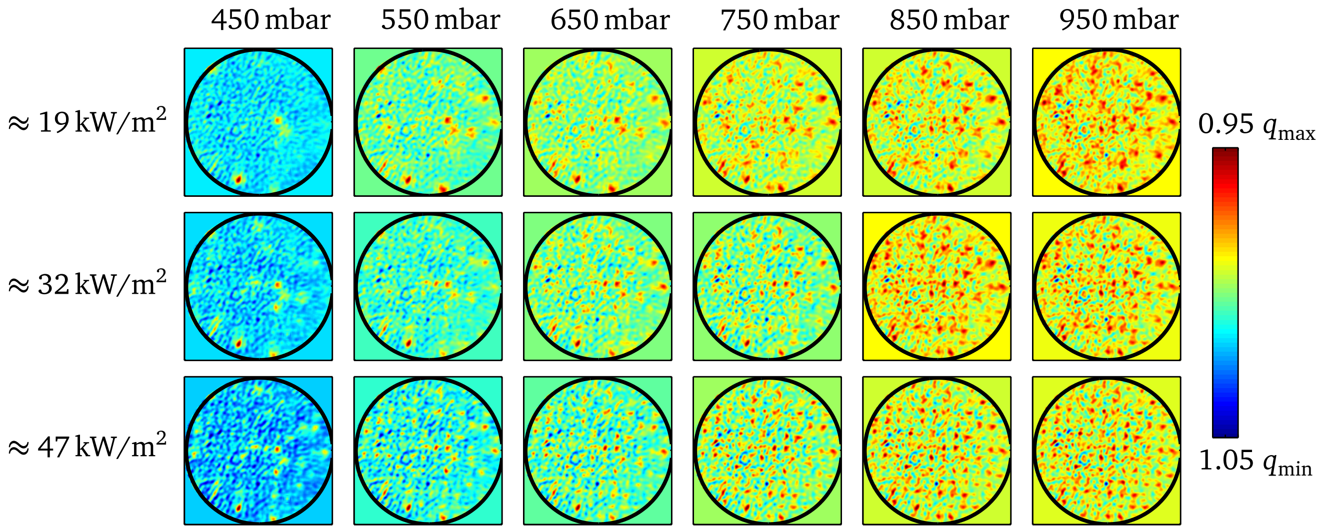

Figure 5.35: Time-averaged heat transfer distribution of a structured foil - S = 600 µm

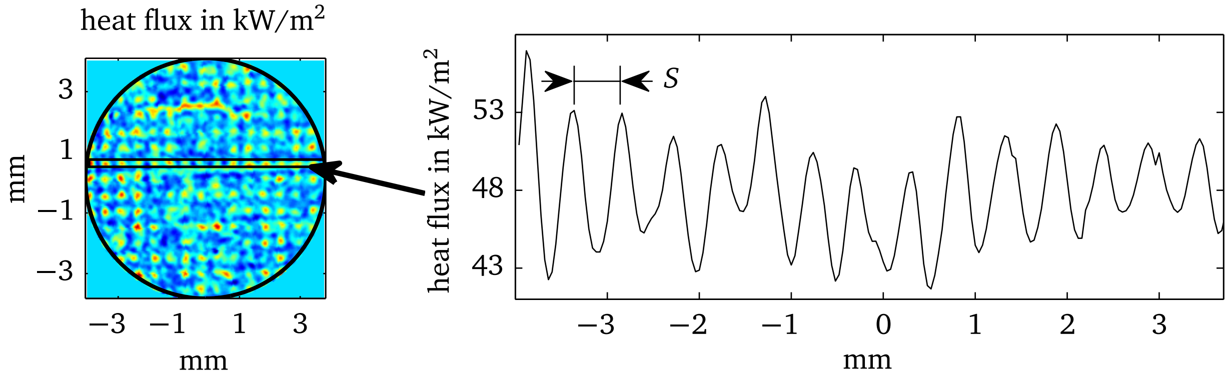

(a) Heat flux distribution **(b)** Heat flux of a single segment

Figure 5.36: Heat flux distribution for the structure foil - S = 500 µm, p = 950 mbar

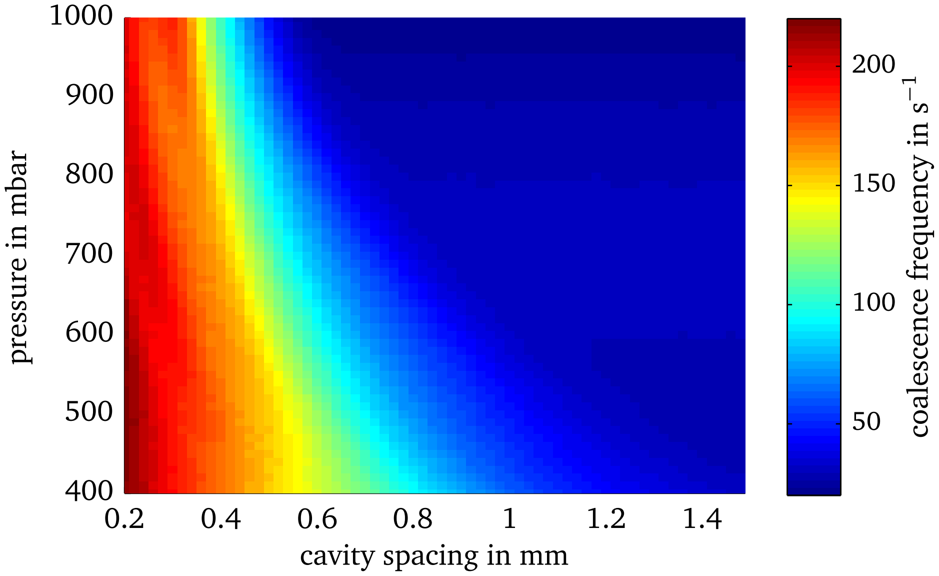

Figure 5.37: Simulated coalescence frequency for a structured foil - S = 500 µm

where n is the number of cavities in a row[1], the number of investigated cavity spacings and pressures is reduced. The time calculated is limited to 12 s[2]. The results of the simulation are shown in Fig. 5.37. It can be seen that the coalescence frequency does not have a probability distribution for a specific pressure as it has been observed for the case of two cavities shown in section 5.2.1. A clear limit caused by the used assumptions can be seen. For lower pressures coalescence frequencies of over 100 coalescences per second are calculated. Comparing these values to the results of the experiments (Fig. 5.4), the calculated frequency is higher than the bubble frequency at the single cavity. This results from the assumption that a coalescence does not affect the bubble dynamics. Therefore, in this model a bubble can coalescence not only with one but with multiple other bubbles leading to the shown high frequencies. Nevertheless, it can be seen that the effects leading to a probability distribution at two cavities is suppressed as coalescence can also occur from cavities with a larger distance than the spacing of two single cavities next to each other.

Oscillations in heat transfer

In Fig. 5.38 a further phenomenon is shown observed within the measurement presented in this section. Using the example of the 600 µm structured foil on the left side the spatial averaged heat flux and temperature is plotted over time. On the right side a frequency analysis is shown. The frequency analysis is performed using a Fast Fourier transformation within Matlab. Comparable to the results of section 5.1.2 oscillations in the heat flux over time can be found. The temperature oscillations correspond to the heat flux oscillations. For a case without boiling (top row) oscillations with two characteristic frequencies are observed. These oscillations are at least one order of magnitude smaller than the oscillations for a case with boiling. They are attributed to the measurement and control systems. With increasing pressure the oscillations of the heat flux and temperature are reduced in amplitude and increased in frequency. This result can be attributed to a similar effect as observed within the single bubble experiments (cf. Fig. 5.13). For a single bubble the superheat is increased if boiling at a cavity is interrupted even just for

---

[1] The equation is valid for a quadratic field of cavities.

[2] The calculation time for the shown simulation is approximately two weeks parallelized on eight cores (Intel Xeon X5675).

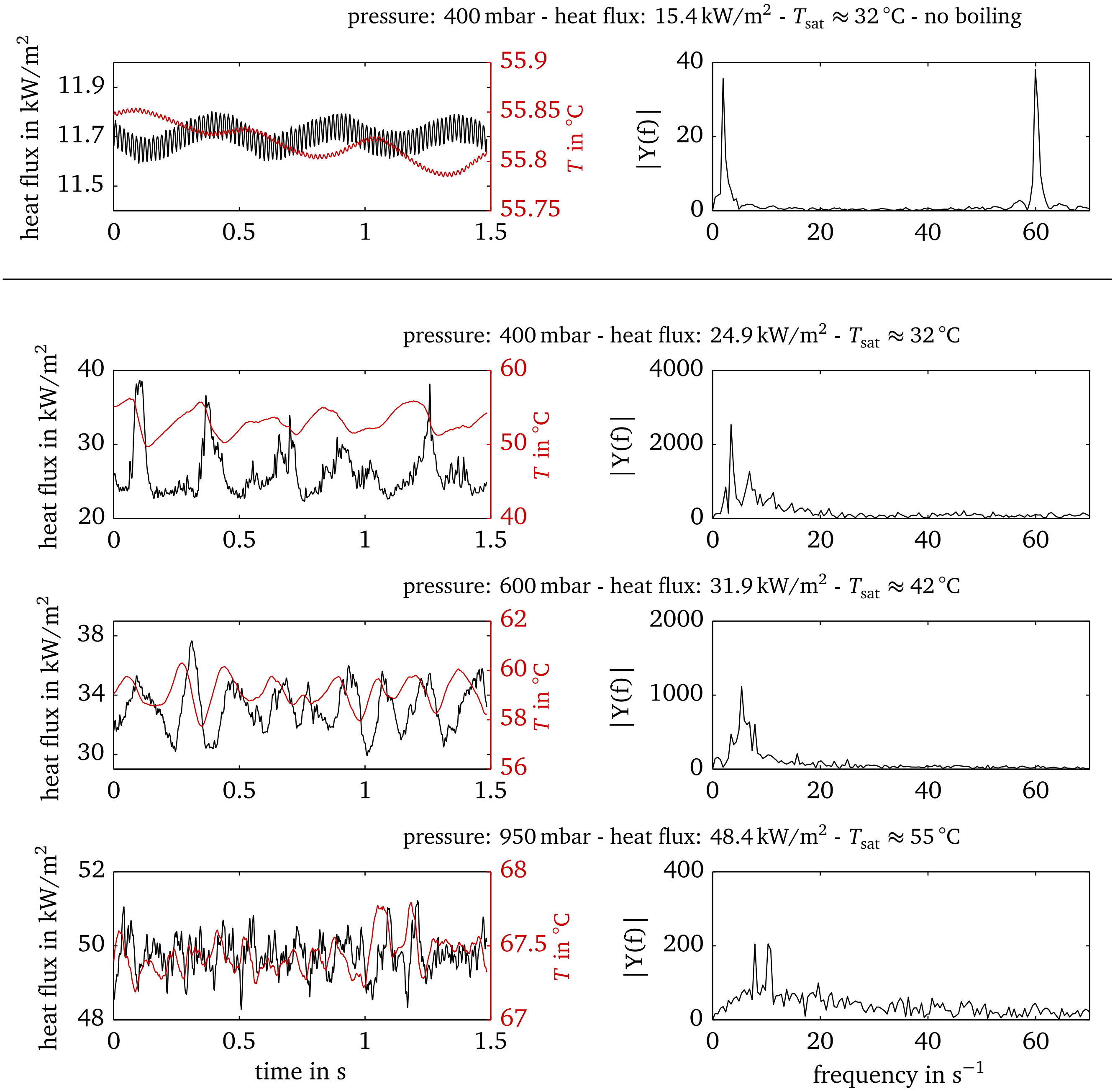

Figure 5.38: Heat flux oscillation for boiling experiments on a structured foil - S = 600 µm

a short period of time. For a subsequent nucleation a higher heat flux is observed. For the structured foils a nucleation at an arbitrary position leads to a nucleation at a neighboring cavity. This process continues until the temperature of the whole foil is decreased and the nucleation of further bubbles declines. Afterwards, the foil heats up leading to the shown oscillation. For higher pressures and heat fluxes the heat transfer becomes more uniform and the described phenomena vanishes. In Fig. 5.39 and Fig. 5.40 this effect is shown by a series of heat flux profiles. At 48 ms (last picture in the second row) a bubble nucleates[1] followed by an increased heat flux and number of active cavities. Afterwards (second half of Fig. 5.39) the heat flux and the number of active cavities is reduced and the foil heats up again. Another bubble initiates a further increase in heat flux and number of active cavities (first picture in the fifth row of Fig. 5.40). In addition it can be observed that after an initial nucleation several bubbles nucleate quite close to or even on an existing contact line.

5.2.3 Bubble interactions on a single embedded wire

In the previous section it is shown that the distance between the cavities can affect the heat transfer performance. Therefore in this section the interdependence of the bubble's size and nucleation site distance within a boiling process without artificial cavities is discussed. As the observation of such processes is not possible with the used planar heater a different test setup is used. In Fig. 5.41 the test facility is shown. The test cell ① is sintered out of stainless steel and provides connections for temperature ② and pressure measurement ③. During the sintering process internal channels ⑤ are integrated for the temperature control of the test cell. The heater ⑥ is implemented in the cell and consists of a constantan wire ⑧ with a diameter of 0.6 mm casted in epoxy resin ⑨. The wire is electrically connected by copper rods ⑦. The top side of the heater is grinded to enable a direct contact of the constantan wire with the working fluid on a width of 0.25 mm. Further information about this test facility can be found in [118]. Due to the higher thermal heat resistance of the casting compound and the small area where the constantan wire is in contact with the working fluid the bubbles nucleate mainly in a single row. Therefore, the observation of bubble diameter and nucleation site distance is possible. Experiments are performed with FC-72 as working fluid in a pressure range of 0.4 bar to 1.9 bar. In this setup the heat flux could not be measured. Therefore the electrical load is varied to perform experiments from the onset of nucleate boiling up to the critical heat flux. An automatic evaluation of the bubble departure diameter is not possible due to the huge number of bubbles. Therefore the diameter is calculated by a mean average of the bubble height and width at departure.

In Fig. 5.42 the bubble departure diameter is plotted over pressure and compared to the FRITZ equation (Eq. 2.4). As expected the bubble departure diameter decreases with increasing pressure. Furthermore, the characteristic qualitative bad agreement with the FRITZ equation can be seen for lower pressures. For higher pressures the FRITZ equation represents the measurement data well comparable to Fig. 5.2. This indicates that the dynamic effects discussed in section 5.1 influence the bubble departure diameter in this pressure range. In Fig. 5.43 the nucleation site distance is plotted over pressure. A similar profile as in Fig. 5.42 can be seen. For comparison in Fig. 5.44 the nucleation distance is plotted over the bubble departure diameter. Each asterisk represents an averaged value for all measurements performed at a single pressure value. The results show a linear dependency of the nucleation site distance S on the bubble departure diameter d_b

$$S = 1.396\, d_\mathrm{b} - 0.370\,\mathrm{mm}. \tag{5.6}$$

---

[1] This is indicated by the high heat flux.

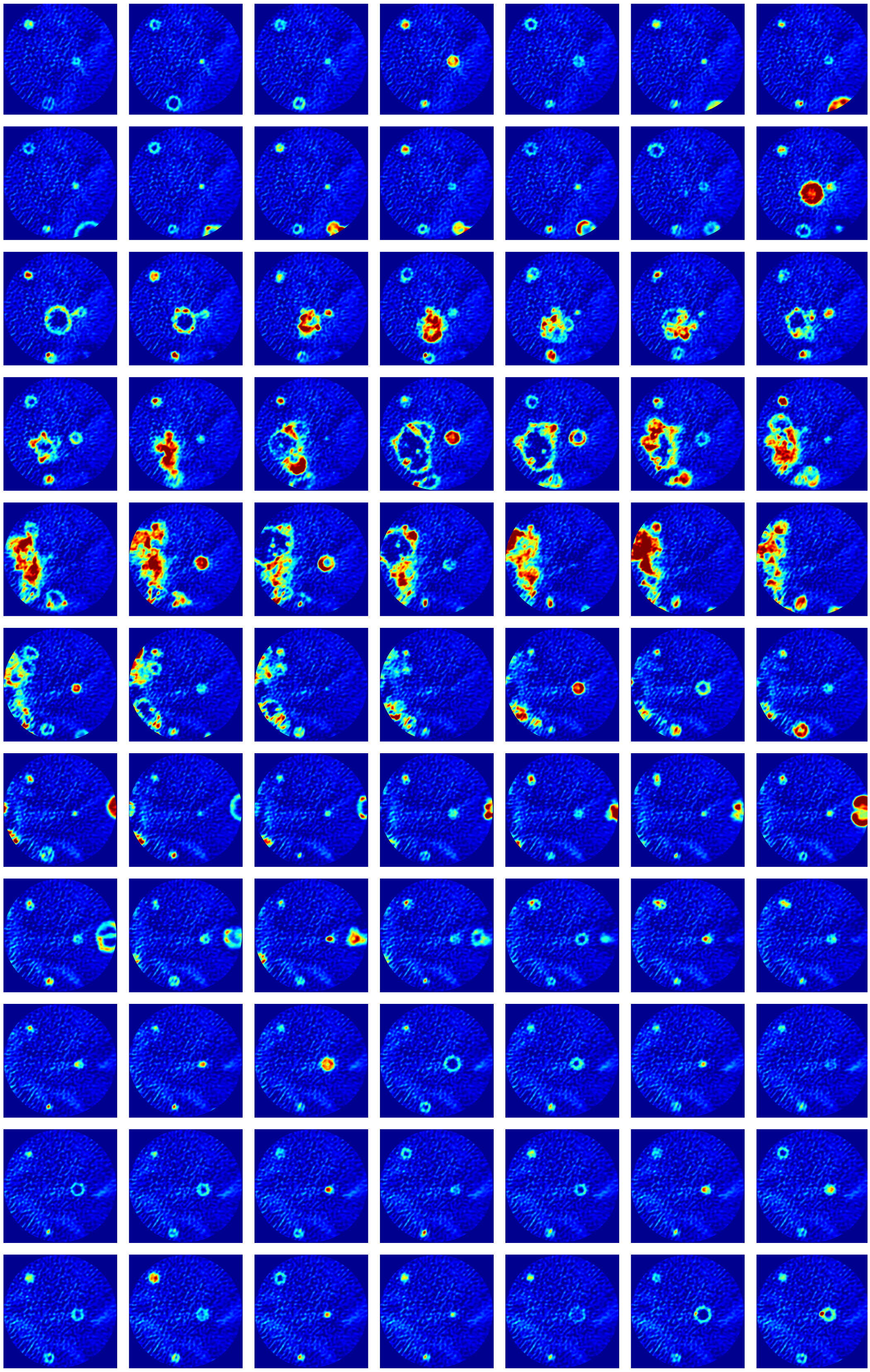

Figure 5.39: Heat flux oscillation - S = 600 µm; p = 400 mbar; q = 14 kW/m^2; time increment = 4 ms/picture

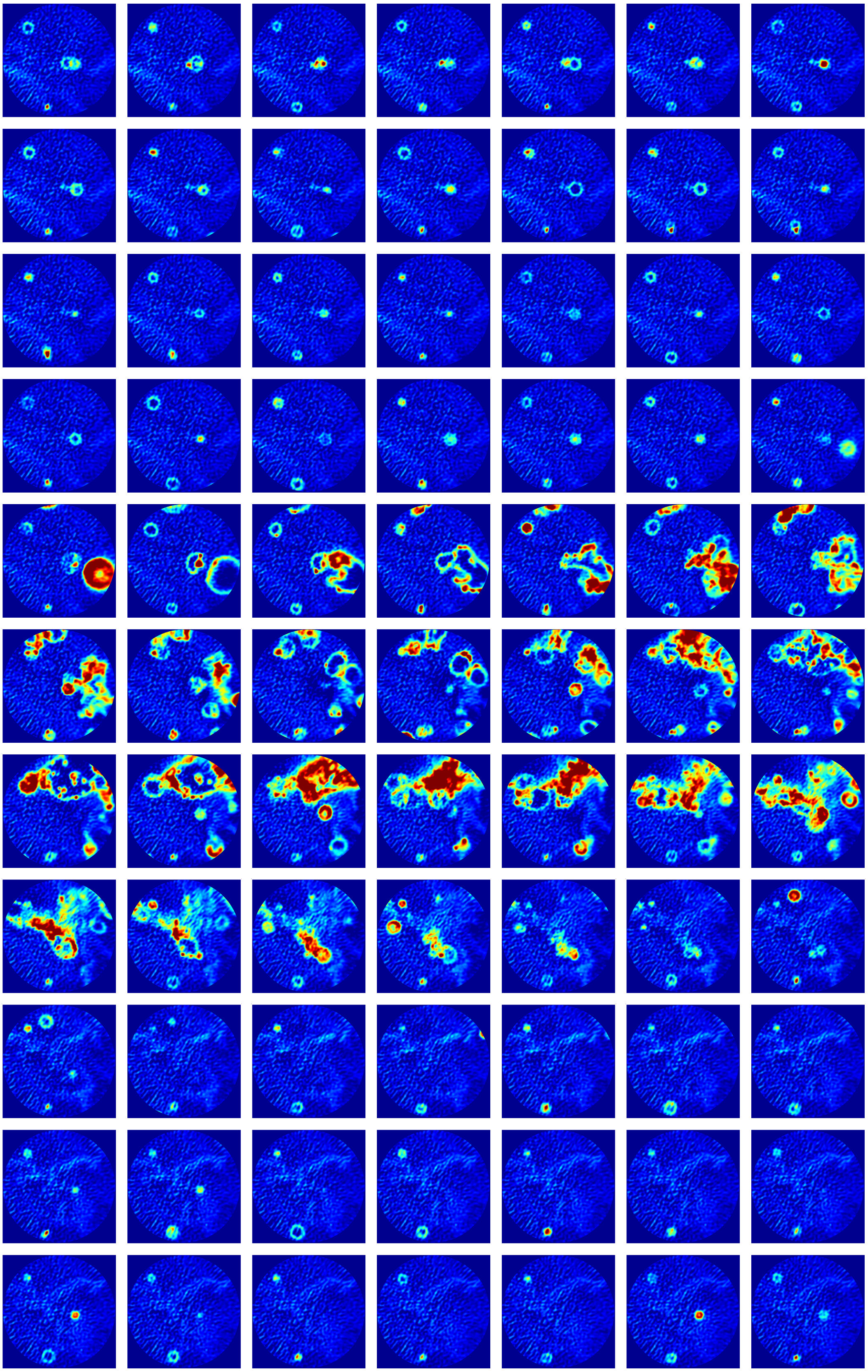

Figure 5.40: Heat flux oscillation (continued) - S = 600 µm; p = 400 mbar; q = 14 kW/m^2; time increment = 4 ms/picture

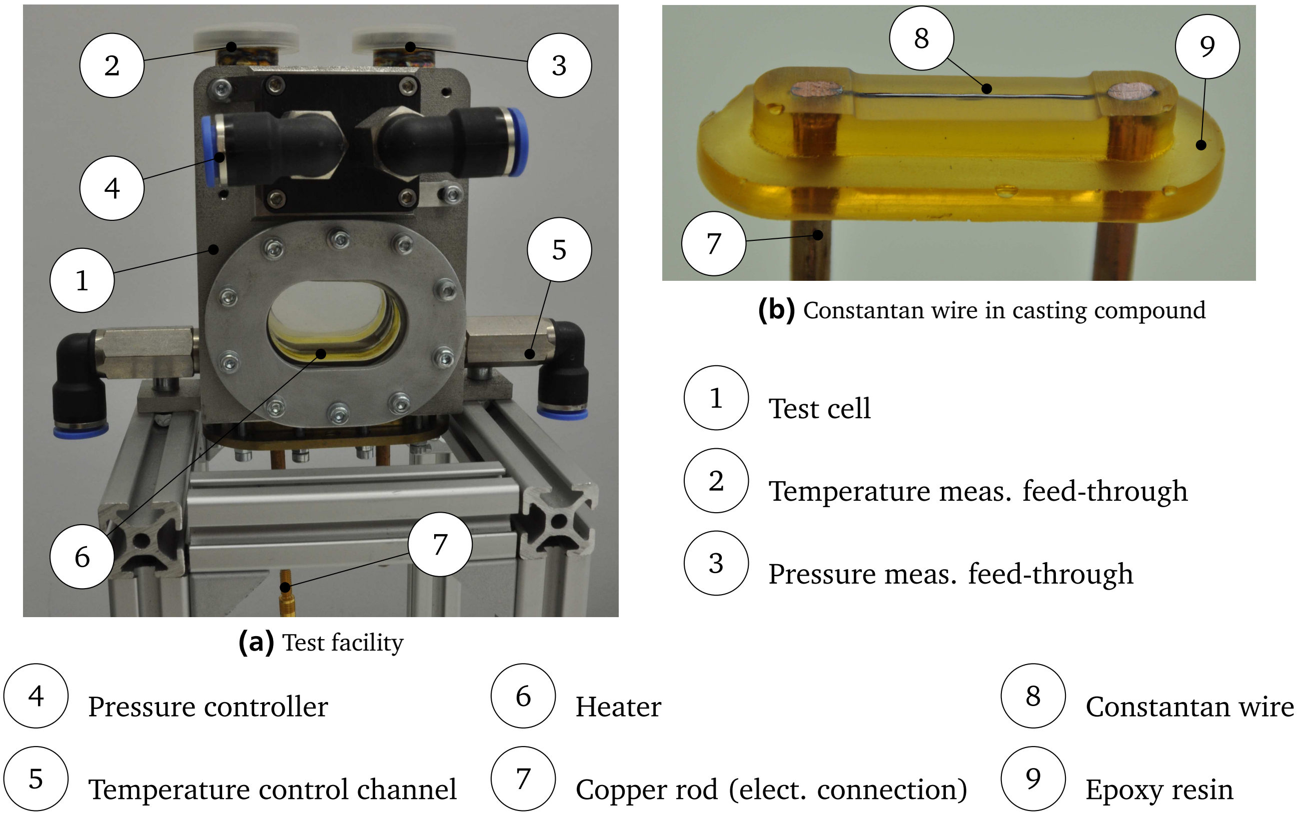

(a) Test facility

(b) Constantan wire in casting compound

Figure 5.41: Test cell for boiling on a single embedded wire

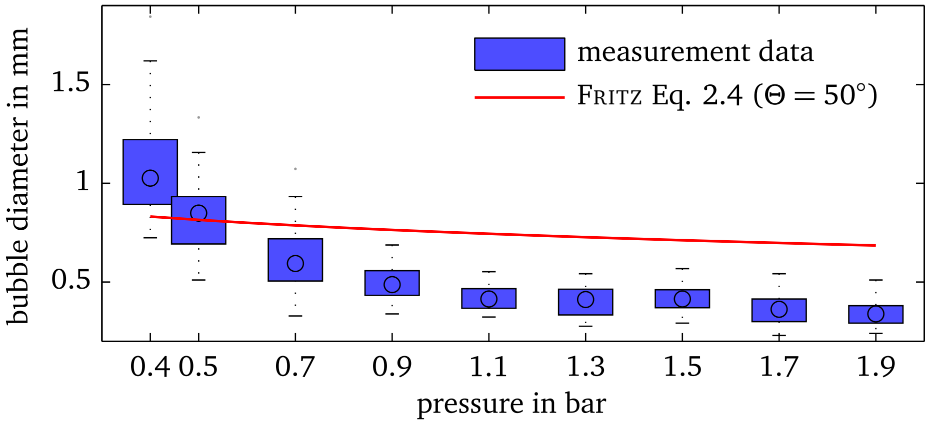

Figure 5.42: Influence of pressure on the bubble departure diameter for boiling on an embedded wire

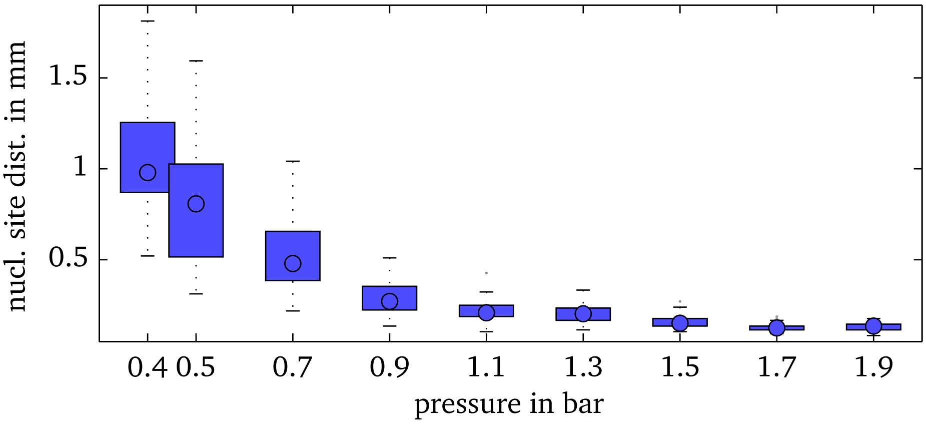

Figure 5.43: Influence of pressure on the nucleation site distance for boiling on an embedded wire

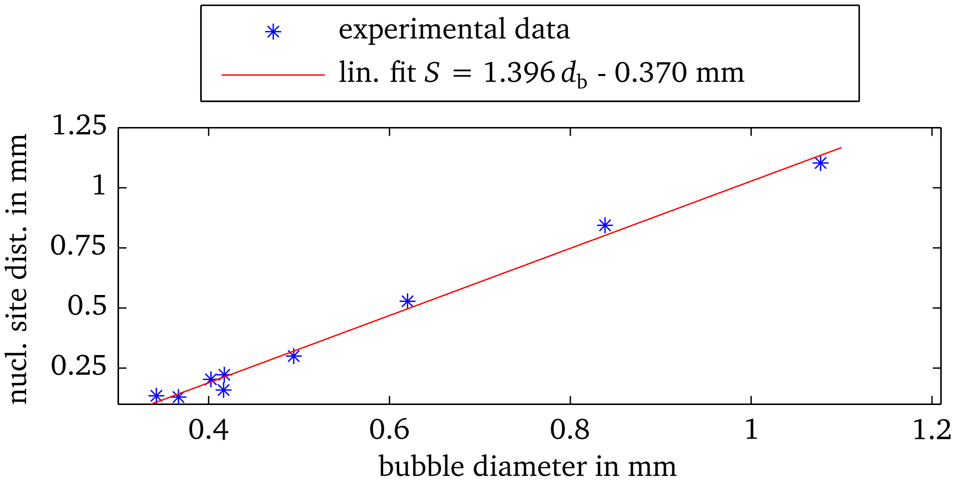

Figure 5.44: Interdependence of the bubble departure diameter and the nucleation site distance

Neglecting the axis intercept the dependency indicates that within this experiment nucleation is hindered for a spacing parameter of $S_{sp} < 1.4$. This is caused by the interaction of a nucleation site with a neighboring bubble.

5.3 Concluding remarks of the experimental results

Three conclusions can be drawn based on all experimental results presented in this thesis. The first one concerns the dynamic effects affecting the departure diameter of a bubble, the second one the influences on bubble nucleation by the interaction with another bubble, and the third one the possible enhancement in technical boiling processes by surface treatment focusing on an enhanced number of bubble coalescences.

The results of this thesis (see Fig. 5.2 and Fig. 5.42) as well as results from literature (e.g. [27]) have shown a unsatisfactory qualitative agreement between the equation for the calculation of the bubble diameter (e.g. Eq. 2.4) and the experimental results for lower pressures. The results obtained in section 5.1 can give an explanation for this unsatisfactory qualitative agreement. It is shown that the transition from contact line to microlayer evaporation is accompanied by an increase in the interface velocity of the bubble. As the equations (e.g. by FRITZ Eq. 2.4 and SCHWEIZER Eq. 2.25) are based on a static force balance they cannot reproduce the highly dynamic processes of microlayer evaporation. In the following an estimation of the influence of microlayer evaporation is presented. It should be noted that the presented estimation is not suitable for a calculation of a bubble departure diameter. It rather should give an impression of the different characteristics obtained by application of the different approaches. As can be seen in Fig. 5.14 and Fig. 5.16, no significant increase in the size of the bubble can be observed after the microlayer has evaporated. Therefore, assuming that in this case the whole amount of vapor is generated by evaporation from the microlayer, the volume of the bubble can be calculated. Following this assumption the mass M_{ml} of the liquid in the microlayer is converted to the mass M_{v} of the vapor inside the bubble during microlayer evaporation

$$M_{\mathrm{v}} = \frac{4}{3}\pi\,(d_{\mathrm{eq}}/2)^3\,\rho_{\mathrm{v}} = \delta_{\mathrm{ml}}\,\pi\frac{(d_{\mathrm{eq}}/2)^2\,\sin^2\Theta}{U_{\mathrm{eq,ap}}^2}\rho_{\mathrm{l}} = M_{\mathrm{ml}} \tag{5.7}$$

with

$$U_{\mathrm{eq,ap}} = \frac{d_{\mathrm{eq}}}{d_{\mathrm{ap}}} = \sqrt[3]{0.5 + 0.75\,\cos\Theta - 0.25\,\cos^3\Theta}. \tag{5.8}$$

This leads to

$$d_{\mathrm{eq}} = \frac{3}{2}\frac{\delta_{\mathrm{ml}}\,\sin^2\Theta}{U_{\mathrm{eq,ap}}^2}\frac{\rho_{\mathrm{l}}}{\rho_{\mathrm{v}}}, \tag{5.9}$$

where $U_{\mathrm{eq,ap}}$ defines the conversion factor from the apparent to the equivalent diameter.

For the calculation a spherical segment is assumed. In Fig. 5.45 the calculated bubble departure diameter is shown for Eq. 5.9 and compared to Eq. 2.4 (FRITZ). The experimental results from the single bubble experiments (cf. section 5.1) and the experiments on the embedded wire (cf. section 5.2.3) are shown. For Eq. 5.9 a contact angle of $\Theta = 60°$ and a microlayer thickness of 3 µm is assumed. For the FRITZ equation a contact angle of $\Theta = 30°$ is used to compensate the overestimation discussed in section 5.1. It can be seen that for lower pressures the profile of Eq. 5.9 fits the experimental data qualitatively better than the FRITZ equation. A change in contact angle and microlayer thickness is equivalent to a multiplication with a constant factor and therefore has no influence on the general profile of the curves. It is worth underlining again that the given equation cannot be used for a general calculation of the bubble departure diameter. This can easily be seen as for example no influence of gravity is included. Also, even if not the whole amount of vapor is generated by the evaporation of the microlayer the highly dynamic processes in the growing phase of the bubble can cause the increase in the bubble departure diameter. In this area further research is required.

It can be seen in Fig. 5.45 that the bubble departure diameter for the single bubble experiment is larger than for the experiment on the embedded wire. The deviation is increasing with decreasing pressure. A possible explanation is the thermal and hydrodynamic interaction between the bubbles nucleated on the embedded wire (cf. section 2.3.1) compared to the single bubble experiments. As for a single bubble experiment the surface next to the artificial cavity is prepared in a way to prevent nucleation, a higher temperature and/or larger dimension of the superheated layer can be assumed at this position. Compared to a boiling process with several bubbles nucleating next to each other this may lead to larger bubbles due to an enhanced evaporation at the liquid-vapor interface. The same interactions might be a reason for the contradiction between the results presented in Figs. 5.39, 5.40, and 5.44. Whereas for the experiments with multiple artificial cavities a promoting effect on nucleation could be observed by

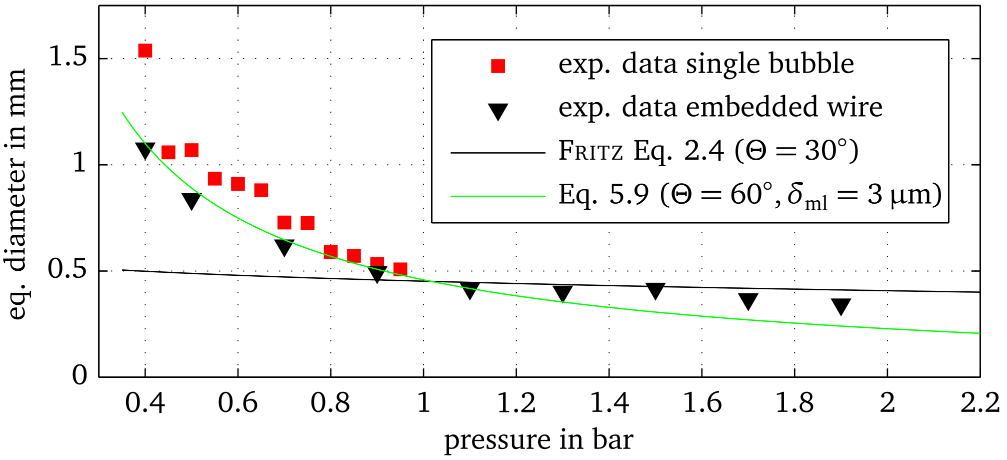

Figure 5.45: Bubble departure diameter - Equation for microlayer evaporation

the presence of another liquid-vapor interface, for experiments on the embedded wire the existence of a bubble prevented another one from nucleation. In section 5.1 it was shown that a cavity where no boiling occurs follows some kind of hysteresis. Therefore, the presence of a contact line close by can help to overcome this hysteresis. In contrast, for a stable boiling process at a cavity the reduction of temperature by the neighboring bubble may have a hindering effect. Nevertheless, due to the number of influencing factors (like heat flux, material properties, different required superheat, etc.) the reasons leading to the described phenomena cannot be verified.

An enhancement of the heat transfer coefficient in a technical boiling process by a surface treatment aiming at the enhancement of coalescence probability could not be observed. This kind of surface treatment as used in section 5.2.2 is based on specific cavities having a lower necessary superheat than the areas in between. Considering that no significant enhancement could be observed concerning coalescence processes, a surface treatment aiming at a uniform low necessary superheat seems to be more reasonable in the opinion of the author.

CHAPTER 6

Summary and Conclusion

Nucleate boiling is one of the oldest technical processes. Thanks to constant improvements, boiling processes are found in a lot of industrial and private applications. Despite the large number of investigations the underlying physical principles of boiling processes are still not sufficiently understood. The existing correlations for the design and construction of boiling equipment are, almost exclusively, empirically based. Therefore, a prediction of boiling processes for novel fluids, geometries, or system parameters is not sufficiently possible. In order to improve the understanding of the physical phenomena highly resolved experiments with a single or a few interacting bubbles need to be conducted. Together with numerical simulations and boiling research on technical length scale this might lead to a better predictability and an enhancement in efficiency.

Within this thesis experimental research is performed for nucleate pool boiling on a horizontal, flat plate for a single and interacting bubbles. In addition, the validity of the results obtained for the bubble coalescence of two bubbles is investigated on a technical length scale. A test setup is designed and fabricated for measurements of boiling processes on a 20 μm thick stainless steel foil. The simultaneous observation of the bubble's shape and the temperature profile on the backside of the thin foil are achieved by high-speed infrared and black/white cameras. The used foils are heated by Joule heating and the artificial cavities are produced by laser surface treatment. All experiments are performed using FC-72 as working fluid. Attention is paid especially to the reliability of the test setup as well as the data evaluation. Especially the accuracy of the temperature measurement using an infrared camera and the subsequent calculation of the heat flux from the foil to the fluid are considered. Thereby it is shown that the infrared measurement technique offers the most accurate method for measurements within the necessary high temporal and spatial resolution. Nevertheless, it is shown that especially the calculation of the heat flux is quite sensitive to the made assumptions and calculation methods. Therefore, a quantitative comparison is only possible for measurements performed under exactly the same conditions and using the equivalent evaluation method. The influence of the surface treatment on the calculated heat flux is also investigated. A non-homogeneous heating is found. This effect is neglected in the further evaluation due to the limited area of influence and the unknown exact position as well as structure of the cavity. Furthermore, the magnitude of the heat flux deviation by a structured surface compared to the influences on the heat flux profile by the boiling process itself is small.

For the single bubble experiments the bubble departure diameter and frequency are evaluated for varying pressure and heat flux. The heat flux is adapted to the individual pressures to ensure boiling at a single cavity. The necessary heat flux for the nucleation of a single bubble is decreasing with increasing pressure. The bubble departure diameter is decreasing with increasing pressure. The departure diameter is slightly increased for a higher heat flux. The bubble frequency is less affected by a change in pressure. A moderate increase with increasing pressure and heat flux can be observed. A closer analysis of the bubble cycle gives evidence that this increase can be mainly attributed to an increase in the waiting time. An explicit dependency of the heat flux on bubble departure diameter or frequency cannot be detected. Rather, both are affected by a change in heat flux. The decrease of the necessary superheat for nucleation predicted by the literature is validated experimentally. Further, differences in the development of individual bubbles are observed. Bubbles nucleated after a longer waiting time generally have a higher interface velocity at nucleation and achieve a larger departure diameter. Regarding the heat flux profiles for these bubbles an increase in the transferred heat and a circular-shaped filled area of high heat flux is observed after nucleation. These results point to microlayer evaporation. For bubbles nucleated without a previous waiting time a ring-shaped heat flux profile is observed indicating contact line evaporation. By combining these results with the experimental observations published in literature a first step for a combination of the so far rather competitively discussed models is achieved. In addition, a possible explanation for the deviation of the bubble departure diameter to common equations based on a static force model, especially for low pressures, is presented. Within these experiments an oscillation in the transferred heat is also observed. The frequency and amplitude of the oscillation is decreasing with increasing pressure.

For bubble coalescence experiments different foils with a cavity spacing of 300 µm and 500 µm are used. The cavities are produced with the same surface treatment used for the single cavity. Using the 500 µm foil a probability distribution for the horizontal coalescence frequency is observed over pressure. By application of a Monte-Carlo simulation the bubble coalescence frequency is simulated over larger ranges of pressures and cavity distances. The results of the simulation have a similar probability distribution and fit the experimental data qualitatively well. For a smaller cavity distance the maximum coalescence frequency occurs at a higher pressure. This result is validated by the simulation and theoretical analysis. Further, the coalescence frequency is increased with increasing heat flux, which is mainly attributed to a general increase in bubble frequency. For bubble coalescence an increase in heat flux can be observed. A possible reason for this behavior is the increased contact line velocity and a possible remaining droplet (for smaller pressures) which is observed in the experiment. An increase of approximately 10 % in heat flux seems feasible to the author. Due to a simultaneous decrease in superheat ($\approx 2\,^\circ$C) an increase in the heat transfer coefficient of 20 % - 30 % results.

In order to verify whether the increasing effect of coalescence on heat transfer can be observed for experiments with structured foils containing multiple artificial cavities, measurements are performed with a cavity spacing of 500 µm and 600 µm and compared to an unstructured reference foil. Within these experiments no significant influence of possible coalescence is observed. In general an increase in the heat transfer coefficient by structured foils can be seen in accordance with the literature. For the heat transfer coefficient the well-known increase is observed with increasing pressure and heat flux. In a comparison between both structured foils it is found that the heat transfer is hindered by fixing the nucleation sites to the artificial cavities. A reason for this is given by adapting the previously used Monte-Carlo simulation to boiling on a structured surface. It can be seen that the coalescence frequency does not have a maximum for a specific pressure. In contrast, the coalescence frequency is increased with decreasing cavity spacing and pressure. This is caused by the possibility of coalescence of bubbles nucleated at cavities with a larger distance. Furthermore, the very high calculated coalescence frequencies show a clear limit to this simulation resulting from the used assumptions. Nevertheless, the obtained results give a good impression of possible coalescence phenomena. Furthermore, oscillations in heat transfer could be observed. It is found that bubble nucleation can be promoted in the presence of another liquid-vapor interface. This effect spreads over the whole surface followed by an increase in foil temperature with less boiling. Through arbitrary nucleation the process starts again. For the experiments on the structured foils an oscillation in heat flux is observed similar to the experiments for single bubbles. In contrast to the single bubble experiments where this effect is related to a hysteresis herein, this effect is mainly attributed to a nucleation initiated by the nucleation of a bubble close by.

For a further analysis of these phenomena an additional experiment is performed on a single embedded wire. It is shown that there is a linear relationship between the nucleation site distance and the bubble diameter. For a spacing parameter $S_{sp} < 1.4$ nucleation is hindered by the interaction of the nucleation site with a neighboring bubble. Therefore it can be concluded that a surface treatment aiming at the enhancement of coalescence probability is less efficient than a surface with a comparable surface treatment over its entire area.

Concerning the results presented in this thesis several possibilities for further research can be mentioned. Experimental investigations of a wider range of properties and system parameters are desirable. Aside from experiments on a technical length scale almost all fundamental experiments are performed with water or refrigerants (mostly FC-72). As these fluids have one of the lowest (refrigerant) and highest (water) heat of evaporation several effects might be covered up to now. The huge number of influencing factors make a comparison of different results even more difficult if the experiments are performed under different measurement setups. Alongside pure substances the investigation of mixtures and suspensions offers a wide field for further investigation motivated by their current application in technical processes. The experimental observation of single phenomena observed in boiling processes should be performed further, due to the opportunity provided by complex systems. For example the evaporation of a liquid layer at a defined interface velocity as performed by IBRAHEM [69] seems to be reasonable for a more detailed differentiation of the single phenomena. Such dependencies cannot be investigated in nucleate boiling as the interface velocity cannot be set but is dependent on several system and fluid properties. Another promising possibility is the investigation of the transition from contact-line-based to microlayer-based evaporation. It has great potential for a deeper understanding of pool boiling processes. Within this thesis it has been shown that the velocity of the interface is an influencing factor. It has to be assumed that further influencing factors exist, like heat of evaporation, surface tension, viscosity, and contact angle. The mentioned interface velocity itself is not a primarily factor but a result of the fluid/material properties and system conditions. As an individual investigation of these properties is not possible in experimental research, numerical simulation represents a huge opportunity. Through principle-based results within this topic, flow boiling investigations could also profit as similar phenomena like advancing and receding contact lines occur in these processes.

Bibliography

[1] Abarajith, H. S., Dhir, V. K., Warrier, G., and Son, G., Numerical Simulation and Experimental Validation of the Dynamics of Multiple Bubble Merger During Pool Boiling Under Microgravity Conditions, *Annals of the New York Academy of Sciences*, 1027(1):235–258, 2004.

[2] Agarwal, D. K., Welch, S. W. J., Biswas, G., and Durst, F., Planar Simulation of Bubble Growth in Film Boiling in Near-Critical Water Using a Variant of the VOF Method, *Journal of Heat Transfer*, 126(3):329–338, 2004.

[3] Aktinol, E. and Dhir, V., Numerical Simulation of Nucleate Boiling Phenomenon Coupled with Thermal Response of the Solid, *Microgravity Science and Technology*, 24(4):255–265, 2012.

[4] Arlabosse, P., Tadrist, L., Tadrist, H., and Pantaloni, J., Experimental analysis of the heat transfer induced by thermocapillary convection around a bubble, *Journal of Heat Transfer*, 122(1):66–73, 2000.

[5] Auracher, H. and Buchholz, M., Experiments on the fundamental mechanisms of boiling heat transfer, *Journal of the Brazilian Society of Mechanical Sciences and Engineering*, 27(1), 2005.

[6] Auracher, H. and Marquardt, W., Experimental studies of boiling mechanisms in all boiling regimes under steady-state and transient conditions, *International Journal of Thermal Sciences*, 41(7):586 – 598, 2002.

[7] Bae, S., Kim, M., and Kim, J., Improved technique to measure time- and space-resolved heat transfer under single bubbles during saturated pool boiling of FC-72, *Experimental Heat Transfer*, 12(3):265–278, 1999.

[8] Barthes, M., Reynard, C., Santini, R., and Tadrist, L., Experimental Study of a Single Vapour Bubble Growth: Heat and Mass Transfer Analysis - Influence of Non-condensable Presence on the Onset of Marangoni Convection, in *Annals of the Assembly for International Heat Transfer Conference 13*, Sydney, Australia, 2006.

[9] Bayazit, B. B., Hollingsworth, D. K., and Witte, L. C., Heat Transfer Enhancement Caused by Sliding Bubbles, *Journal of Heat Transfer*, 125(3):503, 2003.

[10] Blum, J., Marquardt, W., and Auracher, H., Stability of boiling systems, *International Journal of Heat and Mass Transfer*, 39(14):3021–3033, 1996.

[11] Bonjour, J., Clausse, M., and Lallemand, M., Experimental study of the coalescence phenomenon during nucleate pool boiling, *Experimental Thermal and Fluid Science*, 20(3-4):180–187, 2000.

[12] Bowring, R., *Physical Model, Based on Bubble Detachment, and Calculation of Steam Voidage in the Subcooled Region of a Heated Channel*, HPR / OECD Halden Reactor Project, Institutt for Atomenergi, OECD Halden Reactor Project, 1962.

[13] Bronstein, I. N. and Semendjajew, K. A., *Taschenbuch der Mathematik*, pp. 944–945, Deutsch, Thun [u.a.], 2001, ISBN 3817120052.

[14] Buchholz, M. and Auracher, H., Improved optical probes and their validation for local measurements in two phase flows, in *Proceedings of the German-Japanese Workshop on Multi-Phase Flow*, Karlsruhe, Germany, 2002.

[15] Buchholz, M., Auracher, H., Lüttich, T., and Marquardt, W., A study of local heat transfer mechanisms along the entire boiling curve by means of microsensors, *International Journal of Thermal Sciences*, 45(3):269–283, 2006.

[16] Calka, A. and Judd, R. L., Some aspects of the interaction among nucleation sites during saturated nucleate boiling, *International Journal of Heat and Mass Transfer*, 28(12):2331–2342, 1985.

[17] Carey, V. P., *Liquid-vapor phase-change phenomena: An introduction to the thermophysics of vaporization and condensation processes in heat transfer equipment*, Taylor and Francis, New York, 2nd edn., 2008, ISBN 1591690358.

[18] Carey, V. P., Molecular-level modeling of interfacial phenomena in boiling processes, in *Proceeding of the 8th International Conference on Boiling and Condensation Heat Transfer*, Lausanne, Switzerland, 2012.

[19] Carey, V. P., Conversation at ECI 8th International Conference on Boiling and Condensation Heat Transfer, 6th June 2012.

[20] Çengel, Y. A. and Ghajar, A. J., *Heat and mass transfer: Fundamentals & applications*, McGraw-Hill, New York, 4th edn., 2011, ISBN 0077366646.

[21] Chamarthy, P., Dhavaleswarapu, H. K., Garimella, S. V., Murthy, J. Y., and Wereley, S. T., Visualization of convection patterns near an evaporating meniscus using µPIV, *Experiments in Fluids*, 44(3):431–438, 2008.

[22] Chatpun, S., Watanabe, M., and Shoji, M., Experimental study on characteristics of nucleate pool boiling by the effects of cavity arrangement, *Experimental Thermal and Fluid Science*, 29(1):33–40, 2004.

[23] Chatpun, S., Watanabe, M., and Shoji, M., Nucleation site interaction in pool nucleate boiling on a heated surface with triple artificial cavities, *International Journal of Heat and Mass Transfer*, 47(14-16):3583–3587, 2004.

[24] Chekanov, V. V., Interactions of centers in nucleate boiling, *Teplofizika Vysokikh Temperatur*, 15:121–128, 1977.

[25] Chen, T. and Chung, J., Coalescence of bubbles in nucleate boiling on microheaters, *International Journal of Heat and Mass Transfer*, 45(11):2329–2341, 2002.

[26] Chen, T. and Chung, J. N., Heat-transfer effects of coalescence of bubbles from various site distributions, *Proceedings of the Royal Society A: Mathematical, Physical and Engineering Sciences*, 459(2038):2497–2527, 2003.

[27] Cole, R., Bubble frequencies and departure volumes at subatmospheric pressures, *AIChE Journal*, 13(4):779–783, 1967.

[28] Cole, R. and Shulman, H., Bubble departure diameter at subatmospheric pressures, *Chemical Engineering Progresses Symposium Series*, 62:6–16, 1966.

[29] Cooper, M. and Lloyd, A., The microlayer in nucleate pool boiling, *International Journal of Heat and Mass Transfer*, 12(8):895–913, 1969.

[30] Delgoshaei, P. and Kim, J., Microscale heat transfer measurements during subcooled pool boiling of pentane: Effect of bubble dynamics, in *Proceedings of the 14th International Heat Transfer Conference*, Washington D.C., USA, 2010.

[31] Demiray, F. and Kim, J., Microscale heat transfer measurements during pool boiling of FC-72: effect of subcooling, *International Journal of Heat and Mass Transfer*, 47(14-16):3257–3268, 2004.

[32] Dhavaleswarapu, H. K., Chamarthy, P., Garimella, S. V., and Murthy, J. Y., Experimental investigation of steady buoyant-thermocapillary convection near an evaporating meniscus, *Physics of Fluids*, 19(8):082103, 2007.

[33] Dhavaleswarapu, H. K., Garimella, S. V., and Murthy, J. Y., Microscale Temperature Measurements Near the Triple Line of an Evaporating Thin Liquid Film, *Journal of Heat Transfer*, 131(6):061501, 2009.

[34] Dhir, V. K., Simulation of boiling - How far we have come!, in *Proceeding of the ECI International Conference on Boiling Heat Transfer*, Florianopolis, Brazil, 2009.

[35] Duan, X., Philips, B., McKrell, T., and Buongiorno, J., Synchronized high-speed video, infrared thermometry and PIV data for validation of interface-tracking simulations of nucleate boiling phenomena, in *Proceeding of the 8th International Conference on Boiling and Condensation Heat Transfer*, Lausanne, Switzerland, 2012.

[36] Eddington, R., Kenning, D., and Korneichev, A., Comparison of gas and vapour bubble nucleation on a brass surface in water, *International Journal of Heat and Mass Transfer*, 21(7):855–862, 1978.

[37] Esmaeeli, A. and Tryggvason, G., A front tracking method for computations of boiling in complex geometries, *International Journal of Multiphase Flow*, 30(7-8):1037–1050, 2004.

[38] Europäisches Parlament, Richtlinie {2006/40/EG} des europäischen Parlaments und des Rates über Emissionen aus Klimaanlagen in Kraftfahrzeugen und zur Änderung der Richtlinie {70/156/EWG} des Rates.

[39] Fischer, S., Herbert, S., Sielaff, A., Slomski, E. M., Stephan, P., and Oechsner, M., Experimental Investigation of Nucleate Boiling on a Thermal Capacitive Heater Under Variable Gravity Conditions, *Microgravity Science and Technology*, 24(3):139–146, 2012.

[40] Forster, H. K. and Zuber, N., Dynamics of vapor bubbles and boiling heat transfer, *AIChE Journal*, 1(4):531–535, 1955.

[41] Fournier, J. A., Phan, C. L., and Bohn, R. K., Microwave spectroscopy and characterization of the helical conformer of perfluorohexane, *ARKIVOC Journal*, pp. 5–11, 2011.

[42] Fritz, W., Berechnung des Maximalvolumens von Dampfblasen, *Physikalischen Zeitschrift*, 36(11):379–384, 1935.

[43] Fuchs, T., Kern, J., and Stephan, P., A Transient Nucleate Boiling Model Including Microscale Effects and Wall Heat Transfer, *Journal of Heat Transfer*, 128(12):1257–1265, 2006.

[44] Gerardi, C., Buongiorno, J., Hu, L.-w., and McKrell, T., Measurement of nucleation site density, bubble departure diameter and frequency in pool boiling of water using high-speed infrarad and optical cameras, in *Proceeding of the ECI Interantional Conference on Boiling Heat Transfer*, Florianopolis, Brazil, 2009.

[45] Gerardi, C., Buongiorno, J., Hu, L.-w., and McKrell, T., Study of bubble growth in water pool boiling through synchronized, infrared thermometry and high-speed video, *International Journal of Heat and Mass Transfer*, 53(19-20):4185–4192, 2010.

[46] Gjerkeš, H. and Golobič, I., Pool boiling CHF on a laser heated thin plate, *International Journal of Heat and Mass Transfer*, 43(11):1999–2008, 2000.

[47] Gjerkeš, H. and Golobič, I., Measurement of certain parameters influencing activity of nucleation sites in pool boiling, *Experimental Thermal and Fluid Science*, 25(7):487–493, 2002.

[48] Golobič, I. and Gjerkeš, H., Interactions between laser-activated nucleation sites in pool boiling, *International Journal of Heat and Mass Transfer*, 44(1):143–153, 2001.

[49] Golobič, I., Petkovsek, J., Baselj, M., Papez, A., and Kenning, D. B. R., Experimental determination of transient wall temperature distributions close to growing vapor bubbles, *Heat and Mass Transfer*, 45(7):857–866, 2009.

[50] Golobič, I., Petkovsek, J., Gjerkes, H., and Kenning, D., Horizontal chain coalescence of bubbles in saturated pool boiling on a thin foil, *International Journal of Heat and Mass Transfer*, 2011.

[51] Golobič, I., Petkovsek, J., and Kenning, D. B. R., Bubble growth and horizontal coalescence in saturated pool boiling on a titanium foil, investigated by high-speed IR thermography, *International Journal of Heat and Mass Transfer*, 55(4):1385–1402, 2012.

[52] Gorenflo, D., *VDI-Wärmeatlas*, p. Hab, Springer, Berlin and Heidelberg and New York, 2006, ISBN 3540255044.

[53] Gorenflo, D. and Kenning, D., *VDI Heat Atlas*, pp. 755–784, Springer, Berlin and Heidelberg, 2010, ISBN 3540778764.

[54] Han, C.-Y. and Griffith, P., The mechanism of heat transfer in nucleate pool boiling—Part I, *International Journal of Heat and Mass Transfer*, 8(6):887–904, 1965.

[55] Han, C.-Y. and Griffith, P., The mechanism of heat transfer in nucleate pool boiling—Part II, *International Journal of Heat and Mass Transfer*, 8(6):905–914, 1965.

[56] Hardt, S. and Wondra, F., Evaporation model for interfacial flows based on a continuum-field representation of the source terms, *Journal of Computational Physics*, 227(11):5871–5895, 2008.

[57] Heng, Y., Karalashvili, M., Mhamdi, A., and Marquardt, W., A multi-level adaptive solution strategy for 3D inverse problems in pool boiling, *International Journal of Numerical Methods for Heat & Fluid Flow*, 21(5):469–493, 2011.

[58] Heng, Y., Mhamdi, A., Gross, S., Reusken, A., Buchholz, M., Auracher, H., and Marquardt, W., Reconstruction of local heat fluxes in pool boiling experiments along the entire boiling curve from high resolution transient temperature measurements, *International Journal of Heat and Mass Transfer*, 51(21-22):5072–5087, 2008.

[59] Heng, Y., Mhamdi, A., and Marquardt, W., Efficient reconstruction of local heat fluxes in pool boiling experiments by goal-oriented adaptive mesh refinement, *Heat and Mass Transfer*, 46(10):1121–1135, 2010.

[60] Heng, Y., Mhamdi, A., Wagner, E., Stephan, P., and Marquardt, W., Identification of boiling heat fluxes in a single-bubble nucleate boiling experiment using a three-dimensional transient heat conduction model, *Journal of Physics: Conference Series*, 135:012051, 2008.

[61] Henry, C. D., Kim, J., Chamberlain, B., and Hartman, T. G., Heater size and heater aspect ratio effects on subcooled pool boiling heat transfer in low-g, *Experimental Thermal and Fluid Science*, 29(7):773–782, 2005.

[62] Hoffmann, J., *Taschenbuch der Messtechnik: Mit 62 Tabellen*, Fachbuchverl. Leipzig im Carl Hanser Verl., München, 4th edn., 2004, ISBN 3446228608.

[63] Hohl, R., Blum, J., Buchholz, M., Lüttich, T., Auracher, H., and Marquardt, W., Model-based experimental analysis of pool boiling heat transfer with controlled wall temperature transients, *International Journal of Heat and Mass Transfer*, 44(12):2225–2238, 2001.

[64] Höhmann, C., *Temperaturmessverfahren zur räumlich hochauflösenden Untersuchung des Wärmetransports an einem verdampfenden Flüssigkeitsmeniskus*, Ph.D. thesis, Institut für Technische Thermodynamik, Technische Universität Darmstadt, Darmstadt, Germany, 2004.

[65] Hsu, Y. Y., On the Size Range of Active Nucleation Cavities on a Heating Surface, *Journal of Heat Transfer*, 84(3):207, 1962.

[66] Hutter, C., Kenning, D., Sefiane, K., Karayiannis, T., Lin, H., Cummins, G., and Walton, A., Experimental pool boiling investigations of FC-72 on silicon with artificial cavities and integrated temperature microsensors, *Experimental Thermal and Fluid Science*, 34(4):422–433, 2010.

[67] Hutter, C., Sefiane, K., Karayiannis, T., Walton, A., Nelson, R., and Kenning, D., Nucleation site interaction between artificial cavities during nucleate pool boiling on silicon with integrated micro-heater and temperature micro-sensors, *International Journal of Heat and Mass Transfer*, 55(11-12):2769–2778, 2012.

[68] Ibrahem, K., Abd Rabbo, M., Gambaryan-Roisman, T., and Stephan, P., Experimental investigation of evaporative heat transfer characteristics at the 3-phase contact line, *Experimental Thermal and Fluid Science*, 34(8):1036–1041, 2010.

[69] Ibrahem, K., Abd Rabbo, M. F., Gambaryan-Roisman, T., and Stephan, P., Experimental Investigation of Micro-Scale Heat Transfer at an Evaporating Moving 3-Phase Contact Line, in *Proceedings of the 14th International Heat Transfer Conference*, pp. 783–790, Washington D.C., USA, 2010.

[70] Ibrahem, K., Rabbo, M. F. A., Gambaryan-Roisman, T., and Stephan, P., Experimental and numerical investigation of evaporative heat transfer in the vicinity of the 3-phase contact line, in *Proceedings of the 3rd International Conference on Thermal Issues in Emerging Technologies Theory and Applications (ThETA)*, pp. 207–215, Cairo, Egypt, 2010.

[71] Iida, Y. and Kobayasi, K., Distributions of Void Fraction above a Horizontal Heating Surface in Pool Boiling, *Bulletin of JSME*, 12(50):283–290, 1969.

[72] Israelachvili, J. N., *Intermolecular and surface forces*, Acad. Press, London [u.a.], 2nd edn., 1997, ISBN 0123751810.

[73] Jawurek, H., Simultaneous determination of microlayer geometry and bubble growth in nucleate boiling, *International Journal of Heat and Mass Transfer*, 12(8):843–848, 1969.

[74] Jiang, Y. Y., Osada, H., Inagaki, M., and Horinouchi, N., Wall Thermal Conductivity Effects on Nucleation Site Interaction During Boiling: An Experimental Study, in *Proceedings of the 14th International Heat Transfer Conference*, pp. 637–646, Washington D.C., USA, 2010.

[75] Jingliang, B., Xipeng, L., and Christopher, D. M., Effects of bubble coalescence dynamics on heat flux distributions under bubbles, *AIChE Journal*, 59(5):1735–1745, 2012.

[76] Jung, S. and Kim, H., Synchronized measurement of liquid-vapor phase and temperature distribution on a boiling surface during single nucleate boiling, in *Proceedings of the 8th International Conference on Multiphase Flow ICMF*, Jeju, Korea, 2013.

[77] Kenning, D., Wall temperature patterns in nucleate boiling, *International Journal of Heat and Mass Transfer*, 35(1):73–86, 1992.

[78] Kenning, D., Kono, T., and Wienecke, M., Investigation of boiling heat transfer by liquid crystal thermography, *Experimental Thermal and Fluid Science*, 25(5):219–229, 2001.

[79] Kenning, D. and Yan, Y., Pool boiling heat transfer on a thin plate: features revealed by liquid crystal thermography, *International Journal of Heat and Mass Transfer*, 39(15):3117–3137, 1996.

[80] Kenning, D. B. R. and Bustnes, O.-E., Liquid crystal studies of sliding vapour bubbles, *Heat and Mass Transfer*, 45(7):867–880, 2009.

[81] Kenning, D. B. R., Bustnes, O. E., and Yan, Y., Heat transfer to a sliding vapour bubble, *Multiphase Science and Technology*, 14(1):75–94, 2002.

[82] Kern, J., *Modellierung und numerische Berechnung des Wärmeübergangs beim Blasensieden binärer Gemische*, VDI-Verl., Düsseldorf, als ms. gedr. edn., 2002, ISBN 9783183727032.

[83] Kern, J. and Stephan, P., Investigation of Decisive Mixture Effects in Nucleate Boiling of Binary Mixtures Using a Theoretical Model, *Journal of Heat Transfer*, 125(6):1116–1122, 2003.

[84] Kern, J. and Stephan, P., Theoretical Model for Nucleate Boiling Heat and Mass Transfer of Binary Mixtures, *Journal of Heat Transfer*, 125(6):1106–1115, 2003.

[85] Kim, H. and Buongiorno, J., Detection of liquid–vapor–solid triple contact line in two-phase heat transfer phenomena using high-speed infrared thermometry, *International Journal of Multiphase Flow*, 37(2):166–172, 2011.

[86] Kim, H. and Buongiorno, J., Development of an Infrared-based visualization technique to study phase dynamics on boiling surfaces, in *Proceedings of the 4th International Conference on Heat Transfer and Fluid Flow in Microscale*, Fukuoka, Japan, 2011.

[87] Kim, J., Review of nucleate pool boiling bubble heat transfer mechanisms, *International Journal of Multiphase Flow*, 35(12):1067–1076, 2009.

[88] Koffman, L. D., *Experimental Observation of the Microlayer in vapor bubble growth on a heated solid*, Ph.D. thesis, California Institute of Technology, Pasadena, USA, 1980.

[89] Koffman, L. D. and Plesset, M. S., Experimental Observations of the Microlayer in Vapor Bubble Growth on a Heated Solid, *Journal of Heat Transfer*, 105(3):625–632, 1983.

[90] Kunkelmann, C., *Numerical Modeling and Investigation of Boiling Phenomena*, Ph.D. thesis, Institut für Technische Thermodynamik, Technische Universität Darmstadt, Darmstadt, Germany, 2011.

[91] Kunkelmann, C., Ibrahem, K., Schweizer, N., Herbert, S., Stephan, P., and Gambaryan-Roisman, T., The effect of three-phase contact line speed on local evaporative heat transfer: Experimental and numerical investigations, *International Journal of Heat and Mass Transfer*, 55(7-8):1896–1904, 2012.

[92] Kunkelmann, C. and Stephan, P., CFD Simulation of Boiling Flows Using the Volume-of-Fluid Method within OpenFOAM, *Numerical Heat Transfer, Part A: Applications*, 56(8):631–646, 2009.

[93] Kunkelmann, C. and Stephan, P., Modification and extension of a standart Volume-of-Fluid solver for simulating boiling heat transfer, in *Proceeding of V European Conference on Computational Fluid Dynamics*, Lisbon, Portugal, 2010.

[94] Kurul, N. and Podowski, M. Z., Multidimensional effects in forced convection subcooled boiling, in *Proceedings of 9th International Heat Transfer Conference*, vol. 2, pp. 21–25, Jerusalem, Israel, 1990.

[95] 3M, Fluorinert™ Electronic Liquid FC-72, 28.06.2000, online source last downloaded 18.11.2013, http://multimedia.3m.com/mws/mediawebserver?66666UuZjcFSLXTtnxTE5XF6EVuQEcuZgVs6EVs6E666666--.

[96] Mann, M., *Ein Mikrozonenmodell zur Beschreibung der Blasenbildung und des Wärmeübergangs beim Sieden*, VDI-Verl., Düsseldorf, 2001, ISBN 3183708035.

[97] Maxwell, J. C., *Theory of heat*, Longmans, Green, and Co., 1871.

[98] Migliaccio, C. P., Dhavaleswarapu, H. K., and Garimella, S. V., Temperature measurements near the contact line of an evaporating meniscus V-groove, *International Journal of Heat and Mass Transfer*, 54(7-8):1520–1526, 2011.

[99] Mikic, B. and Rohsenow, W., A New Correlation of Pool-Boiling Data Including the Effect of Heating Surface Characteristics, *Journal of Heat Transfer*, 91(2):245–250, 1969.

[100] Moore, F. D. and Mesler, R. B., The measurement of rapid surface temperature fluctuations during nucleate boiling of water, *AIChE Journal*, 7(4):620–624, 1961.

[101] Mukherjee, A. and Dhir, V. K., Study of Lateral Merger of Vapor Bubbles During Nucleate Pool Boiling, *Journal of Heat Transfer*, 126(6):1023–1039, 2004.

[102] Mukherjee, A. and Kandlikar, S. G., Numerical study of single bubbles with dynamic contact angle during nucleate pool boiling, *International Journal of Heat and Mass Transfer*, 50(1-2):127–138, 2007.

[103] Myers, J. G., Yerramilli, V. K., Hussey, S. W., Yee, G. F., and Kim, J., Time and space resolved wall temperature and heat flux measurements during nucleate boiling with constant heat flux boundary conditions, *International Journal of Heat and Mass Transfer*, 48(12):2429–2442, 2005.

[104] Nam, Y., Aktinol, E., Dhir, V. K., and Ju, Y. S., Single bubble dynamics on a superhydrophilic surface with artificial nucleation sites, *International Journal of Heat and Mass Transfer*, 54(7-8):1572–1577, 2011.

[105] Nancy Gail Johnson <ngj@me.umn.edu>, original published by Karl Geisler on http://www.me.umn.edu/courses/me/me5348/fc72.html: Email, 03.04.2013.

[106] Nimkar, N. D., Bhavnani, S. H., and Jaeger, R. C., Effect of nucleation site spacing on the pool boiling characteristics of a structured surface, *International Journal of Heat and Mass Transfer*, 49(17-18):2829–2839, 2006.

[107] Nukiyama, S., The Maximum and Minimum Values of the Heat Q Transmitted from Metal to Boiling Water under Atmospheric Pressure, *Journal of the Society of Mechanical Engineers, Japan*, 37:367–374, 1934.

[108] Pennisi, E., Human Evolution: Did Cooked Tubers Spur the Evolution of Big Brains?, *Science*, 283(5410):2004–2005, 1999.

[109] Piccinini, F., Lucarelli, E., Gherardi, A., and Bevilacqua, A., Multi-image based method to correct vignetting effect in light microscopy images, *Journal of Microscopy*, 248(1):6–22, 2012.

[110] Potash, M. and Wayner, P., Evaporation from a two-dimensional extended meniscus, *International Journal of Heat and Mass Transfer*, 15(10):1851–1863, 1972.

[111] Raad, T. and Myers, J. E., Nucleation studies in pool boiling on thin plates using liquid crystals, *AIChE Journal*, 17(5):1260–1261, 1971.

[112] Raj, R. and Kim, J., Heater Size and Gravity Based Pool Boiling Regime Map: Transition Criteria Between Buoyancy and Surface Tension Dominated Boiling, *Journal of Heat Transfer*, 132(9):091503, 2010.

[113] Raj, R., Kim, J., and McQuillen, J., Subcooled Pool Boiling in Variable Gravity Environments, *Journal of Heat Transfer*, 131(9):091502, 2009.

[114] Raj, R., Kim, J., and McQuillen, J., Gravity Scaling Parameter for Pool Boiling Heat Transfer, *Journal of Heat Transfer*, 132(9):091502, 2010.

[115] Rule, T. D. and Kim, J., Heat Transfer Behavior on Small Horizontal Heaters During Pool Boiling of FC-72, *Journal of Heat Transfer*, 121(2):386, 1999.

[116] Safra, J. E. and Aguilar-Cauz, J. (eds.), *Encyclopædia Britannica*, vol. 11, Chicago, 15th edn., 2009, ISBN 9781593398378.

[117] Sato, T., Koizumi, Y., and Ohtake, H., Experimental Study on Fundamental Phenomena of Boiling Using Heat Transfer Surfaces With Well-Defined Cavities Created by MEMS (Effect of Spacing Between Cavities), *Journal of Heat Transfer*, 130(8):084501, 2008.

[118] Schuck, J., Untersuchung der Blasenkoaleszenz und des Keimstellenabstands auf technischen Heizern sowie der Einflüsse beim Erreichen der kritischen Wärmestromdichte, B. Sc. thesis, Darmstadt, Germany, 2012.

[119] Schweizer, N., *Multi-Scale Investigation of Nucleate Boiling Phenomena in Microgravity*, Ph.D. thesis, Institut für Technische Thermodynamik, Technische Universität Darmstadt, Darmstadt, Germany, 28.12.2010.

[120] Senthil kumar, D., Murugesan, K., and Gupta, A., Numerical Analysis of Interaction Between Inertial and Thermosolutal Buoyancy Forces on Convective Heat Transfer in a Lid-Driven Cavity, *Journal of Heat Transfer*, 132(11):112501, 2010.

[121] Sgheiza, J. E. and Myers, J. E., Behavior of nucleation sites in pool boiling, *AIChE Journal*, 31(10):1605–1613, 1985.

[122] Shin, S. and Juric, D., Modeling Three-Dimensional Multiphase Flow Using a Level Contour Reconstruction Method for Front Tracking without Connectivity, *Journal of Computational Physics*, 180(2):427–470, 2002.

[123] Shoji, M. and Takagi, Y., Bubbling features from a single artificial cavity, *International Journal of Heat and Mass Transfer*, 44(14):2763–2776, 2001.

[124] Shu, B., *Numerische Simulation des Blasensiedens mit Volume-Of-Fluid- und Level-Set-Methode*, Ph.D. thesis, Technische Universität Darmstadt, Darmstadt, Germany, 2009.

[125] Siedel, S., Cioulachtjian, S., and Bonjour, J., Experimental analysis of bubble growth, departure and interactions during pool boiling on artificial nucleation sites, *Experimental Thermal and Fluid Science*, 32(8):1504–1511, 2008.

[126] Siedel, S., Cioulachtjian, S., Di Bari, S., Robinson, A. J., and Bonjour, J., Experimental investigation on the local curvature of bubble interface during boiling on a single nucleation site, in *Proceeding of the 8th International Conference on Boiling and Condensation Heat Transfer*, Lausanne, Switzerland, 2012.

[127] Siedel, S., Cioulachtjian, S., Robinson, A. J., and Bonjour, J., Experimental determination of the force acting on a bubble during boiling on a single nucleation site, in *Proceeding of the 8th International Conference on Boiling and Condensation Heat Transfer*, Lausanne, Switzerland, 2012.

[128] Sielaff, A., Dietl, J., Herbert, S., and Stephan, P., The influence of system pressure on bubble coalescence in nucleate boiling, *Heat Transfer Engineering*, 35(5):420–429, 2014.

[129] Slomski, E. M., *Funktionsorientierte Mikrostrukturierung von Chromnitrid-Beschichtungen mittels hybrider PVD-Technologie*, Ph.D. thesis, Institut für Werkstoffkunde, Technische Universität Darmstadt, Darmstadt, Germany, 2012.

[130] Snyder, N. and Edwards, D., Summary of conference on bubble dynamics and boiling heat transfer: Memo 20-137, 1956.

[131] Sodtke, C., *Untersuchungen zur Sprühkühlung an mikrostrukturierten Oberflächen*, vol. 156 of *TTD-Berichte aus dem Fachgebiet Technische Thermodynamik, TU Darmstadt*, VDI-Verl., Düsseldorf, 2007, ISBN 9783183156191.

[132] Sodtke, C., Ajaev, V. S., and Stephan, P., Evaporation of thin liquid droplets on heated surfaces, *Heat and Mass Transfer*, 43(7):649–657, 2007.

[133] Sodtke, C., Kern, J., Schweizer, N., and Stephan, P., High resolution measurements of wall temperature distribution underneath a single vapour bubble under low gravity conditions, *International Journal of Heat and Mass Transfer*, 49(5-6):1100–1106, 2006.

[134] Son, G. and Dhir, V. K., Numerical simulation of nucleate boiling on a horizontal surface at high heat fluxes, *International Journal of Heat and Mass Transfer*, 51(9-10):2566–2582, 2008.

[135] Son, G., Dhir, V. K., and Ramanujapu, N., Dynamics and Heat Transfer Associated With a Single Bubble During Nucleate Boiling on a Horizontal Surface, *Journal of Heat Transfer*, 121(3):623–631, 1999.

[136] Son, G., Ramanujapu, N., and Dhir, V. K., Numerical Simulation of Bubble Merger Process on a Single Nucleation Site During Pool Nucleate Boiling, *Journal of Heat Transfer*, 124(1):51–62, 2002.

[137] Stephan, K. and Preusser, P., Wärmeübergang und maximale Wärmestromdichte beim Behältersieden binärer und ternärer Flüssigkeitsgemische, *Chemie Ingenieur Technik*, 51(1):37, 1979.

[138] Stephan, P., *Wärmedurchgang bei Verdampfung aus Kapillarrillen in Wärmerohren*, VDI-Verlag, Düsseldorf, 1992, ISBN 9783181459195.

[139] Stephan, P., *Thermodynamik: Grundlagen und technische Anwendungen*, Springer, Berlin and Heidelberg, 18th edn., 2009, ISBN 3540928944.

[140] Stephan, P. and Busse, C. A., Analysis of the heat transfer coefficient of grooved heat pipe evaporator walls, *International Journal of Heat and Mass Transfer*, 35(2):383–391, 1992.

[141] Stephan, P. and Hammer, J., A new model for nucleate boiling heat transfer, *Heat and Mass Transfer*, 30(2):119–125, 1994.

[142] Stephan, P., Sielaff, A., Fischer, S., Dietl, J., and Herbert, S., A contribution to the basic understanding of nucleate boiling phenomena: generic experimental and numerical simulations, in *3rd International Forum on Heat Transfer*, Nagasaki, Japan, 2012.

[143] Theofanous, T., Dinh, T., Tu, J., and Dinh, A., The boiling crisis phenomenon: Part II: dryout dynamics and burnout, *Experimental Thermal and Fluid Science*, 26(6-7):793–810, 2002.

[144] Theofanous, T., Tu, J., Dinh, A., and Dinh, T., The boiling crisis phenomenon: Part I: nucleation and nucleate boiling heat transfer, *Experimental Thermal and Fluid Science*, 26(6-7):775–792, 2002.

[145] Thomann, H. and Frisk, B., Measurement of heat transfer with an infrared camera, *International Journal of Heat and Mass Transfer*, 11(5):819–826, 1968.

[146] Thomson, W., *Popular lectures and addresses*, vol. 1, Macmillan and Co, 1889.

[147] Tryggvason, G., Bunner, B., Esmaeeli, A., Juric, D., Al-Rawahi, N., Tauber, W., Han, J., Nas, S., and Jan, Y.-J., A Front-Tracking Method for the Computations of Multiphase Flow, *Journal of Computational Physics*, 169(2):708–759, 2001.

[148] Vogt, J., *Entwicklung neuartiger Particle Image Thermometry Methoden zur hochauflösenden Messung von Temperatur- und Geschwindigkeitsfeldern in Flüssigkeiten*, Ph.D. thesis, Institut für Technische Thermodynamik, Technische Universität Darmstadt, Darmstadt, Germany, unpublished.

[149] Wagner, E., *Hochauflösende Messungen beim Blasensieden von Reinstoffen und binären Gemischen*, Shaker, Aachen, 2009, ISBN 3832278818.

[150] Wagner, E., Sprenger, A., Stephan, P., Koeppen, O., Ziegler, F., and Auracher, H., Nucleate boiling at single artificial cavities: Bubble dynamics and local temperature measurements, in *Proceedings in the 6th International Conference on Multiphase flow, ICMF*, Leipzig, Germany, 2007.

[151] Wagner, E. and Stephan, P., Experimental study of local temperature distribution and heat transfer mechanisms during nucleate boiling of binary mixtures, in *Proceedings of th 5th European Thermal-Sciences Conference EUROTHERM*, Eindhoven, the Netherlands, 2008.

[152] Wang, H., Pan, Z., and Garimella, S. V., Numerical investigation of heat and mass transfer from an evaporating meniscus in a heated open groove, *International Journal of Heat and Mass Transfer*, 54(13-14):3015–3023, 2011.

[153] Wayner, P. C., Kao, Y. K., and LaCroix, L. V., The interline heat-transfer coefficient of an evaporating wetting film, *International Journal of Heat and Mass Transfer*, 19(5):487–492, 1976.

[154] Welch, S. W. J., Direct simulation of vapor bubble growth, *International Journal of Heat and Mass Transfer*, 41(12):1655–1666, 1998.

[155] Welch, S. W. J. and Rachidi, T., Numerical Computation of Film boiling including conjugate heat transfer, *Numerical Heat Transfer, Part B: Fundamentals*, 42(1):35–53, 2002.

[156] Yan, Y., Kenning, D., and Cornwell, K., Sliding and sticking vapour bubbles under inclined plane and curved surfaces, *International Journal of Refrigeration*, 20(8):583–591, 1997.

[157] Zhang, L. and Shoji, M., Nucleation site interaction in pool boiling on the artificial surface, *International Journal of Heat and Mass Transfer*, 46(3):513–522, 2003.

[158] Zuber, N., Hydrodynamic aspects of boiling heat transfer, Los Angeles, USA, 1959.

[159] Zuber, N., Nucleate boiling. The region of isolated bubbles and the similarity with natural convection, *International Journal of Heat and Mass Transfer*, 6(1):53–78, 1963.

List of Figures

Individual figures are used with the kind permission of Elsevier (2.7, 2.12, 2.17, 2.24), John Wiley & Sons (2.11), Taylor & Francis (2.15), and Forschungszentrum Karlsruhe (now Karlsruher Institut für Technologie) (2.16). The figures 2.13, 2.22, and 2.25 are used with the permission of ASME against payment of 50 $.

List of Tables

CHAPTER A

Appendix

A.1 Original introduction to boiling by Maxwell

From: THEORY OF HEAT [97, pp. 23–26]

> *When a liquid in an open vessel is heated to a temperature such that the pressure of its vapour at that temperature is greater than the pressure at a point in the interior of the liquid, the liquid will begin to evaporate at that point, so that a bubble of vapour will be formed there. This process, in which bubbles of vapour are formed in the interior of the liquid, is called boiling or ebullition. When water is heated in the ordinary way by applying heat to the bottom of a vessel, the lowest layer of the water becomes hot first, and by its expansion it becomes lighter than the colder water above, and gradually rises, so that a gentle circulation of water is kept up, and the whole water is gradually warmed, though the lowest layer is always the hottest. As the temperature increases, the absorbed air, which is generally found in ordinary water, is expelled, and rises in small bubbles without noise. At last the water in contact with the heated metal becomes so hot that, in spite of the pressure of the atmosphere on the surface of the water, the additional pressure due to the water in the vessel, and the cohesion of the water itself, some of the water at the bottom is transformed into steam, forming a bubble adhering to the bottom of the vessel. As soon as a bubble is formed, evaporation goes on rapidly from the water all round it, so that it soon grows large, and rises from the bottom. If the upper part of the water into which the bubble rises is still below the boiling temperature, the bubble is condensed, and its sides come together with a sharp rattling noise, called simmering. But the rise of the bubbles stirs the water about much more vigorously than the mere expansion of the water, so that the water is soon heated throughout, and brought to the boil, and then the bubbles enlarge rapidly during their whole ascent, and burst into the air, throwing the water about, and making the well-known softer and more rolling noise of boiling. The steam, as it bursts out of the bubbles, is an invisible gas, but when it comes into the colder air it is cooled below its condensing point, and part of it is formed into a cloud consisting of small drops of water which float in the air. As the cloud of drops disperses itself and mixes with dry air the quantity of water in each cubic foot diminishes as the volume of any part of the cloud increases. The little drops of water begin to evaporate as soon as there is sufficient room for the vapour to be formed at the temperature of the atmosphere, and so the cloud vanishes again into thin air. The temperature to which water must be heated before it boils depends, in the first place, on the pressure of the atmosphere, so that the greater the pressure, the higher the boiling temperature. But the temperature requires*

to be raised above that at which the pressure of steam is equal to that of the atmosphere, for the pressure of the vapour has to overcome not only the pressure due to the atmosphere and a certain depth of water, but the cohesion between the parts of the water of which the effects are visible in the tenacity of bubbles and drops. Hence it is possible to heat water 20° F. above its boiling point without ebullition. If a small quantity of metal-filings are now thrown into the water, the vapour by forming itself against the angular surface of these filings get an advantage over the cohesion of the water, and produces a violent boiling, almost amounting to an explosion. If a current of steam from a boiler is passed into a vessel of cold water, we have first the condensation of steam, accompanied with a very loud simmering noise, and a rapid heating of the water. When the water is sufficiently heated, the steam is not condensed, but escapes in bubbles, and the water is now boiling. If the boiler is at a high pressure, the steam from it will be at a temperature much above the boiling point in the open air, but in the passing through the water in the open vessel it will cause some of it to evaporate, and when it issues from the water the temperature will be exactly that of the boiling point. For this reason, in finding the boiling point of a thermometer the instrument should not be allowed to dip in the water, but should be held in the steam. As an instance of a different kind, let us suppose that the water is not pure, but contains some salt, such as common salt, or sulphate of soda, or any other substance which tends to combine with water, and from which the water must separate before it can evaporate. Water containing such substances in solution requires to be brought to a temperature higher than the boiling point of pure water before it will boil. Water, on the other hand, containing air or carbonic acid, will boil at a lower temperature than pure water till the gas is expelled. If steam at 100° C. is passed into a vessel containing a strong solution of one of the salts we have mentioned, which has a tendency to combine with water, the condensation of the steam will be promoted by this tendency, and will go on even after the solution has been heated far above the ordinary boiling point, so that by passing steam at 100° C. into a strong solution of nitrate of soda, Mr. Peter Spence[1] has heated it up to 121°·1 C. The steam, however, which escapes, is still at 100° C. If water at a temperature below 100° C. be placed in a vessel, and if by means of an air-pump we reduce the pressure of the air on the surface of the water, evaporation goes on and the surface of the water becomes colder than the interior parts. If we go on working the air-pump, the pressure is reduced to that of vapour of the temperature of the interior of the fluid. The water then begins to boil, exactly as in the ordinary way, and as it boils the temperature rapidly falls, the heat being expended in evaporating the water. This experiment may be performed without an air-pump in the following way : Boil water in a flask over a gasflame or spirit-lamp, and while it is boiling briskly cork the flask, and remove it from the flame. The boiling will soon cease, but if we now dash a little cold water over the flask, some of the steam in the upper part will be condensed, the pressure of the remainder will be diminished, and the water will begin to boil again. The experiment may be made more striking by plunging the flask entirely under cold water. The steam will be condensed as before, but the water, though it is cooled more rapidly than when the cold water was merely poured on the flask, retains its heat longer than the steam, and continues to boil for some time.

---

[1] Transactions of the British Association, 1869, p. 75.

Table A.1: Saturation data for FC-72 [105]

P	T	α	β	c_p	Δh_v	k	η	ν	Pr	ρ_l	ρ_v	σ
		x10^8	x10^3			x10^2	x10^4	x10^7				x10^2
atm	°C	m^2/s	1/K	J/(kg K)	J/kg	W/(m K)	N s/m^2	m^2/s	-	kg/m^3	kg/m^3	N/m
0.085	0	3.312	1.5	1011.01	99181.7	5.877	9.496	5.41	16.336	1755.29	1.371	1.334
	5	3.287	1.511	1018.73	98000	5.818	8.742	5.031	15.305	1737.54	1.802	1.288
0.144	10	3.263	1.523	1026.45	96818.2	5.76	8	4.652	14.257	1719.78	2.234	1.241
	15	3.232	1.535	1034.17	95593.4	5.702	7.43	4.356	13.476	1705.66	2.859	1.195
0.232	20	3.202	1.546	1041.89	94368.5	5.643	6.868	4.06	12.68	1691.54	3.484	1.15
	25	3.167	1.558	1049.61	93094.4	5.585	6.437	3.831	12.097	1680.33	4.357	1.104
0.361	30	3.131	1.571	1057.34	91820.3	5.526	6.011	3.601	11.5	1669.12	5.231	1.059
	35	3.094	1.583	1065.06	90497	5.468	5.68	3.423	11.064	1659.4	6.41	1.015
0.54	40	3.057	1.596	1072.78	89173.6	5.41	5.353	3.245	10.616	1649.68	7.589	0.9708
	45	3.019	1.609	1080.5	87788.8	5.351	5.091	3.103	10.279	1640.58	9.136	0.9271
0.785	50	2.981	1.622	1088.22	86403.9	5.293	4.831	2.961	9.932	1631.48	10.683	0.8838
	55	2.944	1.635	1095.94	84969.8	5.234	4.608	2.84	9.648	1622.58	12.738	0.8409
	56.6	2.932	1.639	1098.41	84510.9	5.216	4.537	2.801	9.555	1619.73	13.396	0.8273
1.109	60	2.906	1.648	1103.66	83535.7	5.176	4.388	2.719	9.355	1613.67	14.793	0.7985
	65	2.872	1.662	1111.39	82046.2	5.118	4.183	2.609	9.085	1603.46	17.516	0.7565
1.529	70	2.837	1.676	1119.11	80556.6	5.059	3.982	2.499	8.807	1593.25	20.238	0.715
	75	2.807	1.69	1126.83	79024.1	5.001	3.799	2.403	8.559	1581.12	23.721	0.6739
2.062	80	2.776	1.705	1134.55	77491.5	4.942	3.618	2.306	8.305	1568.99	27.203	0.6334
	85	2.751	1.719	1142.27	75928.1	4.884	3.432	2.209	8.027	1554.08	31.59	0.5933
2.726	90	2.726	1.734	1149.99	74364.7	4.826	3.249	2.111	7.743	1539.16	35.976	0.5538
	95	2.709	1.749	1157.71	72782.9	4.767	3.195	2.102	7.758	1520.13	41.486	0.5149
3.541	100	2.692	1.765	1165.44	71201	4.709	3.14	2.092	7.772	1501.1	46.996	0.4766
	105	2.684	1.78	1173.16	69446.9	4.65	3.084	2.088	7.78	1477.05	53.811	0.4388
4.529	110	2.676	1.796	1180.88	67692.7	4.592	3.028	2.084	7.787	1452.99	60.625	0.4018
	115	2.679	1.813	1188.6	65993.9	4.534	2.963	2.082	7.768	1423.5	69.061	0.3654
5.713	120	2.683	1.829	1196.32	64295.1	4.475	2.898	2.079	7.747	1394.01	77.496	0.3297
	125	2.702	1.846	1204.04	62214.8	4.417	2.82	2.078	7.688	1357.46	88.023	0.2947

7.117	130	2.723	1.863	1211.77	60134.4	4.358	2.742	2.076	7.624	1320.9	98.55	0.2606
	135	2.762	1.881	1219.49	57641.6	4.3	2.649	2.075	7.514	1276.84	112.068	0.2274
8.771	140	2.804	1.899	1227.21	55148.8	4.242	2.557	2.074	7.397	1232.78	125.586	0.1952
	145	2.87	1.917	1234.93	52059	4.183	2.447	2.073	7.223	1180.24	143.815	0.1639
10.71	150	2.944	1.935	1242.65	48969.2	4.125	2.337	2.072	7.039	1127.69	162.044	0.1339
	155	3.052	1.954	1250.37	45048.5	4.066	2.207	2.071	6.785	1065.47	188.631	0.1051
12.96	160	3.175	1.974	1258.09	41127.7	4.008	2.077	2.07	6.519	1003.25	215.217	0.0779
	165	3.353	1.993	1265.82	35692.9	3.95	1.926	2.07	6.172	930.49	259.178	0.0525
15.58	170	3.562	2.013	1273.54	30258	3.891	1.775	2.069	5.808	857.72	303.138	0.0294
	175	4.189	2.034	1281.26	12459.2	3.833	1.477	2.068	4.937	714.06	485.117	0.0097
18.17	178.5	4.804	2.048	1286.66	0	3.792	1.269	2.068	4.305	613.5	612.502	0

The data are fitted by

$$t_{sat}[\text{in } ^\circ\text{C}] = -86.699 + 143.278\ {p_{sat}}^{0.204}[\text{in bar}]. \tag{A.1}$$

A further correlation is given by 3M [95]

$$Log_{10}(\text{p}[\text{in pa}]) = 9.729 - (1562/\text{T}[\text{in K}]). \tag{A.2}$$

This correlation seems to be less reliable as for a degassed fluid the temperature of the liquid was ≈ 1 K higher than the calculated saturation temperature using the pressure measurement. Therefore the correlation A.1 is used.

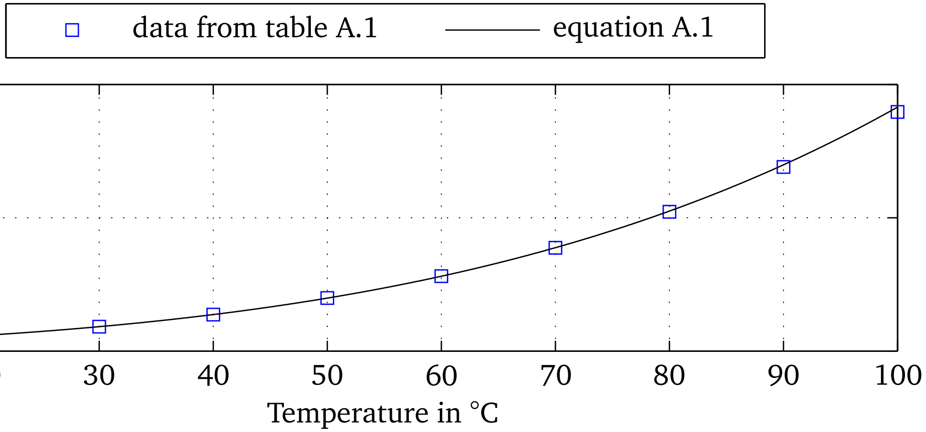

Figure A.1: Vapor pressure curve for FC-72

A.3 Purchased parts

Test cell

Component	Company	Description
Bellow-type valve	Swagelok	SS-4H-TH3 (6.7×10^{-11} mbar l/s)
Glasses (short optical path)	Edmund Optics	47523 1/4 λ ⌀50 mm VIS 0 Coat
Glasses (long optical path)	Edmund Optics	49134 1/4 λ ⌀50 mm 532 nm V-Coat
IR-transparent glass	Edmund Optics	63208 CaF_2 1/2 λ ⌀30 mm
Pressure equalization bellow	Fresenius Kabi	Applix Pump Set PZN-1600050[1]
Adehsive tape	3M	Tape 8940
Adehsive tape (chemical resistant)	Fresenius Kabi	Applix Pump Set PZN-1600050
Sealant	Eriks	EPDM FDA[2]-Compound 559003
Coating of stainless steel foil	CRC Kontakt Chemie	Graphit 33
Laser	Melles Griot	620–700 nm; $<$ 500 mW

Pressure equalization

Component	Company	Description
Pressure controller	Bachofen / Marsh Bellofram	T3120 120TE0A015P2000

Measurement and control devices

Component	Company	Description
Pressure transducer	WIKA	Model P-30 0 bar to 1 bar abs.
Power PC Controller	National Instruments	cRio-9022
Chassis for cRio	National Instruments	cRio-9114
RTD Analog Input Module	National Instruments	cRio-9217
±10 V Analog Input Module	National Instruments	cRio-9205
TTL dig. In/Out Module	National Instruments	cRio-9403
±10 V Analog Output Module	National Instruments	cRio-9264
Thermocouple Module	National Instruments	cRio-9213
High-speed camera (VIS)	High Speed Vision	SpeedCam MacroVis EoSens
High-speed camera (VIS)	Photron	FASTCAM-X 1024 PCI
High-speed camera (IR)	Indigo Systems Corporation	Phoenix-Mid
Illumination	High Speed Vision	HIB-Multihead
Thermostat	Huber	Ministat 125
Power supply	Delta Elektronika	SM 15–100

A.4 Heating foil

	Symbol	Value	Uncertainty
Thermal conductivity	k_f	18 W/(m K)	≤ 20 %
Density	ρ_f	$7800\,\mathrm{kg/m^3}$	≤ 2 %
Heat capacity	c_p	477 J/(kg K)	≤ 5 %
Electrical resistance at 20 °C	ρ_{20}	$0.73 \times 10^{-3}\,\Omega\,\mathrm{m}$	$0.03 \times 10^{-3}\,\Omega\,\mathrm{m}$
Temperature coefficient	α_t	0.005/K	0.001/K
Thickness	δ_f	$20 \times 10^{-6}\,\mathrm{m}$	$2 \times 10^{-6}\,\mathrm{m}$
Width	W_f	$24 \times 10^{-3}\,\mathrm{m}$	$5 \times 10^{-4}\,\mathrm{m}$
Temperature	t_f	30 °C to 80 °C	0.3 °C
El. current	I	7 A to 24 A	0.01 A

Table A.3: Properties of the used stainless steel foil

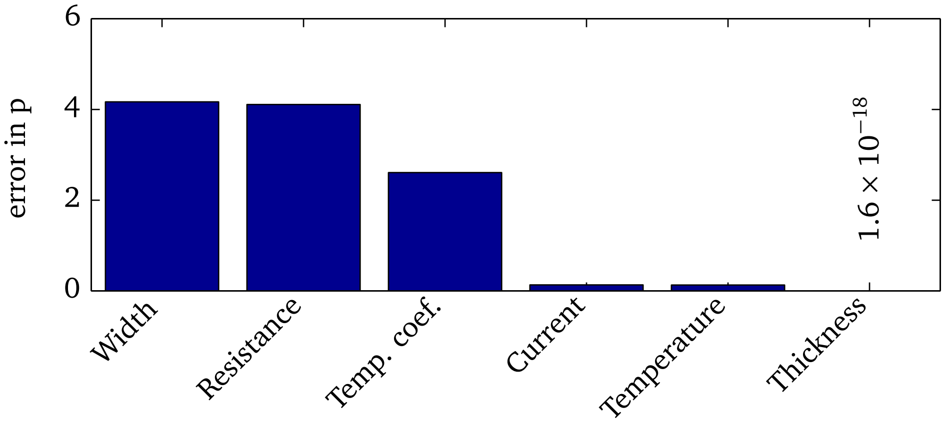

Figure A.2: Error distribution of heat source calculation - T = 50°C, I = 15 A

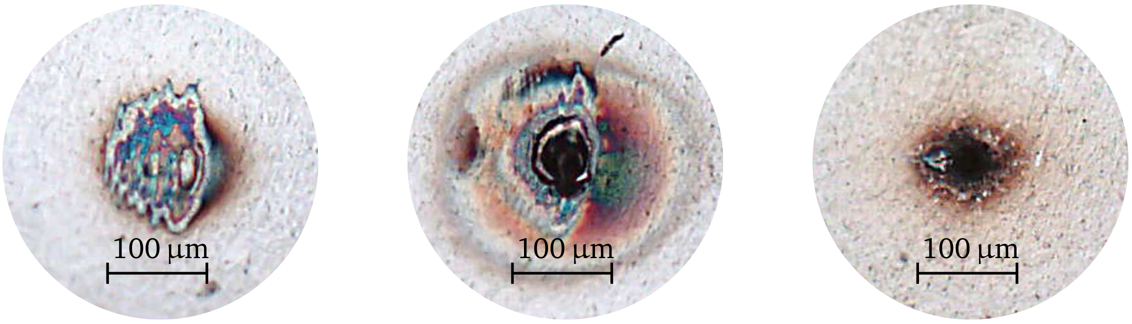

(a) 1.6 mm out of focal point **(b)** 0.8 mm out of focal point **(c)** in focal point

Figure A.3: Cavities created with different distances of the foil to the focal point

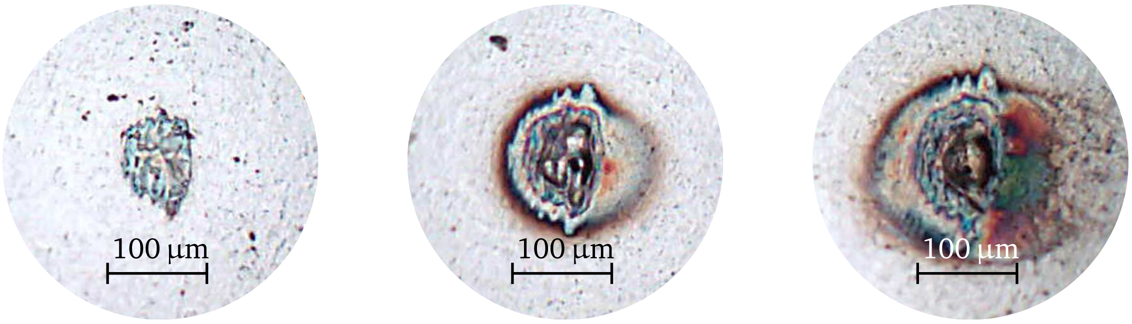

(a) 15 A **(b)** 18 A **(c)** 25 A

Figure A.4: Cavities created with different laser power (input current)

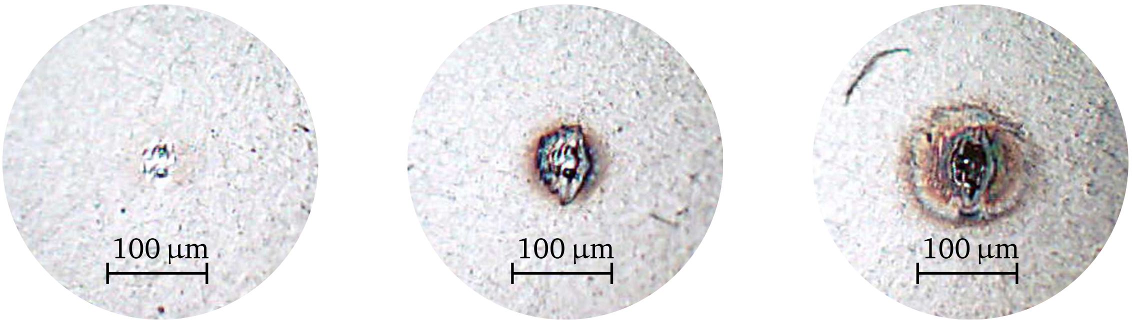

(a) 10 pulses **(b)** 30 pulses **(c)** 90 pulses

Figure A.5: Cavities created with a different number of laser pulses

(a) 20 µs **(b)** 180 µs **(c)** no external waiting time

Figure A.6: Cavities with a different waiting time between each pulse

Table A.4: Parameter for cavities produced by laser surface treatment

Used components	telecentric lenses (f = 77 mm) vacuum straintable
Focus point	f = 212.4 mm (1 mm out of focal distance)
Intensity	15.5 A
Geometry	

```
R=0.002
x1=R
x2=0
P=50
K = 0
JUMP 0,0
BURST
FOR Q = 1 TO P
        JUMP x1,x2
        BURST
        K = K + (2*3.14159)/P
        x1 = R*COS(K)
        x2 = R*SIN(K)
NEXT
```

A.6 Detection of a bubble departure

In Eq. A.6 the combined requirement for the detection of a bubble departure is shown, where X is the position of the apparent contact line in pixels and N the number of the picture

$$\begin{gathered}\Big[\Big(X_{\mathrm{cl,l}}(N+1) == \mathrm{nan}\Big) \vee \Big(X_{\mathrm{cl,l}}(N) \neq \mathrm{nan}\Big)\Big] \wedge \\ \Big[\Big(X_{\mathrm{cl,r}}(N) - X_{\mathrm{cl,l}}(N) + 1\ \mathrm{pixel} < X_{\mathrm{cl,r}}(N-1) - X_{\mathrm{cl,l}}(N-1)\Big) \vee \\ \Big(X_{\mathrm{cl,r}}(N) - X_{\mathrm{cl,l}}(N) + 1\ \mathrm{pixel} < X_{\mathrm{cl,r}}(N+1) - X_{\mathrm{cl,l}}(N+1)\Big)\Big]\,.\end{gathered} \tag{A.3}$$

A.7 Dependency of the heat flux calculation on the direction of the temperature gradient

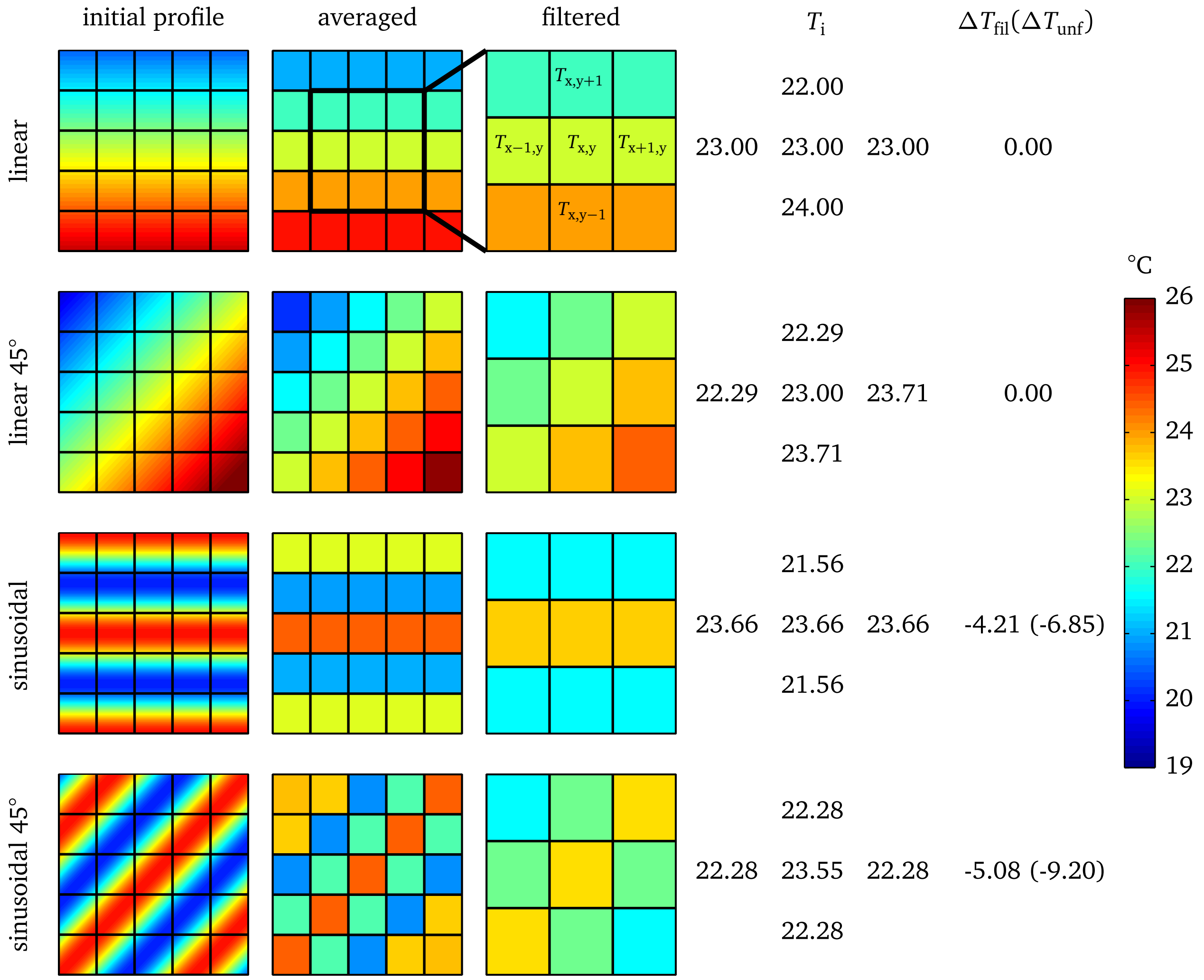

Figure A.7: Dependency of the heat flux calculation on the direction of the temperature gradient

In Fig. A.7 the dependency of the heat flux calculation on the direction of the temperature gradient is shown. In the left column the initially calculated temperature can be seen for a linear and a sinusoidal profile. Both are shown for a vertical and a diagonal (45°) growth direction. In the second column the temperature is averaged for the shown grid of 5 x 5 elements. The third column shows the central 3 x 3 elements after the application of a Gaussian filter. The used filter has a size of $n_1 = n_2 = 3$ and $\sigma_n = 0.5$ (cf. section 4.2.2). The heat flux q at the position x, y is calculated via

$$q = q_0 + k_H\, \delta \left(\frac{\partial^2 T}{\partial x^2} + \frac{\partial^2 T}{\partial y^2} \right) - \rho_H\, c_{p,H}\, \delta\, \frac{\partial T}{\partial \tau}. \tag{A.4}$$

For demonstration purposes the system is taken to be in a steady state in this example. The source term q_0 and the material properties are assumed to be equal. In this case the differences in the calculated heat flux for the vertical and diagonal temperature gradients result from the second derivative of the temperature in x and y direction

$$\triangle\, T = \left(\frac{\partial^2 T}{\partial x^2} + \frac{\partial^2 T}{\partial y^2} \right). \tag{A.5}$$

As mentioned in section 4.2.2, the second derivative in x direction is approximated by

$$\frac{\partial^2 T}{\partial x^2} \approx \frac{T_{\mathrm{x+1,y},\tau} - T_{\mathrm{x,y},\tau}}{\Delta x^2} + \frac{T_{\mathrm{x-1,y},\tau} - T_{\mathrm{x,y},\tau}}{\Delta x^2}. \tag{A.6}$$

As the approximation in y direction is calculated equivalently, the differences in the calculated heat flux for $\Delta x = \Delta y = 1$ can be further reduced to

$$\Delta T/\Delta x^2 \approx T_{\mathrm{x+1,y}} - 2T_{\mathrm{x,y}} + T_{\mathrm{x-1,y}} + T_{\mathrm{x,y+1}} - 2T_{\mathrm{x,y}} + T_{\mathrm{x,y-1}}. \tag{A.7}$$

The temperatures of the used elements are shown in the fourth column. The calculated results of Eq. A.7 are shown in the right column for the filtered and unfiltered temperature field. The value for the unfiltered temperature field is presented in brackets. The analytic solution of the second derivative of the temperature gradient $\triangle\, T_{\mathrm{ana}}$ (cf. Eq. A.5) is

$$\triangle\, T_{\mathrm{ana,lin}} = 0\,\mathrm{K/m^2} \;\; \text{(linear)} \tag{A.8}$$

for the linear temperature gradient and

$$\triangle\, T_{\mathrm{ana,sin}} = -11.9\,\mathrm{K/m^2} \;\; \text{(sinusoidal)} \tag{A.9}$$

for the sinusoidal temperature profile. As the same function is used, these results are equal for the vertical and diagonal case for each function. Out of this example major conclusions can be drawn. For a temperature profile of first order the heat flux calculation is not influenced by averaging and filtering or by the direction of the temperature gradient. If the temperature is a function of a higher order a clear dependency of filtering and averaging can be observed. Further, the calculated heat flux is influenced by the direction of the temperature gradient (cf. Fig. 4.13).

A.8 Boxplot

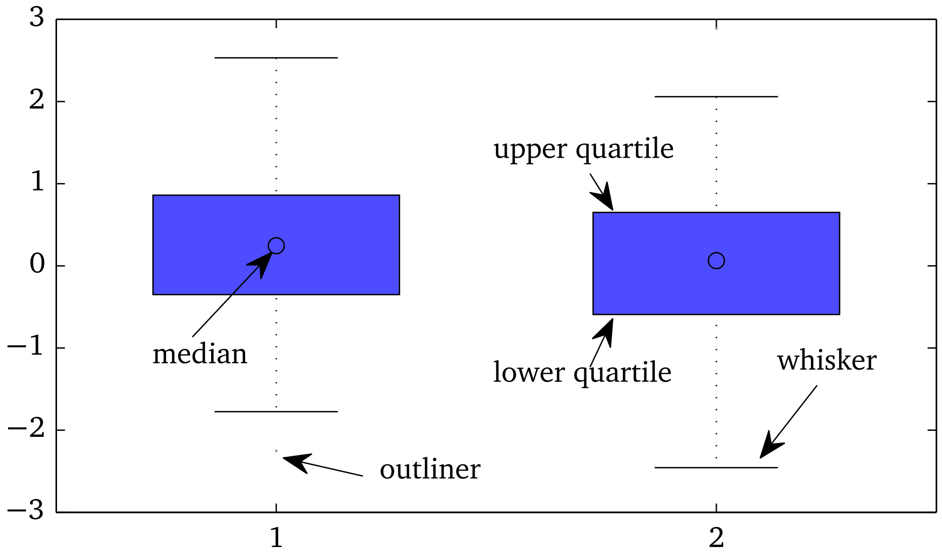

Figure A.8: Explanation of a boxplot

A *boxplot* is a convenient way of plotting statistical data. In Fig. A.8 an example of randomly generated values is shown. The upper and lower quartile represents the area containing 50 % of the data. This is called the interquartile range (IQR). The end of the whiskers represents the last data point within the 1.5 × IQR range. Values located outside of this range are shown as outliers. The circle represents the median value of the data, separating the higher half of the data from the lower one. Especially for a smaller sample size the median value is less prone to outliers than the mean value, representing the arithmetic average.

A.9 Measurement uncertainties

Measurand	**Measured value**	**Measurement uncertainty**
Temperature (PT100)		± 150 mK
Pressure		$\leq$ 1 mbar
Bubble departure diameter	1.46 mm	43 %
	0.5 mm	36.6 %
Interface / contact line velocity	0.1 m/s, 1503 fps	78.2 %
	0.5 m/s, 1503 fps	25.8 %
For the IR measurement no uncertainty can be quantified as explained in section 4.2		

Table A.5: Measurement uncertainties

The calculation of the uncertainty of the interface / contact line velocity is performed comparable to the bubble departure diameter (cf. Eq. 4.3) with $\Delta X_p = 3$ pixel and 3004 frames per second.

A.10 Single bubble heat flux

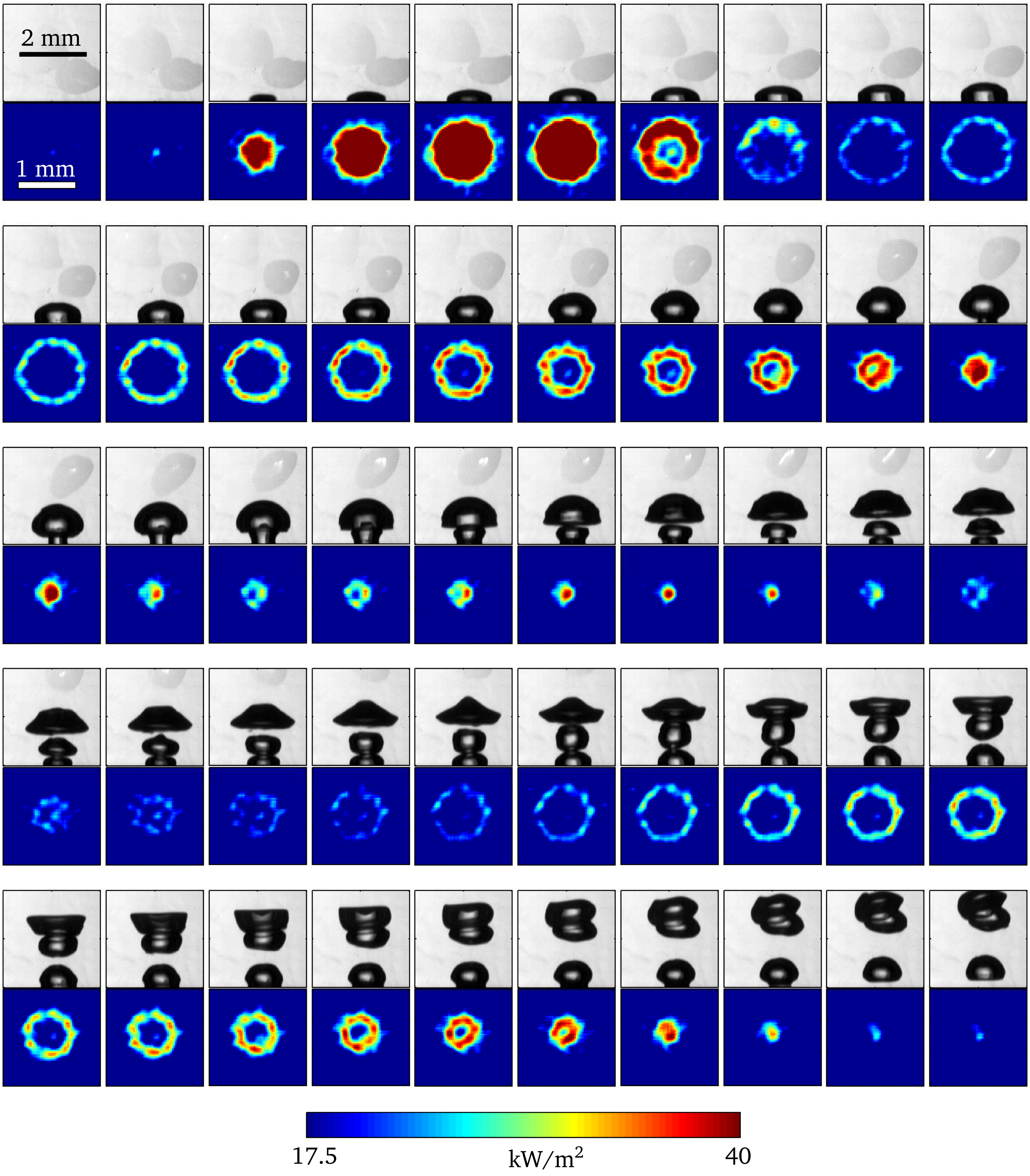

Figure A.9: Heat flux profile and bubble shape at 450 mbar (time increment = 0.665 ms/picture)

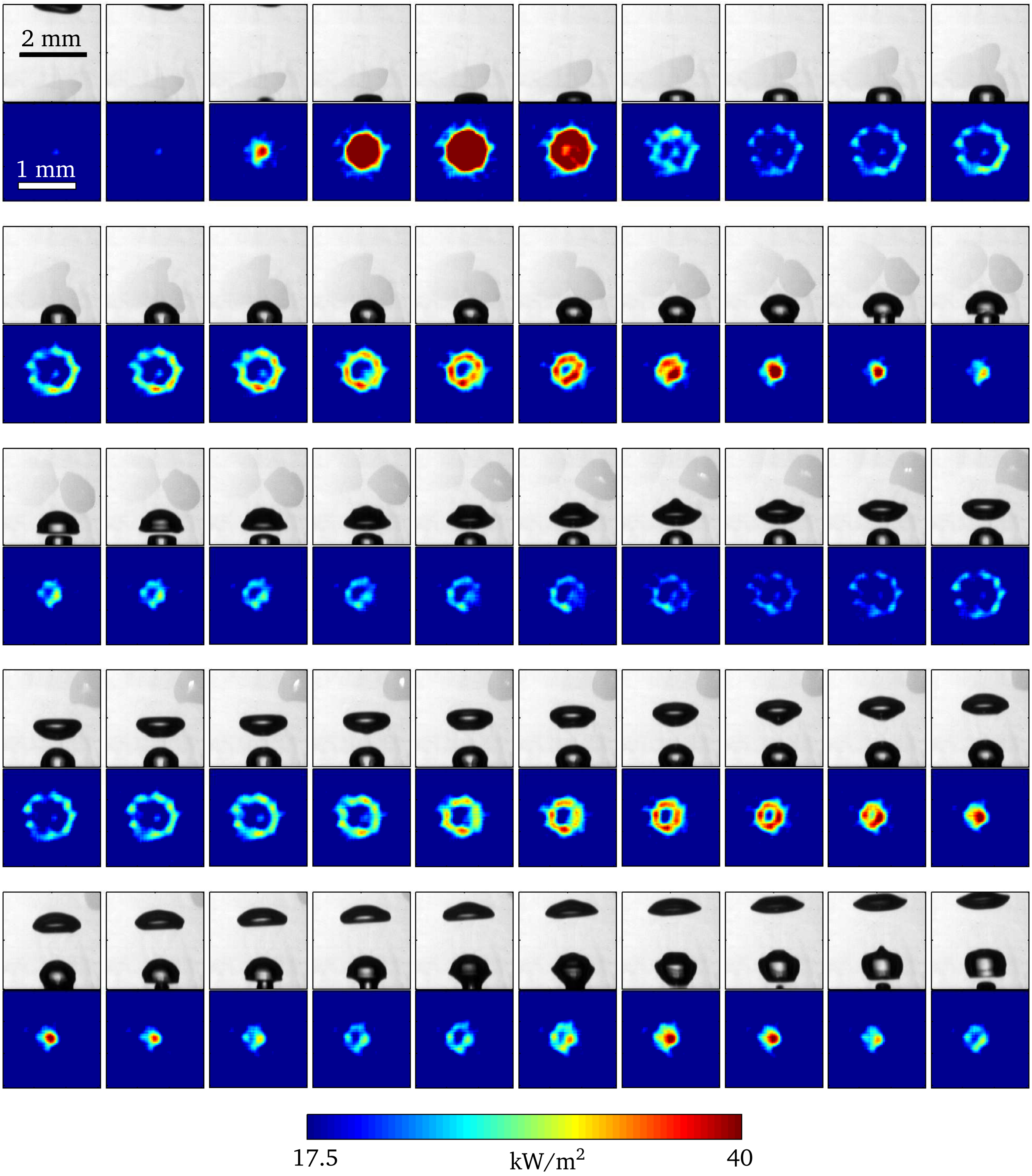

Figure A.10: Heat flux profile and bubble shape at 500 mbar (time increment = 0.665 ms/picture)

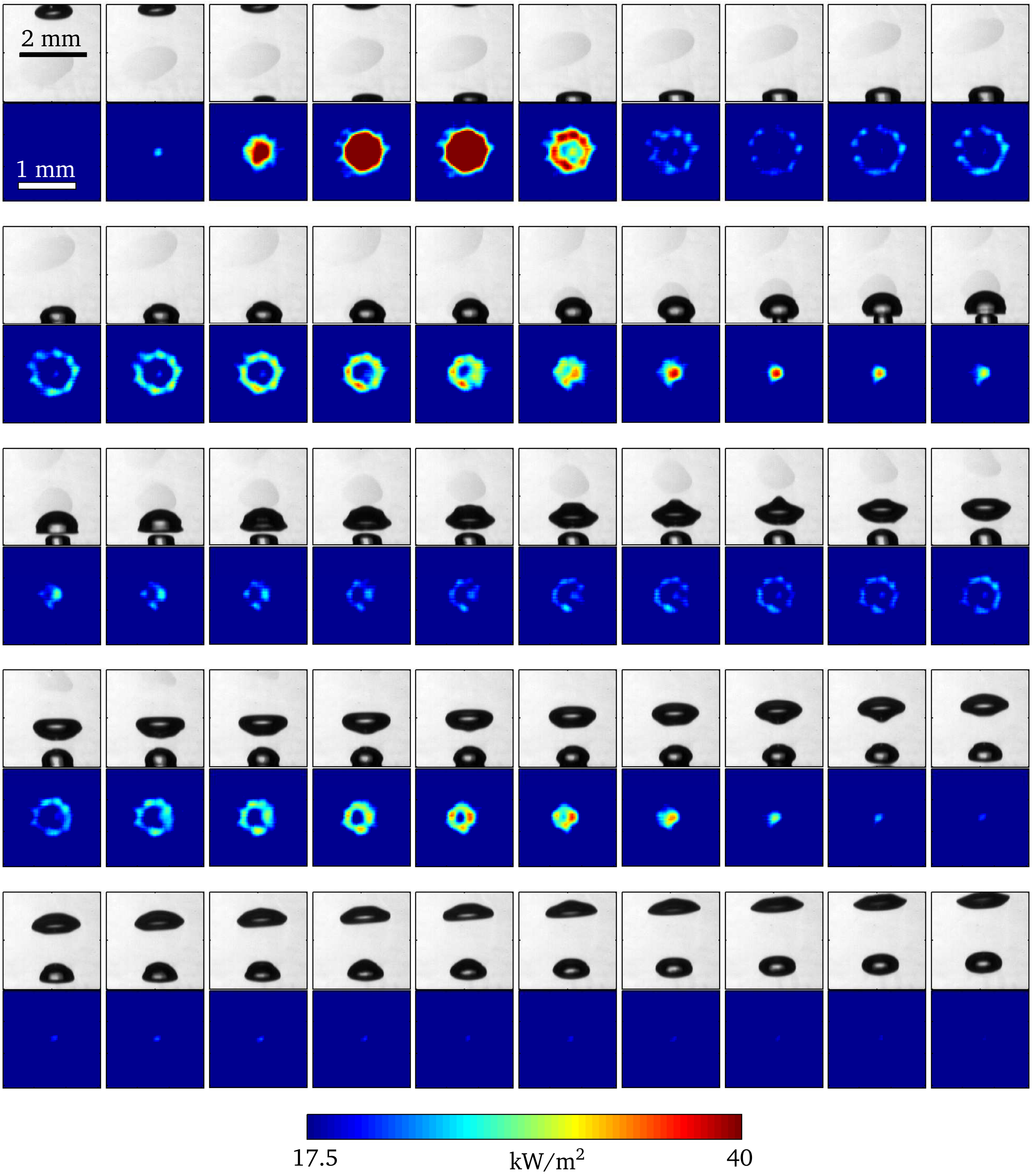

Figure A.11: Heat flux profile and bubble shape at 550 mbar (time increment = 0.665 ms/picture)

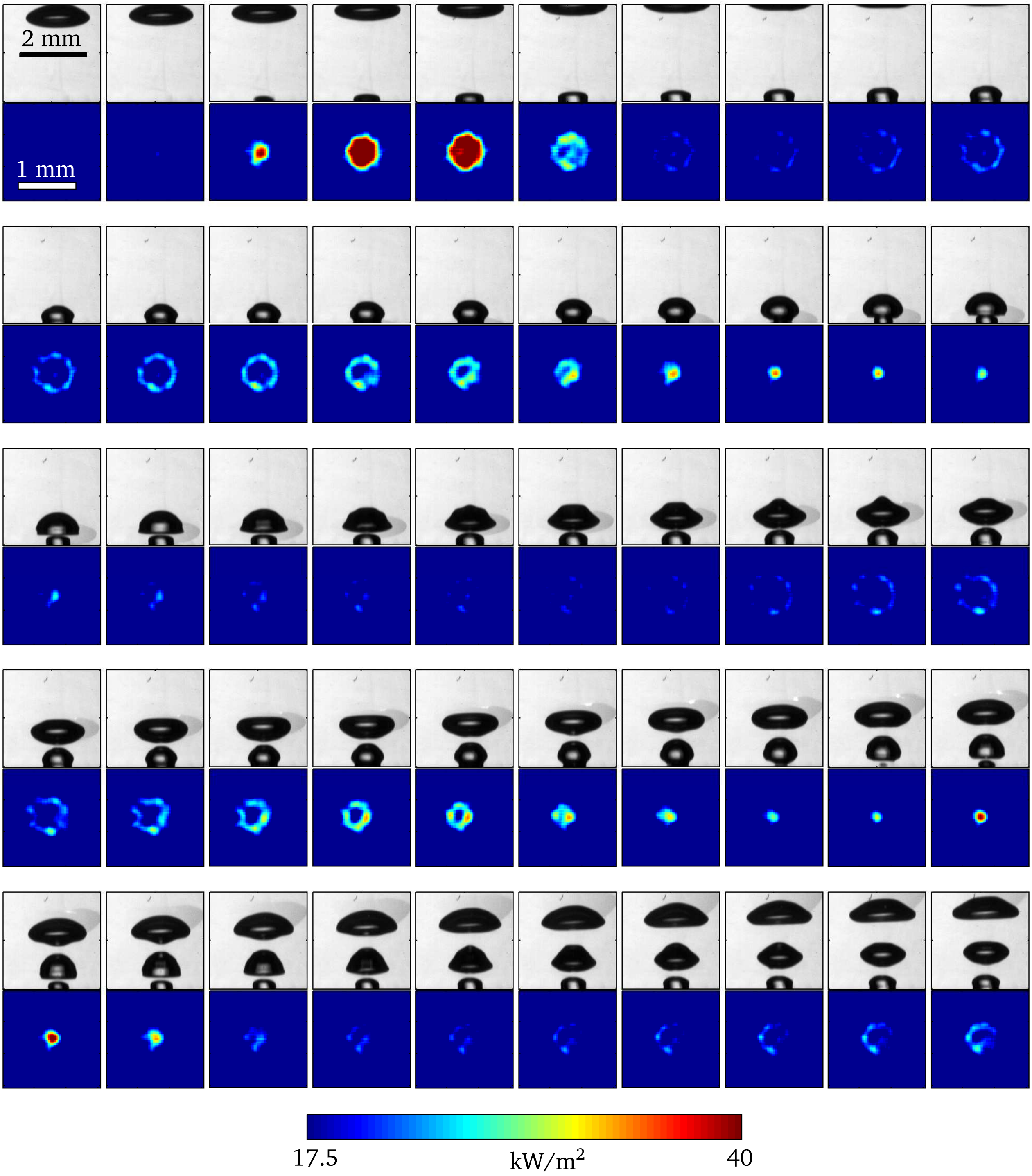

Figure A.12: Heat flux profile and bubble shape at 600 mbar (time increment = 0.665 ms/picture)

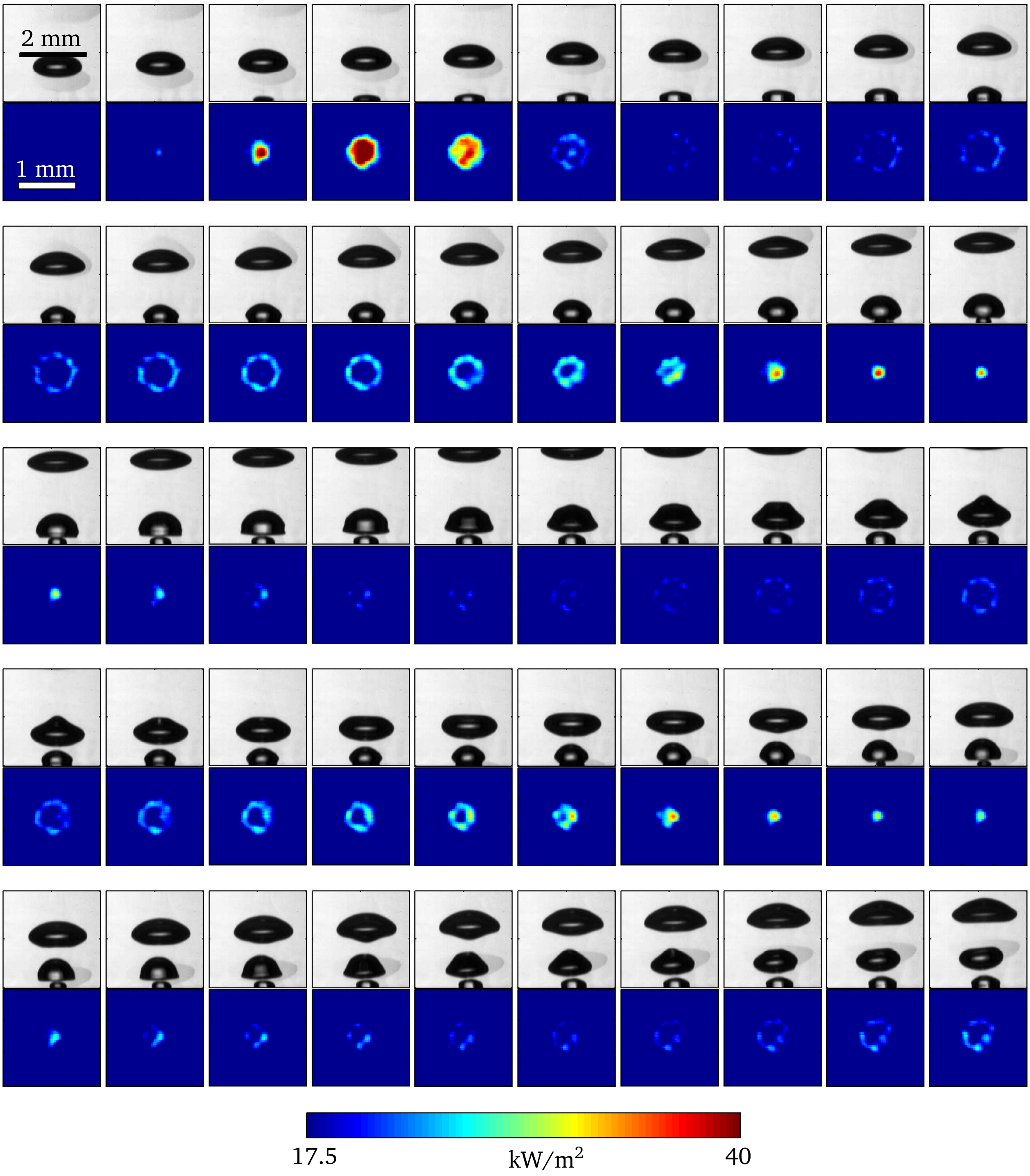

Figure A.13: Heat flux profile and bubble shape at 650 mbar (time increment = 0.665 ms/picture)

Curriculum Vitae

Axel Sielaff

Diplom-Ingenieur

*08. Mai 1983 in Langenhagen

Viktoriastraße 69
64293 Darmstadt

Schulbildung

1989 - 1993	Grundschule in Ilten
1993 - 1995	Orientierungsstufe in Sehnde
1993 - 2002	Gymnasium in Lehrte, Abschluss: Abitur

Wehrdienst

06/2002 - 03/2003	Wehrdienst

Studium

10/2003 - 09/2008	Maschinenbau an der Leibniz Universität Hannover Abschluss als Diplom-Ingenieur im November 2008 Vertiefungsrichtung: Energie- und Verfahrenstechnik

Berufliche Tätigkeit

seit 11/2008	Wissenschaftlicher Mitarbeiter am Institut für Technische Thermodynamik der TU Darmstadt